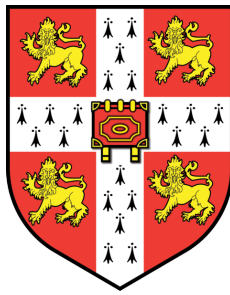


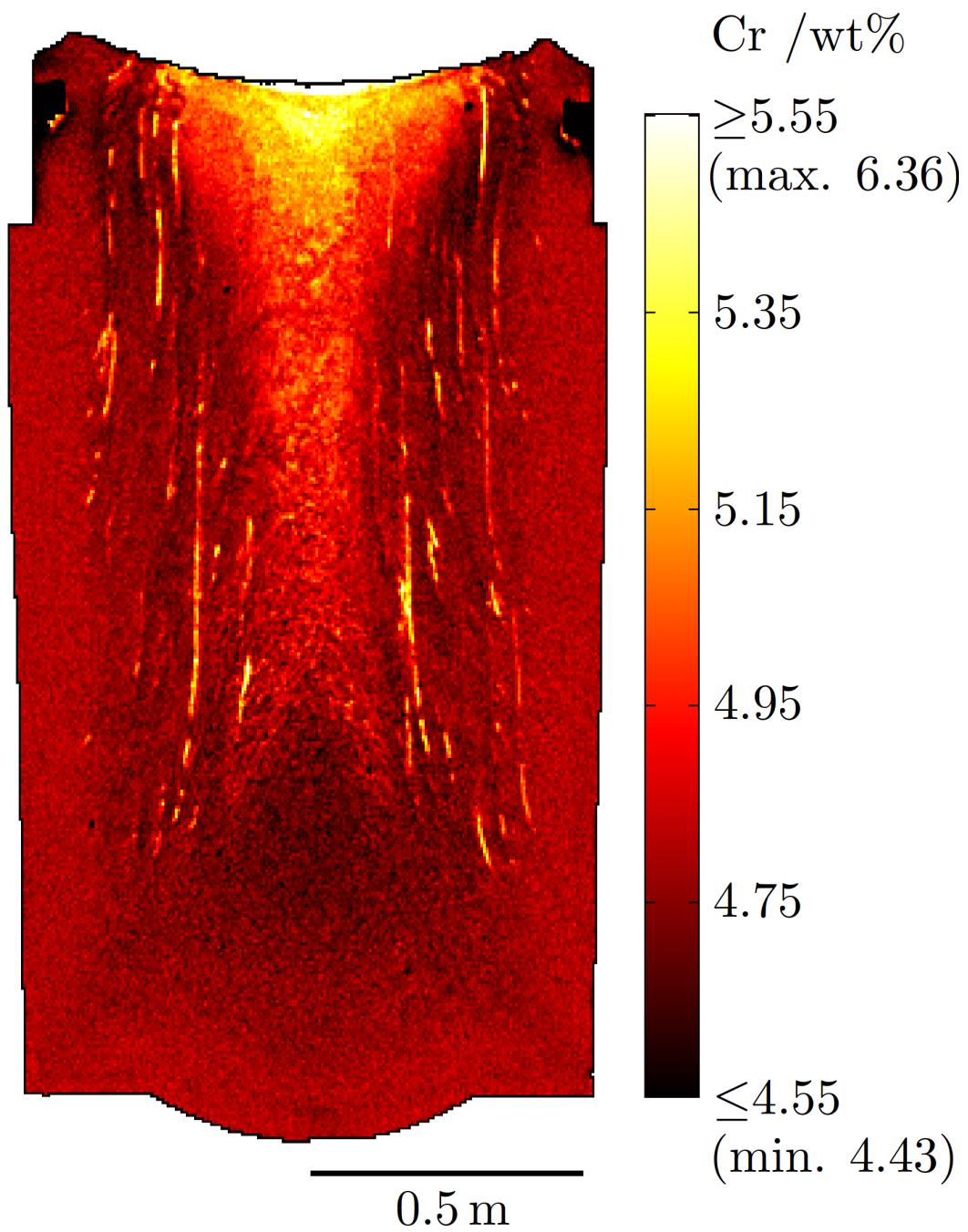
Macrosegregation in Steel Ingots



Edward John Pickering
Fitzwilliam College
University of Cambridge

A thesis submitted for the degree of
Doctor of Philosophy
September 2014

Note that for reasons of commercial sensitivity, the aspect ratios of some of the ingots presented in the figures in this thesis have been changed. Any scale bars provided in such figures refer only to horizontal distances. Ingots have also had their flutes (patterned outer surfaces) removed, and some figures have been pixelated.



Declaration

This thesis is:

- my own work and contains nothing that is the outcome of work done in collaboration with others, except where indicated in the text;
- not substantially the same as any that I have submitted for a degree or diploma or other qualification at any other university; and
- does not exceed the prescribed limit of 60,000 words.

Aspects of this work have been published in the literature as follows (in order of submission):

- E.J. Pickering, Macrosegregation in Steel Ingots: The Applicability of Modelling and Characterisation Techniques, *International Journal of the Iron and Steel Institute of Japan*, 53:935-949, 2013 (Chapter 2).
- E.J. Pickering and H.K.D.H. Bhadeshia, The Consequences of Macroscopic Segregation on the Transformation Behaviour of a Pressure-Vessel Steel, *Journal of Pressure Vessel Technology*, 136:031403, 2014 (Chapter 4).
- E.J. Pickering and M. Holland, Detection of Macrosegregation in a Large Metallic Specimen Using XRF, *Ironmaking and Steelmaking*, 41:493-499, 2014 (Chapter 7).

- E.J. Pickering and H.K.D.H. Bhadeshia, Macrosegregation and Microstructural Evolution in a Pressure-Vessel Steel, *Metallurgical and Materials Transactions A*, 45:2983-2997, 2014. (Chapter [4](#)).
- E.J. Pickering, S.S. Al-Bermani and J. Talamantes-Silva, Application of Criterion for A-Segregation in Steel Ingots, *Materials Science and Technology*, in press (Chapter [6](#)).

A handwritten signature in black ink, appearing to read 'E.J. Pickering', with a long, sweeping underline.

E.J. Pickering
Cambridge, September 2014

Acknowledgements

First, I'd like to extend my sincerest thanks to my academic supervisor, Prof. Harry Bhadeshia, and my industrial supervisors, Dr. Daniel Cogswell (Rolls-Royce) and Dr. Jesus Talamantes-Silva (Sheffield Forgemasters) for their continuous support over the past three years. Whether I have required clarification of an academic point, extra funds for an ambitious new experiment, or a persuasive force to get things moving around Forgemasters, they have always delivered. In particular, I'd like to thank them all for giving me the freedom to pursue what I felt relevant to my PhD, and for providing a working environment free from pressure and constant evaluation.

I have been very fortunate to collaborate not only with my industrial sponsors, Rolls-Royce Power Engineering plc, who I must acknowledge for their generous sponsorship, but also with Sheffield Forgemasters International and Geotek Ltd. I've interacted with so many helpful people at Forgemasters that I am not able to mention them all here, but special thanks must go to Dr. Sinan Al-Bermani, Connor Chesman, Dr. Peter Davies, Dave Pearson, Annalies Brackley, Ian Frost, Michael Howson, Toby Jennings and Dr. Michael Blackmore. At Geotek, Dr. Peter Schultheiss, Dr. Melanie Holland and Peter Hugget have been fantastic to work with - not only were they as excited as I was about the experiments we were doing, but were also continuously concerned with the reliability and reproducibility of the measurements we gathered. Without them, and their kindness in charging me 'mate's rates', two of the chapters in this thesis would not have been written.

The staff working at the Department of Materials Science and Metallurgy in Cambridge must be some of the friendliest in the university, and they have helped create a very relaxed environment that I've enjoyed working in (when I've managed to spend time out of Sheffield or Daventry, that is!) Special thanks must go to Anita Bailey, our superb group secretary, for putting up with my odd requests and constant need to submit expenses claim forms and purchase orders. Her and Anne Chippendale certainly make a formidable team, and I've very much enjoyed our chit-chat when I've ventured upstairs. In accounts, Beccy Stamford and Claire Davies must be thanked for being so efficient processing all my expenses, and my thanks must also be passed to James Goodchild for suffering me when I rushed to him with so many urgent purchase orders! Paul Stokes and Ken Thorn in the workshop, as well as Kevin Roberts in the process lab, have always been very helpful. Dave Saul and Terry Mosdall have offered me some great advice on sample prep, and have been very generous in allowing me to use their facilities in the teaching lab. For provision of laboratory facilities, Prof. Lindsay Greer and Prof. Mark Blamire need to be acknowledged here also.

I'd like to thank all my fellow Phase-Transformation Group members for their friendship and assistance over the past three years, in particular discussions with Steve Ooi, Chris Smith, Wil Solano, Lin Sun, Mathew Peet, Hector Pous-Romero, James Nygaard, Lucy Fielding and Tim Ramjaun have been very useful. Elsewhere in academic circles, Prof. Christoph Beckermann at the University of Iowa and Prof. Andreas Ludwig at the University of Leoben have made very constructive comments about my planned work, and have offered a great deal of encouragement. Conversations with Prof. Merton Flemings and Prof. Andy Howe have also been enlightening. Dr. Geoff West at Loughborough helped me greatly in my quest to find grain-boundary phosphorus segregation, and I'm still in awe of how fast he can prepare TEM specimens in the FIB (usually under 2

hours!). I am also greatly indebted to Professor Grae Worster for being so generous with his time and so patient with me during our discussions of the Rayleigh number and other fluid-flow concepts. Learning from him has been a highly rewarding experience.

I have been lucky enough to spend over 400 hours teaching during my PhD, both supervising at Fitzwilliam College and demonstrating in the department. My utmost appreciation must be passed to Dr. Noel Rutter and Dr. James Elliott for providing me with the opportunity to undertake this teaching, and to Harry for allowing me to! Grants from The Ironmongers' Company, The Worshipful Company of Tin Plate Workers and The Worshipful Company of Leathersellers have allowed me to attend conferences abroad and maximise the spending power of my research funds.

The relaxing time I've spent with my friends throughout my PhD has been invaluable, and I feel privileged to have spent time with such exceptional people. I could not have asked for better friends than Cat Yeoh, James Nygaard, Jack Rowbotham, Laura von Hardenberg, Ella Westby, James Metcalfe, Stephen Thomson, Alan Jamieson, Joe Turner, Garrett Ziolk, Claire Armstrong, Pete Walker, Yulia Ievskaya and Christian Füllgrabe (in addition to many PT-group members). A special mention must be given to my good friend, Peter Walsh, the supreme editor and scrutiniser, for his assistance tidying various cover letters and applications. His expert analysis on the complexities of Jason Statham films has also been a joy to hear.

Finally, I cannot comprehend finishing this foreword without thanking my wonderful family for their love and support over the past three years: my grandparents (including the famous F.B. Pickering), my uncles and aunts, my Godmother Ann, and all my cousins. Liz and Bill Geary (auntie and uncle) have been more than generous in allowing me to stay at their house over the past couple of years

whenever I've been working at Forgemasters (which over the past year has probably averaged two days per week). This not only allowed me to undertake all of my work with Forgemasters (staying in hotels would have been prohibitively expensive), but also meant I had great company in the evening and a lot of very good food! To my wonderful mother and father, thank you for your words of wisdom, love and care. And lastly, all my love to my brother, Tim, and my sister, Roo - not only my siblings, but also my best friends. They are evidently two of the most incredible human beings to have ever existed, despite the fact they probably still don't know what steel is...

Abstract

The macro-scale segregation of alloying elements during the solidification of steel continues to cause problems for manufacturers of large ingots, despite significant progression in both casting techniques and computer modelling in recent decades. Non-uniform distributions of additions within an ingot can cause significant microstructural variations across the material after working and heat treatment, leading to inhomogeneous properties.

It can be found that the integrity of a component is critically affected by results of macrosegregation, and because the results are practically impossible to reverse, the rejection of material that falls outside specification is a possibility. It is true that the vast majority of the world's steel is now continuously cast, but ingot casting is still required for the production of certain heavy industrial components which comprise large high-cost single-piece sections, such as the pressure vessels required for power generation. It is therefore not surprising that the prediction and prevention of macrosegregation in steel ingots remains the subject of a considerable research effort to this day.

This thesis examines the effects of macrosegregation on the microstructure and mechanical properties of the world's most common pressure-vessel steel, SA508 Grade 3, which is used extensively in critical nuclear applications. The effect of A-segregation, a particular type of macrosegregation defect often found in large ingots, is a particular focus of this research. It is found that the enriched material contained within A-segregates produces a significantly harder and finer

microstructure than the bulk material following standard heat treatments. It can also undergo intergranular brittle failure during impact testing, resulting in reduced impact energies and increasing the scatter found in results.

With the results of specific investigations into SA508 Grade 3 in mind, this thesis also assesses more general methods for predicting the location and severity of A-segregation. Shortcomings in current modelling techniques are highlighted, before validation exercises are carried out to determine the effectiveness of a simple predictive criterion recently proposed. This criterion, based on a dimensionless Rayleigh number, is found to be a valuable tool if implemented carefully, and is markedly better when compared to existing simple criterion and complex macromodels in terms of its applicability in an industrial setting. Nevertheless, the validity of applying the Rayleigh criterion to ingot castings is called into question, and reasons are outlined for why it is not strictly appropriate for many casting scenarios. In light of this, the basis of a new criterion for A-segregation is proposed, which retains a simple form whilst being physically meaningful.

The thesis concludes with an examination of the macrosegregation present in a 12.3-tonne steel ingot, which was cast, sectioned and analysed specifically to evaluate casting defects. Using a variety of large-scale assessment techniques, casting conditions were documented and the effects of macrosegregation on ingot structure revealed in remarkable detail. It is hoped that this investigation, which has developed into the most comprehensive of its kind, will provide the future modelling community with a reputable case study for comparison and validation.

Contents

Contents	19
Nomenclature	25
1 Introduction	29
2 Macrosegregation in Steel Ingots: Prediction, Prevention and Characterisation	33
2.1 Introduction	33
2.2 An Overview of Macrosegregation	
Phenomena in Ingots	33
2.2.1 A-Segregation	35
2.2.2 Negative Base Segregation	38
2.2.3 V-Segregation	39
2.2.4 Other Segregation	39
2.3 Modelling Macrosegregation	41
2.3.1 Flemings et al.	41
2.3.2 Multi-Domain Models	44
2.3.3 Continuum Models	45
2.3.3.1 Multi-Phase Models	47
2.3.3.2 Extension to Multi-Component Systems	48
2.3.3.3 21st Century Developments	49
2.4 Macromodel Shortcomings	50
2.4.1 Computational Requirements	51
2.4.2 Input Parameters and Auxillary Models	52
2.4.2.1 Microsegregation Models	52

2.4.2.2	The Permeability Problem	56
2.4.2.3	Dendrite-Arm Spacings	58
2.5	Simplified Approaches	60
2.5.1	The Niyama Criterion	62
2.5.2	The Suzuki and Rayleigh-Number Criteria	63
2.6	Methods for Preventing Macrosegregation	64
2.6.1	ESR, VAR and Derivatives	65
2.6.2	Other Methods	67
2.7	Measuring Macrosegregation in Steel Ingots	71
2.8	Summary and Future Prospects	74
3	Project Background	77
3.1	Motivation, Aims and Scope	77
3.2	High-Integrity Shell Production Route	81
3.2.1	Casting Assembly	81
3.2.2	Casting Procedure	82
3.2.3	Forging and Machining	84
3.2.4	Heat Treatment	87
4	The Effect of Macrosegregation on Microstructural Evolution	91
4.1	Introduction	91
4.2	Experimental	91
4.2.1	SA508 Grade 3 Material	91
4.2.2	Microstructural Investigations	93
4.3	Results	95
4.3.1	Dilatometry	95
4.3.2	Quenched Microstructures	98
4.3.3	Tempered Microstructures	103
4.3.4	Chemistry	104
4.3.5	Hardness	104
4.3.6	Partial-Transformation Experiments	110
4.4	Discussion	111
4.4.1	Evolution of Microstructure and Hardness	111
4.4.2	The Severity of A-segregation	116
4.5	Summary and Conclusions	121

5	The Effect of A-Segregation on Impact Energy	123
5.1	Introduction	123
5.2	Experimental	124
5.3	Results	127
5.3.1	As-Received Material	127
5.3.2	Charpy Impact Tests	128
5.4	Discussion	132
5.4.1	Limitations of Investigation	132
5.4.2	% Ductile Fracture	133
5.4.3	Charpy Scatter and Intergranular Failure	133
5.4.4	Material Integrity	137
5.5	Summary and Conclusions	139
6	Predicting and Tracking A-Segregation	143
6.1	Introduction	143
6.1.1	The Origins of a Rayleigh Criterion	144
6.1.1.1	Application to Mushy Zones	148
6.2	The Torabi Rad et al. Rayleigh Criterion	150
6.2.1	Evaluation of the Rayleigh Number	151
6.2.2	Modelling and Experimentation	152
6.2.3	Results	155
6.2.3.1	Ingot 1	155
6.2.3.2	Ingot 2	156
6.2.4	Discussion	159
6.2.4.1	Limitations and Sensitivities	159
6.2.4.2	A Comparison of Grade 3 and Grade 4N	164
6.2.5	Summary and Conclusions	167
6.3	The Validity of Torabi Rad et al.'s Criterion	169
6.3.1	Development of New Criterion	170
6.3.2	Application of the New Criterion	173
6.3.3	Criterion Development	175
6.3.3.1	A Sticking Point: Compensatory Flows	177
6.4	Synoptic Discussion: Reducing the Occurrence of A-segregation	179
6.4.1	Segregation vs Porosity and Inclusion Retention	180

6.5	Managing Segregation Defects and Porosity	180
6.5.1	Assessment of Tracking Procedure	181
7	Measuring Macrosegregation	185
7.1	Introduction	185
7.2	Experimental	187
7.3	Results	188
7.3.1	Spatial Resolution	188
7.3.2	Mapping	188
7.3.3	Dwell-Time Variation	190
7.3.4	Surface Roughness	190
7.4	Discussion	194
7.5	Practical Implications	196
7.6	Summary and Conclusions	199
8	A Case Study of Macrosegregation in a Steel Ingot	201
8.1	Introduction	201
8.2	Experimental	202
8.2.1	Ingot Selection	202
8.2.2	Casting Apparatus and Procedure	202
8.2.3	Post-Casting Analysis	207
8.3	Results	212
8.3.1	Thermal Data	212
8.3.2	Dimensional Data	213
8.3.3	Porosity	213
8.3.4	Macrosegregation Measurements	220
8.3.5	Macrostructure	220
8.3.6	Microstructure	226
8.3.7	A-segregates	234
8.4	Discussion	234
8.4.1	XRF as an Assessment Technique	243
8.5	Summary and Conclusions	244
9	Concluding Remarks	247

10 Scope for Future Work	251
A Materials Properties	255
A.1 Gray Cast Iron Properties	255
A.2 Ceramic Properties	257
A.3 Sand Properties	258
References	261

Nomenclature

Variables and Symbols

The units for the variables listed below follow the International System of Units (SI), unless stated otherwise in the text.

α	Ferrite
α_T	Thermal diffusivity
β	Solidification shrinkage ($(\rho_s - \rho_l)/\rho_s$)
γ	Austenite
θ	Cementite
λ	Dendrite arm spacing - subscripts '1' and '2' added for primary and secondary spacings, respectively
μ	Dynamic viscosity
ν	Kinematic viscosity
ρ	Density - subscripts 'l' for liquid, 's' for solid, and 0 for reference
σ	Standard deviation - subscripts 'p', 'b', '*' and 'net' for peak, background, theoretical and net, respectively
τ	Time
B	Density gradient (in the liquid)
C	Number of counts - subscripts 'p' and 'b' for peak and background, respectively

C	Concentration - subscript 'l' for liquid, other subscripts often added for particular elements
D_l	Diffusion coefficient in the liquid
d	Diameter
F	Force
f	Volume fraction - subscripts 's' for solid and 'l' liquid
G	Temperature gradient
g	Acceleration due to gravity (scalar)
\mathbf{g}	Acceleration due to gravity (vector)
h	Height
K	Permeability (scalar)
\bar{K}	Local average permeability
\mathbf{K}	Permeability (tensor)
M_s	Martensite start temperature
m	Mass
N_y	Niyama number
p	Pressure
R	Isotherm speed (also casting speed) - subscript 'v' for in vertical direction Isotherm velocity
Ra	Rayleigh number
r	Radius
t	Time - subscript 'F' for freezing
T	Temperature
\dot{T}	Cooling rate
u	Fluid velocity
V	Volume

v	Local velocity of interdendritic liquid relative to solid (vector)
W	Fluid speed in vertical direction

Acronyms

APC	Anti-piping compound
ASME	American Society of Mechanical Engineers
CAD	Computer-aided design
CET	Columnar-to-equiaxed transition
DBTT	Ductile-to-brittle transition temperature
DC	Direct-chill
EDX	Energy-dispersive X-ray spectroscopy
EPMA	Electron-probe microanalysis
ESR	Electroslag remelting
FE	Finite element
FEG	Field emission gun
FIV	Final insulating value
LSRE	Local solute redistribution equation
OES	Optical emission spectroscopy
RPV	Reactor pressure vessel
SEM	Scanning electron microscope (microscopy)
SIMS	Secondary-ion mass spectrometry
STEM	Scanning transmission electron microscope (microscopy)
TC	Thermocouple
TEM	Transmission electron microscope (microscopy)
VAR	Vacuum-arc remelting
XRF	X-ray fluorescence spectroscopy

Chapter 1

Introduction

When alloys solidify, solute is partitioned between the solid and liquid to either enrich or deplete interdendritic regions. This naturally leads to variations in composition on the scale of micrometres, i.e., to microsegregation. Macrosegregation, however, refers to chemical variations over length scales approaching the dimensions of the casting, which for large ingots may be of the order of centimetres or metres. Microsegregation can be effectively removed by homogenisation heat treatments, but it is practically impossible to remove macrosegregation due to the distances over which species are required to diffuse. Almost all macrosegregation is undesirable for casting manufacturers as the chemical variations can lead to changeable microstructural and mechanical properties.

The primary aim of the work detailed in this thesis was the investigation of macrosegregation in the world's most popular pressure-vessel steel, SA508 Grade 3, which is extensively used in critical nuclear applications. In particular, focus is given to a specific type of segregation, A-segregation, and its effect on microstructural and mechanical properties in the alloy. The chapters found in the latter half of this thesis, however, are concerned with techniques and phenomena that are not just of relevance to SA508 Grade 3, but are more generally applicable to large steel ingots.

This thesis begins, in Chapter 2, with an introductory review of the literature that explores our current understanding of macrosegregation phenomena, and

goes on to assess the development of predictive macrosegregation models to date and highlights the shortcomings of these approaches. Methods of macrosegregation prevention and measurement are also briefly surveyed. The context of the research performed is described in Chapter 3, which also introduces the steels and production processes of interest. The investigations that are then presented in Chapters 4 to 8 can be broadly split into two categories. First, the effects of macrosegregation (specifically A-segregation) in large SA508 Grade 3 forgings are examined: Chapter 4 is concerned with its effects on microstructural evolution, whilst Chapter 5 studies the impact that A-segregation can have on the results of Charpy V-notch tests. Second, investigations are presented that are more widely applicable to steels: Chapter 6 evaluates procedures that can be used to efficiently predict and track macrosegregation defects in large forgings, and Chapter 7 assesses a method for accurately measuring segregation over large length scales. Chapter 8 is devoted to a detailed case study of macrosegregation in a 12 ton ingot, cast purely for research purposes. This section of the thesis draws together many of the topics addressed in previous chapters. Finally, concluding remarks are given in Chapter 9 and the scope for future work is examined in Chapter 10.

Chapter 2

Macrosegregation in Steel Ingots: Prediction, Prevention and Characterisation

2.1 Introduction

This literature review examines the development of predictive methods for macrosegregation, assesses the viability of their use today in an industrial environment, and goes on to highlight the key factors limiting their effectiveness. Potential strategies for macrosegregation mitigation are also explored, as are methods of segregation detection.

2.2 An Overview of Macrosegregation Phenomena in Ingots

The first examinations of macrosegregation phenomena in steel ingots were carried out many decades ago, and although our understanding of the processes leading to segregation has improved considerably, the same defects can still be observed in ingots made today [1; 2]. These, shown in Fig. 2.1, include A-segregation, V-segregation and negative base segregation (bottom cone).

Up to the mid-1960s, solute buildup at the tips of the advancing solid interface was believed to be the predominant cause of macrosegregation phenomena in ingots [1; 3; 4; 5; 6]. However, subsequent work has not supported this idea. It is now recognised that the majority of solute is rejected sideways from a growing dendrite, enriching the mushy zone, and that accumulation in front of dendrite tips is negligible - the boundary layer has a thickness of the order of D_1/R (D_1 is the diffusion coefficient in the liquid and R is the dendrite tip velocity), which for ingot solidification may only be $\approx 10^{-5}$ m [7].

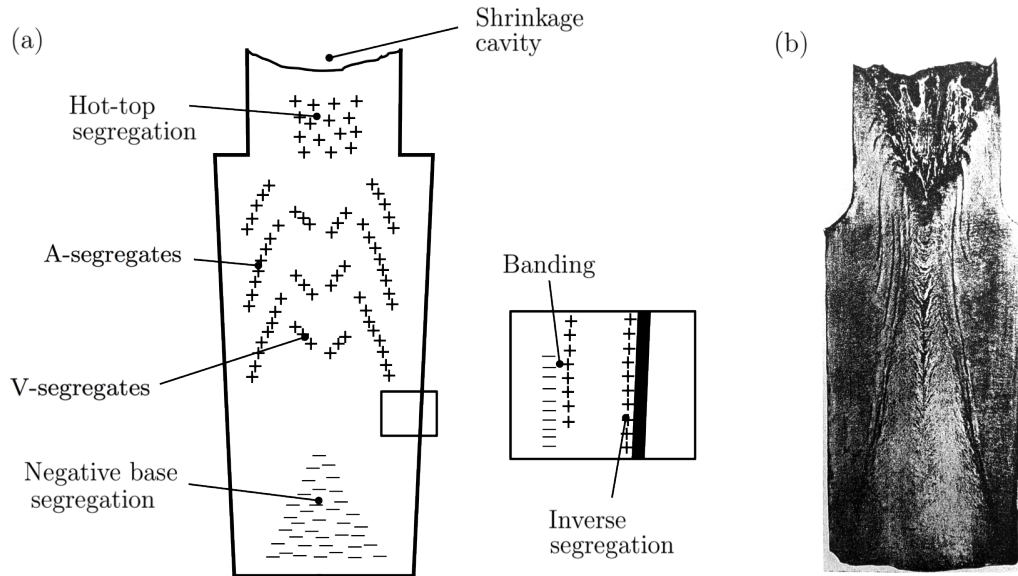


Figure 2.1: Schematic of the different types of macrosegregation that can be found in large ingots. Positive segregation is denoted by + symbols (regions enriched in solute) and negative by - (regions depleted). Similar figures can be found in other macrosegregation reports [8]. (b) Macroetched section of a 10 ton steel ingot [1], no compositional information given.

All types of macrosegregation originate from mechanisms of mass transfer during solidification. The movement of enriched liquid and depleted solid, Fig. 2.2, can occur through a number of processes:

- Convective flows, Fig. 2.2a, due to density gradients caused by temperature and composition variations in the liquid. The thermal and solutal buoyancy

contributions can either aid or oppose each other depending on whether local temperature and concentration fields cause liquid density to increase or decrease. The convection due to the coupled action of temperature and solute is known as *thermosolutal* convection.

- Movement of equiaxed grains or solid fragments which have either nucleated heterogeneously in the melt, become detached from dendrites due to remelting/stress, or have separated from the mould wall after pouring, Fig. 2.2b. Equiaxed grains in steels are denser than the surrounding liquid and will hence tend to sink. This mechanism, along with convective fluid flow, is a dominant macrosegregation process in large ingots.
- Flow to account for solidification shrinkage and thermal contraction of the liquid and solid on cooling, Fig. 2.2c.
- Deformation of the solid network due to thermal stresses, shrinkage stresses and metallostatic head (i.e., the pressure provided by the liquid metal above), Fig. 2.2d.
- Imposed flows due to pouring, applied magnetic fields, stirring, rotation etc.

The complex interplay between these mechanisms makes accurate modelling of macrosegregation phenomena a formidable challenge, often involving complicated mathematical treatments. Thus, before such models are discussed, some qualitative explanations of how these mechanisms lead to macrosegregation defects are given below.

2.2.1 A-Segregation

A-segregates arise due to the flow of solute-rich interdendritic fluid via thermosolutal convection. They are characterised in the final solidified microstructure as channels of enriched solid, which can have near-eutectic composition. Their formation mechanism can be described as follows: in steels the enriched interdendritic liquid will often be less dense than the bulk liquid (due to enrichment in light elements such as C, Si, S and P), and will hence tend to rise. As the liquid moves towards the bulk liquid and the top of the ingot it will increase in

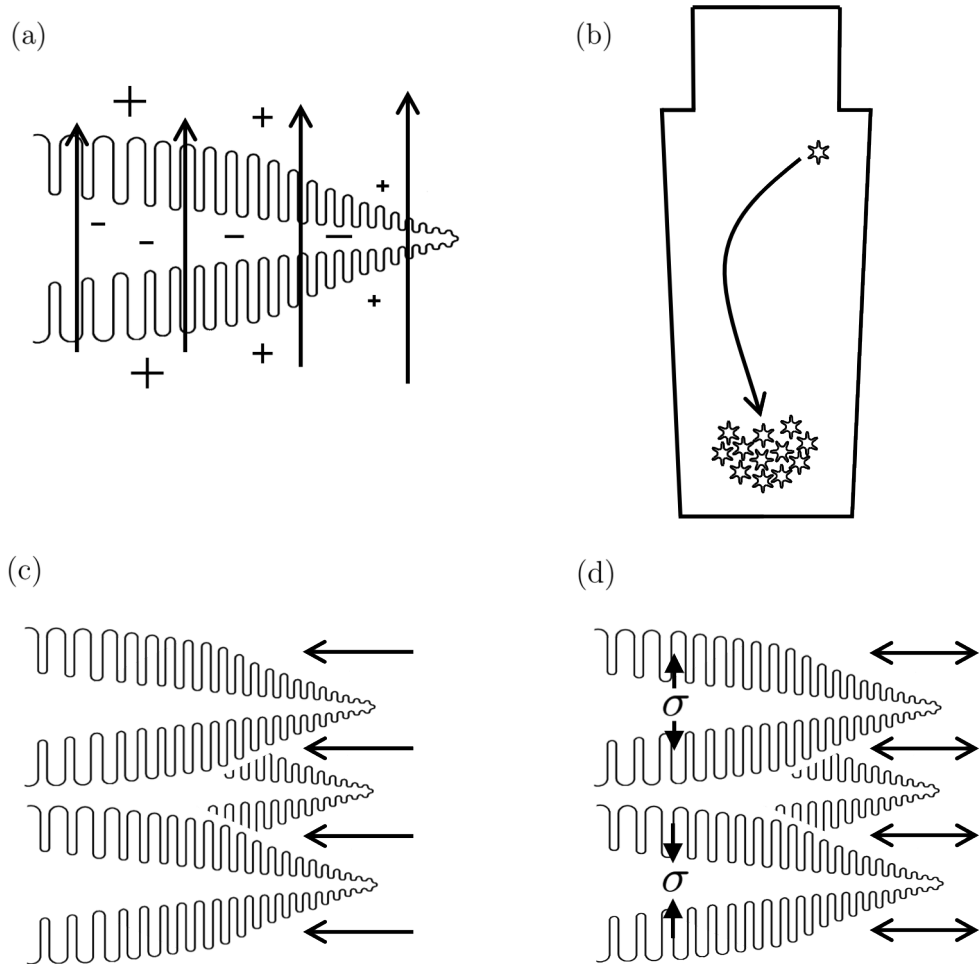


Figure 2.2: Schematic of the processes which lead to mass transport during ingot solidification. (a) Convective flows in the enriched interdendritic liquid passed the depleted solid dendrites (+ symbols denote enrichment in solute in the liquid, whilst - denote depletion in the solid), (b) grain sedimentation (more generally solid movement), (c) liquid flow to feed solidification shrinkage and (d) mushy-zone deformation. Note that the columnar solid in (a), (c) and (d) has grown from the mould wall.

temperature, but its composition will remain nearly constant due to slow mass diffusion (it will therefore be out of equilibrium with the solid it encounters). This hotter enriched liquid then causes delayed growth or remelting of the solid around it, creating persistent solute-enriched channels. A-segregates are also commonly referred to as ‘channel segregates’, or ‘freckles’ or ‘chimneys’ when they arise in directionally-solidified castings (when the melt is cooled from below, for instance during the casting of single crystal nickel-based superalloy turbine blades).

The prevalence of A-segregation has meant it is perhaps the most investigated of all macrosegregation phenomena, not only in steels, but also many other systems. Some of the earliest studies which identified the importance of mushy-zone fluid flow on macrosegregation were made by the Japanese steel industry in the 1950s, and focused on A-segregates. Kawai was one of the first to attribute their formation in ingots to the gravity-induced flow of enriched mushy-zone liquid [9], whilst others confirmed that liquid density changes due to composition were of critical importance (by reducing the Si content and increasing Mo levels, it was found that A-segregation could be minimised, since they decrease and increase liquid density, respectively) [10; 11; 12]. Later on, Suzuki et al. found that A-segregates started to form in the mushy zone when the fraction solid was between 0.3 and 0.35, and that their growth persisted until the fraction solid was as high as 0.7 [13].

Similar results were found by investigations of the $\text{NH}_4\text{Cl-H}_2\text{O}$ system, a favourite of researchers because its transparent liquid allows the mushy zone to be directly observed during solidification. Particularly noteworthy $\text{NH}_4\text{Cl-H}_2\text{O}$ studies were carried out by McDonald and Hunt, and Copley et al., and demonstrated that increased solidification times (and alloy freezing ranges) increased the severity of channel segregation [14; 15; 16; 17; 18; 19]. The Pb-Sn system was also the subject of a considerable research effort [20; 21; 22; 23; 24]. Streat and Weinberg not only examined compositional and liquid-density effects in Pb-Sn, but also the extent of fluid drag within the mushy-zone network (i.e., the permeability, discussed below) on channel formation. The nucleation mechanism and stability of channel segregates were likewise investigated experimentally and theoretically in a number of studies [25; 26; 27].

A-segregates are a particular concern for the manufacturers of pressure vessels, as they can be retained through the wall thicknesses of vessels even after extensive forging. They are hence a key focus of this thesis, as will become clear in later chapters.

2.2.2 Negative Base Segregation

It has been proposed that negative base segregation can arise in ingots due to two processes: (i) the settling of partially-solidified solute-depleted (negatively-segregated) equiaxed grains at the bottom of the ingot under the action of gravity and (ii) the general rise of solute-enriched liquid upwards. There has been some dispute over which of these mechanisms is predominant: early investigations by Marburg and others suggested that the flow of enriched liquid upwards was the dominant factor, citing the appearance of negative segregation in ingots which apparently contained no equiaxed zone [3; 5]. But in reality it is rarely the case that steel ingots undergo fully columnar solidification, and more recent modelling investigations have tended to lend greater significance to grain sedimentation [28].

It has been found that the equiaxed zone in a low-alloy steel ingot may extend to well over half its height [28; 29], and that the equiaxed grains at the very base of the ingot are more globular in form than those found further up the ingot (globular grains are rounder and not so branched, equiaxed grains typically start growing in this form before becoming dendritic) [28; 30; 31]. Disconnected grains can form through a number of mechanisms, which include heterogeneous nucleation in the melt and dendrite-arm detachment in the columnar zone [32]. The predominant mechanism is usually detachment due to the action of convective flows or shrinkage stresses. Note that if the density of enriched liquid is higher than the bulk (as is possible, for instance, if the steel is rich in heavy elements like Mo), then flow in the mushy zone will be generally downwards, and this may reduce the severity of both negative base segregation and any positive segregation (enrichment) at the ingot top.

2.2.3 V-Segregation

During the final stages of ingot solidification the centre of the casting is usually occupied by a network of loosely-connected equiaxed grains. It is thought that V-segregates arise due to the fissuring of such networks under action of metallostatic head (i.e. the weight of material above) and solidification shrinkage, see Fig. 2.3, which leads to the formation of open shear planes that can fill with any remaining liquid [33; 34; 35]. This remaining liquid will have been enriched throughout solidification by convective flows from the mushy zone, and also by solidification in the final cavity, and it solidifies to produce positively-segregated solid. Indeed, the solidification of enriched material at the end of solidification generally produces the often-referred-to *centreline* segregation.

Despite being regularly observed, V-segregation is generally not well understood other than through the mechanism given above. Theoretical treatments and models of V-segregate formation in ingots have yet to be produced and are likely to prove challenging as they would need to account for phenomena including equiaxed grain sedimentation, equiaxed mushy zone deformation and fluid flow. Nevertheless, the total lack of literature on V-segregation in ingots is perhaps indicative of a further issue - the disinterest of manufacturers in the subject. It is often the case that the centres of ingots are removed after casting (as will be shown in Chapter 3) or that the effects of V-segregation are insignificant for end applications. Not only would modelling of V-segregation be a great challenge, but it may not prove to be particularly useful.

2.2.4 Other Segregation

Hot-top segregation, banding and inverse segregation are other examples of defects that can arise during ingot casting. Their formation and severity, like most of the other macrosegregation defects, is dependent on casting procedures and ingot size, and hence they will not always be observed in large ingots.

Flemings described hot-top segregation as the positive segregation which can arise below the tops of ingots (i.e., below the head) due to the flow of enriched

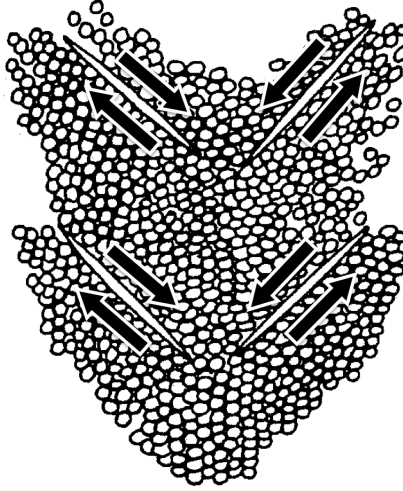


Figure 2.3: Schematic showing formation of V-segregates through shearing on preferred planes during settling and compression of equiaxed grains. Adapted from [34].

liquid from the head of the ingot during the latter stages of solidification. If the temperature gradient moving away from the top surface of an ingot is conducive to solidification (due to insufficient insulation, for example) then a dendritic front will advance downwards from the head surface. Enriched, cool liquid from this solidification may then flow downwards and enrich the liquid below the top [8; 36]. During the early stages of solidification this enriched liquid may spread throughout the large melt pool, but during the final stages (when solidification at the top is most likely) the enriched liquid will remain at the centre and top of the ingot [37]. Improvements in hot-top practices, driven primarily by the need to reduce ingot porosity, have led to reduced levels of hot-top segregation in modern-day ingot making. Note that the hot-top segregation described here is distinct from the general positive segregation often observed at the top of steel ingots (within the head), which is formed due to the advection of enriched liquid upwards.

Bands of segregation (not to be confused with microstructural banding, which is discussed later in this thesis) are thought to result from abrupt changes in

temperature profile across the mushy zone during the early stages of solidification, which may be caused by thermal pulses from convection or changes in heat transfer due to air gap formation (i.e., unsteady heat flow) [37]. Flemings and co-workers suggested that solute-rich bands can be formed due to the remelting of solid and expansion of the mushy zone, and that changes in conditions which lead to acceleration of the liquidus isotherm toward the ingot centre will also give a similar result. They also suggested that solute-poor bands are formed when the mushy zone size is reduced [36]. However, it is not clear to the author how banding can be understood from these arguments in a qualitative sense.

Inverse segregation refers to the positive segregation which can arise directly adjacent to the cold wall of a mould, which is thought to form due to the motion of enriched interdendritic fluid towards the wall to feed solidification shrinkage in the early stages of solidification [8; 38; 39]. Its effects are not observed later on in the casting process because buoyancy-driven flow dominates mass transport. Inverse segregation is found most prominently in direct-chill (DC) casting of aluminium alloys, but its significance in steel ingot casting is likely to be low and it is hard to find investigations on the subject.

2.3 Modelling Macrosegregation

2.3.1 Flemings et al.

The first pioneering work on macrosegregation modelling was carried out by Flemings et al. in the late 1960s [36; 40]. They began by considering the effect of fluid flow resulting from solidification shrinkage only, i.e., the density difference between solid and liquid, and developed the local solute redistribution equation (LSRE) now so familiar to macromodellers:

$$\frac{\partial f_1}{\partial C_1} = - \left(\frac{1 - \beta}{1 - k} \right) \left(1 + \frac{\mathbf{v} \cdot \nabla T}{\partial T / \partial t} \right) \frac{f_1}{C_1} \quad (2.1)$$

where f_1 is the volume fraction liquid, C_1 the concentration of the liquid, $\beta = (\rho_s - \rho_l) / \rho_s$ the solidification shrinkage, k the equilibrium partition ratio, \mathbf{v} the

local velocity of the interdendritic fluid relative to the solid, T the temperature and t time. This was the first treatment to account for the effect of macroscopic fluid flows on solute redistribution. The expression was found by conserving mass and solute within a volume-element of mush, Fig. 2.4, and assuming that mass transfer was due only to liquid flow (not diffusion) and that the solid was stationary and its density was constant - no pore formation was allowed. Further details of its derivation can be found in [40]. Analytical solutions were found by assuming a linear temperature gradient within the mushy zone (hence values of liquid fraction and the rate of solidification were fixed) for unidirectional solidification with planar isotherms. With zero interdendritic flow velocity and no shrinkage, equation 2.1 reduces to the well-known Scheil equation [41; 42; 43]. This also happens when the flow is exactly that required to feed solidification shrinkage. Positive segregation results when the flow velocity is slower or in an opposite direction to shrinkage flow (i.e., fluid flows from cold to hot), whilst negative segregation results when the flow velocity is of greater magnitude in the same direction (i.e., fluid flows from hot to cold) [37]. Solutions of the LSRE were used to predict the formation of solute-rich and solute-poor bands as a result of thermal fluctuations, and also to show the formation of inverse and hot-top segregation [44]. The LSRE model was later extended to ternary systems [45].

Work by the same group later expanded the LSRE model to include the effect of fluid flow in the mushy zone due to buoyancy [47]. Differences in liquid density due to both thermal and solutal effects were accounted for (thermosolutal convection), but because a temperature gradient within the mushy zone was still assumed (and concentration related to temperature via the phase-diagram liquidus), the density of the liquid was a function only of local temperature.

In order to calculate flow velocities in the mushy zone, the resistance to liquid movement provided by the dendritic network needs to be accounted for. To this end, Mehrabian et al. used Darcy's law for flow within a porous medium to modify liquid velocities according to gravity and pressure drops across a volume

element of dendritic mush:

$$\mathbf{v} = -\frac{K}{\mu} (\nabla p + \rho_l \mathbf{g}) \quad (2.2)$$

where μ is the dynamic viscosity of interdendritic fluid, K is the permeability of the mushy zone, p the pressure, and \mathbf{g} the acceleration due to gravity. Previous experimental work had showed that the use of Darcy's law was reasonable [48], although it can only be applied to slow, laminar flow with uniform and constant liquid fraction [49]. This was then combined with conservation equations to produce an expression for the pressure distribution in the mush during solidification, and hence fluid velocities were calculated.

By accounting for density-driven flow, and not just shrinkage, Mehrabian et al. demonstrated that buoyancy-driven flows could lead to A-segregate formation. If the simple LSRE equation 2.1 is considered momentarily, by recognising that the magnitude of $\nabla T/(\partial T/\partial t)$ is equivalent to the isotherm speed R , equation 2.1 can be re-written:

$$\frac{\partial f_1}{\partial C_1} = -\left(\frac{1-\beta}{1-k}\right) \left(1 + \frac{\mathbf{v}}{R}\right) \frac{f_1}{C_1} \quad (2.3)$$

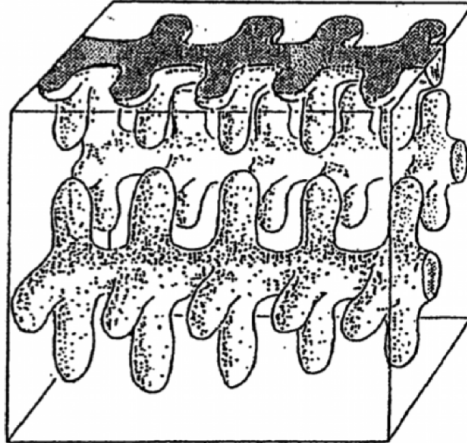


Figure 2.4: Schematic of volume element in mushy zone considered when developing conservation equations. Based on Fig. 2 in [46].

By examining this expression, it can be seen that local remelting (i.e., an increase in liquid fraction) occurs if fluid velocities in the direction of isotherm movement are greater than the isotherm velocities:

$$\frac{|\mathbf{v}|}{R} > 1 \quad (2.4)$$

as $\partial f_1/\partial C_1$ becomes positive. In other words, the movement of cooled enriched liquid across isotherms towards the liquidus results in local remelting and the formation of persistent channels.

One of the limiting simplifications in the works by Mehrabian, Flemings et al. is that their models required the input of an experimental or assumed temperature gradient in the mushy zone, and did not use energy conservation equations to find the transient values. Furthermore, despite recognising the effects of both solute concentration and temperature on liquid buoyancy, the two parameters were always dependently related (the composition of liquid was determined by the phase diagram at a given temperature) and their profiles fixed by the imposed temperature field. They also neglected fluid flow in the bulk liquid and the coupled flows between the bulk and mushy regions. It was not until the development of multi-domain models, and later continuum models, in the 1980s, that the simplifications were gradually removed.

2.3.2 Multi-Domain Models

In multi-domain models conservation equations for mass, solute, momentum and energy are developed for each region (liquid, mushy and solid) and coupled across the moving boundaries between them. For instance, fluid momentum in the bulk liquid is typically described by Navier-Stokes equations for laminar convective flow, whilst in the mushy zone Darcy's law is used. One of the earliest attempts to predict transient mushy zone temperature fields by coupling energy and momentum equations was accomplished through a multi-domain model developed by Fujii et al. [50]. They examined the macrosegregation in a low-alloy steel through the use of a modified LSRE for multicomponent alloys which accounted for com-

plete solid diffusion of interstitials (lever rule behaviour) and Scheil behaviour for substitutionals. Importantly, the density of the liquid in their model was a function of *both* local concentration and temperature and the two fields were no longer fixed. Ridder et al. were the first to examine the effect of natural convective flows in the bulk liquid on interdendritic flows in the mushy zone [51]. They did so by coupling equations for flow velocity and pressure in each domain across the liquidus interface. For the bulk liquid, energy and momentum equations were used but solutal effects were not considered [52]. Despite its originality in dealing with bulk liquid flows, the treatment did not predict mushy zone temperatures, requiring an *a priori* knowledge. Perhaps the first truly predictive model for energy and momentum transport, which also examined bulk-liquid flows, was given by Szekely and Jassal [53]. They used expressions for energy and momentum in the solid, mushy and bulk-liquid zones and coupled the equations using temperatures and velocities at the domain boundaries.

A key problem with the multi-domain approach, however, is that it requires the tracking of the boundaries between solid, mushy zone and bulk liquid. This is often a difficult task, particularly as the boundaries can take on complex morphologies. In using continuum models this difficulty is removed as they comprise a single set of equations which is equally valid over the solid, mushy zone and bulk liquid.

2.3.3 Continuum Models

Bennon and Incropera recognised the suitability of continuum formulations for the liquid-solid transformation in the late 1980s and produced a model for a binary system by combining constitutive equations through simple mixture theory (for the full set of equations, see [54]). As is usual in continuum formulations, the momentum equations used (in two dimensions) were based on the Navier-Stokes equations for fluid flow, but were altered by the addition of the Darcian term which accounts for the resistance of stationary solid in the mushy zone. Assumptions included laminar Newtonian flow in the liquid with constant viscosity, and the Boussinesq approximation, which states that differences in liquid density are

small enough to be neglected apart from when they are multiplied by \mathbf{g} (inertial differences between two fluids are ignored but weight differences are included). Closure of the model required the coupling of the enthalpy (temperature) and solutal fields, which was accomplished by assuming lever-rule equilibrium solidification [55]. The continuum formulation meant that the need for a moving numerical grid was eliminated and the only boundary conditions included in the model were those applied to external domain surfaces. As a result, the first direct numerical predictions of A-segregation were presented.

At almost the same time, Beckermann and Viskanta [56] developed a set of continuum equations almost identical to that of Bennon and Incropera but for the form of the momentum equation. Their formulation, however, used a volume-averaging approach (this is generally thought to be more rigorous [57]) to obtain macroscopic conservation equations from microscopic relations for each phase, which were then combined to produce a single set of equations valid in all regimes. Direct solution of microscopic equations on a small scale is impractical because of the highly complex interfacial geometries in the mushy zone, but when they are averaged over a suitable volume element, the scale of the problem is changed giving manageable macroscopic relations. For details of the volume-averaging procedure and the form of the macroscopic volume-averaged formulations, see [57]. Further exploration of aspects of the volume-averaging procedure and assumptions were made by Ganesan, Poirier, and Voller et al. [49; 58].

Following the pioneering works highlighted above, many studies used similar or modified versions of the same continuum equations to examine a number of different solidification phenomena, including channel formation in directionally-solidified alloys [59; 60; 61; 62; 63; 64], the effect of solidification shrinkage and pore formation [65; 66; 67; 68; 69; 70; 71; 72; 73; 74], and the effect of transformation-induced strains [75; 76; 77]. Many authors have also examined the particular formulations and assumptions of the original models [78; 79; 80; 81].

2.3.3.1 Multi-Phase Models

A shortcoming of early continuum approaches was that they failed to account for the interaction between liquid and solid phases. Important solidification features, such as local solid concentrations, were simply averaged over both phases or unaccounted for. In particular, this meant that the solid transport which is known to form negative base segregation in ingots was not calculable [57] and model results were commonly at odds with experiment. The first studies which attempted to account for solid advection used two approaches. The first used a single momentum equation in which the velocity of a volume element of mush was switched at a certain stage of solidification [82; 83] or through a continuously-varying function [84; 85]. The other approach, developed by Ni and Beckermann, involved the use of a ‘two-phase’ model in which separate volume-averaged conservation equations were used for the solid and liquid phases and included interfacial transfer terms [86; 87; 88]. The relative movement of solid and liquid (and momentum transfer between them) was accounted for by using an effective solid viscosity, the value of which changed according to the local solid fraction. If the solid formed a continuous structure, the solid viscosity was set to infinity - i.e., the solid was assumed perfectly rigid - or if it did not, solid viscosity was varied between zero and infinity depending on the nature of the solid environment.

The strength of the two-phase approach is that liquid/solid velocity relationships don’t have to be imposed and that phenomena such as the settling of free solid grains can be modelled. Furthermore, it can predict liquid and solid interfacial compositions and temperatures, and can also incorporate nucleation and grain-growth calculations [57]. Wang and Beckermann utilised a two-phase model to examine features of equiaxed dendritic solidification, including the settling of equiaxed grains and the columnar-to-equiaxed transition (CET) commonly observed in steel ingots [89; 90; 91]. A key feature of their approach was the introduction of a grain envelope, Fig. 2.5, a fictitious surface which acted as an artificial boundary between the interdendritic and extradendritic liquid. Across the envelope interface, microscopic equations describing grain growth and liquid composition could be linked to macroscopic terms.

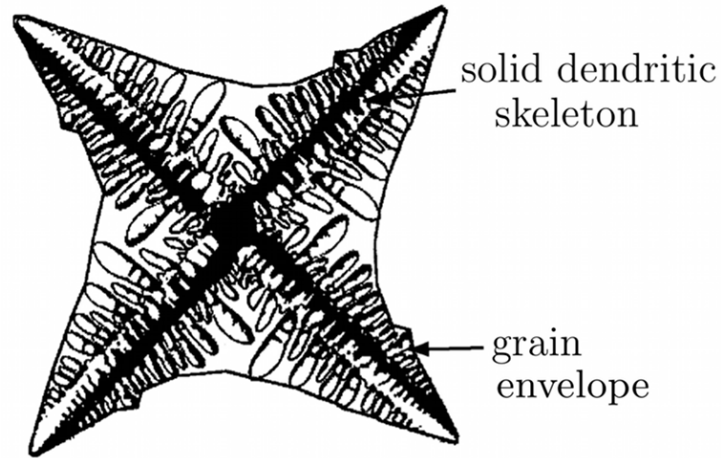


Figure 2.5: Representation of a grain by an envelope containing a solid skeleton and interdendritic liquid. Adapted from [30].

2.3.3.2 Extension to Multi-Component Systems

Most metals of commercial interest are not idealised binary systems, but are multicomponent alloys which can have complex solidification paths. From the mid-1990s, macrosegregation modellers began to adapt their continuum formulations to deal with multicomponent systems of varying complexity. Difficulties arise when moving to three or more system components that are not found with binary alloys - a given liquidus temperature can be reached through more than one alloy composition, and significant variations in partition coefficients and liquidus slopes can occur. Schneider and Beckermann presented the most comprehensive early multicomponent two-phase model [92]. They solved species conservation equations in the liquid and solid for each system component, and coupled the energy and species conservation equations through thermodynamic equilibrium requirements at the solid/liquid interface. The model was not restricted to either lever or Scheil partitioning, but accounted for varying levels of solid-state diffusion. It was later applied to freckle formation in Ni-based superalloys [93; 94; 95; 96; 97; 98], producing one of the earliest studies in three dimensions. Other multicomponent approaches were presented by Vannier et al. [31] and Krane and Incropera [99; 100], but have not been widely used.

2.3.3.3 21st Century Developments

Following on from the pioneering two-phase models of Beckermann et al., many studies in the past decade have focused on the generation, growth and movement of equiaxed grains in convecting melts, and in particular the CET. Beckermann highlighted the need for such research in 2000 [101], and it is certainly key for the prediction of negative base segregation in ingots. One would suppose that such models would also be an essential starting point for the prediction of V-segregation, and would be useful to those predicting the location of A-segregates (A-segregation is often found in equiaxed zones, as well as columnar zones, in ingots).

Investigations during the 21st century included the extension of two-phase models [28; 30; 102], for instance to account for the different behaviours of globular and dendritic equiaxed grains, as well as generation of new formulations [103; 104], such as the three-phase treatment of Ludwig, Wu et al. (the phases were stationary columnar solid, equiaxed solid and parent melt) [105; 106; 107]. Martorano et al. [108] examined the viability of a CET criterion based on the arrest of columnar solidification by the solute field of growing equiaxed grains ahead (so-called ‘soft-blocking’). This was compared to the ‘classical’ mechanical blocking criterion, in which equiaxed grains ahead of a columnar front physically impede its progress.

The group of Wu, Ludwig et al. later drew on the ideas of two previous equiaxed solidification models [89; 90; 109; 110; 111] by using a two-phase method to compute the velocities of so-called “hydrodynamic phases”, whilst solving for mass transport and solute over three phase regions, the so-called “thermodynamic phases” [112; 113]. The interdendritic melt and the solid dendrites, confined in a grain envelope, were regarded as one hydrodynamic phase sharing the same velocity, with the other being the extradendritic liquid. The three distinct thermodynamic phase regions were the solid dendrites, the interdendritic melt and the extradendritic melt. This model was subsequently extended to mixed columnar-equiaxed solidification which required five thermodynamic phase regions: solid

dendrites in equiaxed grains, the interdendritic melt between equiaxed dendrites, solid dendrites in the columnar zone, the interdendritic melt between columnar dendrites, and the extradendritic melt [114; 115] and three hydrodynamic phases (the same as in their original three-phase treatment).

Recently, Ludwig et al. have used their original binary three-phase model [105] to compute macrosegregation in a 2.45 ton steel ingot [116; 117]. When compared to two-phase model results and experimental measurements, it was found the results of the two and three phase simulations were significantly different, and the simplified columnar-only two-phase scheme more accurately reproduced experimental findings. It was suggested that the three-phase approach could have introduced too many equiaxed grains, or that the experimental ingot had undergone mostly columnar solidification.

Other studies in the past decade or so have examined the optimisation of numerical solution methods and solution schemes [118; 119; 120; 121; 122; 123; 124] (following on from Ahmad et al. in 1998 [125]) as well as the incorporation of mechanical stresses [126; 127] into simulations. A significant body of work, however, has been completed using highly-simplified binary single-phase simulations (for instance [128; 129; 130; 131; 132; 133]). This is almost certainly because of the complexities and excessive computing times associated with large multiphase simulations, as will be discussed in the following section.

2.4 Macromodel Shortcomings

There seems to be a general concensus amongst macromodellers that it would be unwise to rely on even the best macrosegregation models of ingot casting for quantitative results, and that basic trends are often not predicted reliably, particularly in commercial codes [134; 135]. The reasons for this appear to stem from two sources: the computational requirements of complex macromodels (which in turn impose constraints and compromises on models), and uncertainties associated with input parameters and auxillary models.

2.4.1 Computational Requirements

In 1999 Gu and Beckermann [136] utilised the multicomponent two-phase model of Schneider and Beckermann [92] to predict macrosegregation patterns in a large cuboidal commercial ingot measuring $1.016 \times 2.083 \times 2.819$ m. It was recognised, however, that in order to predict A-segregates, computing times would have been prohibitively long (years) for the required mesh size, despite the reduced geometry used. In relation to this problem, a year later Beckermann predicted that macromodels which included the generation, growth and settling of equiaxed grains, with sufficiently small mesh sizes to resolve flow patterns associated with A-segregates (i.e., on a scale of a few millimeters) for large ingots would be unavailable for at least the next decade [101]. Today, some fourteen years on, macromodels which include equiaxed grain motion are restricted to binary systems and small geometries struggle to resolve A-segregates, and are too computationally expensive for use in industry [30; 106; 116]. According to Voller et al., models which solve equations on the nanometre scale and coupled them to macroscopic heat and mass transfer terms will not be computationally feasible until at least 2050 [137].

The computational demands of macrosegregation models have often led modellers to reduce the size of the system modelled, to increase mesh sizes or introduce significant simplifications. This is particularly evident in studies introducing new theory or examining model sensitivity to certain parameters. The CET investigations referred to above used only binary systems and small geometries, and the model of Ludwig et al., for instance, was incapable of predicting A-segregate formation [106]. Indeed, many recent studies have resorted to the original treatments by Bennon and Incropera and Beckermann et al. to deliver their predictions [128; 129; 130; 131; 132].

Reducing the size of the model system can drastically reduce times, and using symmetry is certainly essential, but results can only be scaled up to larger problems with caution (macrosegregation will not normally arise in small ingots because they solidify more rapidly). Increasing mesh sizes often means that cer-

tain features, such as A-segregates, are not resolved and changes can significantly affect computed segregation patterns, see Fig. 2.6 [30]. To resolve channel segregates, mesh sizes need to be smaller than channel widths (usually of the order of a few millimetres) [59; 60; 92; 95; 118; 138] and need to be even less if results are to be mesh independent [118; 138]. Introducing too many simplifications can also gravely impact a model's predictive power. Commercial software packages are often guilty of making significant simplifications in order to deliver sensible computing times in an industrial setting [119; 120; 139; 140; 141; 142], and as a result neglect key macrosegregation phenomena, such as equiaxed grain sedimentation. Consequently, their results often appear to provide little predictive insight.

2.4.2 Input Parameters and Auxillary Models

Another issue which continues to plague macrosegregation models is their dependence on the input parameters and auxillary models fed into them, which are themselves topics of investigation and development. Examples of typical input parameters include density-change coefficients, partition coefficients, liquidus slopes, conductivities, dendrite arm spacings, heat capacities, latent heats and number densities of equiaxed-grain nuclei. Slight variations in such values have been found to influence (often significantly) model results [81; 92; 105; 115; 116], and although there are software packages which are able to deliver some of these parameters in steels [143], outputs from them can be limited in their current form (for instance, only values for equilibrium solidification are calculated) and certain parameters, such as those relating to equiaxed grain nucleation, can only be determined experimentally [144]. Clearly this is not an ideal situation for those wishing to compare alloys quickly. Similar uncertainty surrounds the auxillary models of microsegregation and permeability which must be supplied to macrosegregation simulations.

2.4.2.1 Microsegregation Models

Microsegregation models are of utmost importance to macrosegregation investigators. It is the microsegregation of elements on the dendritic scale which

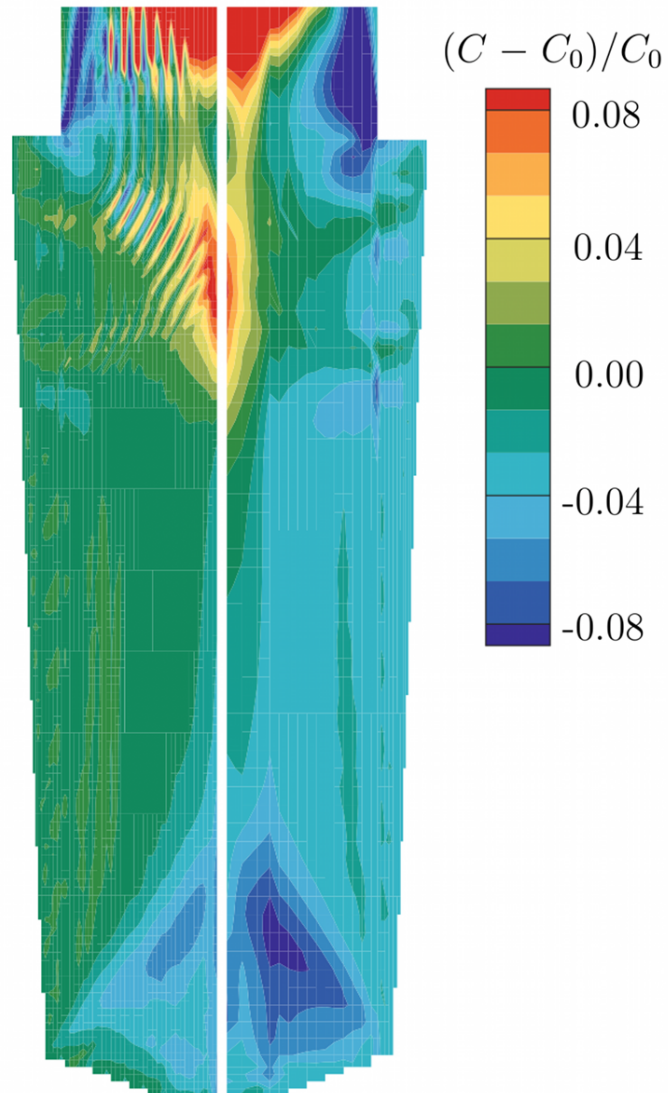


Figure 2.6: Effect of the grid density on the predicted carbon macrosegregation for an ingot. The model used a fixed solid phase. Left: fine grid. Right: coarse grid. Adapted from [30]. The results of using the fine grid appear to show some sort of channels forming at the top of the ingot. However, the channels appear to be of non-segregated material, and it is not clear whether they are an artefact of the model or not.

ultimately leads to enrichment of the liquid and macro-scale advection of species. It is obvious that different results should be expected if one uses an equilibrium lever rule microsegregation model and compares it to a non-equilibrium Scheil treatment [41; 42; 43], but there is a huge range between these two extreme cases (characterised by incomplete solute diffusion in the solid) which is not so easily modelled. Furthermore, microsegregation in steels often falls in this intermediate area due to the mixture of interstitial and substitutional elements present and the range of solidification times given by various casting processes.

Notable analytical or semi-analytical treatments of this solute redistribution problem have been presented by Brody and Flemings [145], Clyne and Kurz [146], Ohnaka [147] and Kobayashi [148]; the Clyne-Kurz-Ohnaka models were later modified by Ganesan [149] and Voller and Beckermann [150]. Their resulting liquid fraction profiles for a 0.5C-3Mn-3Ni (wt%) alloy are compared to the standard lever-rule and Scheil cases in Fig. 2.7, from which it is clear that microsegregation model selection can significantly influence the predicted solidification behaviour. Despite their attractiveness in terms of calculation speed (neglecting Kobayashi's treatment [151]), these somewhat simplified approaches are not readily applied to steels which can exhibit complications such as the peritectic transition and the effects of multiple alloying additions. Instead, finite-difference approaches have often been used to better predict the onset and effects of the peritectic and other transitions. Ueshima et al. predicted the start of the peritectic using empirical relationships based on local solid concentrations [152], whilst Howe et al. introduced 'carbon equivalents' for alloying elements such that the effect of each partitioned species on the peritectic temperature was accounted for in a pseudo-binary model [153; 154]. More recently the use of thermodynamic databases in steel microsegregation models has become popular [155; 156; 157; 158] and kinetic effects have also been incorporated into models [111; 159; 160; 161; 162; 163; 164; 165]. Nevertheless, adding such complexity into macrosegregation models often comes at great computational expense, and consequently there has been some development of rapid microsegregation models for incorporation into macromodels [166]. For those seeking further details on microsegregation models, the review by Kraft and Chang [167] is a useful starting point.

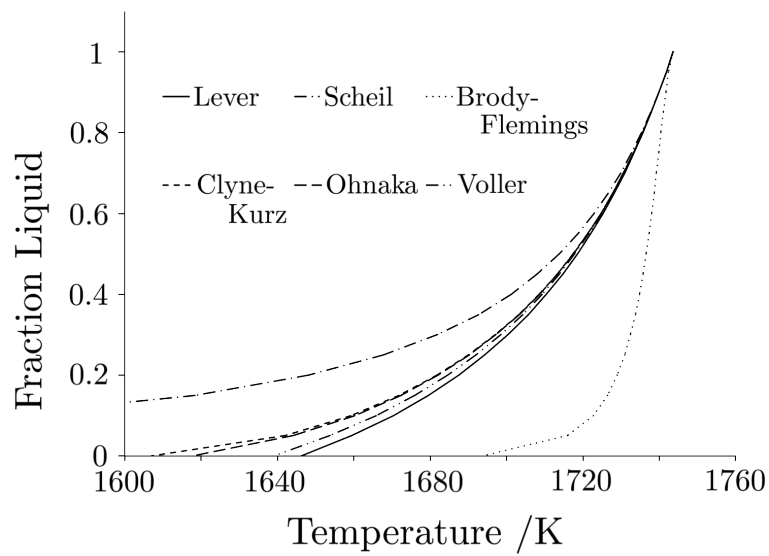


Figure 2.7: Liquid fraction vs temperature plots for a 0.5C-3Mn-3Mo (wt%) alloy found using various microsegregation models. Partition coefficients were obtained from binary phase diagrams. Where needed, the secondary dendrite arm spacing used was 750 μm and the solidification time 5000 seconds (to reflect large ingot solidification). Diffusion information was taken from [168]. Note that the Brody-Flemings treatment is known to give erroneous results for long solidification times [146] (i.e., for moderate or high diffusive homogenisation).

2.4.2.2 The Permeability Problem

In order to accurately predict fluid flow through the mushy zone, its permeability, K , must be known. K is a second-order tensor by definition, such that it depends on the direction of fluid flow relative to a porous geometry, but experimenters and macromodellers have usually assumed it to be isotropic or to comprise only two components (in directions parallel and perpendicular to primary dendrite arms). Nevertheless, the development of models for K has represented a formidable challenge for many years, and rightly so. It depends strongly on factors such as local liquid fraction, dendrite arm spacings and dendrite morphologies, and hence not only varies continuously within a mushy zone, but can also vary from alloy to alloy. Estimations of permeability functions have been made by approximating the geometry of the mushy zone and using specialist forms of Darcy's law, such as the Hagen-Poiseuille model for flow through a bundle of capillary tubes or the Blake-Kozeny (also known as the Carman-Kozeny) model for flow through a packed bed of solids. Many studies have sought to experimentally verify these models [21; 22; 48; 169; 170; 171], but another common approach has been to find functions by fitting experimental results directly to Darcy's law [170; 172; 173; 174; 175; 176].

At high liquid fractions, greater than about 0.7, flow is no longer within an interconnected dendritic network but between dendrite arms. Experimental studies tend to fail in this regime due to the ripening and fragility of dendrites, yet flow here is still of great importance. To avoid these practical constraints, studies by McCarthy, Poirier and others have predicted permeabilities using computer simulations of flow parallel and perpendicular to primary dendrite arms, often through a finite-element Navier-Stokes solver with idealised or experimentally-determined meshes (Fig. 2.8) [177; 178; 179; 180; 181; 182; 183; 184; 185]. Many of these studies used the specific surface area (surface area to volume ratio) of the mush in their permeability relations to capture the effect of dendrite morphology more completely [178; 179; 181]. More fundamentally, some authors have suggested that changes must be made to momentum equations to accurately capture flows at high liquid fractions (that Darcy's law on its own is not sufficient) [61; 178].

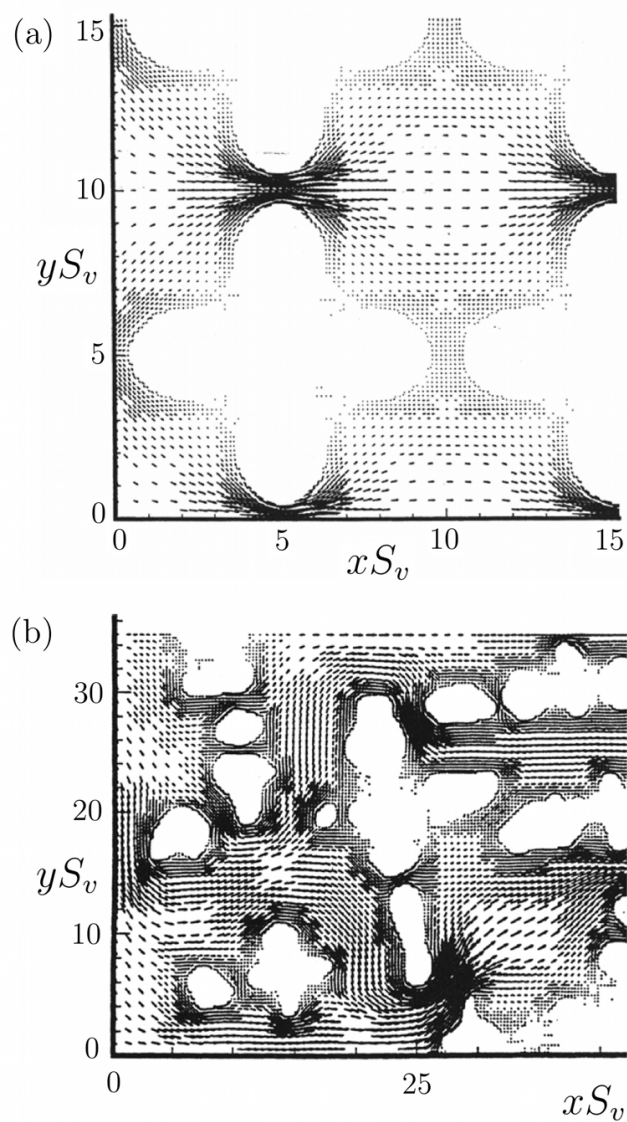


Figure 2.8: Velocity vector plots for flow through (a) idealised array of dendrites and (b) experimentally-measured dendritic array. Taken from [178].

As regards incorporation into macromodels, researchers have typically taken two approaches, either using a single permeability relation approximate for all liquid fractions (e.g., a Blake-Kozeny function) or switching between functions based on the local fraction liquid (often a Blake-Kozeny relationship is used at low

liquid fractions and at high fractions a suitable relationship based on computer simulations) [71; 72; 73; 74; 92; 93; 96; 97; 171]. Results of macromodels have demonstrated that the use of different mushy-zone permeability functions, and neglect of permeability anisotropy, can have a significant effect on the macrosegregation predicted, including the number, length and orientation of channel segregates [71; 99; 128; 129; 186].

The treatments described above have considered only the permeability of mushy zones during columnar solidification, yet it is clear that a significant proportion of solidification (and segregation) in large steel ingots occurs in the equiaxed regime. Wang et al. examined the permeability of equiaxed structures in the mid 1990s, finding that fluid drag was a function of various terms including arm spacings and grain densities, but recently this complex subject appears to have received little attention [187]. It is evident that an improved understanding of grain growth and motion in a convecting melt would only better the predictive power of multi-phase models [101].

2.4.2.3 Dendrite-Arm Spacings

Permeability relations are typically functions of both primary and secondary dendrite arm spacings (understandably, it is usual to find expressions for flow perpendicular to primary arms to be more dependent on secondary-arm spacings than those for flow parallel), and this can lead to further complications when using them in calculations. In many different ferrous and non-ferrous alloys, both primary- and secondary-arm spacings have been shown to exhibit a striking relationship with cooling rate over several orders of magnitude, see Fig. 2.9 for secondary-arm spacings in steels. An increase in cooling rate leads to a decrease in both primary- and secondary-arm spacings. Yet despite this clear trend, there are still issues associated with the prediction of arm spacings.

The cooling rate during solidification can be expressed as a product of the temperature gradient G and the growth (isotherm) velocity R , and hence on the basis of graphs such as Fig. 2.9 expressions using a single exponent, c , were developed:

$$\lambda = b(GR)^{-c} = b\dot{T}^{-c} \quad (2.5)$$

where λ is the arm spacing (subscripts 1 and 2 usually added for primary and secondary spacings, respectively), a , b and c are constants, and \dot{T} is the local cooling rate (\dot{T} not only varies spatially, but can also vary significantly at a given position during solidification - \dot{T} is rarely constant at any point). Although it is true to say that G and R can have different effects on arm spacings when varied independently [189; 190; 191; 192; 192; 193; 194], in ingots G and R are coupled by heat flow, and as such they can be combined into a single variable with a single exponent. Expressions which have been developed for dendrite arm spacings in steels have often taken this form [34; 189; 195; 196; 197; 198], see the selection presented in Table 2.1. By evaluating these expressions for typical casting conditions, it is readily found that the secondary-arm spacings calculated match reasonably well, whilst primary-arm spacings can vary considerably. This is problematic, as even small variations in arm spacings will significantly affect the results of permeability models which rely on primary spacings. There is

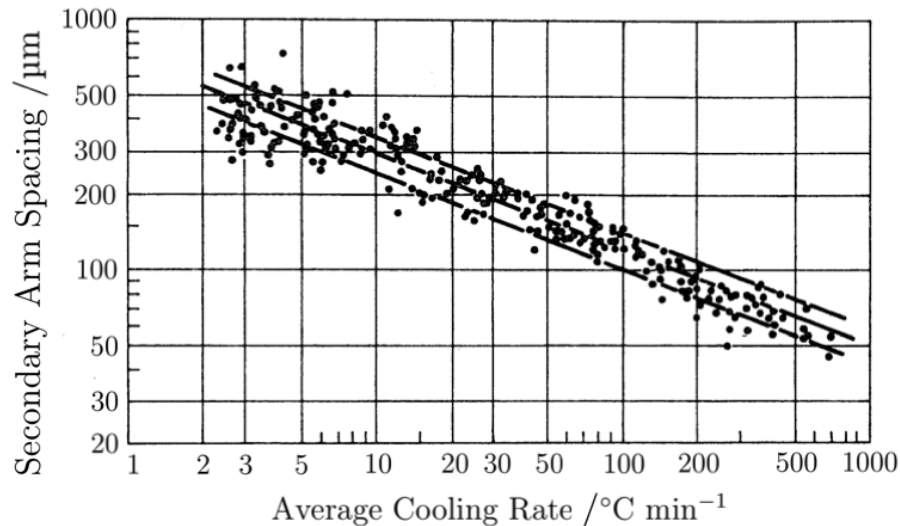


Figure 2.9: Experimental data for secondary dendrite arm spacings in commercial steels containing 0.1-0.9wt% C. Adapted from [188]. Primary-arm spacings follow a similar relationship with cooling rate [189].

currently a lack of primary-arm spacing relations that account for the effect of alloying elements other than carbon, and which also assess the potential influence of primary solidification phase (whether it be delta ferrite or austenite).

For secondary-arm spacings, despite the agreement that can be obtained between relations, it is evident that these models do not truly reflect the more complicated behaviour of secondary-arm spacing observed in reality. Secondary-arm spacings, unlike primary spacings, are known to change moving through the mushy zone due to coarsening (Gibbs-Thomson effect), with kinetics that are likely to vary with composition [7; 189; 190; 191; 195; 196; 197; 199; 200; 201; 202; 203; 204; 205]. Accounting for this coarsening is very important in both microsegregation and permeability models, which can be implemented at any location within the mushy zone. Theoretical secondary-arm relations which account for coarsening have been developed [7; 202; 203], but they are often more complicated and require many more input parameters (hence, they can deliver very different results to the expressions in Table 2.1). There are a number of microsegregation models which have accounted for secondary-arm coarsening directly, see [150] for example, but the effect on permeability has not been dealt with in great detail, and studies usually work with an approximate secondary spacing that is kept constant. Clearly further study of dendrite-arm spacings in steels is required. These investigations may also wish to assess the effect of fluid flow on spacings [101].

2.5 Simplified Approaches

It is clear that the computation times required for current macrosegregation models of large ingots are excessive and that the corresponding results often fail to predict well-known trends. Development of these macromodels should still be an important aim of the macrosegregation-modelling community, particularly in anticipation of greater computational capacity, but at present there is a need for simplified approaches which can be rapidly implemented whilst still making realistic predictions. Users in industry don't want to spend time running a lengthy macromodel, especially if its results are not likely to be useful.

Table 2.1: Expressions for primary and secondary dendrite arm spacings in steels.
 C_i is the concentration of element i in wt%.

Source	Expressions (in μm)	Notes
Suzuki et al. [188]	$\lambda_2 = 146\dot{T}^{-0.386}$	Found by fitting data for low-alloy steels given in Figure 2.9. Valid for $0.14 < C_C < 0.88$.
Jacobi et al. [189]	$\lambda_1 = 283\dot{T}^{-0.49}$ $\lambda_2 = 109\dot{T}^{-0.44}$	Found for a 0.59C-1.1Mn (wt%) alloy.*,**
El-Bealy [195]	$\lambda_1 = 279\dot{T}^{-0.206}C_C^{-0.019-0.492C_C}$ $\lambda_2 = 148\dot{T}^{-0.38}$	Found by fitting data for various low-alloy steels. λ_1 expression only valid for $0.15 < C_C < 1.0$, λ_2 only for $C_C < 0.53$.*
Won et al. [196]	$\lambda_2 = 143.9\dot{T}^{-0.362}C_C^{0.550-1.996C_C}$	Found by fitting data for various low-alloy steels. Only valid for $0.15 < C_C$.*
Cicutti et al. [198]	$\lambda_2 = 113\dot{T}^{-0.38}$	Found by fitting data from [206] for $C_C=0.15$.
Ogino et al.	$\lambda_2 = 123\dot{T}^{-0.33}e^{(-0.281C_C+0.175C_{\text{Mn}}-0.063C_{\text{Cr}}-0.0136C_{\text{Mo}}-0.091C_{\text{Ni}})}$	Presented in [207].

*Other expressions are also given in these references for different compositional ranges.

** Note that a $t^{0.5}$ dependency ($\dot{T}^{-0.5}$) would imply that microsegregation is independent of \dot{T} , since the dendrite arm spacing (λ) and the solute diffusion distance ($x \sim \sqrt{Dt}$) have the same $t^{0.5}$ dependency (the increased diffusion distance given by a slower cooling rate would be matched by the increased arm spacing).

It has been demonstrated that making certain simplifications to models can reduce computing times whilst still delivering similar results - for instance, Schneider and Beckermann demonstrated that when the number of system components was restricted only to those which segregated and influenced buoyancy most critically, similar results were found to when a full set of components was used [92]. Nevertheless, even when binary alloys are considered in fairly simple commercial codes (such as Magma [141], THERCAST [139], ProCAST [142]) full macrosegregation calculations can still take days or weeks to run on the small computer clusters used in industry.

In order to reduce macrosegregation, manufacturers are often able to alter a number of processing parameters (e.g., melt superheat, head height, mould design) and make small changes to the alloy composition. Consequently, there is a need to compare castings conditions and their likely effects on macrosegregation quickly. This can be accomplished using criterion models, which although simple, are often found to be very effective. These include the Niyama criterion for porosity, and Rayleigh-number and Suzuki criteria for channel segregate formation. The assessment of these numbers can be accomplished simply through the manipulation of the results of a ‘purely-thermal’ computation, i.e. one which computes only the temperature field and ignores fluid flow and macrosegregation. Conveniently, it has been found that the temperature fields predicted by simple heat conduction analysis are nearly identical to those predicted in a fully-coupled macrosegregation simulation [136].

2.5.1 The Niyama Criterion

The Niyama criterion is a good example of a simple treatment which has allowed industry modellers to rapidly predict shrinkage porosity in ingots. Although porosity is not a topic of this review, the treatment is certainly worth examining as an illustration of how simple criteria can be formulated and applied. It is given below, written as a condition *for* pore formation [208]:

$$N_y = \frac{dT/dx}{\sqrt{dT/dt}} < \sqrt{\frac{c_1}{\Delta p_{\text{crit}}}} \quad (2.6)$$

where Ny is the Niyama number, Δp_{crit} is some critical pressure drop across the mushy zone and c_1 is a constant. This relation is found by simple manipulation and integration of Darcy’s Law in one dimension to find the pressure drop due to incomplete shrinkage flow. Pores are nucleated when this pressure drop exceeds a critical value (note that this criterion is only valid to predict shrinkage porosity and not the porosity which arises due to dissolved gases). The value for c_1 can be found by integration, but the value of Δp_{crit} must be found experimentally for each alloy (For Fe-C steels $Ny \approx 0.7$). Nevertheless, even if Δp_{crit} is not known, the criterion is still able to highlight regions most susceptible to porosity: Niyama values are readily mapped onto an ingot geometry and their relative magnitudes compared [209].

2.5.2 The Suzuki and Rayleigh-Number Criteria

As discussed above, channel segregates are common in various casting processes and it is useful to be able to predict the likelihood of their formation in a given region, even if their precise location cannot be determined. A number of criteria for the prediction of A-segregates can be found in the literature, most relating to freckle formation in Ni-based alloys, and they are typically some function of the thermal gradient, G , and isotherm speed, R [16; 210; 211]:

$$G^a R^b \leq c \tag{2.7}$$

where a , b and c are constants. Channel-segregate formation depends on the complex interplay of a number of factors, which may appear separate from G and R , including the permeability of the mushy zone and the liquid-density changes due to solute partitioning. However, relations like equation 2.7 have been shown to be effective because many of these factors depend in some way on R and G . For instance, the permeability is typically a function of dendrite-arm spacings, and these are known to depend on the cooling rate, \dot{T} (see above), which is the product of R and G . For static steel ingots with carbon concentrations around 0.7wt%, Suzuki and Miyamoto found that $a = 1$, $b = 2.1$ and $c = 8.75$ [211]; this ‘Suzuki criterion’ has since been used in a number of commercial software packages.

However, there is a key problem with the Suzuki criterion, and that is that the constants a , b and c are not alloy independent, and have been shown to vary significantly from steel to steel [212]. For accurate implementation, these constants would need to be determined for each alloy through experimentation, which restricts its predictive capabilities. A promising alternative to Suzuki-like criteria is the use of a criterion based on a dimensionless Rayleigh number [213; 214; 215; 216]. Rayleigh numbers measure the ratio of the buoyancy forces driving convective fluid flow to the retarding frictional forces inhibiting it: classically in heat flow problems, if a Rayleigh number is below a critical value for a fluid, heat transfer is mainly through conduction, if above, it is mainly through convection - and in theory a single critical value should be valid for a whole system of alloys. Rayleigh numbers for channel-segregate prediction explicitly account for the effects of liquid-density changes due to segregation and mushy-zone permeability, and have already been successfully developed for freckling in directionally-solidified alloys [213], [214]. Recently, Torabi, Beckermann et al. have developed the following Rayleigh number for steel ingots [217]:

$$\text{Ra} = \frac{(\Delta\rho/\rho_0)g\bar{K}}{R\nu} \quad (2.8)$$

where Ra is the Rayleigh number, \bar{K} is the mean permeability, $\Delta\rho/\rho_0$ the fractional density change, g gravity, R the liquidus isotherm speed, and ν the kinematic viscosity. The use of this criterion to predict A-segregation in steel ingots is the focus of Chapter 6 in this thesis, and further details of its application can be found there. Limitations and sensitivities associated with its application are highlighted in that chapter, and questions are also raised as to whether its application to mushy zones moving sideways (perpendicular to gravity) is truly valid.

2.6 Methods for Preventing Macrosegregation

Over the decades, numerous techniques and process modifications have been investigated with the aim of reducing macrosegregation in cast products, and they

have varied considerably in both their complexity and success rate. They all incorporate, to varying extents, the two principal (and somewhat opposing) strategies that can be used to reduce macrosegregation: (i) decrease the relative movement of microsegregated solid and liquid, and (ii) mix and refine the liquid and solid to induce homogeneity.

The relative movement of liquid and solid can be reduced by minimising the driving force for movement (this has already been discussed above with respect to compositional changes and A-segregation, see the previous Section and Section 2.2.1), or by decreasing the time for advective processes to occur (i.e., reduce the solidification time), which can usually be equated to minimising the distances over which movements are possible. Simple alterations can be made to casting processes to achieve the latter, including changes in the geometry and size of the ingot mould to extract heat more rapidly (large, cast iron moulds are used for this precise reason, and hollow ingot moulds are becoming increasingly popular) and the use of reduced superheats. More elaborate methods have included the addition of solid steel balls to solidifying melts to extract heat [218]. It is often the case, however, that decreased solidification times lead to increased levels of porosity and inclusion retention. Although centreline porosity in ingots can be partially combated by inducing a more directional (bottom-top) solidification, more specialist methods are typically needed to reduce both segregation and porosity/inclusion retention simultaneously. Remelting techniques are examples of such processes.

2.6.1 ESR, VAR and Derivatives

Two remelting techniques that have become increasingly popular for large steel ingots are electroslag remelting (ESR), Fig. 2.10a, and vacuum-arc remelting (VAR), Fig. 2.10b, which have been a part of standard production routes for smaller high-integrity nickel-, titanium- and iron-based components for a number of years. They both essentially involve the remelting of an ingot that is used as a consumable electrode: an arc is struck between this ingot and the base of a water-cooled mould (the temperature of which is constrained to control solidifica-

tion rates), gradually remelting the ingot from bottom to top and re-solidifying it below. In VAR, this process is conducted under vacuum, which allows dissolved gases such as N, O and H to escape from the steel, and it can also reduce the concentration of high vapour pressure species like C, S and Mg. Currently capability limits the maximum weight of VAR ingots to around 50 ton, and ESR to around 70 ton. ESR is not performed under vacuum, and therefore could be used for ingots hundreds of tons in weight (inert atmospheres or reduced pressures are sometimes used). Instead, refinement is achieved through the use of a high-reactive slag on top of the remelted melt pool, which removes inclusion-forming species. For small ingots less than 50 tons in weight, ESR or VAR might be preceded by vacuum-induction melting. This process uses induction to melt ingots under vacuum, providing an extra stage of refinement and homogenisation.

The incremental unidirectional solidification which theoretically should be delivered by ESR and VAR should naturally eliminate centreline porosity and segregation, and prevent the formation of negative-base and V-segregation [219]. Nevertheless, centreline (radial) and channel-type segregation have been found in ESR and VAR ingots in many alloy systems [220; 221; 222; 223; 224; 225]. It appears that significant segregation can still occur in the melt pools of these processes, and that increasing the size of ingots and altering process parameters such as power input can often serve to enlarge these pools, increase solidification times and augment fluid flow (although it should be noted that VAR generally delivers faster solidification times than ESR, and is often used in preference for segregation-sensitive alloys) [224; 225]. The electromagnetic field generated by arcing in these processes can also significantly influence fluid flow and hence segregation (see below). In the case of large steel ingots, one might surmise that the top-bottom segregation in the consumed ingot will be transferred to the product and would be difficult to remove.

A unique variation of ESR is found in a process referred to as central-zone remelting [226]. In this process, the core of an ingot is punched out (see Section 3.2.3 for details of this) and remelted back into the original ingot by using the punched core as the electrode. This allows for the refinement of the steel in the core, which can

be heavily segregated and inclusion rich, and a reduction in centreline porosity and segregation. It is even possible to use an electrode of a different composition, permitting the creation of composite ingots with different alloy chemistries at their centres (delivering, for example, a hard outside and tough centre). Although this process may at first appear redundant for the creation of pressure vessels, which require hollow cores, it can in fact be used in a controlled manner to eliminate segregation defects on the inner surfaces of vessels - by trepanning and remelting a core of the correct size, a pressure vessel can be produced with an inner surface that is less defective. It has also been claimed that the process can be used for ingots in excess of 300 tons in weight, far larger than for conventional ESR. Despite these apparent advantages, however, it seems the process has not been popular since its conception in the late 1960s.

2.6.2 Other Methods

A technique recently investigated to reduce top-bottom segregation in very large ingots is the multiconcentration pouring (or multiple pouring) process, which aims to alleviate macrosegregation by changing the composition of melt added by each successive ladle added to an ingot [124; 133; 227]. This is carried out such that the first ladle to be added is the most enriched in additions, whilst the final is the most depleted in solute, reversing the usual top-bottom trend seen after solidification. There are a number of apparent issues with this methodology, however. First, great care must be taken on its implementation - if the density of the enriched liquid is such that it sinks relative to the bulk (unusual, but possible in some steels), then the concentration scheme would need to be inverted to avoid increasing macrosegregation. Second, it seems unlikely that the desired concentration fields in the liquid would be maintained if the ladles are poured in quick succession, as convection currents would rapidly homogenise the melt [124]. Pouring with longer time periods between successive ladles could improve segregation by providing a more stage-wise process (similar to VAR and ESR), but this would then negate the need for multiple ladle compositions. Complex macrosegregation patterns could easily arise.

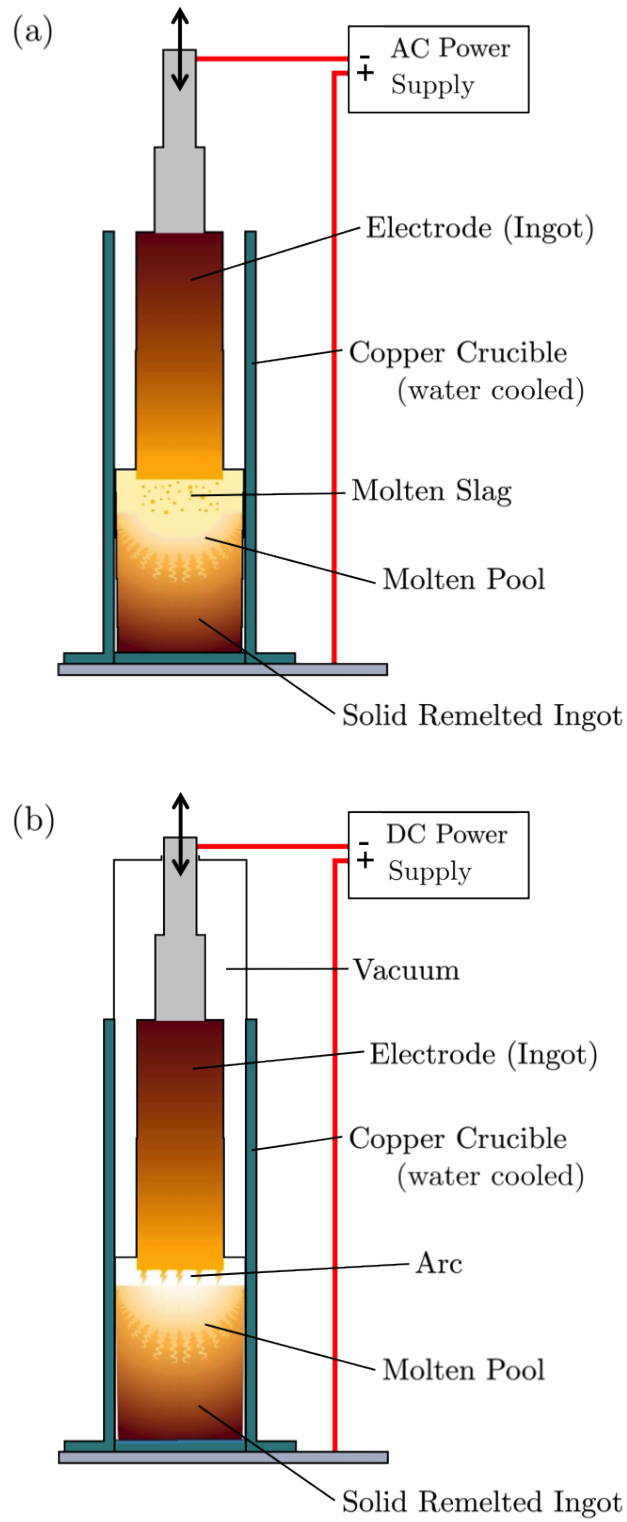


Figure 2.10: Schematics of (a) the ESR process and (b) the VAR process.

It seems reasonable that the application of centrifugal (radial) forces to a solidifying ingot should reduce the vertical fluid flow that leads to macrosegregation. This premise was investigated in the 1970s in a number of studies [228; 229; 230], and specifically in respect to A-segregates later on [25; 231; 232]. The success of this process appears to be system dependent, and whilst segregation could be eliminated or reversed in some alloys [230], little effect was seen in others [228]. This is perhaps because the imposition of mould rotation leads to extensive mixing of the melt, and can result in effects besides simply reducing consistent vertical flows. Indeed, this was known well before investigations into how mould rotation could be doctored to carefully influence convective flows. The first patent for a process which sought to reduce macrosegregation by mixing through rotation was taken out by Brinell in 1910, and since there have been various elaborations on the general principal, see Fig. 2.11 [233; 234; 235]. In a similar way, mould agitation methods employing vibration, mechanical stirring or oscillation (in which the direction of mould rotation is periodically reversed) have also been explored [228; 236; 237]. It has been well known for decades that disturbing the residual liquid in a such a way during casting can have a refining effect for a number of reasons, including enhanced convective cooling, reduced temperature gradients in the melt, and increased solid fragmentation and advection - all of which promote the CET and formation of equiaxed grains. Electromagnetic stirring and vibration processes have also been extensively applied to refine structures and reduce segregation in aluminium alloys and the continuous casting of steels [238; 239; 240; 241]. Note that equiaxed solidifications by no means guarantees less macrosegregation, but the application of magnetic stirring can make this more likely by increasing mixing, inhibiting channel formation (they cannot form if the solid is in motion) and by increasing cooling rates.

It must be noted, however, that the results of the application of the liquid agitation methods above are by no means always successful or easy to predict. The turbulent flows introduced by forced mixing add another level of complexity to macromodels that are already inadequate; they can lead to increased macrosegregation [239] and the development of other defects (e.g., white banding in steels [243]). In ESR and VAR processes, there are concerns that the magnetic field

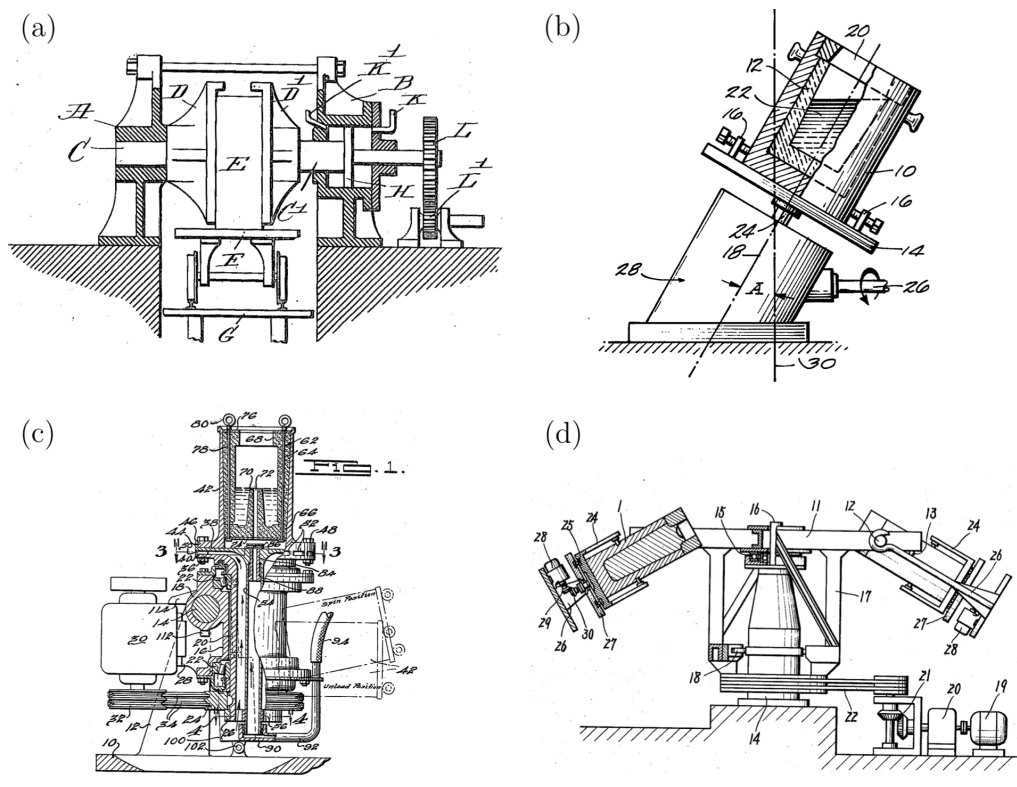


Figure 2.11: Various methods patented for rotating and precessing moulds during ingot casting. (a). Brinell's rotation of ingot (labelled E) about horizontal axis [233]. (b). Hellowell's inclined rotation [235]. (c). Nelson's centrifugal casting [242]. (d). Tanoue's centrifugal casting method designed to remove inclusions from the centres of ingots [234]

generated by the arc could be a key factor in the formation of defects such as freckles [225]. It should also be recognised that the application of electromagnetic stirring to the static casting of large steel ingots would be impractical (limited by the field penetration).

Promotion of the CET and refinement of cast structures can also be achieved through the use of inoculants in steel melts. It has been found that the addition of Ti can lead to the formation of TiN, TiC and oxide particles that act as heterogeneous nucleation sites for solidification, leading to the increased formation of equiaxed grains [244; 245; 246; 247; 248]. V, Nb and Zr can also have similar effects, and the same particles which promote solid nucleation can also pin austenite grain boundaries, delivering further improvements to mechanical properties. Poole et al. noted that TiN was only suitable for refining steels that solidified with ferrite as the primary phase, which was attributed to the lattice mismatch between austenite and TiN [248]. Inoculation is very common in the casting of aluminium alloys [249; 250].

2.7 Measuring Macrosegregation in Steel Ingots

It is often the case in the macrosegregation modelling literature that results are given without comparison with experimental measurements, or at least not in any greater detail than a qualitative appraisal. A principal reason for this is the lack of appropriate good-quality experimental data. There are a number of problems associated with obtaining macrosegregation measurements and other related quantities from cast products, which include the great cost of production and analysis, lack of suitable test material (binary alloys are often used in models but rarely used in industry) and the immense difficulties associated with sectioning ingots and accurately measuring their characteristics. It is quite clear that not only are more reliable materials property data and greater model computability required, but there is also a great need for first-rate case studies - validation is very much part of the macrosegregation modelling problem.

Reducing the size of ingots used for macrosegregation studies can cut the great

expense and time required for analysis of large ingots. This must be done with great care, however, as small ingots typically do not display macrosegregation to the same extent as larger castings due to the reduced cooling times. Researchers have employed sand moulds and other artificial means to help impose large-ingot cooling rates on small ingots [23; 211; 251], but a comparison has not been made between small controlled-rate ingots and their larger counterparts. Indeed, a key problem is that cooling rates during the casting of a single ingot can vary dramatically with time - solidification is quick to start with, as heat is rapidly extracted from the melt, but as the ingot mould heats up this rate can slow dramatically. It is very difficult to recreate these conditions accurately using anything other than a full-sized ingot mould.

There are a range of standard processes available for qualitative assessment of steel ingots, including macroetching and sulphur printing, which are comprehensively summarised by Vander Voort in references [252; 253]. These provide a useful insight into ingot features which may be compared with model results, such as grain structure and segregate distribution and morphology. It should be noted, though, that the power of sulphur print methods has been somewhat diminished in modern steels by their low sulphur contents [254]. Radioactive isotopes have also been used in various studies to examine fluid-flow patterns [255; 256; 257]. However, the ultimate aim for macrosegregation models is for them to be able to make quantitative predictions. It is, after all, the chemistry of segregated areas and their reponse to heat treatment which determines mechanical properties.

Following sectioning, quantitative chemical analysis on ingots has usually been accomplished through trepanning samples in a set array and then subjecting them to chemical analysis. This was very common in pre-1950 studies, when the wet chemical analysis techniques were popular, and is still in use today [30; 107] alongside various other chemical analysis techniques including combustion analysis and atomic absorption spectroscopy [258]. Milling chips have also been used to assess segregation in a similar way to trepanned material [19]. There are two problems with this characterisation scheme, however. First, the chemical analysis step is laborious and expensive, even with relatively straightforward techniques such

as energy-dispersive X-ray spectroscopy (EDX) and electron-probe microanalysis (EPMA). Second, the way in which results have been used has often been questionable - there are examples of grid results being extrapolated to create contour maps [30; 117; 259], see for example Fig. 2.12. Although this gives an overview of macro-trends, it provides little detail of the finer-scale segregation patterns which are observed, and cannot be relied upon to give upper and lower bounds for segregation severity (strangely, trepanning does not seem to have been guided by the results of macroetching).

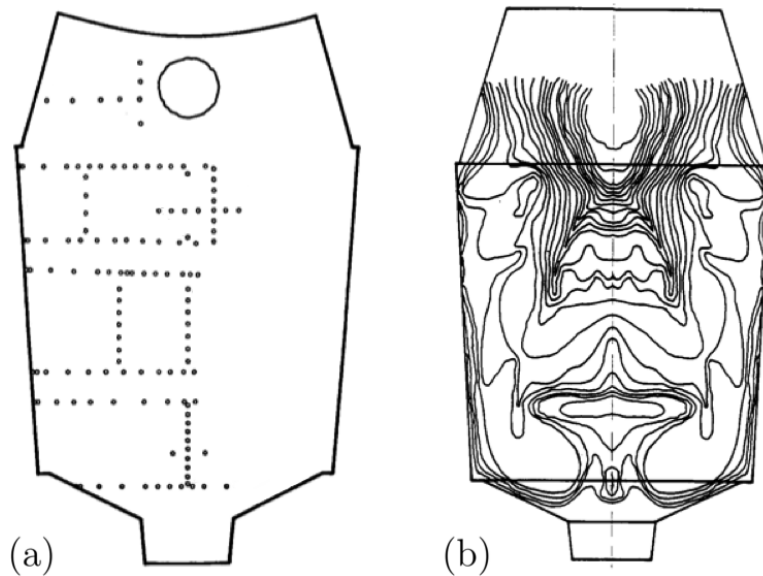


Figure 2.12: Schematic of (a) trepanning scheme (sampling points marked by dots) and (b) extrapolation of carbon concentration results in 180 ton ingot. Adapted from [259].

There are techniques, however, which may have the ability to map segregation in greater detail, such that individual A-segregates can be analysed. Miyamura et al. utilised a scaled-up EPMA process which was capable of analysing macro sections, but it was restricted to 30×10 cm slabs [254]. Tkadleckova et al. used a portable optical-emission spectrometer for point analyses without trepanning, which might prove to be a promising technique, but a sparse grid was used and there appears to have been considerable noise associated with the results [260].

Other alternative techniques for validation purposes include dump testing ingots (removing the liquid before full solidification and analysing solid structure and liquid chemistry [13]) and direct liquid sampling during solidification [28; 211], but these have their own complications. At present, macro-scale X-ray fluorescence spectroscopy (XRF) is perhaps the most promising method for macrosegregation detection. Chapter 7 in this thesis assesses the viability of using this technique.

Any investigator planning to perform a macrosegregation case study must remember that quantitative results are of little use if they aren't accompanied by the appropriate casting data, such as mould temperature profiles during solidification, mould design and alloy chemistry. However, if these are presented alongside accurate segregation measurements and qualitative macrostructure findings, as they are for the ingot examined in Chapter 8 of this thesis, then the resulting case study is likely to prove a more useful validation tool for future modellers.

2.8 Summary and Future Prospects

Our understanding of macrosegregation in steel ingots has progressed immensely over the past century. Particularly since the advent of macrosegregation modelling in the 1960s, our ability to predict macrosegregation has led to significant advances in our comprehension of the defects that can arise in ingots and our ability to mitigate them.

Modern-day multiphase models couple together conservation equations for mass, species, momentum and energy, alongside many auxiliary relations, in schemes which have the capability to predict inhomogeneities like A-segregation and base segregation. Theoretical treatments of the complex behaviours present in solidifying ingots, such as equiaxed grain growth and movement, are advancing. Nevertheless, much of the predictive power of macromodels is still inaccessible or of limited use for a number of reasons, especially in the case of large multicomponent steel ingots. Principal amongst them is the impractical computational demands that complex macromodels require - on a small computer cluster even the simplest commercial codes can take weeks to run a macrosegregation model

for a binary alloy ingot of moderate size. In order to make computation times manageable, modellers often introduce simplifications, reduce mesh sizes and decrease system sizes, but this in turn can mean the models are unable to resolve key phenomena, and deliver results which are significantly departed from experimental measurements. Further issues are associated with input parameters and auxiliary models, such as permeability functions and dendrite arm spacings. All of these taken together mean that for most practical purposes, macrosegregation models cannot be relied upon to give quantitative results for ingots and may not even be suitable for qualitative predictions. Issues associated with experimentally measuring macrosegregation and generating case studies for validation are only compounding modelling problems.

For manufacturers and researchers aiming to rapidly assess the effect of casting conditions and alloy compositions on macrosegregation, it seems that more simple approaches are worth pursuing at present, such as using a Rayleigh-number criterion for A-segregate prediction. The required variables for such a criterion can be quickly estimated through empirical relations and other models, e.g. Howe's microsegregation model [166] or software packages like JMatPro [143], and mapped onto the results of a simple thermal macromodel.

The difficulties associated with macrosegregation modelling are so often formidable, but novel solutions which comprise reduced complexity whilst delivering accurate predictions are a promising alternative. Presently, the need for such treatments for steel ingots is paramount as manufacturers deal with increased demands from the growing power-generation industry.

Chapter 3

Project Background

3.1 Motivation, Aims and Scope

Rolls-Royce plc oversees the production of nuclear steam-raising plants through its Nuclear business. At the heart of such plants lies the reactor pressure vessel (RPV) into which the fuel rods are placed and water is circulated to extract heat. It is a critical component to the safe operation of the plant, and is required to maintain its integrity during decades of service. Current nuclear power plants, designed for 40 year lifetimes, are coming to the end of their lives, and there is considerable demand for the production of new plants with enhanced designs and materials.

Materials and production methods for current-generation high-integrity pressure vessels, such as RPVs and steam generators, are well developed. The most common steel used for such vessels is ASME SA508 Grade 3 Class 1 (hereafter referred to as Grade 3, chemical composition range in Table 3.1), a low-alloy pressure-vessel steel chosen for its high toughness, reasonable cost, and reliable service over many decades. This is the most common pressure-vessel steel in the world today. It is likely, however, that future high-integrity vessels will use steels with higher strengths and toughnesses than Grade 3, with the high-nickel A508 Grade 4N steel (hereafter referred to as Grade 4N) being the most likely candidate (this material is currently used in nuclear fuel transportation flasks), Table 3.1.

Table 3.1: Specification chemical compositions of SA508 Grade 3 and SA508 Grade 4N steels taken from the ASME for pressure vessels (American Society of Mechanical Engineers [263]). Units are wt%.

SA508 Grade 3				
C	Si	Mn	P	S
0.25 (max)	0.15-0.4	1.2-1.5	0.025 (max)	0.025 (max)
Cr	Ni	Mo	V	Al
0.25 (max)	0.4-1	0.45-0.6	0.05 (max)	-
SA508 Grade 4N				
C	Si	Mn	P	S
0.23 (max)	-	0.2-0.4	0.020 (max)	0.020 (max)
Cr	Ni	Mo	V	Al
1.5-2	2.8-3.9	0.4-0.6	0.05 (max)	-

It is absolutely essential that there is the utmost confidence with regards to the use of Grade 4N, and it must be shown that the material not only begins with superior properties to Grade 3, but that it maintains these properties throughout its lifetime. Designers must be sure that the effects of potential defects in the steel, such as those generated by macrosegregation, do not compromise the material's integrity in the long term [261; 262].

This thesis focusses on the segregation that can be found in high-integrity shell forgings, such as the hollow cylinders which form the main bodies of RPVs and steam generators. In the case of RPVs, top and bottom closure heads are welded to these shells, and four or more cylindrical cores are trepanned from them to allow for the attachment of water-exchange nozzles, which are also welded in position, Fig. 3.1.

A supplier of large forgings to the nuclear industry is Sheffield Forgemasters

International, who produce high-integrity vessels from starting ingots weighing up to 200 tons. A typical manufacturing route for shell forgings is described in Sections 3.2.2 and 3.2.3 later in this chapter. As will be described in these sections, the centres of the ingots used are punched out during production, removing much of the severe centreline porosity and segregation (V-segregation) that can be expected. Thus, prediction of these defects is not within the scope of this project (this is fortunate, since accurate modelling of this segregation is not well developed). Instead, A-segregation is the primary focus, as they can be retained through the wall thicknesses of shell forgings [264; 265; 266]. The followings aims were formulated, and are each addressed in the subsequent chapters in this thesis:

- Assess the impact of A-segregation present in a Grade 3 high-integrity shell forging on start-of-life microstructural and mechanical properties.
- Develop capabilities for the prediction of the location and severity of A-segregates in large ingots, and for the tracking of segregated material through forging processes to final components.
- Develop the capability to detect, and measure the chemical composition of, macrosegregation defects (including A-segregates) in large forgings.
- Compare the Grade 3 and Grade 4N materials in terms of their theoretical susceptibility to A-segregation.
- Examine how the impact of A-segregation can be minimised in both Grade 3 and Grade 4N large forgings through ingot selection, casting practice and material removal.

Note that realising these aims will not only allow for the impact of A-segregation in current Grade 3 and future Grade 4N forgings to be examined, but will also allow for the segregation present in historic forgings to be assessed retrospectively. Furthermore, many of the methods that are to be developed in this thesis, such as those for A-segregation prediction, tracking and measurement, are intended to be more widely applicable to large forgings made from any grade of steel. It is hoped that the use of these methods will allow for the production of higher-quality components with extended lifetimes.

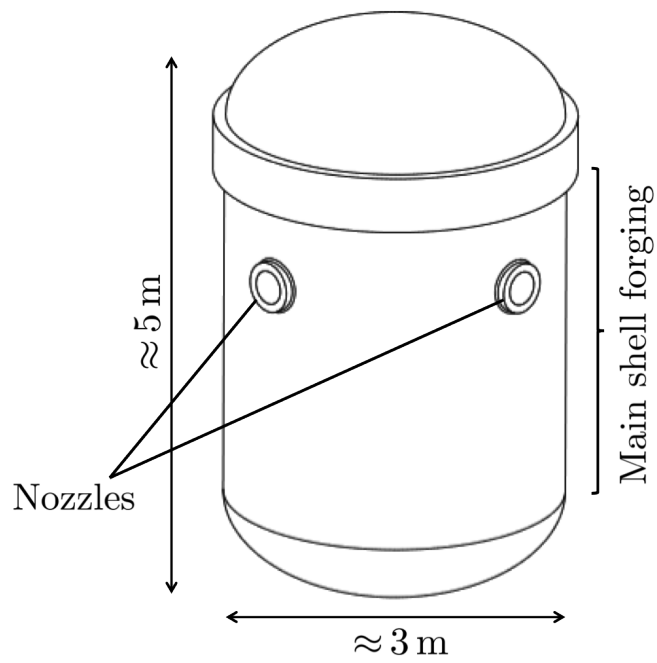


Figure 3.1: Schematic of RPV assembly, which is produced by welding together a number of sub-elements.

3.2 High-Integrity Shell Production Route

This section outlines the casting, forging and heat treatment procedures that are used to generate a Grade 3 high-integrity shell forging from a 200 ton ingot. These steps, which can be relatively complex, must be well understood if the segregation present in such forgings is to be interpreted, and any recommendations are to be made for improvements.

3.2.1 Casting Assembly

Casting a 200 ton steel ingot requires much more than simply a large mould. Various components must be fitted around the mould to ensure the ingot produced is the correct weight and shape, that its top stays well insulated, and that it can be successfully removed from the mould once formed. These components are listed below and shown in Fig. 3.2.

a). Ingot mould, cast iron. The mould is fluted (in this case, with eight flutes) to ensure sufficient mechanical support for the solid shell of an ingot when it contracts and an air gap begins to form. The mould is also tapered; this is not only to allow for easy extraction of the solid ingot (shrinkage would likely provide this), but in anticipation that porosity in the ingot is likely to be most prominent at the top of the ingot (and hence more deformation can be introduced into the ingot here during forging if it has a wider section).

b). Headbox, cast iron. The liquid metal contracts on solidification so a head of metal must be kept atop the ingot to feed the contraction. This must be kept liquid until the very end of solidification, and ceramic insulation inside the head box is used to help this.

c). Inner base plate, or “sinker”, cast iron. This is placed at the base of the ingot mould and its level can be adjusted to change the size of the ingot produced.

d). Bricks, ceramic. These bricks are part of the head insulation and fixed inside the rim of the headbox, remaining intact for many castings due to protection from tiles.

e). Tiles, ceramic. The tiles are nailed over the brickwork to provide protection, as well as extra insulation, during casting. They are consumable and are

destroyed during the casting and ingot stripping processes.

f). Trunnion block, ceramic. Another consumable ceramic component, these blocks allow for the casting of lifting trunnions directly onto the head of the ingot such that the ingot can be easily removed once solidified.

g). Trunnion disc, ceramic. Made from the same material as the tile, this is used simply to fit on the end of the trunnion block.

h). Packing, sand and metal shot. This is added around the inner base plate to ensure no escape of liquid metal through gaps between the base plate and the mould.

i). Exothermic powder. This is added to the top of the head (onto exposed liquid metal) in an effort to insulate the head metal as fully as possible.

3.2.2 Casting Procedure

A typical route for casting a 200 ton ingot at Sheffield Forgemasters is as follows:

1. Scrap metal is melted in an electric arc furnace before being transferred into ladles - each ladle carries ≈ 100 tons of molten steel, two are therefore required to produce a 200 ton ingot. Fig. 3.3a. The ladles are then moved into vacuum stream degassers where the chemistry of the steel is tailored to specific chemistry requirements - residual hydrogen, oxygen and nitrogen are removed in the vacuum, and other alloying additions may be added. The ladles can then be transferred to special furnaces to ensure the correct superheat before pouring Fig. 3.3b.

2. The casting assembly is constructed within a vacuum tank, which is then pumped down to ensure minimal oxidation and inclusion formation during pouring, Fig. 3.3c.

3. A 'pony' ladle is placed over the vacuum tank. This receives molten steel from the two ladles which are required to fill the ingot mould, Fig. 3.4d.

4. The two ladles are poured in one after the other. Tests are made for metal superheat and chemistry during pouring, Fig. 3.3e.

5. The vacuum tank head is removed and exothermic powder placed directly onto the ingot head, Fig. 3.4a.

6. The ingot is left to solidify for around two days. It is then stripped: the head-



Figure 3.2: CAD drawings of the casting assembly, created using the SolidWorks 2012 software package. Basic dimensions of ingot given. IMAGE HAS BEEN PIXELATED - COMMERCIALY SENSITIVE.

box is removed and the ingot lifted from its assembly by its trunnions, Fig. 3.4b and Fig. 3.4c.

7. The ingot is then taken for heat treatment and forging, Fig. 3.4d and Fig. 3.4e.

3.2.3 Forging and Machining

Once an ingot has been cast, it must be forged and machined precisely to produce the cylindrical shell required. The forging operations take place only when the ingot temperature is between 800 and 1250°C, and consequently the ingot regularly undergoes long furnace treatments between operations. The deformation imposed by forging not only closes residual porosity, but also seeks to break up the as-cast structure of the ingot. The forging process also includes a step that completely removes of the centre of the ingot and the ingot head, eliminating the most heavily-segregated and porous regions. A basic overview of the operations, shown in Fig. 3.5 and Fig. 3.6, is described below:

1. **‘Tagging’**: This operation re-shapes the head such that it can be gripped by the manipulating arm of the forging system, Fig. 3.5a to 3.5b.
2. **‘Saddening’**: This forging operation flattens the flutes on the ingot surface to produce a smooth cylinder. The width of the ingot decreases and it elongates slightly, Fig. 3.5c to Fig. 3.5d.
3. **‘Top and tail’ removal**: The head and bottom of the ingot are removed through hot-cutting, Fig. 3.5d.
4. **‘Upsetting’**: An “upset” involves the compression of the ingot along its long axis, and squashes it into a squat barrel. Its height is usually reduced by a factor of two, and hence it is referred to as a 2:1 upset, Fig. 3.5d to 3.5e.
5. **Hollow punching**: Appropriately-sized rings are successively forced into the body of the forging, removing the middle. The scrap pin-like section which is produced has a length longer than the height of the ingot due to some extrusion, Fig. 3.6a to 3.6d.
6. **‘Becking’**: This increases the diameter of the ingot, now a hollow cylinder. The length of the ingot is not allowed to change, Fig. 3.6e.
7. **Drawing on mandrel**: The length of the piece is increased by pressing it onto a tapered steel cylinder, Fig. 3.6f. The inside diameter is unchanged.

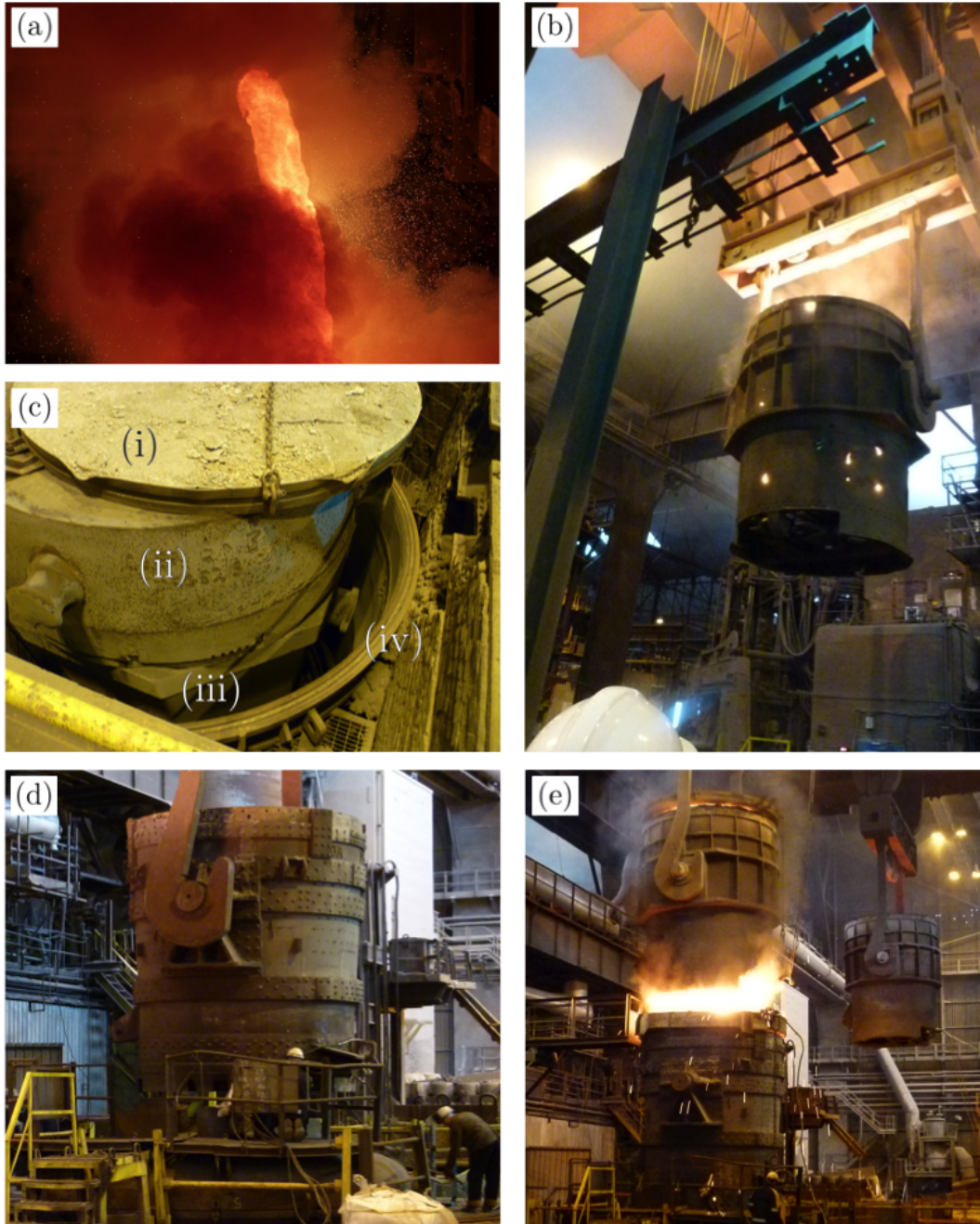


Figure 3.3: (a) Molten steel being poured from the electric-arc furnace into a ladle. (b) Full ladle being moved for degassing and furnace treatment. (c) Casting assembly inside vacuum tank: (i) headbox lid, (ii) headbox, (iii) mould and (iv) vacuum tank. (d) Pony ladle is fixed onto top of sealed vacuum tank. (e) Two ladles are poured consecutively into the casting assembly.

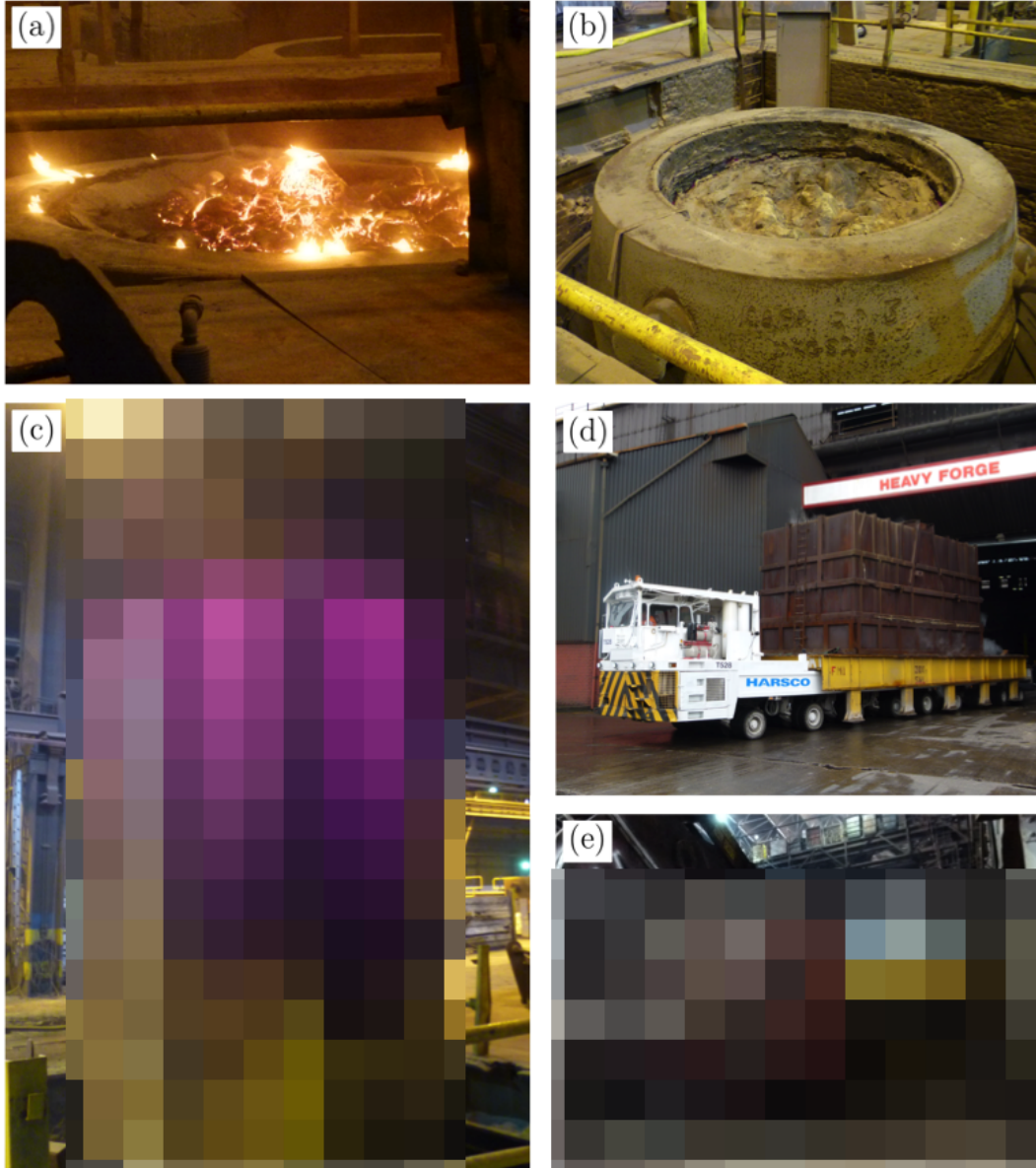


Figure 3.4: (a) Exothermic powder, immediately following addition to top of head. (b) After approximately two days, the ingot has solidified and the powder level has dropped significantly due to shrinkage. (c) Ingot is removed from mould. Note the sinker is stuck to the base (later removed). Purple colour is artefact of camera used. (d) Transportation of ingot to forge under cover. (e) Ingot is immediately placed in furnace for heat treatment before forging. PARTS OF IMAGE HAVE BEEN PIXELATED - COMMERCIALY SENSITIVE.

Table 3.2: SA508 Grade 3 shell forging heat treatment details.

Austenitised at 800°C for 8 h
Water Quenched
Tempered at 645°C for 8 h
Tempered at 605°C for 19 h
Air cooled

8. Finish ‘becking’: This final stage ensures the inside and outside diameters of the piece are correct.

9. Machining to heat-treatment profile: The hollow cylinder is subject to a number of machining operations dependent on precise post-forging geometry and final specification size.

3.2.4 Heat Treatment

The heat treatment imposed on a Grade 3 high-integrity forging after machining to the correct profile is outlined below. The Grade 3 material that is examined in the remainder of this thesis was taken from a cylindrical trepanning that was withdrawn from a production forging before heat treatment (see Fig. 4.1 later for the location and geometry of the trepanned cylinder). For this trepanned material, the heat treatment steps in the table below were performed under conditions that sought to mimick the cooling/heating rates found in large shell forgings (e.g. for the quenching, water was only permitted to contact the flat ends of the cylinder, with insulation being applied around its curved surface). Final machining operations are be carried out on the shell forging after all the heat treatment steps are complete (to remove oxide scale, etc).

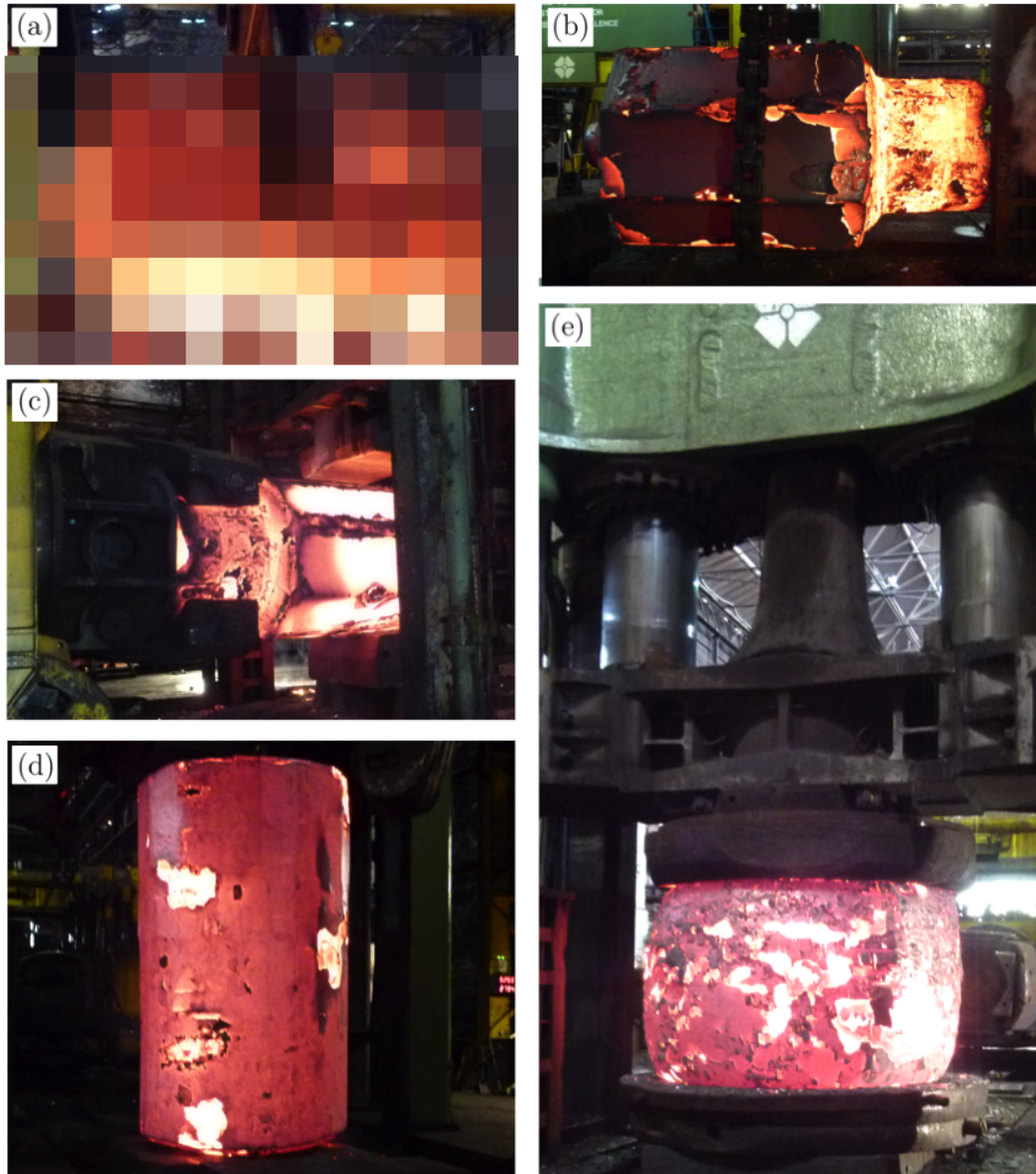


Figure 3.5: The forging procedure: (a) removal from furnace, (b) tagging, (c) saddening (note ingot is gripped by the manipulator), (d) the ingot after saddening and (e) upsetting. PARTS OF IMAGE HAVE BEEN PIXELATED - COMMERCIALY SENSITIVE.

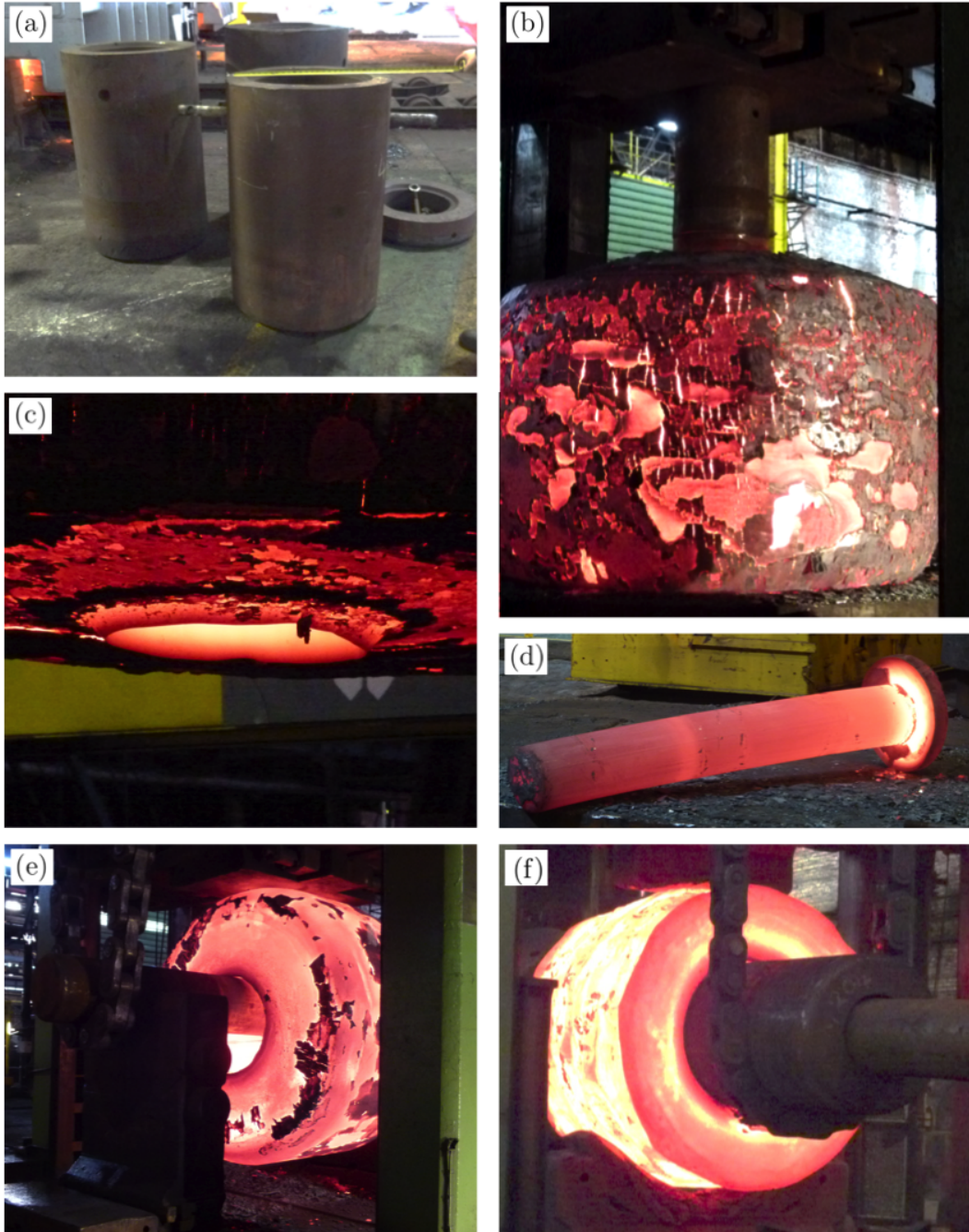


Figure 3.6: The forging procedure continued: (a) the rings used to punch out a cylinder from the upset ingot, (b) the punching operation, (c) the hole in the base of the ingot left by punching, (d) the cylindrical section removed from the centre, (e) becking and (f) drawing.

Chapter 4

The Effect of Macrosegregation on Microstructural Evolution

4.1 Introduction

This chapter examines the effect that the A-segregation present in large Grade 3 forgings can have on microstructural evolution. It is concerned with the phase transformations that occur during two of the heat treatment steps outlined in Table 3.2.4: (i) the quenching operation in which the forging is continuously cooled from austenitisation, and (ii) the tempering heat treatment at 645 °C. The results of dilatometry measurements, partial transformation experiments and scanning and transmission electron microscopy (SEM and TEM) are presented to support its conclusions. The origins of and severity of the segregation present are discussed, and suggestions are made for both how it might be prevented, and how its effects might be suppressed.

4.2 Experimental

4.2.1 SA508 Grade 3 Material

As was described in Section 3.2.4, all the Grade 3 material used for the experiments in this thesis was taken from a cylindrical billet which was trepanned from

a high-integrity shell forging. The overall chemical composition of the ingot cast to produce this forging is given in Table 4.1, as measured using optical-emission spectroscopy (OES). The bulk chemical composition of the trepanned cylinder, which was taken through-thickness from just below the centreline of the forging (with the original head of the ingot being at the top, Fig. 4.1a), is also given in the same table. After simulated heat treatment (Table 8.3), the cylinder was sectioned to produce several plates of material with their surface normals aligned along the vertical axis of the ingot (z -axis in Fig. 4.1b). These plates were ground to a fine surface finish before being etched in 5% aqueous nitric acid solution to reveal macrostructures, Fig. 4.2, with areas of positive chemical segregation being observed as dark features. By examining a succession of plates along the vertical direction, it was found that the elliptical segregates in Fig.4.2 extended through a significant vertical distance, indicating they were ‘A’ type. An indication of the chemical composition of the A-segregates found is given in Table 4.1.

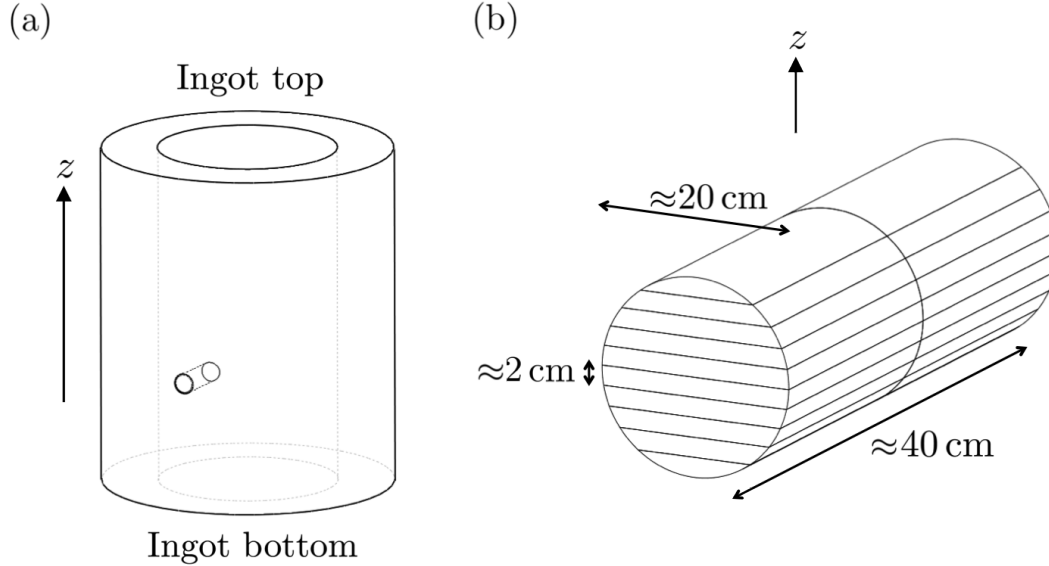


Figure 4.1: Schematics of (a) the position of trepanned cylinder taken for analysis, and (b) the sectioning of the cylinder to produce slabs.

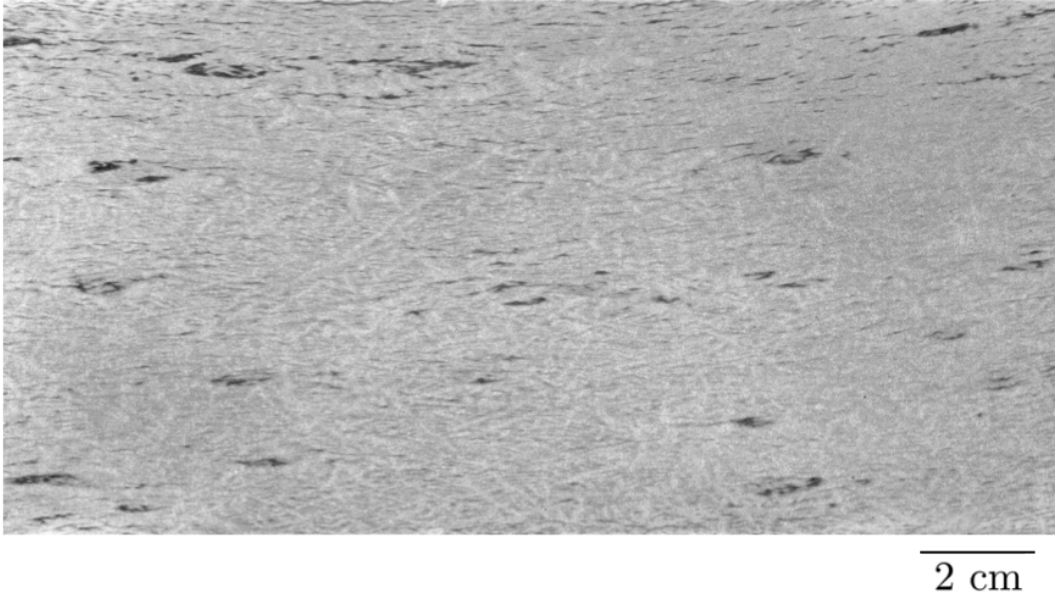


Figure 4.2: Section of the trepanned Grade 3 cylinder, metallographically prepared and macroetched. Dark regions are areas of positive segregation. In this view, the upward direction points towards the ingot centre. The becking forging operations have elongated the segregates tangentially.

4.2.2 Microstructural Investigations

Cylindrical samples measuring 8 mm in diameter and 12 mm in height were taken from regions with and without A-segregation to assess their phase transformation behaviours. A Thermecmastor Z dilatometer was used for monitoring the progress of phase transformations. Transformation temperatures and phase fractions were determined consistently through a linear-offset method [267]. Following dilatometry, samples were sectioned, metallographically prepared and etched in 2% nital before examination under a Leica DM2500 M optical microscope. Chemical spot analyses were performed with a Cameca SX-100 electron probe micro analyser (wavelength-dispersive EPMA), whilst secondary and back-scattered electron imaging was carried out with a CamScan MX2600 field emission gun scanning electron microscope (FEG-SEM). Bright-field and electron diffraction studies were undertaken in the transmission electron microscope using a JEOL 200CX machine with an accelerating voltage of 200 kV. An FEI Tecnai F20 FEG-TEM was used for Scanning TEM energy-dispersive X-ray (EDX) analysis at

Table 4.1: Chemical Composition (wt%) of Grade 3 steel examined, measured using OES.

Chemical Composition of Ingot Cast					
C	Si	Mn	P	S	Cr
0.17	0.23	1.32	0.005	0.001	0.20
Ni	Mo	V	Cu	Al	Sn
0.76	0.51	0.004	0.02	0.019	0.004
Chemical Composition of Trepanned Cylinder					
C	Si	Mn	P	S	Cr
0.18	0.25	1.32	0.005	0.001	0.21
Ni	Mo	V	Cu	Al	Sn
0.74	0.49	0.003	0.025	0.018	0.004
Chemical Composition of an A-Segregate					
C	Si	Mn	P	S	Cr
0.22	0.29	1.62	0.011	0.004	0.26
Ni	Mo	V	Cu	Al	Sn
0.87	0.87	0.005	0.04	0.018	0.007

200 kV. Thin foils were prepared by electropolishing with a solution of 5% perchloric acid, 25% glycerol and 70% ethanol. The voltage, current and temperature during electropolishing were 37 V, 26 mA and 10 °C respectively. Vickers hardness measurements were obtained using a Mitutoyo MVK-H2 hardness testing machine, with a load of 2 kg. Prior-austenite grain size was measured by thermal etching and the linear intercept method, with data obtained from thirteen different fields of the sample and a total of 195 linear intercept lines.

4.3 Results

4.3.1 Dilatometry

Dilatometry measurements were used to characterise phase transformations during cooling from austenitisation. All samples were heated to 940 °C at 10 °C s⁻¹ and held for 30 min before being cooled at 0.1 °C s⁻¹ to room temperature; the austenitisation treatment and cooling rate chosen to mimic a typical cooling rate in the middle of a thick forging during quenching. A summary of the transformation temperatures obtained from this is shown in Table 4.2, which also gives details of the type of transformations measured (further evidence substantiating these assignments is presented later). Fig. 4.3 shows examples of cooling curves from samples with and without A-segregate material. In both cases, a transformation consistent with allotriomorphic ferrite was observed between 650 and 700 °C; the fraction of ferrite and the temperature range over which it formed was greater when the austenite decomposition began at a higher temperature. The material with A-segregation showed considerably more variation in measured ferrite phase fractions, with the lowest being < 0.01 and the highest around 0.19.

The transformation event present at 550 °C is associated with Widmanstätten ferrite. Fig. 4.3 shows that in material without A-segregation this transient was consistently reproduced and composed of two stages - the first leading to an increase in strain between 550 and 500 °C and the second giving very little change in strain from 500 °C until around 400 °C. For samples with A-segregation, the appearance of the transformation occurring after 550 °C is less consistent, although generally the first stage of transformation is not so sharp and there is more activity at lower temperatures. A comparison of typical curves for samples with and without A-segregation is seen in Fig. 4.4. Also shown is evidence of a low-temperature deviation in strain, which is likely to be associated with martensite formation.

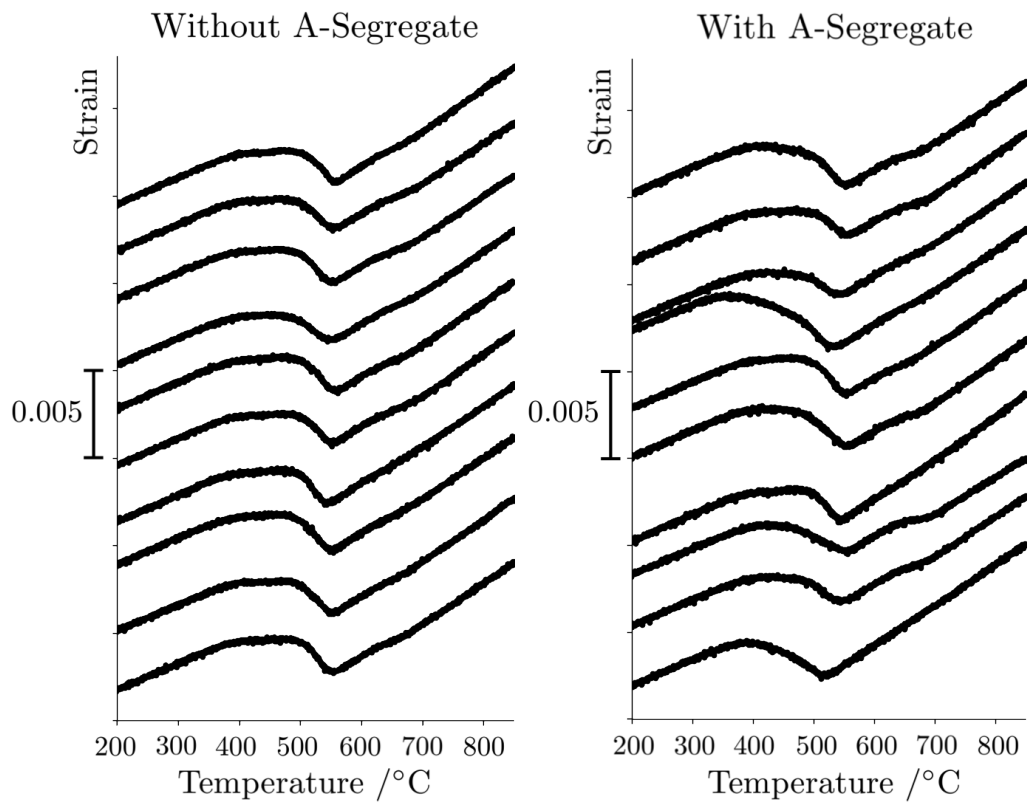


Figure 4.3: Comparison of strain curves for samples with and without A-segregation. Those without A-segregation display more consistent behaviour than those with.

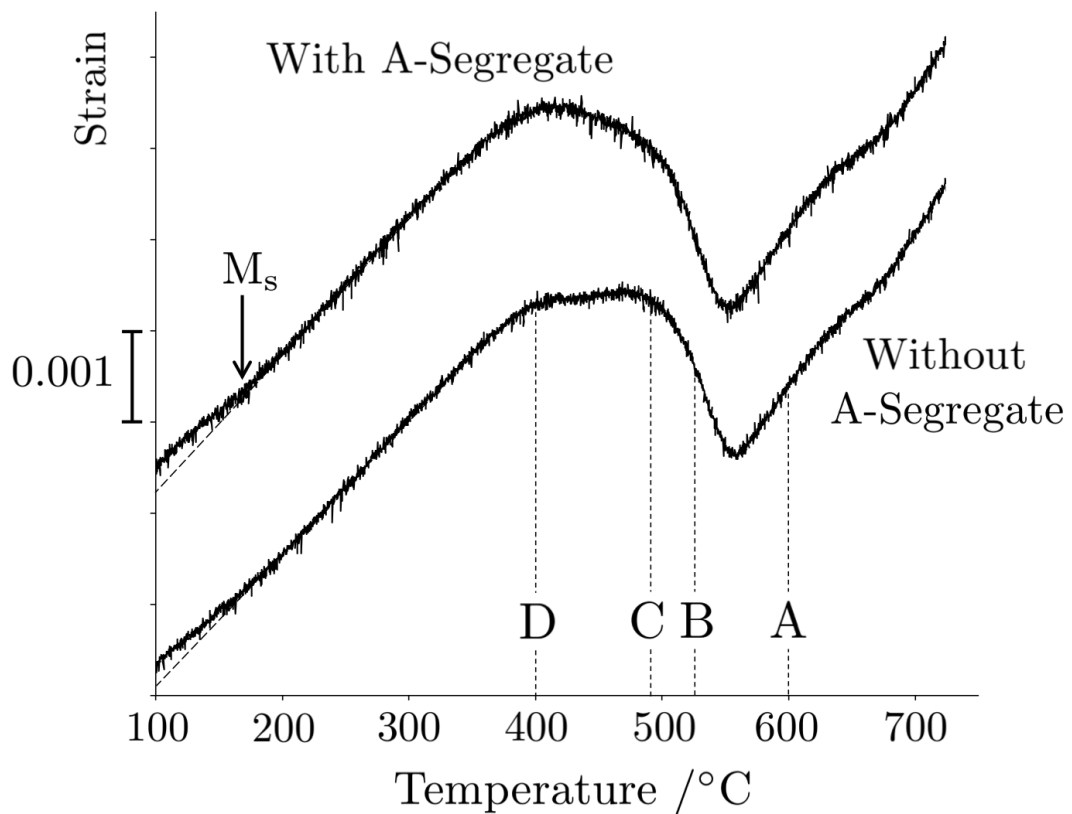


Figure 4.4: Comparison of typical strain curves for material with and without A-segregation. There is evidence of more low-temperature transformation in samples with A-segregation. The points labelled A, B, C and D refer to the temperatures at which the material was quenched during partial transformation experiments. Martensite start temperatures are also highlighted (M_s).

Table 4.2: Dilatometry data; the uncertainties presented are the standard deviations calculated across multiple test results for each sample type. The error in the ‘range’ combines that in the ‘onset’ and ‘end’ temperatures.

	With A-Segregate	Without A-Segregate
Ferrite onset /°C	676 ± 13	672 ± 8
Ferrite end /°C	639 ± 8	640 ± 5
Ferrite range /°C	37 ± 21	32 ± 13
% Ferrite (600 °C)	12 ± 6	13 ± 3
Widmanstätten onset /°C	546 ± 10	553 ± 4
Widmanstätten end /°C	363 ± 14	380 ± 6
Widmanstätten range /°C	183 ± 24	173 ± 10
Martensite onset /°C	153 ± 5	153 ± 4

4.3.2 Quenched Microstructures

Evaluation of quenched microstructures confirmed the identities of the transformations measured by dilatometry, and revealed three distinct microstructures. The first, found in the non-segregated bulk of the material, consisted of Widmanstätten ferrite with occasional allotriomorphic grains (on prior-austenite grain boundaries), Fig. 4.5a. Regions between the coarse ferritic laths were observed to be rich with carbides, Fig. 4.6a. Microstructures very similar to this have previously been reported as upper bainite [268; 269; 270; 271; 272; 273], but the cleanliness of etching, the coarseness of the plates, as well as the lack of carbide precipitation (between small bainitic sub-units), Fig. 4.7a, suggests this is not the case.

Extensive bands of allotriomorphic ferrite formed the second distinct microstructure present. These were a few hundred μm wide and stretched for many hundreds of μm , Figs. 4.5b and c. They could not have resulted purely from ferrite formation on very large prior-austenite grains, as the grain size in the bulk material was found to be $13.3 \pm 0.8 \mu\text{m}$, and $11.6 \pm 0.7 \mu\text{m}$ in A-segregate regions. The grain size was highly non-uniform, see Fig. 4.8, and the scatters indicated (± 0.8

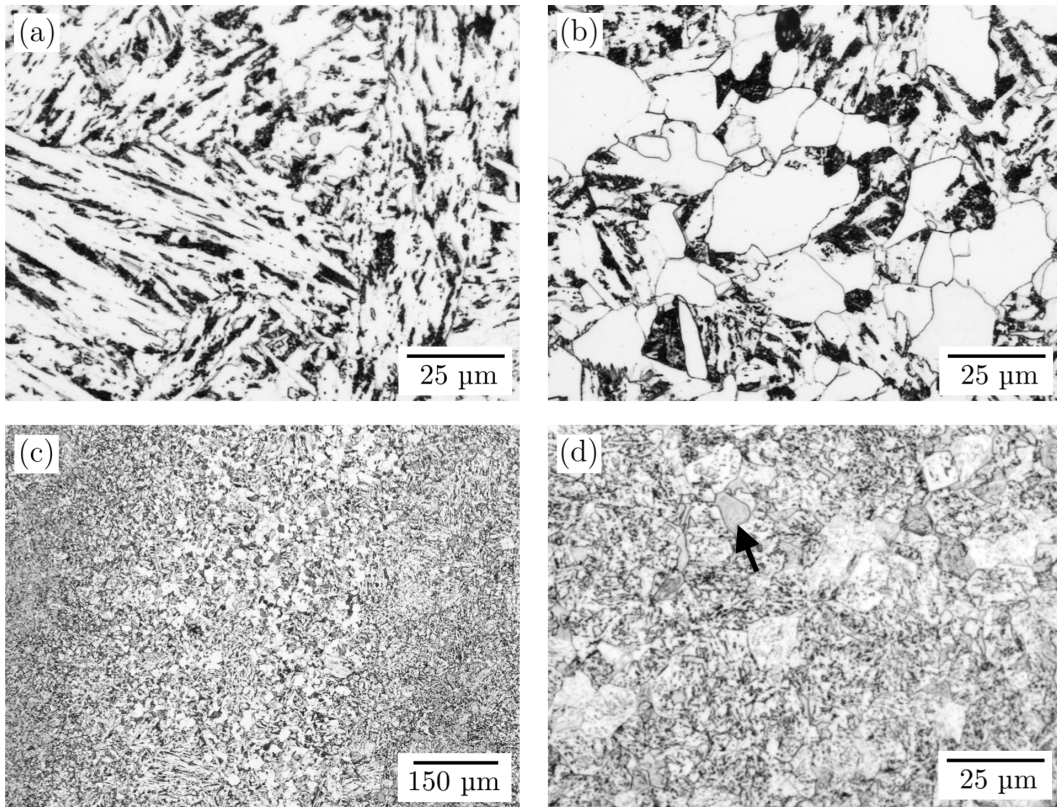


Figure 4.5: Optical microscopy of as-quenched material. (a) the Widmanstätten ferrite bulk. (b) inside allotriomorphic ferrite bands. (c) allotriomorphic ferrite band inside enriched A-segregate material. (d) A-segregate material, with martensite-austenite island highlighted.

and $\pm 0.7 \mu\text{m}$) are the scatters in the size values for each intercept line for each sample - the linear intercept analysis did not account for variation in grain size across individual lines (this was clearly much larger). Fine carbide precipitation was observed inside allotriomorphic grains, Fig. 4.7b, whilst coarse carbide precipitation, similar to that found between the Widmanstätten laths, was observed between the grains.

Electron microscopy revealed that the relatively coarse carbide precipitation observed between the ferritic grains in both the Widmanstätten and allotriomorphic microstructures was not continuous, as might be expected for pearlite, Fig 4.7c. Orientation relationships between the cementite (θ) and the surrounding ferrite (α) were found to be close to the Bagaryatski relationship, Figs. 4.7d, e and f. This relationship is typical in tempered martensite and lower bainite, and thus suggests the carbides are part of a lower-bainite microstructure. The relationship can also be found in pearlite colonies, but is usually associated with nodules nucleated on hyper-eutectoid cementite [274; 275; 276; 277]:

The Bagaryatski orientation relationship:

$$(100)_\theta \parallel (0\bar{1}1)_\alpha$$

$$(010)_\theta \parallel (1\bar{1}\bar{1})_\alpha$$

$$(001)_\theta \parallel (211)_\alpha$$

The third microstructure present was that found in regions enriched in solute by A-segregation, which were found to be darker and more finely-structured than the Widmanstätten bulk in optical micrographs, Fig. 4.5d. Blocky regions of material, which had not been readily etched, were identified under the SEM, Fig. 4.6c, and were particularly prominent in back-scattered electron images, Fig. 4.6d, indicating enrichment in heavy elements and/or a difference in phase. TEM revealed that these regions were composed of retained austenite, Figs. 4.9a and b, and that in some cases this had decomposed into martensite, Fig. 4.9c. These martensite-austenite islands were also occasionally found in the bulk Widmanstätten and allotriomorphic ferrite microstructures, as highlighted in Figs 4.6a and b.

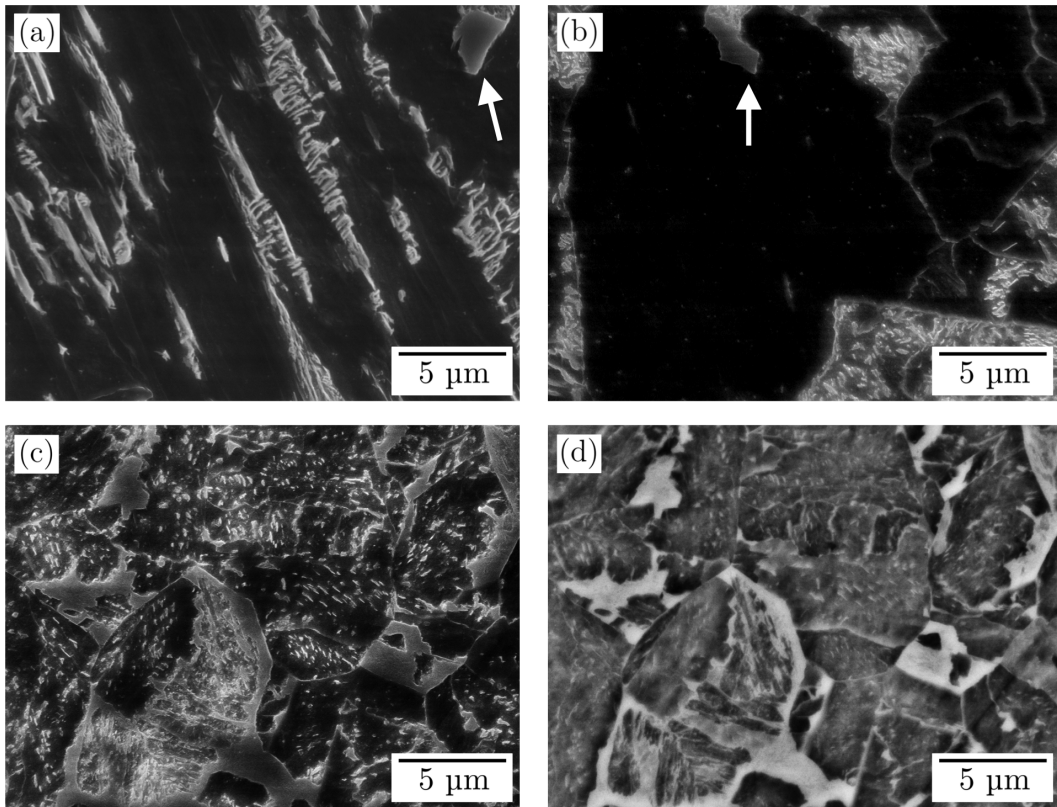


Figure 4.6: Secondary-electron micrographs of the Widmanstätten bulk, allotriomorphic regions and enriched regions are shown in (a), (b) and (c) respectively. Martensite-austenite islands are highlighted. (d) shows a back-scattered electron image of the enriched material in (c), with increased electron yield from martensite-austenite islands.

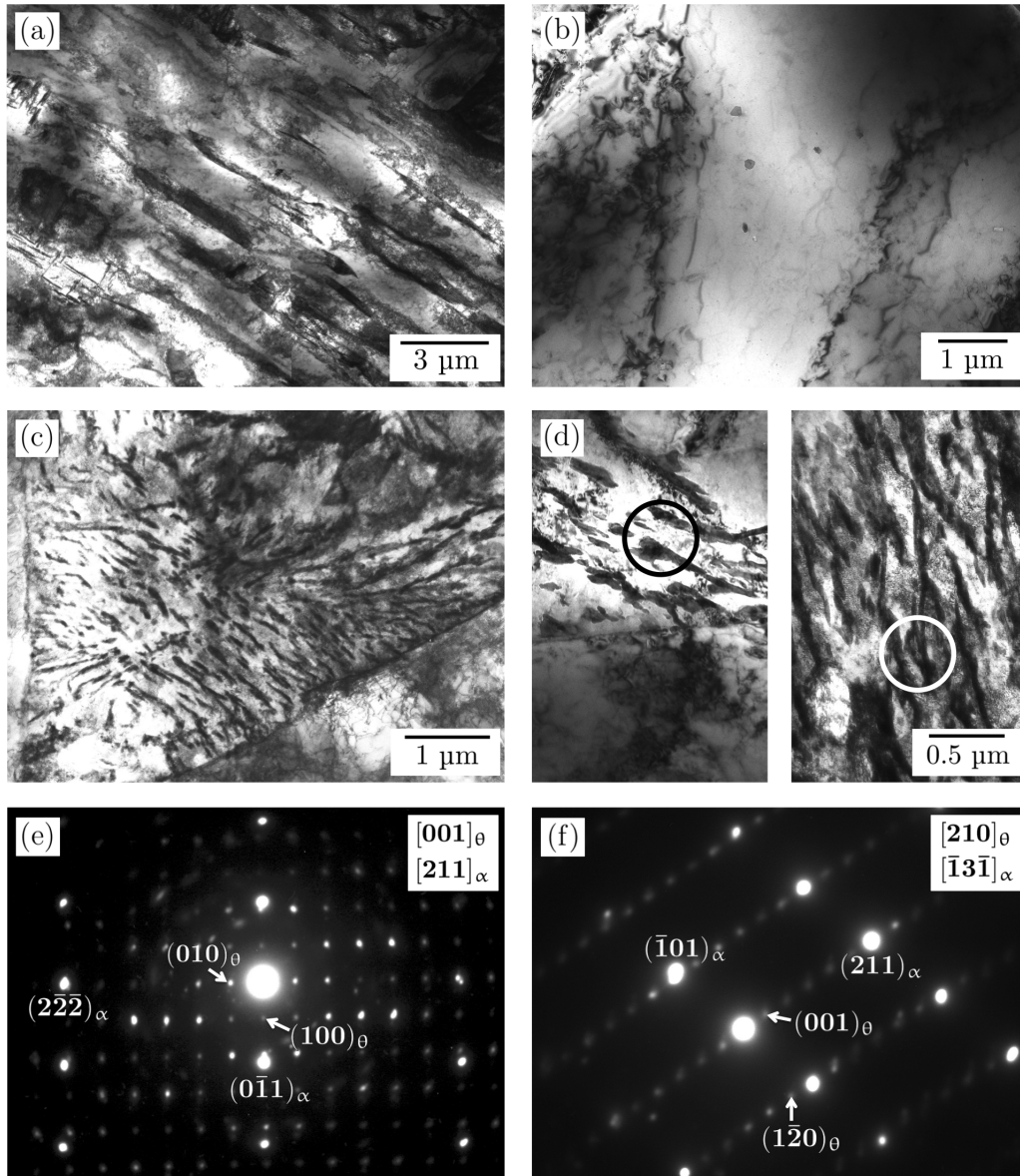


Figure 4.7: TEM bright-field imaging and diffraction. (a) Coarse Widmanstätten ferrite laths with no inter- or intra-lath cementite precipitation. (b) Fine carbide precipitation found within allotriomorphic grains. (c) and (d) show inter-ferrite cementite-rich regions. The electron diffraction patterns in (e) and (f), obtained from the left and right regions highlighted in (d) respectively, confirm cementite and the Bagaryatski orientation.

Elsewhere in A-segregate material, lower bainite appeared to be the most common microstructure between the martensite-austenite islands, Fig. 4.10a, along with some Widmanstätten ferrite. An orientation relationship consistent with Bagaryatski was found in the lower bainite regions and fine platelets were readily distinguished, Fig. 4.10b. In addition to cementite precipitation, distinctive globular/near spherical carbides were also observed, Fig. 4.10c. Bright-field imaging, diffraction and STEM EDX suggested that they were M_6C particles which had formed during the slow cooling from austenitisation. There was no evidence of their presence in non-enriched material.

Small globular MnS and mixed-oxide inclusions (with large dimension not greater than $30\ \mu\text{m}$, and more commonly far smaller) were sparsely distributed in a random fashion throughout all material examined, with a number density of $<30\ \text{mm}^{-2}$ for sizes of $2 - 30\ \mu\text{m}$. In addition, larger MnS inclusions were occasionally found in enriched A-segregate material, Fig. 4.10d, and often appeared elongated in the forging direction. The number density of inclusions with largest dimension $>40\ \mu\text{m}$ was $\approx 0.2\ \text{mm}^{-2}$ within the channels examined.

4.3.3 Tempered Microstructures

Following the simulated quenching heat-treatment, samples were tempered $645\ ^\circ\text{C}$ for 6 hours with heating and cooling rates controlled at $30\ ^\circ\text{C}\ \text{h}^{-1}$ to simulate conditions at the middle of a thick section. This led to the coarsening of cementite, Fig. 4.11, particularly so in the A-segregate material, where Mo_2C also precipitated, Fig 4.12. The martensite-austenite islands decomposed into a ferrite/cementite mixture, but these regions were still more resistant to etchant attack, as highlighted in Figs. 4.11c and d.

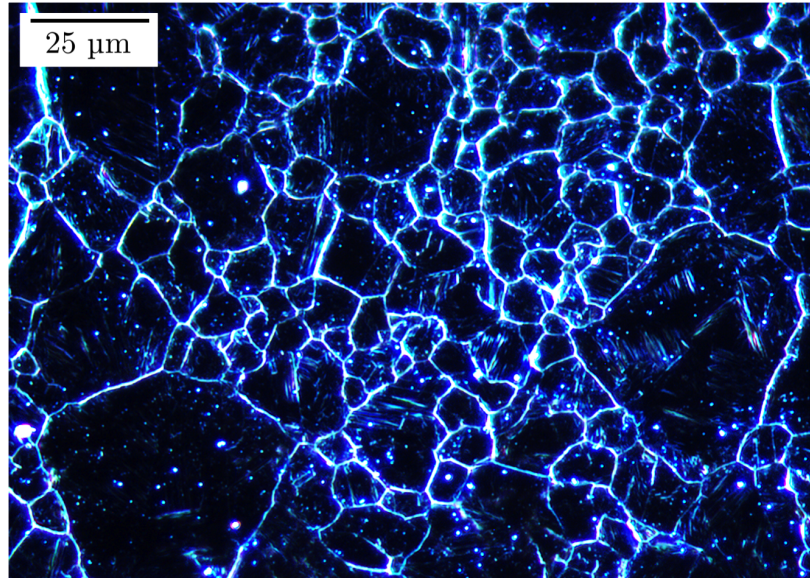


Figure 4.8: Prior-austenite grain structure, exhibiting a non-uniform grain size. Micrograph obtained by thermal etching, and dark-field optical microscopy.

4.3.4 Chemistry

The three microstructurally-distinct regions discovered in as-quenched material were subjected to electron-probe broad-beam spot-analysis, Table 4.3, as well as qualitative mapping, Fig. 4.13. A-segregate material was also specifically targeted using OES; Table 4.1 given an indication of the typical enrichment. These results are consistent with the microstructural observations that indicate a much greater hardenability and propensity to precipitate carbides within the A-segregated regions, which are significantly enriched with respect to manganese, nickel and molybdenum.

4.3.5 Hardness

Vicker's hardness measurements were taken from three distinct regions in as-quenched and as-tempered material: (i) the bands of allotriomorphic ferrite, (ii) the bulk (Widmanstätten ferrite) and (iii) A-segregate regions. Measurements of (i) and (ii) were taken from all samples, whilst measurements of (iii) could only be taken from samples containing A-segregates. Results, given in Table 4.4, show

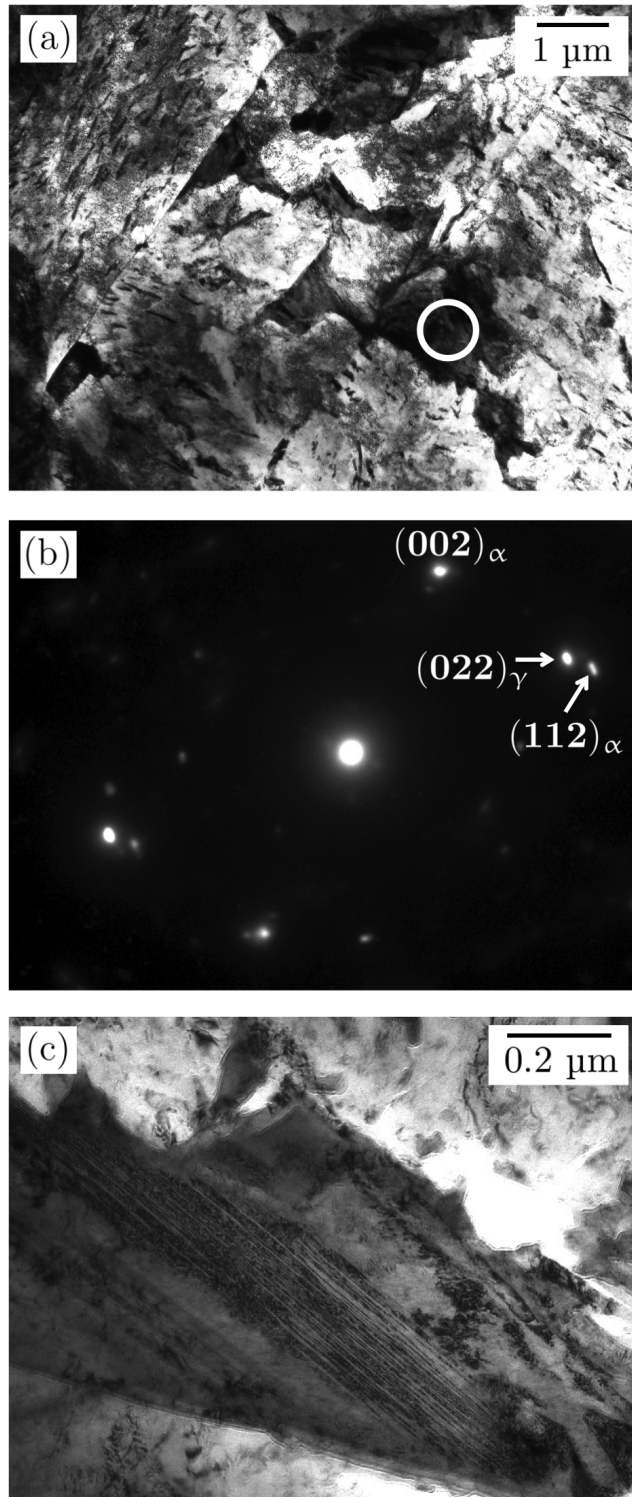


Figure 4.9: Martensite-austenite islands. (a) Islands at prior-austenite grain boundaries. (b) Electron diffraction analysis of the area highlighted in (a). (c) High-carbon twinned martensite within the islands.

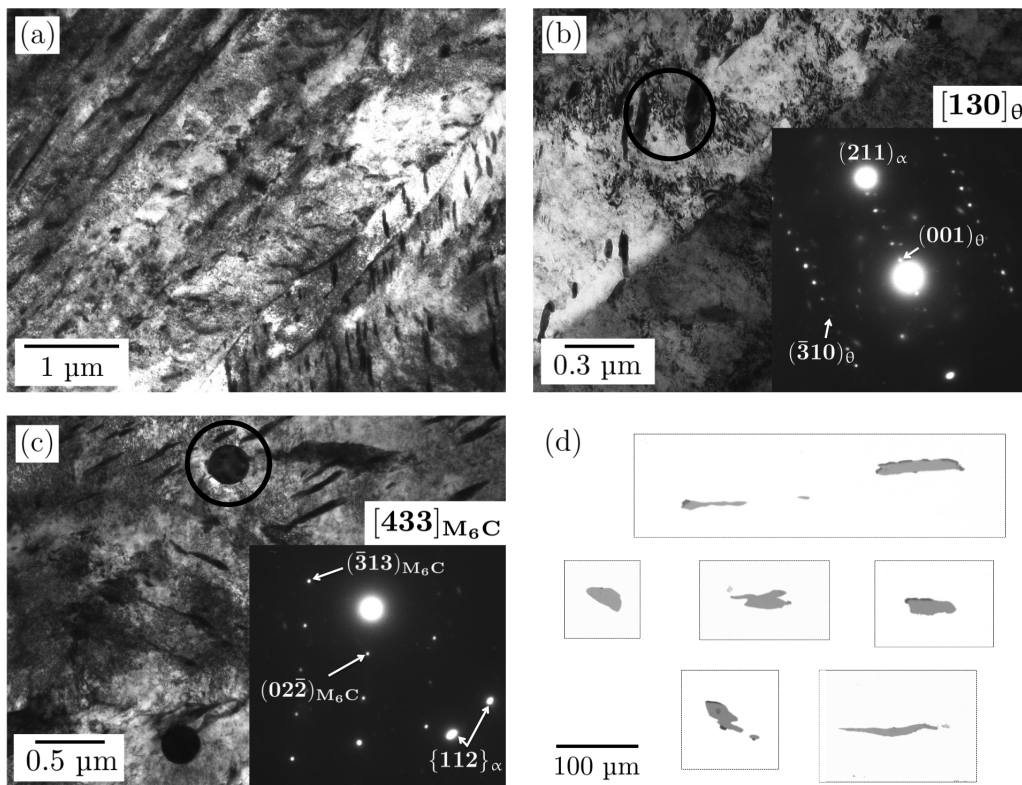


Figure 4.10: A-segregate region. (a) and (b) show TEM images and diffraction analysis consistent with lower bainite. (c) M_6C precipitates found exclusively in A-segregates. (d) Optical images of the larger MnS inclusions, with each box representing a different area of sampled material.

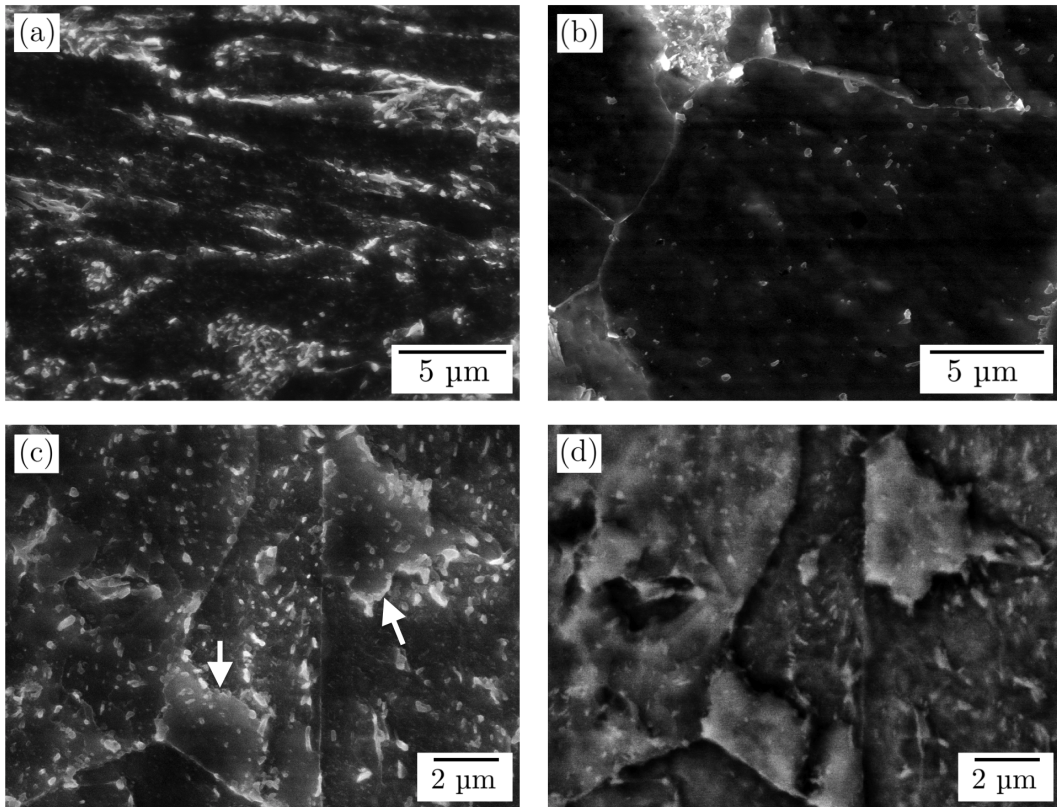


Figure 4.11: SEM images of tempered material in the etched condition. (a), (b) and (c) show secondary-electron images of the Widmanstätten bulk, allotriomorphic ferrite and enriched material respectively. Regions more resistant to etchant are highlighted in (c) and imaged with back-scattered electrons in (d).

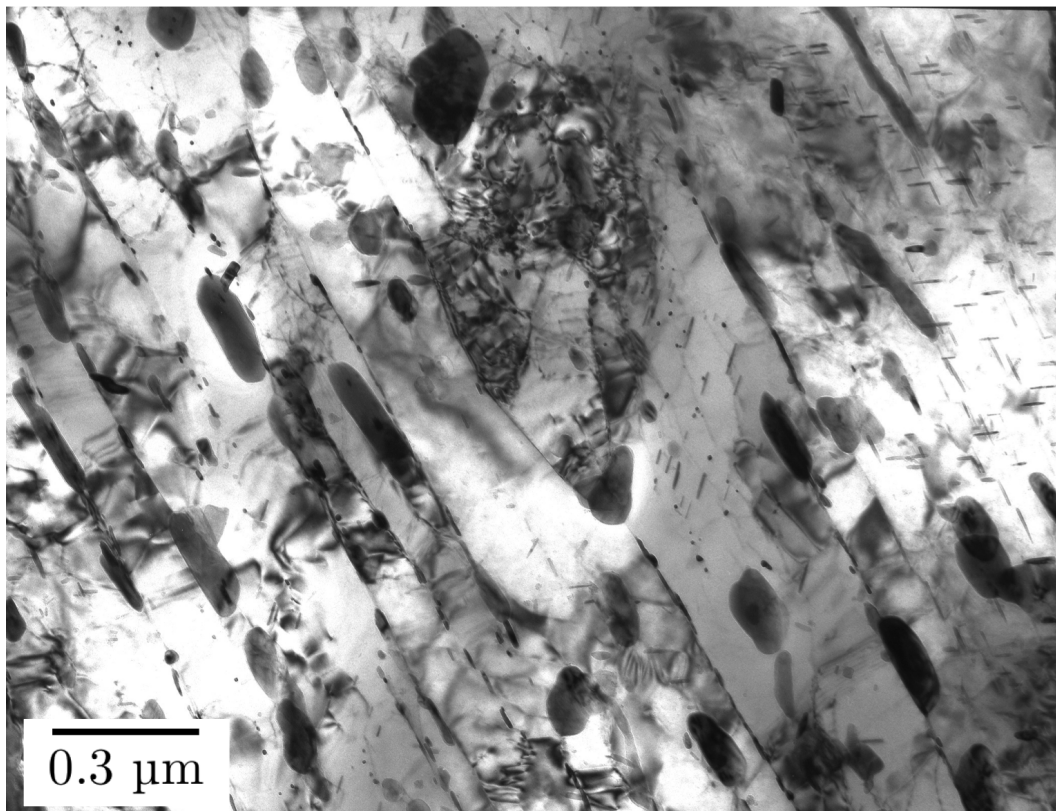


Figure 4.12: Tempered A-segregate material, showing coarse cementite carbides amongst fine bainite plates. Also present are fine needles of Mo₂C.

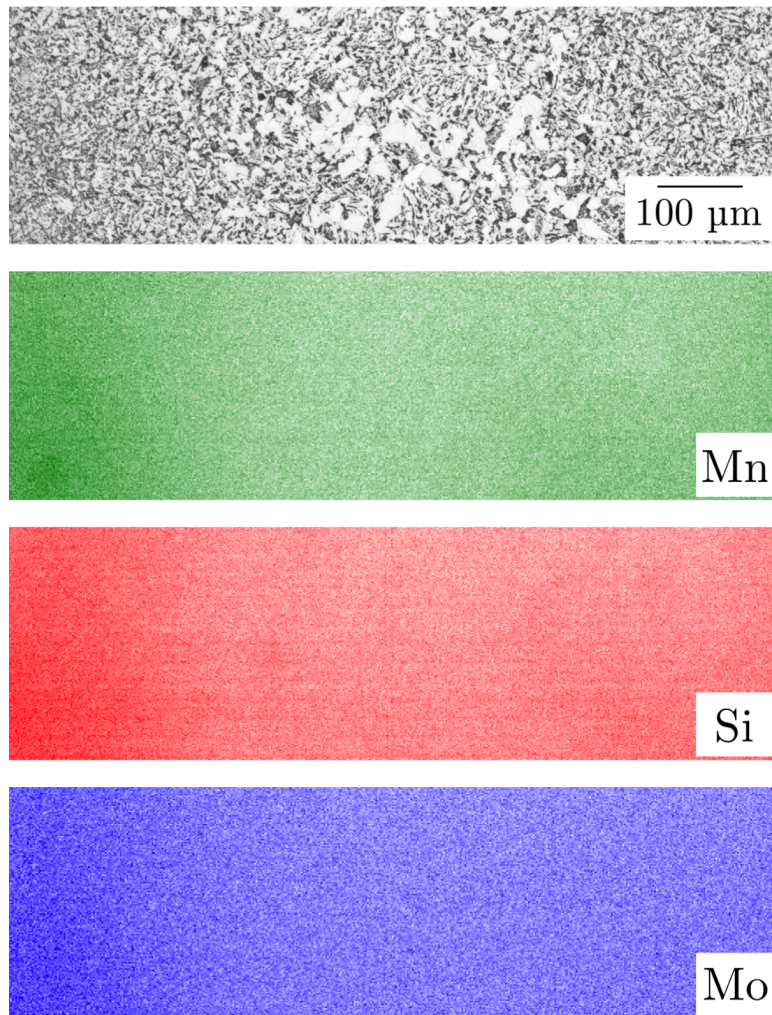


Figure 4.13: Qualitative EPMA mapping showing optical micrograph of region of interest (with A-segregate, allotriomorphic ferrite and Widmanstätten ferrite moving bottom left to top right) alongside maps for Si, Mn and Mo.

Table 4.3: EPMA broad-beam spot analysis (beam width 40 μm). Bold numbers are the composition in wt%, standard deviations are given in parentheses (10 different locations were sampled for each region type) and the italicised figure is the value of C/C_0 calculated using the trepanned cylinder concentrations in Table 4.1 as C_0 values.

Region	Mn	Ni	Mo	Si	Cr
	1.59	0.86	0.62	0.28	0.26
A-Segregate	(0.07)	(0.04)	(0.06)	(0.01)	(0.01)
	<i>1.21</i>	<i>1.17</i>	<i>1.27</i>	<i>1.10</i>	<i>1.22</i>
Allotriomorphic Ferrite	1.26	0.69	0.45	0.24	0.22
	(0.06)	(0.03)	(0.01)	(0.01)	(0.01)
	<i>0.96</i>	<i>0.93</i>	<i>0.93</i>	<i>0.94</i>	<i>1.04</i>
Widmanstätten Ferrite	1.28	0.69	0.47	0.24	0.22
	(0.04)	(0.02)	(0.02)	(0.01)	(0.01)
	<i>0.97</i>	<i>0.94</i>	<i>0.95</i>	<i>0.94</i>	<i>1.05</i>

a significant variation in hardness between the three regions after quenching, but that tempering suppresses the variations and leads to general softening. The size of indentations in as-quenched material ranged from $\approx 150 \mu\text{m}$ across in regions rich in allotriomorphic ferrite to $\approx 100 \mu\text{m}$ in A-segregate material.

4.3.6 Partial-Transformation Experiments

The simulated quench was interrupted at various stages by cooling at $25 \text{ }^\circ\text{C s}^{-1}$ in order to follow the development of microstructure. The points of interruption are indicated in Fig. 4.4. Fig. 4.14 is from regions not containing the segregate; allotriomorphic ferrite dominates above $600 \text{ }^\circ\text{C}$, and the transformation beginning at $550 \text{ }^\circ\text{C}$ is associated with the formation of both primary and secondary Widmanstätten ferrite. The transformation of carbon-enriched regions between Widmanstätten and allotriomorphic grains occurred $\approx 500 - 400 \text{ }^\circ\text{C}$, with the formation of cementite associated with the relatively flat dilatational response over this temperature range. Some austenite remained untransformed at $400 \text{ }^\circ\text{C}$,

Table 4.4: Hardness measurements taken from three distinct microstructures found in material. The \pm scatter in each result is one standard deviation.

Region	Hardness \ HV 2	
	As-Quenched	Tempered
A-Segregate	318 ± 17	240 ± 17
Allotriomorphic Ferrite	210 ± 15	181 ± 11
Widmanstätten Ferrite	243 ± 10	200 ± 10

as highlighted in Fig. 4.14d, and it is likely that some will be retained to lower temperatures.

In contrast, the segregated regions remained untransformed until about 600 °C, with little Widmanstätten ferrite prior to about 500 °C (except where depleted, allotriomorphic-ferrite-rich bands stretched into segregated regions, Fig. 4.5c). The formation of more bainite at lower temperatures, with finer carbide precipitation, appears to have led to the greater change in dilatation 400 °C.

4.4 Discussion

Homogeneous mechanical properties are obviously desirable for pressure vessels, and the macroscopic chemical segregation associated with the solidification of large ingots makes this unlikely [1; 264; 265; 278; 279] - a later part of this thesis, Chapter 5, demonstrates that A-segregation can have a marked effect on Charpy impact test results in Grade 3. In the following discussion, it is assumed that any macrosegregation is undesirable and that its suppression or elimination would prove advantageous.

4.4.1 Evolution of Microstructure and Hardness

The observed transformation sequences can be summarised as follows. In the bulk non-segregated material, allotriomorphic ferrite first nucleates at grain boundaries followed by the formation of Widmanstätten ferrite starting at around 550 °C.

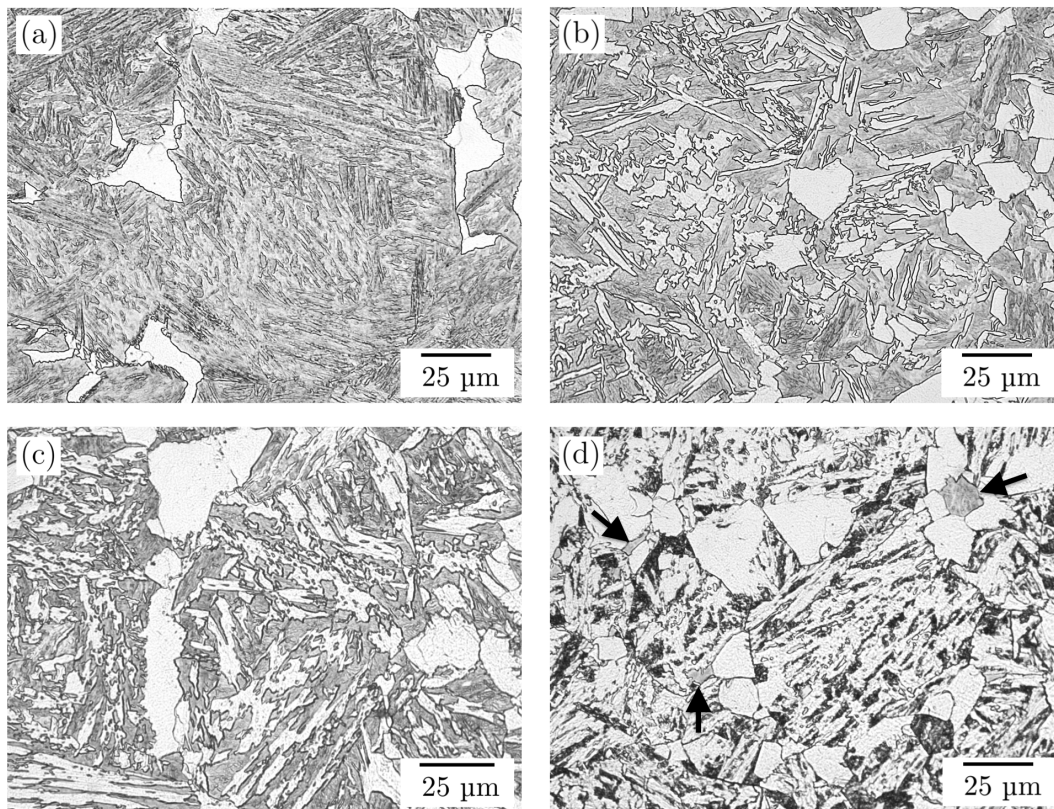


Figure 4.14: Partial-transformation experiments in material without A-segregation. (a)-(d) Microstructures when quenched at points A-D, respectively, in Fig. 4.4. Regions of untransformed material are indicated in (d).

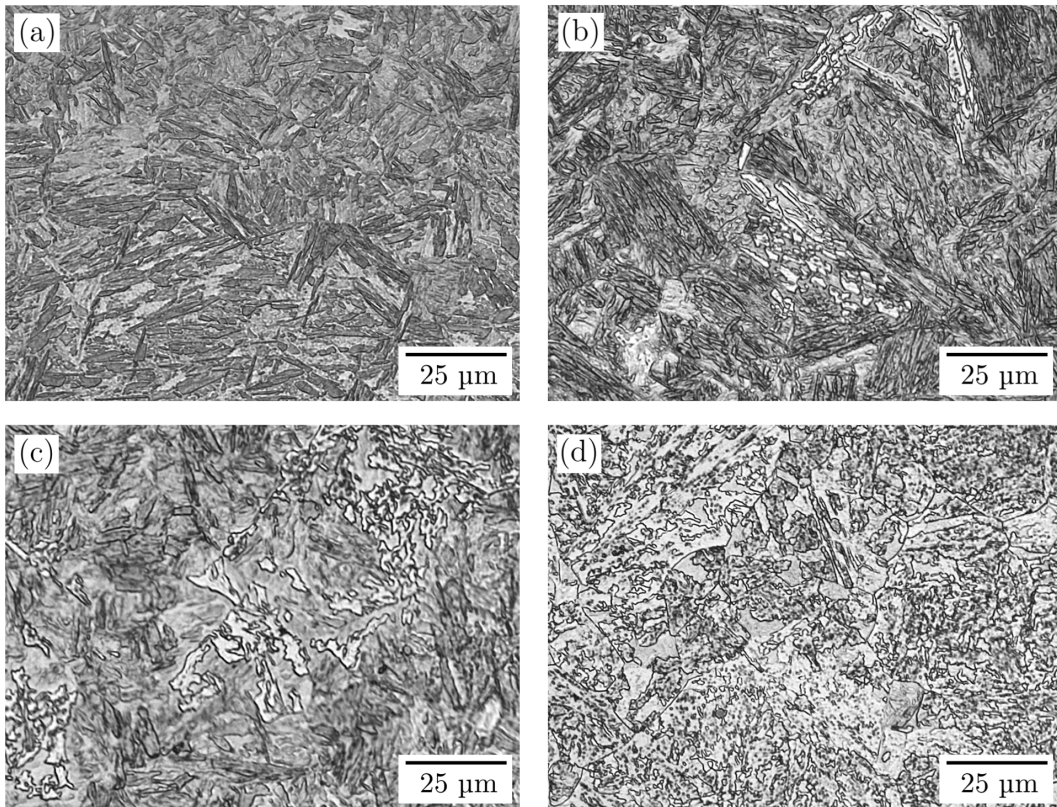


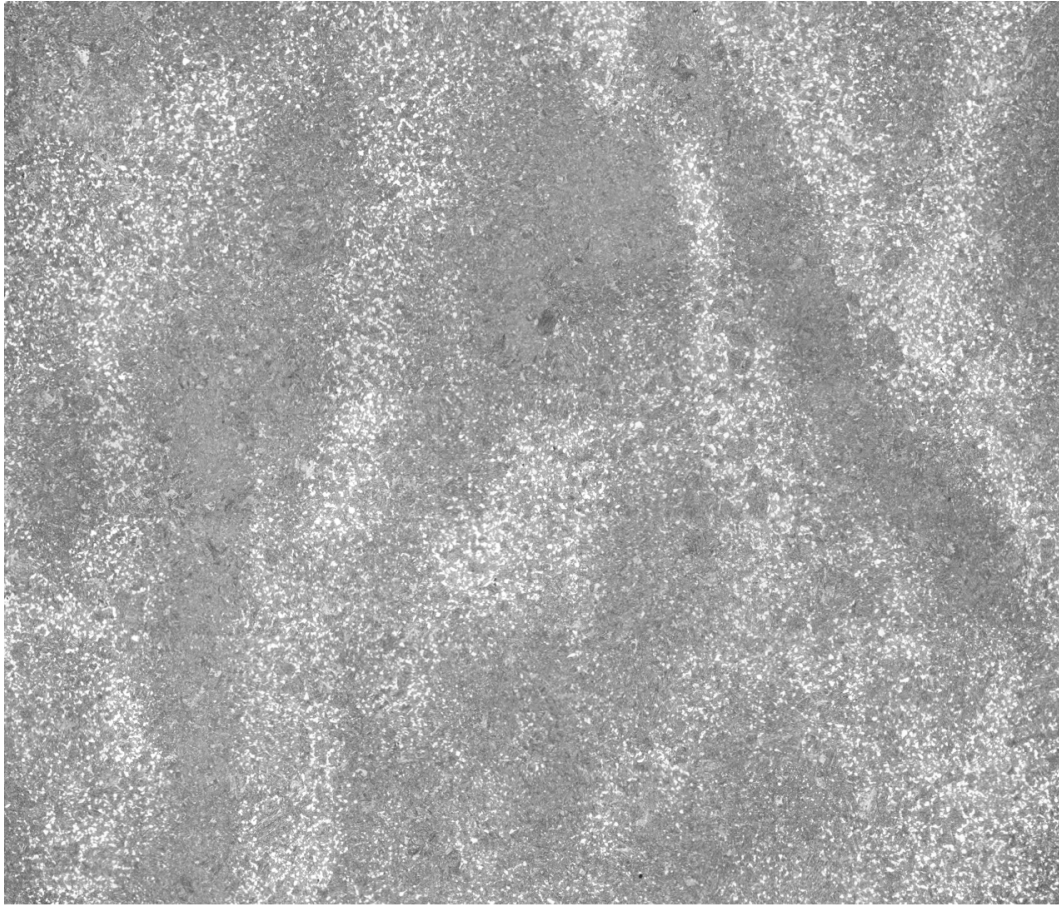
Figure 4.15: Partial-transformation experiments in material with A-segregation. (a)-(d) show microstructures when quenched at points equivalent to A-D (in enriched samples), respectively, in Fig. 4.4.

Carbon is partitioned into the residual austenite as ferrite grows, and the enriched austenite then transforms into lower bainite incorporating coarse carbides. The lack of well-defined fine platelets in this bainite, as well as the coarseness of the carbides, is likely due to a combination of the relatively high temperature of transformation, and the slow cooling rate. The A-segregated regions have sufficient hardenability to avoid allotriomorphic ferrite, and contain only a limited amount of Widmanstätten ferrite, transforming instead to a predominantly lower bainitic microstructure with a residue of martensite-austenite islands.

As-quenched hardness values are consistent with the observed microstructures. Coarse allotriomorphic ferrite is softest, with the finer plates of Widmanstätten ferrite being a little harder. The fine structure of lower bainite and martensite-austenite islands gave a much higher hardness to A-segregated material. Tempering naturally led to a general reduction in hardness, particularly in the segregated regions where the decomposition of the martensite-austenite islands significantly reduced the hardness in spite of the precipitation of Mo_2C particles.

On a coarser scale, microsegregation during solidification leads to the bands of allotriomorphic ferrite at the cores of dendrites, illustrated in Fig. 4.16, which shows a partially transformed sample at a scale consistent with expected primary and secondary dendrite arm spacings in large ingots [77; 188; 189; 196; 199]. It is likely that the scatter in the amount of allotriomorphic ferrite detected, particularly in samples with A-segregates, is due to the probabilistic nature of finding dendrite-arm cores within a sample (some cores evidently protruded into A-segregate channels). Banding of this kind is well known, and is determined not only by solute concentrations but also the heat treatment applied [280; 281; 282; 283; 284; 285]; unlike conventional banding in wrought steels, deformation plays very little role in the nature of the bands observed here.

The microstructural banding observed in wrought-steels can be mitigated by increasing the austenite grain size or the cooling rate from austenitisation [285]. The former is undesirable in that it could lead to a decrease in toughness through increased boundary embrittlement and coarser transformation products. A recent



1 mm

Figure 4.16: Depleted regions at the centres of prior dendrite arms, associated with bands of allotropic ferrite. Material was partially transformed up until point B in Fig. 4.4.

study suggests that cooling rates of 0.2 or $0.4\text{ }^{\circ}\text{C s}^{-1}$ are sufficient to suppress allotriomorphic ferrite formation in Grade 3 [286], and so this was investigated as a remedial method. These cooling rates led to the development of microstructures which were similar to those formed at $0.1\text{ }^{\circ}\text{C s}^{-1}$, Fig. 4.17, although they were free of allotriomorphic ferrite bands, appeared finer, and contained more martensite-austenite islands. A finer microstructure is expected to be tougher if it leads to finer cementite precipitation, and higher cooling rates are often sought in thick sections for this reason. The hardnesses obtained from these samples were not significantly different to the original condition, however, suggesting that the scale of the microstructure had not changed remarkably, Table 4.5. Thus it seems that increasing cooling rates from autenitisation can effectively mitigate the effects of residual microsegregation and would likely only improve bulk toughness through a finer microstructure. Increasing the mid-thickness cooling rate of a large forging to the required level in a commercial setting would, of course, be difficult due to conduction-limited cooling rates.

Table 4.5: Hardness measurements taken from the two distinct microstructures found in material quenched at faster rates. The \pm scatter in each result is one standard deviation.

Region	Hardness \ HV 2			
	$0.2\text{ }^{\circ}\text{C s}^{-1}$		$0.4\text{ }^{\circ}\text{C s}^{-1}$	
	As-Quenched	Tempered	As-Quenched	Tempered
A-Segregate	342 ± 32	252 ± 7	404 ± 29	258 ± 11
Widmanstätten Bulk	246 ± 10	198 ± 8	248 ± 8	198 ± 4

4.4.2 The Severity of A-segregation

Methods for the prediction of A-segregate location are assessed later in Chapter 6, which also discusses options for minimising segregation in Grade 3 (see Section 6.4). Here, however, an attempt is made to determine whether the severity of A-segregation, i.e., the level of element enrichment, is likely to be readily predictable.

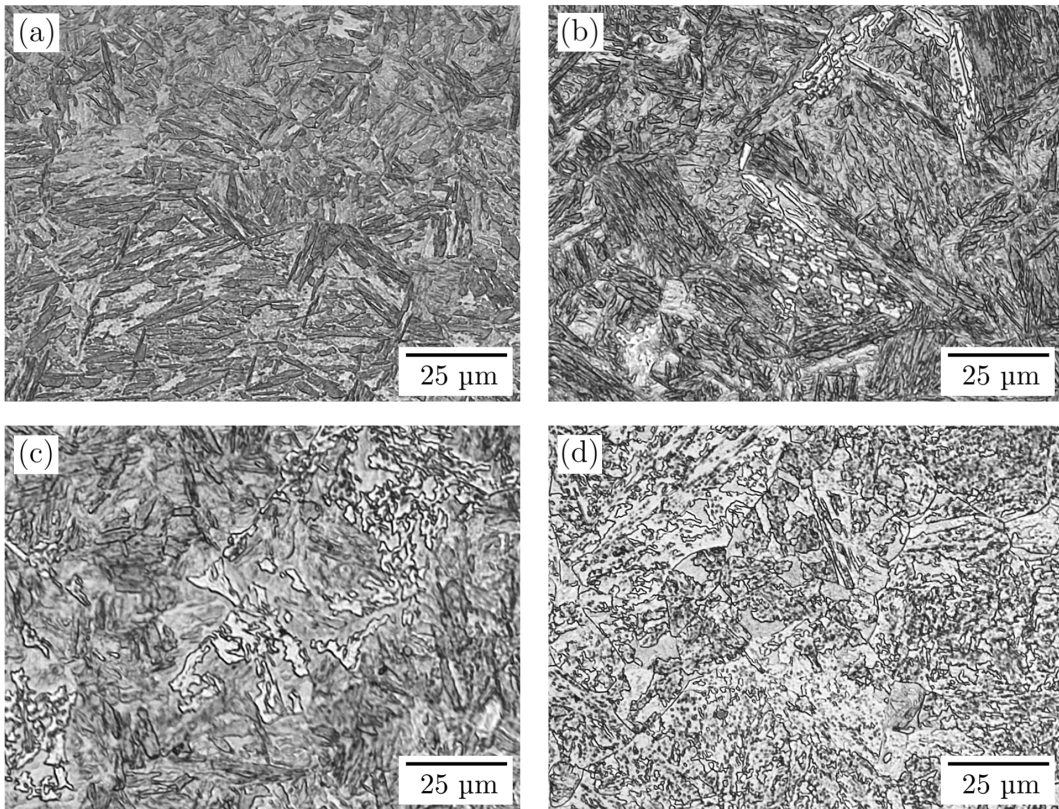


Figure 4.17: Optical micrographs of faster-quenching experiments. (a) $0.2\text{ }^{\circ}\text{C s}^{-1}$ in the bulk, (b) $0.4\text{ }^{\circ}\text{C s}^{-1}$ in the bulk, (c) $0.2\text{ }^{\circ}\text{C s}^{-1}$ in A-segregate and (d) $0.4\text{ }^{\circ}\text{C s}^{-1}$ in A-segregate.

One might expect that the concentration of liquid contained within an A-segregate would lie somewhere between the limiting lever-rule (equilibrium) and Scheil (non-equilibrium) cases, and that the concentrations of each element would be approximately consistent with a certain point in solidification in a given microsegregation model, e.g., a fraction solid of 0.7. To assess this, the enrichment associated with a particular A-segregate was measured using EPMA, Fig. 4.18. The measured concentrations, given in Table 4.6, agree well with those presented in Tables 4.3 and 4.1. A comparison of these data with MTDATA equilibrium and Scheil calculations is made in Table 4.6. It is clear that, contrary to the expectation stated above, the A-segregate liquid retained a composition which is not well predicted, and is unlikely to be using any of the well-known microsegregation models referred to in Section 2.4.2.1 using typical partition coefficients (the partition coefficients used here were calculated in MTDATA, but similar values can be found in standard binary phase diagrams and other texts [4; 287]). It is clear that some species are enriched far beyond the equilibrium limit (Cr and Ni), whilst others retain lower concentrations (Mo, Mn, Si). It is true that the diffusion of species over long periods of time during forging might have led to a higher level of Ni and lower level of Si relative to the other elements but the enrichment of Cr cannot be accounted for in this way.¹

¹Ni and Si are relatively slow and fast diffusers, respectively. The speed of carbon diffusion is far higher than for Si, and it also partitions to the liquid more strongly. Hence, the author believes its concentration measured in Table 4.1 is unlikely to reflect its true enrichment at the end of solidification - it is likely to have been nearer 0.3 wt%, or higher. One could argue that the enrichment of species like Mn within A-segregates might lead carbon to be attracted to enriched areas [281], but MTDATA calculations suggest that the activity of carbon is higher in enriched Grade 3 austenite than in bulk Grade 3 austenite.

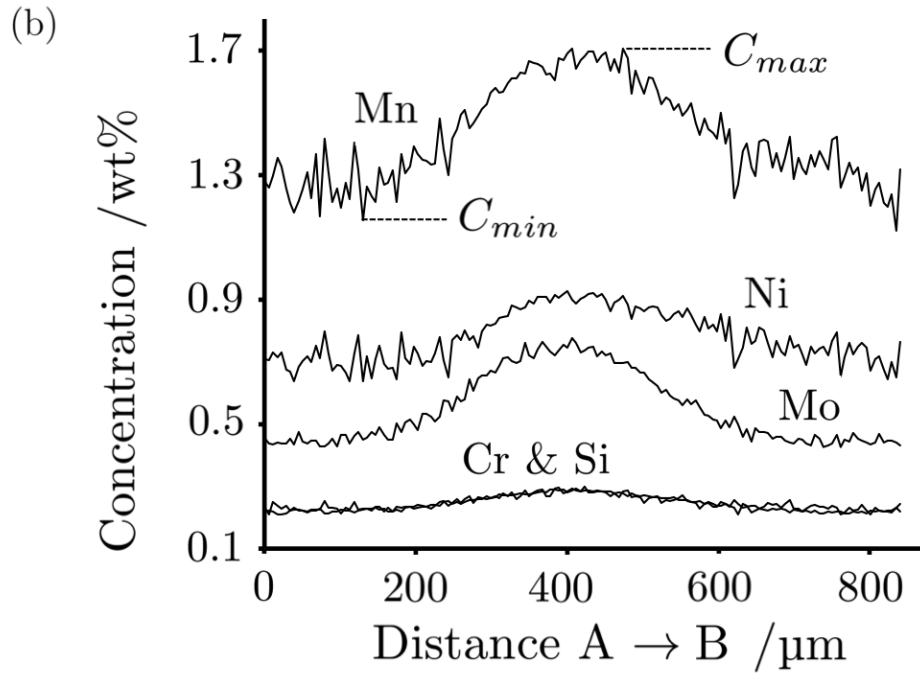
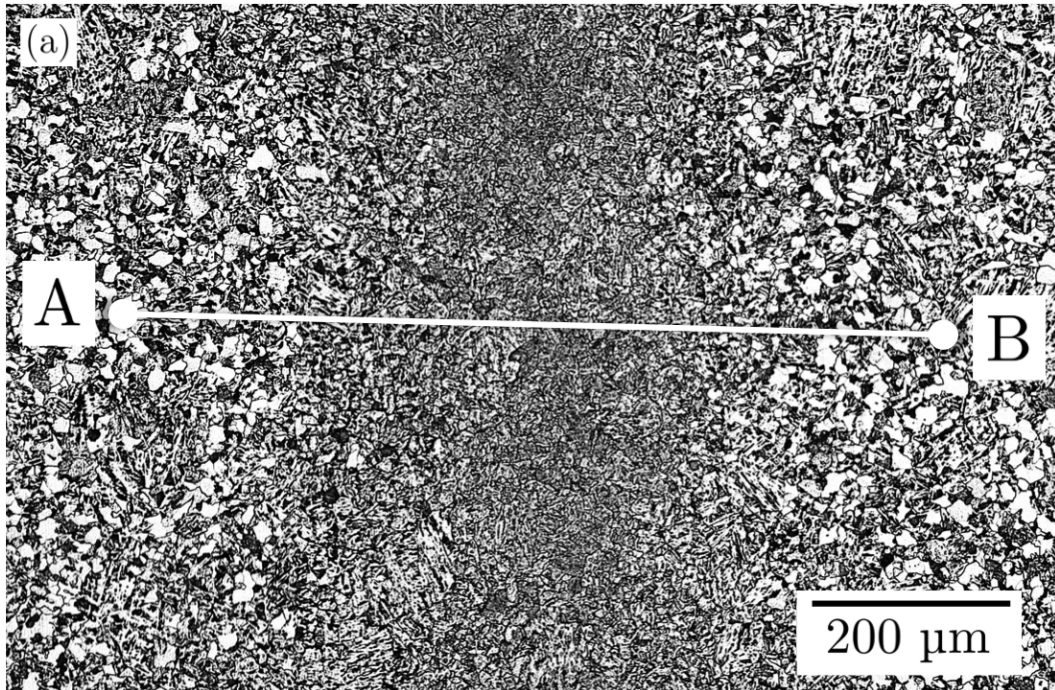


Figure 4.18: EPMA linescan results. (a). Optical micrograph of line analysed, which spanned the distance between two dendrite arms protruding into an A-segregate channel. (b). Plot showing variation in concentration of species, measured using EPMA with a step size of 5.2 μm and probe size of 1 μm.

Table 4.6: Measured compositions of A-segregate and dendrite-arm material, C_{\max} and C_{\min} , which are referred to in Fig. 4.18. The results of MTDATA equilibrium (lever-rule) and Scheil solidification calculations are also shown, giving liquid concentrations when the fraction solid was 0.95 (note P and S were not included in these models). Also included, for comparison, are the EPMA spot analysis results shown in Table 4.3 (10 A-segregate samples), as well as the typical A-segregate composition measured in Table 4.1.

	Concentration /wt%				
	Mn	Ni	Mo	Si	Cr
C_{\max}	1.71	0.92	0.78	0.29	0.30
C_{\min}	1.16	0.64	0.43	0.21	0.21
C_{Lever}	1.78	0.77	0.90	0.40	0.25
C_{Scheil}	4.56	0.93	4.38	0.87	0.4
$C_{\text{EMPA},40\ \mu\text{m}}$	1.59	0.86	0.62	0.28	0.26
C_{OES}	1.62	0.87	0.87	0.29	0.26

4.5 Summary and Conclusions

1. Simulated quenching of segregated Grade 3 material led to appreciable spatial variations in microstructure. In regions enriched in solute, a microstructure of Widmanstätten ferrite (limited amount), lower bainite and martensite-austenite islands was found, whilst the depleted areas at the centres of former dendrite arms saw extensive allotriomorphic ferrite formation.
2. The bulk microstructure was found to be predominantly Widmanstätten ferrite, contrary to previous reports of microstructure, where it has been classified as upper bainite. Regions between Widmanstätten and allotriomorphic ferrite grains, which had been enriched in carbon during transformation, were found to contain lower bainite with coarse cementite particles.
3. The hardness of as-quenched and tempered material varied significantly with the microstructure. The toughness is expected to be influenced by these variations, see Chapter 5.
4. The extensive allotriomorphic ferrite bands observed in the microstructure were a result of solidification-induced segregation. It was found that increasing the cooling rate allowed these bands to be eliminated.
5. The concentration of A-segregate liquid was found to be inconsistent with current microsegregation models and partition coefficients. The severity of A-segregation is examined again in Chapter 8.

Chapter 5

The Effect of A-Segregation on Impact Energy

5.1 Introduction

In this Chapter, the effects of A-segregation on the results of Charpy impact testing of quenched and tempered Grade 3 are assessed. The results of the previous chapter clearly demonstrated A-segregation can significantly influence microstructural evolution and hardness, with the enriched material associated with A-segregates delivering finer and harder microstructures than the bulk. As a consequence, one might initially expect A-segregate material in Grade 3 to be more brittle and less tough than the bulk. However, harder and finer microstructures have been found to deliver better fracture toughness results in tempered (i.e., martensite-free) Grade 3 [272; 288; 289; 290], with tempered martensite providing the best properties (the reasons for this are discussed in Section 5.4.3 below). Hence, the situation is not as clear cut as it might first appear. Here, it is hoped that the results of Charpy V-notch testing of A-segregate material can help clarify the likely consequence of fracturing through A-segregate material, notwithstanding the well-known reality that Charpy impact energies should not be related to fracture toughness values. The effect of A-segregation on the scatter in Charpy impact results will also be discussed.

A number of studies have investigated the effect of A-segregation on fracture properties in Grade 3 or similar compositions [259; 264; 265; 266; 291; 292; 293]. When the impact energies and fracture toughnesses of A-segregates have been specifically measured, significantly lower energies relative to the bulk material have been recorded, as well as a corresponding shift of the ductile-to-brittle transition temperature (DBTT) to higher temperatures [259; 264; 265; 266], Fig. 5.1. Authors have suggested that the increased frequency of coarse MnS precipitates inside A-segregates is responsible for the lower impact energies in both the transitional and upper-shelf regimes [259; 264], and that intergranular failure due to the segregation of embrittling P is another likely cause of lower impact energies [265; 266; 291; 293].

Unlike the Grade 3 examined in the studies referenced above, the material tested here has relatively low phosphorous and sulphur contents (0.005 wt% and 0.001 wt% respectively) and does not contain many large MnS inclusions. SEM is used to characterise the nature of failure in each Charpy specimen, whilst optical microscopy is used to examine the interaction between segregated material and crack paths.

5.2 Experimental

Standard $10 \times 10 \times 50$ mm Charpy V-notch impact specimens were machined from sections of the trepanned cylinder described above (see Fig. 4.1, the heat treatment in Table 3.2.4 and the chemistry in Table 4.1). The specimens were split into two groups: Set A were machined such that the notch of the Charpy specimen lay in the vicinity of an A-segregate (and that this extended across the specimen), whilst the notches of Set B specimens were deliberately placed away from segregates in the bulk material, Fig. 5.2. Note that the machining operation was not always successful in ensuring the notches of all Set A specimens lay directly within segregates. Within each of the Sets, specimens were taken from two radial positions relative to the thickness of the pressure-vessel shell, Fig. 2.2.1b. Charpy tests were undertaken following the standard procedure given in ASTM E23-12c [294]. Ductility percentages were found by measuring the ductile fracture

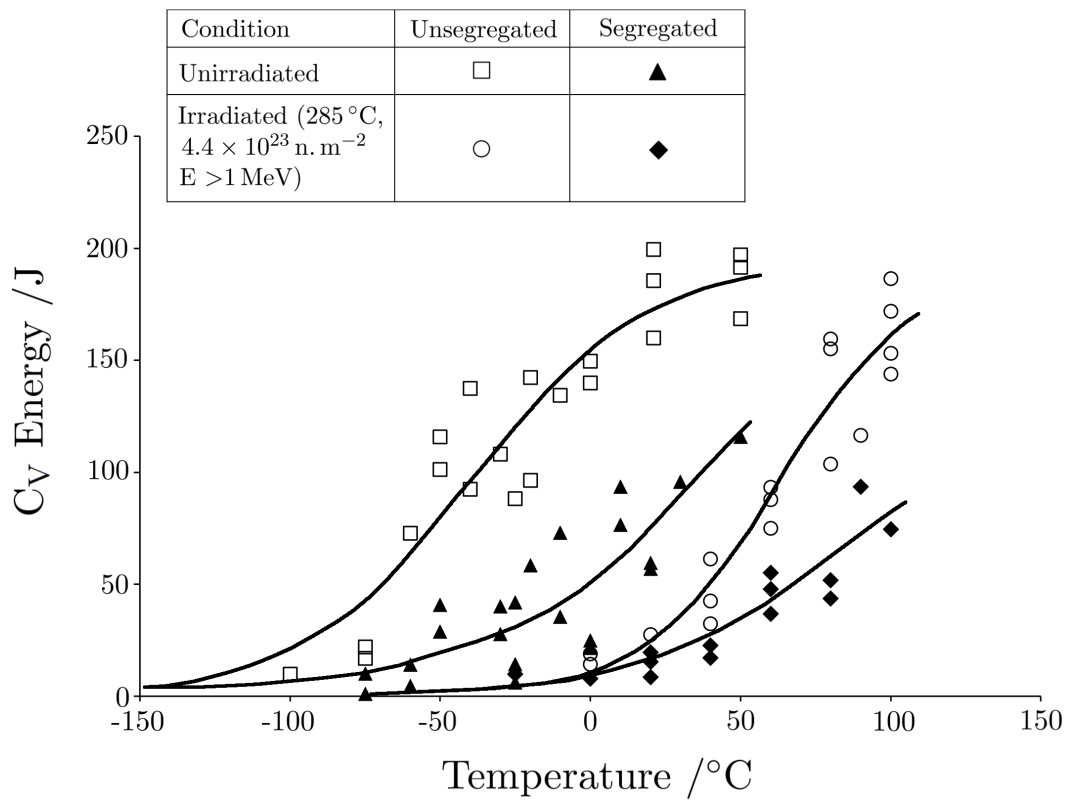


Figure 5.1: Charpy V-notch results for Grade 3-like steel, before and after irradiation, with and without A-seggregate material under the notch. Reproduced from [265]. Similar results can be found in [266].

surface area and comparing this to the total fracture surface area as described in paragraph A4.1.5 in ASTM E23-12c [294]. Specimens from both Sets were tested at temperatures of -50, -35, -20, 0, 22 (room temperature) and 250 °C. At least three samples from each Set were tested at each temperature, and additional tests were performed at 22 °C for Set A. Fractography was carried out using a Leica DM2500 M optical microscope and a JEOL 5800 scanning-electron microscope. Standard metallographic preparation techniques were used, including etching in 5% nital. Hardness measurements were taken using a Mitutoyo MVK-H2 hardness testing machine with a load of 2 kg.

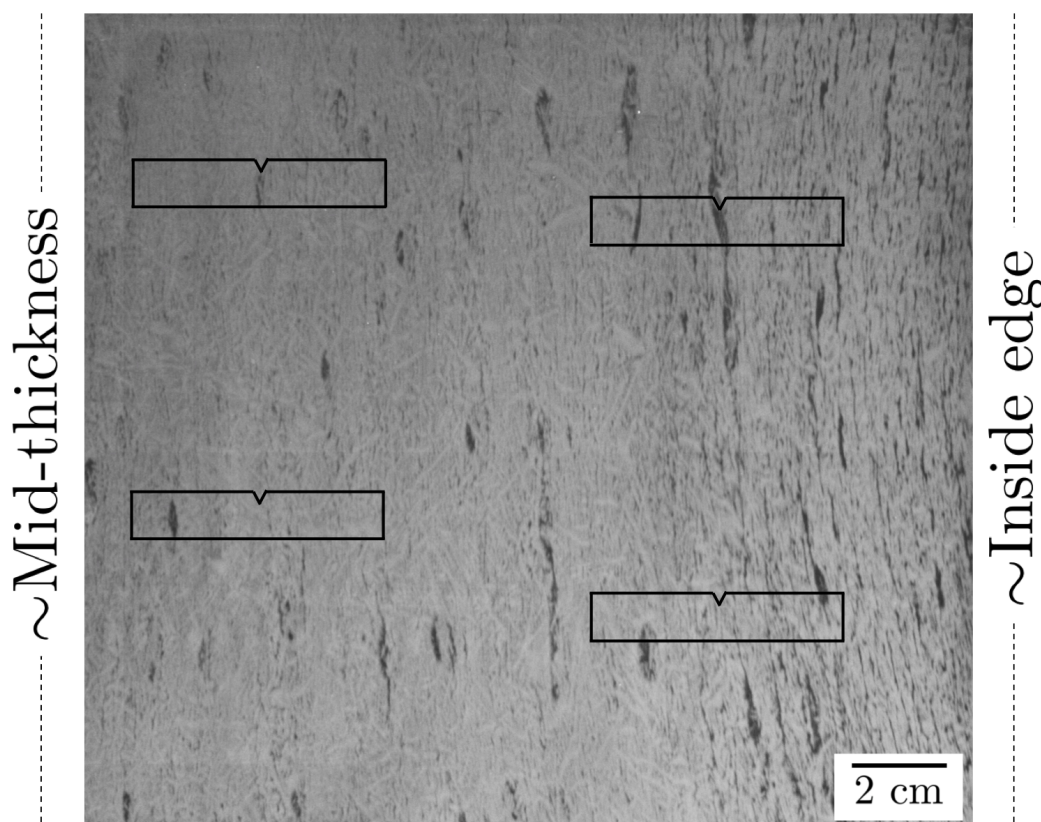


Figure 5.2: The placement of Charpy V-notch specimens extracted for testing. Note the two specimens at the top of the image formed part of Set A, whilst the two lower specimens formed part of Set B, and that the specimens are taken from two radial positions (near the inside, and near the mid thickness).

5.3 Results

5.3.1 As-Received Material

The microstructures typically found in the bulk and A-segregated material are shown in Figs. 5.3a and b respectively. These were formed solely through the heat treatment given in Table 3.2.4, and were not subject to any further changes. Based on the results of Chapter 4 above, it seems sensible to suggest that the bulk microstructure is comprised of a heavily-tempered mixture of Widmanstätten ferrite (light etching) and bainite with coarse carbides (dark etching), whilst the A-segregate material is likely to contain more tempered bainite and tempered austenite-martensite structures. The difference in these microstructures is reflected in hardness measurements of 196 ± 9 HV 2 for the bulk and 243 ± 17 for A-segregated material. No significant variation in either microstructure or hardness was detected based on position relative to the inside of the pressure vessel (apart from very close to the quenched inside edge of the vessel, where the microstructure was finer and harder, but no Charpy specimens were located here).

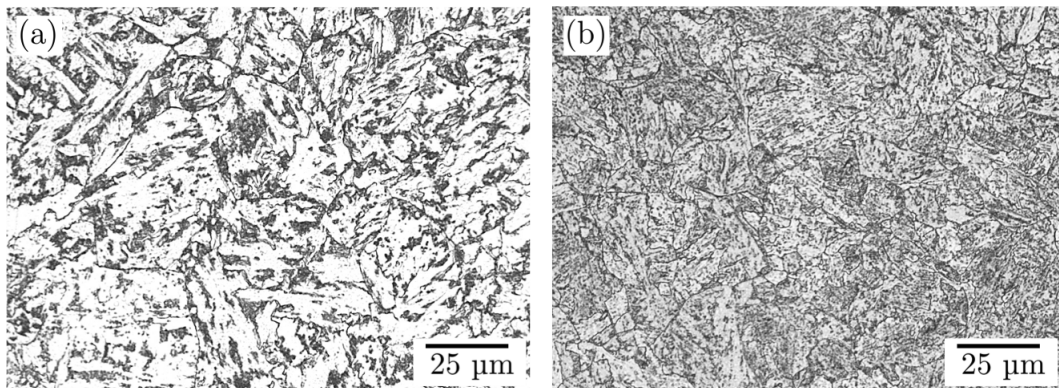


Figure 5.3: Optical micrographs of the fully heat treated material. (a) The non-segregated bulk material, comprising a heavily-tempered microstructure of Widmanstätten ferrite with pockets of lower bainite. (b) The microstructure found inside A-segregate channels, comprising a small amount of fine Widmanstätten ferrite alongside bainite and decomposed martensite-austenite islands, all heavily tempered.

5.3.2 Charpy Impact Tests

The results of Charpy impact tests of samples in Set A and Set B are shown Fig. 5.4. It is immediately evident that there is considerable scatter in results, particularly in Set A around room temperature (22 °C) where more tests were performed. To elucidate potential reasons for this scatter, the material beneath the fracture surfaces of specimens with notably low and high impact energies was examined through optical microscopy. In the case of the scatter in Set A results at room temperature, the relatively low results of 61 and 82 J appear to have been due to the presence of A-segregation across the width of the specimens, and the associated occurrence of intergranular brittle failure, Fig. 5.5. This type of failure appeared to be concentrated in regions with particularly large prior-austenite grains (which were up to an order of magnitude larger than the grains observed in the bulk). Conversely, the notably high result of 214 J was associated with extensive ductility, and limited interaction with enriched material in the vicinity of the crack tip, Fig. 5.6a. Indeed, it was generally found that the presence of A-segregated material around the notch and across the width of specimens in Set A did not always lead to it being included in the crack path, Fig. 5.6b. And even when A-segregate material was intersected by the failure, it did not always lead to the suppression of ductility or a noteworthy decrease in impact energy, Fig. 5.6c.

No systematic variation was found in either of Set A or B based on radial position of extraction (i.e., whether they were near the inside edge or near mid-thickness). For Set B, no A-segregation was detected around the notch during fractographic investigations apart from in the sample delivering 98 J at room temperature, Fig. 5.6d, although intergranular failure was not apparent in this sample. Indeed, apart from the two instances at room temperature highlighted above, intergranular failure was not observed in any of the other test specimens, including those at lower temperatures.

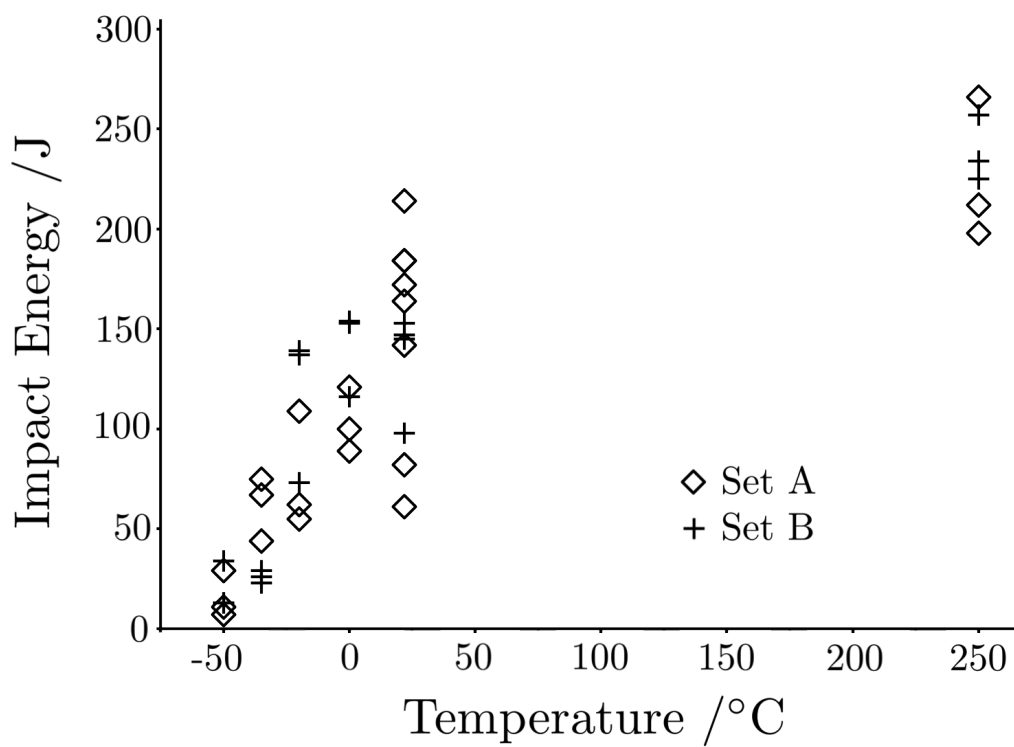


Figure 5.4: Impact energy results for all the samples analysed. Three samples from Set A and three from Set B were fractured at each temperature, with further tests carried out at room temperature (22 °C).

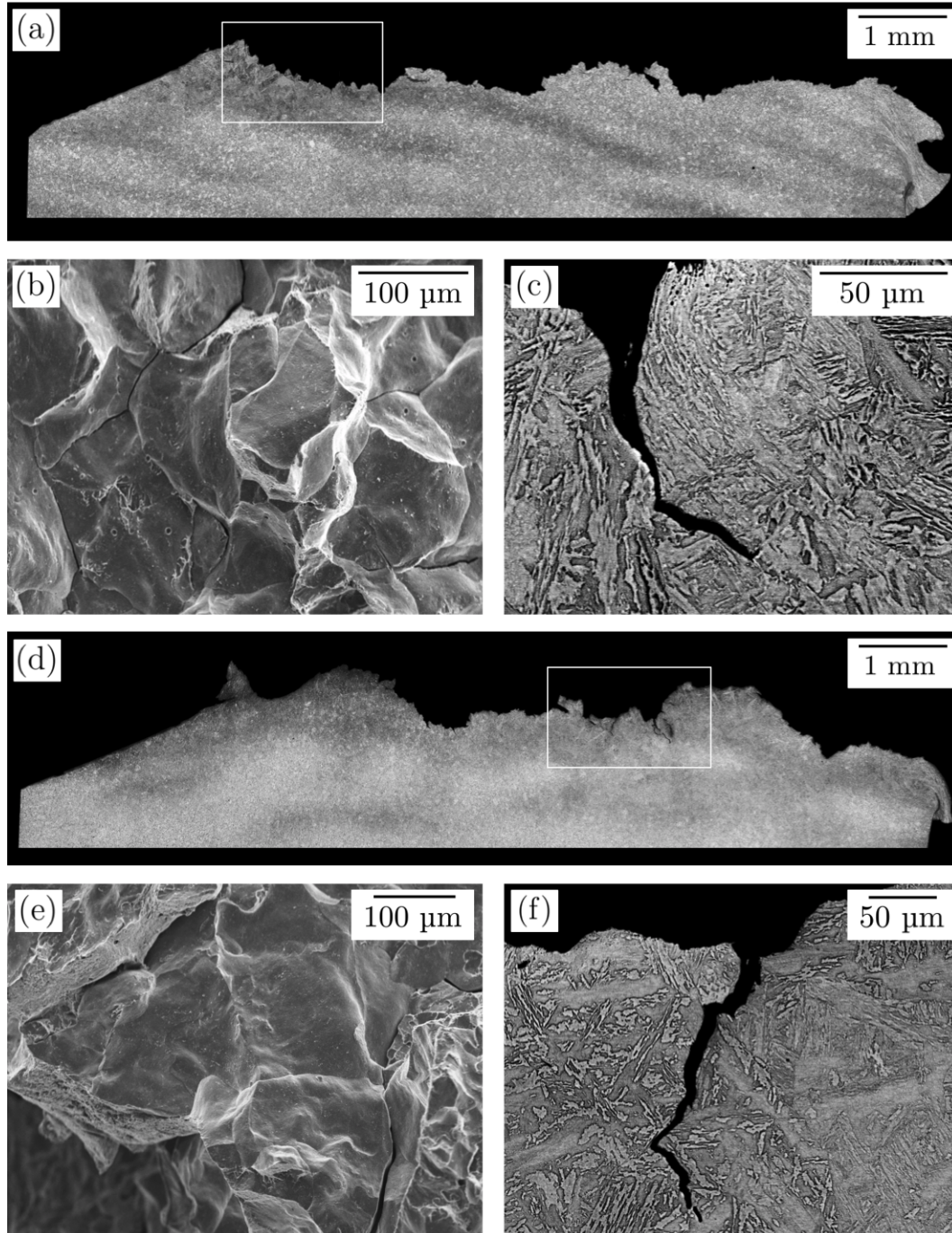


Figure 5.5: Analysis of specimens that exhibited intergranular failure at room temperature (22 °C). (a) Cross section of fracture surface for 61 J specimen (46% ductility), which clearly shows intersection of crack with dark-etching A-segregate material (notch at left). (b) Secondary-electron image of coarse intergranular failure observed (in area highlighted in (a)). (c) Back-scattered electron image of coarse microstructure around intergranular crack (the lighter features are likely to be tempered martensite-austenite islands [295]). (d), (e) and (f) show similar images for the specimen with 82 J impact energy (35% ductility).

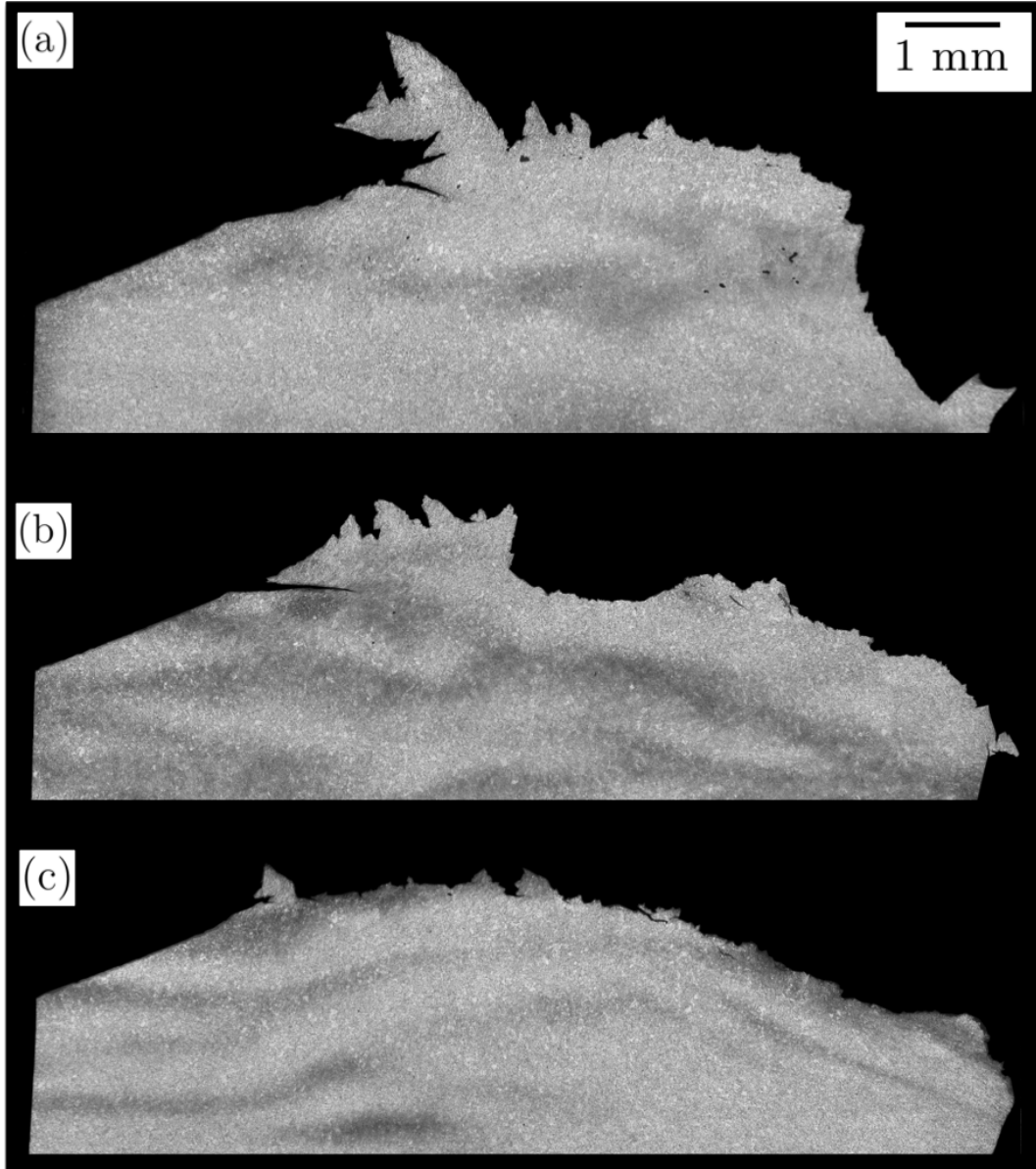


Figure 5.6: (a) Section of fracture surface for specimen in which very little A-segregate material appeared to be included in the crack path. Its impact energy was 214 J (100% ductility) at room temperature (22 °C). The voids evident were typically associated with inclusion debris. (b) A specimen which failed at (-20 °C) with 121 J impact energy (45% ductility), with segregated material existing close to the crack tip and not included in the crack path. (c) A specimen which failed at room temperature with 172 J impact energy (72% ductility), and included A-segregate material extensively in the crack path.

5.4 Discussion

5.4.1 Limitations of Investigation

Before discussing the results presented above in detail, it is worth highlighting some limitations of the present study and the conclusions that can be drawn from it. First, it must be recognised that the precise fraction of segregated material included in the crack path for each specimen is not known, because only one section was taken through each specimen for examination (Figs. 5.5a, 5.5b and 5.6). If extra slices had been taken, they would have undoubtedly revealed that the segregation profile underneath the fracture surface was not constant, as the internal structure of A-segregates is littered with dendrite arms (as seen in the previous chapter). Hence, even though a fracture surface may appear as though it did not include segregated material in Fig. 5.6, it may have done so if another section had been taken. Second, it is well known that although the impact energy of a Charpy test is determined by the energy absorbed across the full length of the crack, if initial ductility precedes brittle failure, then the impact energy will be dominated by the energy absorbed during the ductile stage. Hence, if we consider specimens failing in the ductile-to-brittle transition region, then the apparent effect of segregation could be readily changed or masked according to the position of the segregation, e.g., if ductility is exhibited before segregation is intersected in the brittle region (effect would be suppressed), or if the segregation limits the amount of initial ductility at the notch (effect more obvious). Thus, the effect of segregation can be expected to vary not just with temperature and volume fraction of segregate, but also with the position of segregation in the specimen. Third, Charpy impact energies cannot be readily related to fracture toughness, certainly not in any quantitative sense. So, even if the amount of segregated material present along the crack path was accurately known and its effect on impact energy determined, it would be difficult to relate this to fracture toughness. Collectively, the issues raised above, as well as the fact that samples in Set A did not consistently test only A-segregate material, mean that no transition curves or estimates of DBTT can be made for the A-segregate material verses the bulk.

Finally, it should be noted that the material tested here has been subject to a lengthy heat treatment that may not be representative of a production Grade 3 heat treatment. Changing the heat treatment will have a significant effect on the impact energies measured and the DBTT.

5.4.2 % Ductile Fracture

The % ductility results quoted above were found by comparing the total area of ductile fracture to the total fracture surface area. The results of this are plotted for every sample in Fig. 5.7a, and display a classic J-shaped curve. It is evident that the most outlying result is that at 61 J, which is for a sample that displayed intergranular failure. This suggests that plotting % ductility results obtained in this way could help indicate intergranular failure in the transition region. It certainly appears more useful than the results shown in Fig. 5.7b, which were obtained by measuring only the ductile region before brittle cleavage. It is true that measuring ductility in this way collapses the values more completely to a J-curve, and can potentially help eliminate sample comparison issues associated with gross bulk plasticity or incomplete fracture of the specimens, but it is less likely to highlight instances of intergranular failure.

5.4.3 Charpy Scatter and Intergranular Failure

It is well known that the failure of steels in a Charpy test is effectively a competition between various mechanisms, with the prevailing one being that which operates at the lowest stress. Ductile tearing is usually observed at high temperatures and progresses through void growth and coalescence as a result of widespread plasticity, whereas transgranular brittle crack propagation (cleavage) is triggered by crack nucleation at carbides or other brittle second-phase particles. Both of these mechanisms can be observed in the same Charpy sample in the ductile-to-brittle transition region: here, stable tearing usually precedes brittle cracking, but the onset of cleavage is variable and determined by the occurrence of a suitable flaw ahead of the crack front to initiate brittle failure (e.g., a cracked carbide). This delivers significant scatter in the ductile-brittle transition region, as has been observed in pressure-vessel steels [288; 296; 297; 298], which is only treatable using a

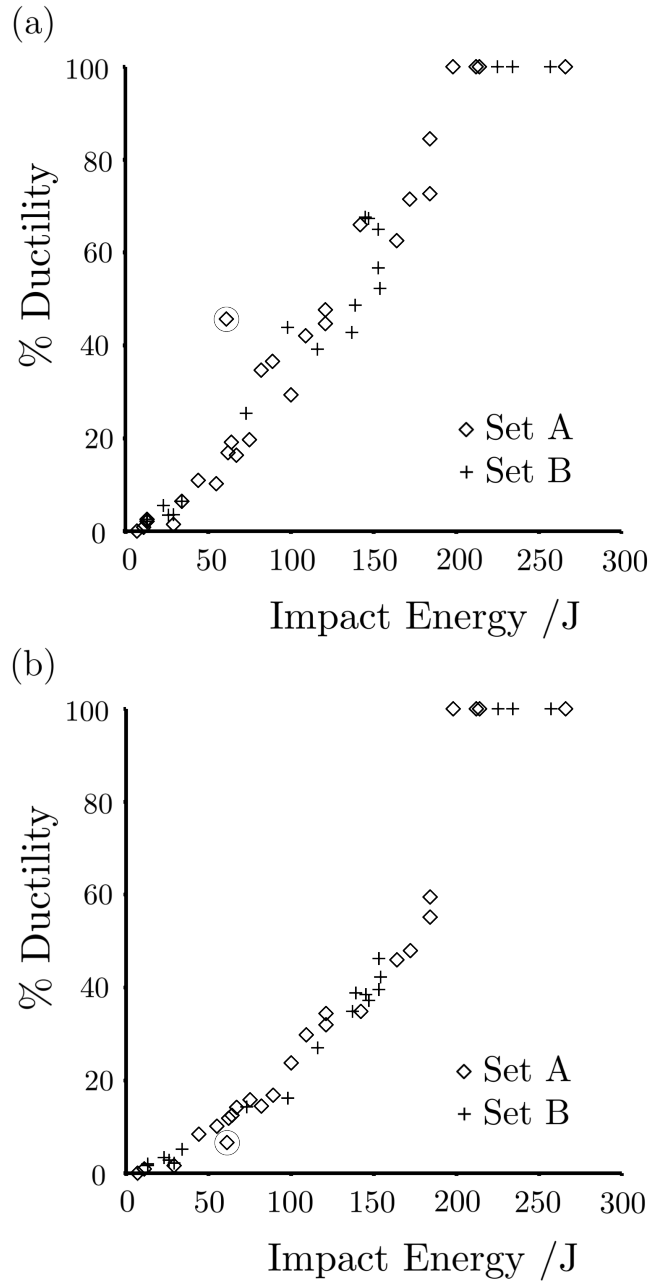


Figure 5.7: % ductility vs impact energy curves using two different calculation methods for % ductility. In (a) % ductility was found by using the total surface area of ductile failure over the whole Charpy specimen, whereas in (b) the ductility was calculated solely based on the area of ductility in front of the notch tip, and ignored any shear occurring alongside or after brittle failure had been initiated. In both (a) and (b) the point corresponding to 61 J is highlighted.

probabilistic approach to fracture [297; 299; 300; 301]. Material inhomogeneities, such as inclusion clusters, can also lead to scatter in the upper shelf [302]. The presence of A-segregate material within a specimen is expected to further increase scatter in Charpy results, not only due to microstructural differences, but also due to the effect of embrittling species. The segregation of embrittling species like P can lead to a third failure mechanism in fracture testing - that of intergranular brittle failure. Such a mechanism of failure absorbs very little energy, and hence can contribute greatly to Charpy scatter.

Here, it is most likely that the primary cause of the grain-boundary embrittlement which led to intergranular failure was the segregation of P to prior-austenite boundaries, the effect of which was then compounded by the particularly large austenite grain sizes and hardnesses associated with A-segregated areas [265; 266; 291; 293]. The reasoning behind this judgement is outlined below.

The embrittlement of grain boundaries in low-alloy steels during tempering (at temperatures up to $\approx 600^\circ\text{C}$) through the segregation of impurity elements (S, P, Sn and Sb) has been investigated for many decades; the excellent review of Guttmann gives an overview of its key features [303].¹ Tempering at 645°C should not lead to significant P embrittlement of Grade 3, even when P levels are quite high. Indeed, it has been found that extensive heat treatment below 530°C is required to initiate intergranular failure [292; 311], and that embrittlement can be reversed by short heat treatments at 630°C and above [279; 292]. So, what has caused the embrittlement of A-segregate material here? It is perhaps possible that sufficient P segregation has occurred at 605°C in A-segregate material for intergranular fracture to occur, but a more likely explanation is that a combination of a slow cooling rate from tempering and the particular microstructural

¹Essentially, it is thermodynamically favourable for these species to segregate to grain boundaries [304; 305; 306; 307] during heat treatments in the range $\approx 350\text{-}600^\circ\text{C}$, and their presence causes the decohesion of these interfaces by withdrawing electron density from the bulk Fe [308; 309]. At higher temperatures, the driving force for their segregation decreases, and hence the embrittlement is reversible by applying a high temperature heat treatment (although a finite amount of P segregation can still occur at high temperatures and in the austenitic regime [303; 310]).

properties of A-segregate material is truly to blame.

As well as being enriched in P, A-segregates are also enriched in other species - C, Cr, Mn, Ni and Mo, Table 4.1. These elements have been shown to directly affect the ability of P to embrittle low-alloy steels, but their effects are not additive (Cr, Mn and Ni enhance it, C and Mo suppress it [303; 312; 313; 314; 315]), and it is unlikely that they have a significant net effect in this regard. Instead, the indirect effect of these elements on embrittlement - through providing a harder microstructure - is likely to be more important. But even a harder microstructure does not appear to have been sufficient for intergranular failure: as shown in Fig. 5.6c, A-segregate material did not always fail in an intergranular manner. Larger prior-austenite grains are also required. This is evidenced by the fact that intergranular failure was seen only in regions consistently displaying very large (100 μm or more) prior-austenite grains.² Increased intergranular susceptibility due to higher hardness and larger austenite grains for a given P segregation level has been well documented [303; 319; 320]. The reason for the large grain size exhibited in A-segregates is still not clear, but it is interesting to note that austenite grain growth is restricted by the formation of AlN at grain boundaries [321], and that Al is the only alloying element in Grade 3 to have a solid/liquid partition coefficient greater than 1 (i.e., it will enrich the solid, not the liquid, and hence will be depleted in A-segregates). In summary, then, segregation of P to prior-austenite grain boundaries will likely have occurred during the slow cooling of the material following tempering. P segregation will have occurred throughout the material, but the higher level of P in A-segregate material, coupled with harder microstructure and large prior-austenite grains also found in these regions, delivered intergranular failure during Charpy testing.

²Note that slow cooling from 605 °C may also, in theory, have led to ferritic boundaries also being enriched in embrittling species (as they are present during this cool) [316]. Explanations for the preferential cracking of prior-austenite boundaries have often been based on the different structure of ferritic versus austenitic boundaries (segregation has been found to vary significantly based on this [303; 314; 317]), but another distinct possibility is that both sets of boundaries are sufficiently enriched, and that prior-austenite boundaries simply present a less tortuous crack path (particularly if they are large) [303; 316; 318].

Attempts were made to confirm the segregation of P to prior-austenite grain boundaries using secondary-ion mass spectrometry (SIMS) across a prior-austenite boundary ahead of a crack, but no P signal could be detected. Further attempts were made using energy-dispersive X-ray analysis in scanning transmission electron microscopy (STEM EDX) on a foil milled from ahead of a crack, Fig. 5.8. However, of the many boundaries that were assessed using line scans, only the boundary highlighted in Fig. 5.8c showed any sign of P segregation. Therefore, no consistent P segregation to grain boundaries was measured. Although some studies have claimed that STEM EDX can resolve the P segregation [322], it has usually been measured using Auger electron spectroscopy on fracture specimens broken in situ under high vacuum.

5.4.4 Material Integrity

In spite of the limitations acknowledged above, the following general statements can be made about the results of this study whilst still providing some insight as to the possible impact of A-segregation on material integrity. Note that these statements primarily concern the lower-shelf and transition regimes, as a limited amount of data were collected in the upper-shelf.

It is evident that the presence of enriched material near the notch does not necessitate it is included in the crack path, and even if it is intercepted, it will not always lead to low impact energy, Fig. 5.6. This is certainly the case if significant ductility is observed elsewhere in the Charpy sample, as this would deliver a high impact energy regardless of brittle segregate failure elsewhere. However, it is very likely that the material contained within A-segregates is embrittled by P, and that if a significant amount of it is included in the crack path, it will deliver intergranular failure and a substantially decreased impact energy when failure is dominated by brittle fracture, Fig. 5.5. This in turn can lead to significantly increased scatter in results around the ductile-to-brittle transition.

It seems reasonable to suggest that the effect of A-segregation should not be a great concern to design engineers if any failure is to occur through a significant

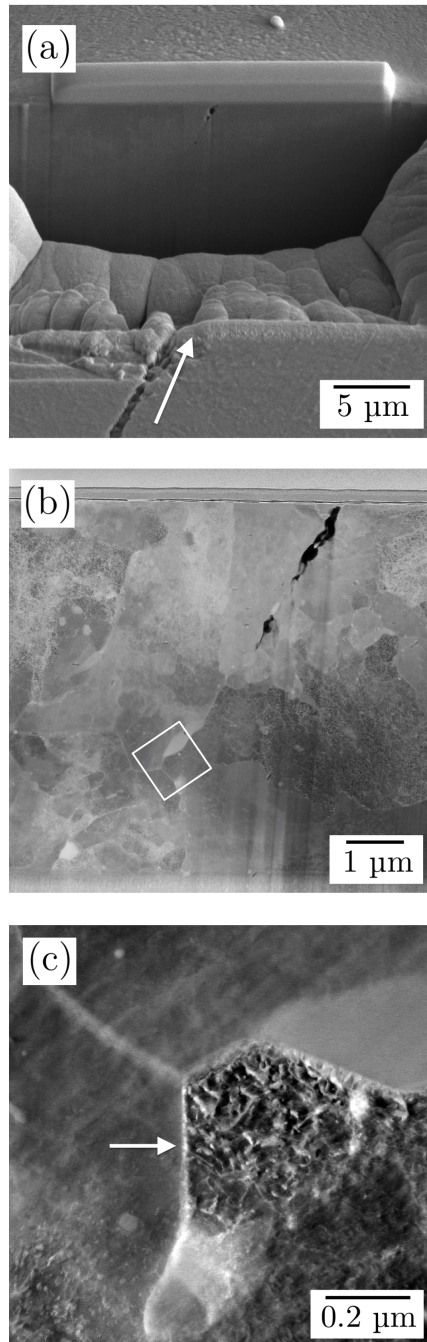


Figure 5.8: STEM-EDX investigations of grain boundaries in A-segregated material, cracked in Charpy testing. (a) Focussed-ion beam milling of foil to include crack. (b) Foil extracted. (c) Line scans revealed the boundary highlighted to be rich in P. The position of (c) is highlighted in (b).

thickness of material in which segregates may only be met occasionally [323]. However, the potential of A-segregated areas to act as sites for crack nucleation should be treated more seriously, particularly where they are likely to intersect weld areas [324]. This would be more likely on the inside surface of pressure vessels, Fig. 2.2.1b (the only sample in Set B which exhibited segregation taken from near the inside edge, demonstrating the increased likelihood of hitting enriched material). Further investigation in this area is warranted.

5.5 Summary and Conclusions

1. Charpy V-notch testing of quenched-and-tempered Grade 3, in which A-segregate material was directly targeted, found that the material sometimes failed by intergranular brittle fracture in A-segregate material. This intergranular failure, found in samples tested at room temperature, delivered significantly lower impact-energy values and contributed to the scatter present in results in the ductile-to-brittle transition.
2. The intergranular failure found in A-segregate material was most likely caused by P embrittlement during slow cooling from tempering, although this could not be explicitly shown by direct measurement of grain-boundary P concentrations. Not only is A-segregated material enriched in P, but it also possesses increased hardness and can exhibit large prior-austenite grains, both of which augmented the effect of P embrittlement to deliver intergranular failure. The reasons behind the increased prior-austenite grain size need to be assessed, although it is suspected that decreased levels of AlN could be to blame.
3. It can be surmised that as long as any failure of a pressure vessel passes through a significant amount of material which has not been embrittled by A-segregation (as would be the case for a radial crack in the material observed in this study), then the effect of A-segregation on overall fracture resistance should be minimal. However, the possibility that A-segregation could lead to cracking during welding operations, or afterwards through

greater susceptibility to environmentally-assisted cracking, is a concern and warrants particular investigation.

4. The effect of A-segregates on upper-shelf properties needs further investigation, as their propensity to contain inclusion debris may have a detrimental effect, and not enough information was collected in this regime by this study.

Chapter 6

Predicting and Tracking A-Segregation

6.1 Introduction

Given the results of the previous chapter, it is evident that the presence of A-segregates in steel components should be avoided if at all possible, and that it would be desirable for manufacturers to be able to predict their locations in castings. Prediction through the use of macromodels, however, is not practicable. As highlighted above in Section 2.4.1, such complex models are too computationally expensive and often cannot deliver useful results. On this basis, this chapter examines the application of more simple criterion for the prediction of A-segregation in steel ingots and castings, based on dimensionless Rayleigh numbers.

The chapter is in three parts. The first part, Section 6.2, assesses the use of a Rayleigh number criterion that was presented recently by Torabi Rad et al. [217], which was introduced in Section 2.5.2 above. This criterion is applied to two case studies of A-segregation in steel ingots, and limitations and sensitivities of the approach are highlighted. At the end of the first section, Grade 3 and Grade 4N compositions are compared in terms of their susceptibility to A-segregation as judged by Torabi Rad et al.'s criterion.

The second part of this chapter, Section 6.3, was written following discussions with Professor Grae Worster at the Department of Applied Maths and Theoretical Physics, University of Cambridge (this communication was made after the work for the first part had already been completed). In these discussions, we assessed the validity of using a critical Rayleigh number when casting is in a side-ways manner, and also outlined a new simple approach to predict A-segregates.

The final part of this chapter, Section 6.4, discusses how A-segregation might be minimised in Grade 3 and what the potential side effects might be for porosity and inclusion retention. It also examines, in Section 6.5.1, the robustness of the tracking technique that is used in Section 6.2 to monitor the location of segregates during forging.

6.1.1 The Origins of a Rayleigh Criterion

Before progressing any further, it would perhaps be useful to understand the physical basis of Rayleigh numbers, and to outline their mathematical derivation. This can be done in a relatively straightforward manner as set out below; it is only when the critical Rayleigh number for a system is assessed that more complex mathematics is required (stability analysis).

Consider the simple arrangement shown in Fig. 6.1, which comprises two equally-sized spheres of fluid with diameter d separated by a height h . They are considered to exist within a liquid that has a vertical gradient of temperature (G), and are hence at two different temperatures ($T_1 < T_2$). The temperature gradient delivers a density gradient, B , which means the two spheres are also of different density ($\rho_1 > \rho_2$) - the higher, colder sphere being more dense (we assume the properties of the two spheres are otherwise the same). The potential energy of the system can be reduced if the two spheres were to switch positions; the total energy given out is:

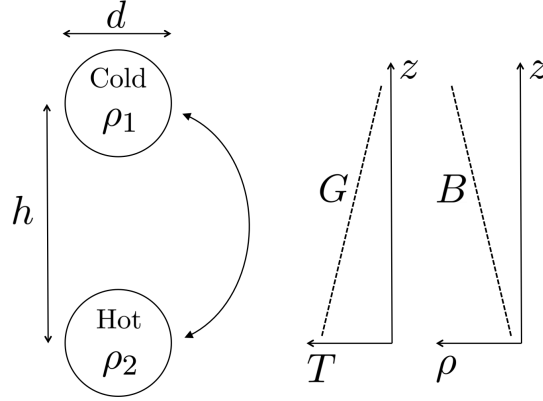


Figure 6.1: A simple system consisting of two identical spheres sitting in a fluid - the top sphere has a higher density than the lower.

$$\text{Energy available} = m_1gh - m_2gh \quad (6.1)$$

$$= \rho_1V_1gh - \rho_2V_2gh \quad (6.2)$$

where g is the acceleration due to gravity. Recognising that $V_1 = V_2 = V$, we have:

$$\text{Energy available} = \Delta\rho Vgh \quad (6.3)$$

$$= \Delta\rho \frac{4}{3}\pi \left(\frac{d}{2}\right)^3 gh \quad (6.4)$$

Ignoring constants, we have:

$$\text{Energy available} \sim \Delta\rho d^3 gh \quad (6.5)$$

and using the fact that $\Delta\rho = Bh$:

$$\text{Energy available} \sim Bd^3 gh^2 \quad (6.6)$$

This energy can be converted into kinetic energy, allowing for the movement of the two spheres to a more stable configuration. There is a resistance to this motion, however, which is provided by the friction at the interface between the moving spheres and the medium that surrounds them. From Stokes' law, which assumes laminar flow and no interaction between the spheres in the system, the drag force (F_D) generated by the movement of a sphere in a viscous fluid given by:

$$F_D = 6\pi\mu ru \quad (6.7)$$

where μ is the dynamic viscosity, r is the radius of the sphere and u the velocity of the sphere. Using d in place of r and removing constants, we have:

$$F_D \sim \mu du \quad (6.8)$$

The energy dissipated over a height h is therefore:

$$\text{Energy dissipated} \sim \mu duh \quad (6.9)$$

$$\sim \mu d \frac{h}{\tau} h \quad (6.10)$$

where the velocity u has been equated to moving over the height h in some time τ . Thus, we only have surplus energy to go into kinetic energy (i.e., sphere movement) if:

$$Bd^3gh^2 \gtrsim \mu d \frac{h^2}{\tau} \quad (6.11)$$

Attention must now be given to the affect of time, τ . If the process of movement takes a long time to complete (τ is large), then there will be opportunity for the spheres to equilibrate in temperature with their surroundings by the heat diffusion. Hence, there will be a loss in driving force for convection and the spheres will become stationary. An appropriate estimate of the this time can be made by assessing the time required for heat diffusion into/out of the spheres (using $x \sim \sqrt{Dt}$):

$$\tau \sim \frac{d^2}{\alpha_T} \quad (6.12)$$

where α_T is the thermal diffusivity. Substituting for τ , we have:

$$Bd^3gh^2 \gtrsim \mu d \frac{h^2}{d^2} \alpha_T \quad (6.13)$$

And rearranging:

$$\frac{Bd^4g}{\mu\alpha_T} \gtrsim 1 \quad (6.14)$$

Now, the frictional force on the fluid (and energy dissipated) can be minimised for a given volume if the spheres are larger. Indeed, this is why fluids tend to move as large masses in such situations, rather than in a stream of small packets. The limiting case is shown in Fig. 6.2, in which $d \approx h$. This allows us to make a final substitution for B , as $B = \Delta\rho/d$ in this case:

$$\frac{\Delta\rho d^3g}{\mu\alpha_T} \gtrsim 1 \quad (6.15)$$

This Rayleigh criterion determines when it is possible for convection flow to relax the metastable arrangement of a more dense fluid lying on top of a less dense fluid. It measures the driving and frictional forces for the required flow, and states that when the frictional force dissipates less energy than is released, then fluid flow is possible. Before this point, the system is stable to perturbation.

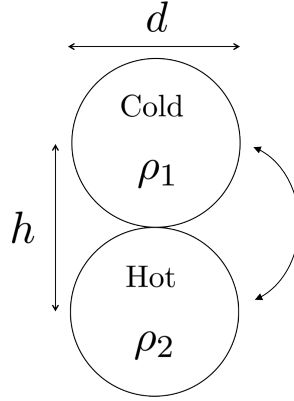


Figure 6.2: Limiting case of Fig. 6.1 when $h \approx d$.

6.1.1.1 Application to Mushy Zones

Equation 6.15 was modified by Worster for convective flows in the mushy zones of directionally-solidified alloys [216]. In such scenarios, as illustrated in Fig. 6.3, the density of the liquid in the mushy zone is changed not by effect of temperature, but by solute rejection (here, it is assumed that the rejected solute makes the interdendritic fluid lighter). The Rayleigh criterion can be altered to suit such systems, and hence the formation of channels (or chimneys) of enriched interdendritic fluid can be predicted (that form freckles in nickel-based alloys and alike).

In mushy zones there is still frictional dissipation when packets of fluid move, but the dissipation is across the surface area of the solid network. This surface area is characterised by the permeability, as discussed in Section 2.4.2.2 above, which scales with some relevant dimension of the solid network, typically dendrite arm spacing:

$$K \sim \lambda^2 \tag{6.16}$$

Hence, two of the d length scales in equation 6.18 (which were associated with the surface area of the spheres in the treatment above) can be replaced with an

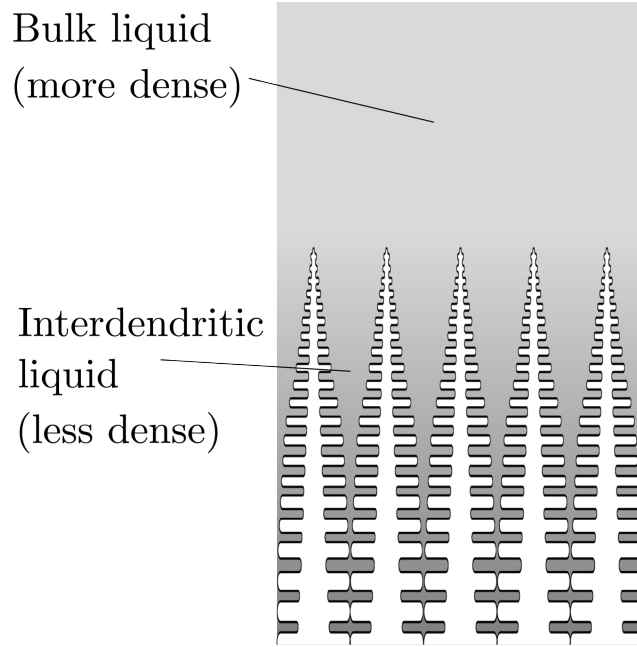


Figure 6.3: Upwards directional solidification of an alloy, in which solute enrichment in the liquid leads to a decrease in its density.

average permeability, \bar{K} , in the mushy zone:

$$\frac{\Delta\rho dg\bar{K}}{\mu\alpha_T} \gtrsim 1 \quad (6.17)$$

where $\Delta\rho$ is now the density change due to the composition gradient in the liquid, not due to temperature - we assume solutal effects are dominant. What about α_T ? Should this be replaced with some sort of solute diffusivity, D ? Worster suggests not, as he argues that the thermal diffusivity is limiting the rate of solid melting (and channel formation), not the solutal diffusivity. This argument is based upon the size of the liquid packet we consider to be moving upwards in the mush. Larger packets are more stable, so if we consider the size of a packet to be comparable to the height of the mushy zone, then the packet encompasses many dendrite arms (many primary, and even more secondary). Hence, even if thermal diffusivity is far higher than solutal, it is thermal diffusion that limits the rate of solid melting as the distance over which heat must diffuse is far greater than the small distances (on the scale of secondary dendrite arms) that solute moves. In

reality, it may be the case that the size of the packets moving are much smaller, in which case solutal diffusion may become rate limiting, but this has not been investigated experimentally. It must be borne in mind that we are considering a scenario in which a mushy zone is at the very edge of stability, and that this may not correspond with the typical examples of channel formation we are familiar with.

Finally, a substitution can be made for the remaining length scale d . As it was shown above, d tends to scale with h , which in the case of mushy zones is the vertical height through which the solid dendrites extend. This height, in turn, is determined by the thermal field, and it can be shown that heat diffusion from the liquid results in it scaling as $h \sim \alpha_T/R$, where R is the casting speed. Making this substitution, we have:

$$\frac{\Delta\rho g\bar{K}}{\mu R} \gtrsim 1 \quad (6.18)$$

Or, using the dynamic viscosity in place of the kinematic viscosity ($\nu = \mu/\rho$):

$$\text{Ra} \equiv \frac{(\Delta\rho/\rho_0)g\bar{K}}{R\nu} \quad (6.19)$$

where ρ_0 is some reference density.

6.2 The Torabi Rad et al. Rayleigh Criterion

The Rayleigh criterion presented by Torabi Rad et al. for use in steel ingots and castings was identical in form to equation 6.19 derived above [217]. From here onwards this will be the only Rayleigh criterion referred to. In their paper, they suggest that a higher Rayleigh number in the mushy zone should correlate with higher levels of fluid flow and A-segregation, and that a critical value should exist at which A-segregates are first found to form. They went on to state that, in theory, this critical value should be valid for whole systems of alloys, allowing for the direct comparison of different steels. Previously-developed

functions of thermal gradient, G , and isotherm velocity, R (such as the popular Suzuki criterion), which do not explicitly account for the effects of mushy-zone permeability and liquid-density changes due to segregation, cannot be applied in the same way as their critical values change from alloy to alloy [16; 210; 211; 212].

Torabi Rad et al. validated the critical value of their Rayleigh number by examining three case studies of sand-cast steel components, as well as historic data on A-segregation in ingot castings (ingots are cast in metal moulds) [211; 212], finding the critical value to be 17 ± 8 . The setting of a range for the critical value is not a particularly useful result for ingot manufacturers. They would prefer a single critical value for the criterion to be specified, representing a conservative lower limit. This is because the range 17 ± 8 can encompass a large volume of material in some castings, and manufacturers would rather use a single value that they can define to separate sound and defective material. Hence, a principal aim of this section of the thesis is to help set a conservative lower limit to the criterion. The other principal purpose is to assess the limitations and sensitivities of the criterion when it is applied to ingot castings. Torabi Rad et al. had to rely on estimation of the thermal parameter R during their assessment of historic data for metal ingots, but here the casting procedure used in both cases was well documented, and hence no estimation of thermal parameters was necessary beyond standard finite-element calculations. These aims are accomplished by examining two case studies of steel ingots, which differ significantly both in terms of ingot size and alloy composition. The first case study examines A-segregation in an as-cast 12 ton steel ingot, the detailed analysis of which is presented in Chapter 8 below. The second looks at the 200 ton high-integrity steel ingot described in previous chapters, through the tracking of segregated regions back from a post-forged section to the original ingot.

6.2.1 Evaluation of the Rayleigh Number

The Rayleigh number given in equation 6.19 can be modified by recognising the dependency of some of its terms on other casting parameters. For instance, the average permeability, \bar{K} , can be expected to be a function of fraction solid and

dendrite arm spacing, and hence of local temperature, alloy carbon concentration and cooling rate. The consolidation of equation 6.15 through such considerations yields equation 6.20, in which the values for ρ_0 and ν have been assumed constant (further details of its generation can found in Torabi Rad et al. [217]).

$$\text{Ra} = 2.38 \times 10^{-6} \times C_C^{1.1-3.99C_C} \Delta\rho \frac{G}{\dot{T}^{1.7232}} \quad (6.20)$$

where C_C is the concentration of carbon in wt%, \dot{T} the local cooling rate in K s^{-1} , G the thermal gradient in K m^{-1} and $\Delta\rho$ has units of kg m^{-3} . For consistency, these terms were evaluated in an identical manner to Torabi Rad et al.: $\Delta\rho$ was taken to be the difference in density between the liquid at the liquidus temperature and at the temperature corresponding to fraction solid = 0.3; and \dot{T} and G were evaluated locally at the average temperature between the liquidus and the fraction solid = 0.3 temperature.

6.2.2 Modelling and Experimentation

The two ingots investigated were labelled Ingot 1 and Ingot 2. The composition and size of Ingot 1 is given in Table 6.1. Ingot 2 was the same 200 ton Grade 3 ingot from which the material investigated in the chapters above was trepanned, Fig. 4.1a and hence its composition is that given at the top of Table 4.1. A solidification simulation was generated for each case in a finite-element (FE) package (ProCast [142]) using a comprehensive knowledge of the casting apparatus (including geometries and materials properties) and parameters (such as superheats and thermal losses). The precise values for the various boundary conditions necessary to set up the models, as well as the relevant materials data, cannot be presented here for reasons of commercial sensitivity. However, they were of the standard type demanded by the FE package (e.g., starting temperatures, conductivities, specific heats) and were not significantly different to the default values contained within the software itself. The models accounted for the formation of a shrinkage gap during solidification, but did not account for fluid flow (this reduced computational times significantly, and it has been suggested that fluid flow has a minimal effect on the thermal parameters in any case

[136; 217]). The average element sizes used for ingot, insulation and mould components were, respectively, 10, 5 and 20 mm for Ingot 1, and 50, 20 and 50 mm for Ingot 2. Refining the mesh size produced smoother variations in Ra values (as Ra was calculated at more points), but did not change the spatial distribution of the results and led to significantly increased computation times. The thermodynamic software package JMatPro [143] was used to generate materials properties files that were loaded into the FE simulation. It was also used to calculate values for $\Delta\rho$. The model for Ingot 1 was validated against thermocouple data obtained from the ingot mould (see Chapter 8 below). The model for ingot 2 was validated using pyrometer measurements of the ingot on removal from its mould.

The results were compared directly to experimental evidence of A-segregation obtained through the sectioning of an as-cast product. For Ingot 2, however, the Rayleigh-number results were verified by measuring the A-segregation present in the trepanned Grade 3 cylinder, and back tracking this to the original ingot casting. The forging simulations were carried out in the DEFORM software package [325], and used conditions set to reproduce the true forging processes, Figs. 3.5 and 3.6, as closely as possible. This included using accurate geometries of the workpiece and forging tools, and realistic numbers and depths of forging bites. Volume conservation was ensured and an estimate of the effect of heat loss during forging was also incorporated. Regions of A-segregation determined through macroetching were reverse-tracked using a point tracking analysis tool, Fig. 6.4a. Local irregularities and asymmetries in forging deformation due to the placement of individual bites, as well as the rotation direction of the workpiece, were averaged out over each complete forging operation. However, an indication of the scatter in the locations of the tracked points was retained by calculating the standard deviations in the radial and axial positions of the points for each operation, and adding these in quadrature to give an overall uncertainty across all the operations. This uncertainty was found to be significant, but the use of this tracking procedure was seen as the only practical alternative to direct sectioning, which would have been prohibitively expensive and laborious.

Ingot 1 was sectioned to produce a large longitudinal section through the full

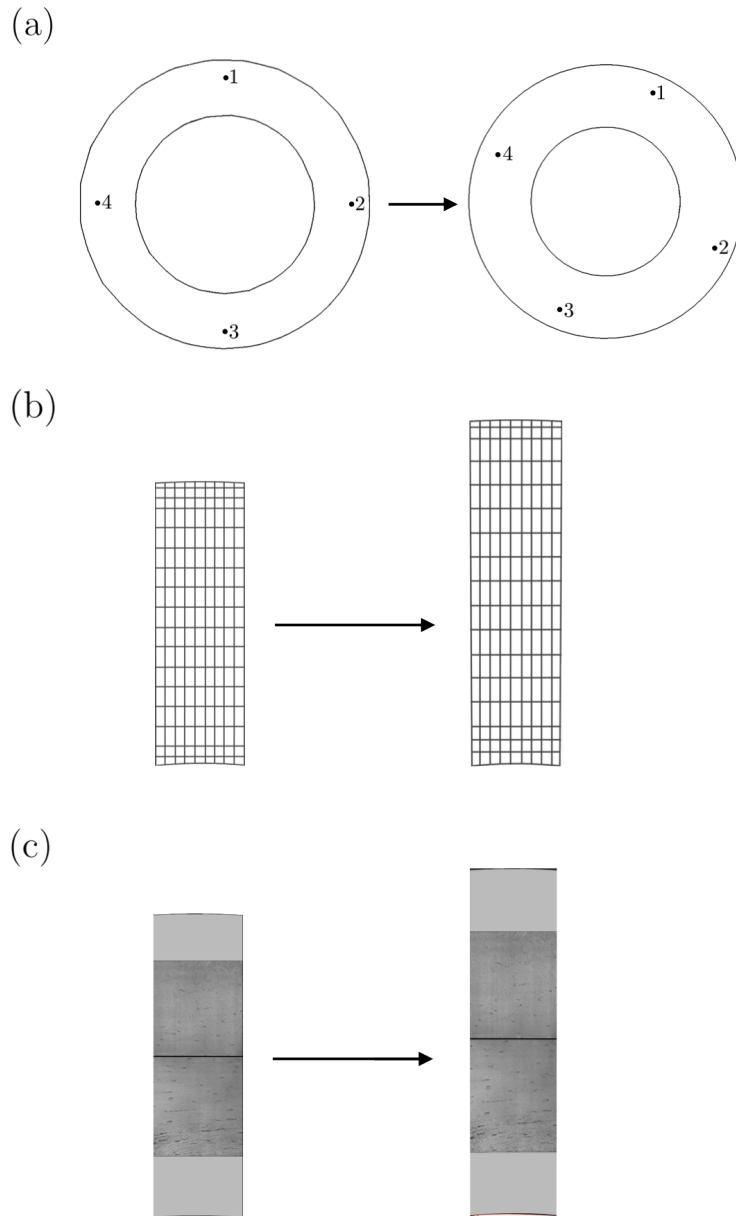


Figure 6.4: (a) An example of using the point-tracking analysis tool for the second becking process (in reverse) of the high-integrity shell forging. (b) A Flow Mesh visualisation of the same forging process through a radial section of the workpiece. (c) The resulting deformation, visualised using image distortion.

Table 6.1: Composition of Ingot 1, ≈ 12.3 tonnes.

Chemistry /wt%					
C	Si	Mn	P	S	Cr
0.79	0.80	0.26	0.007	0.005	4.88
Ni	Mo	V	Cu	Al	
0.22	0.33	0.005	0.08	0.008	

height of the ingot, which was then metallographically prepared. The chemistry of this surface was mapped using a macro-scale X-ray fluorescence (XRF) technique (examined in the next chapter of this thesis) to determine the location of segregates. For Ingot 2, the sections of material examined were the slabs cut from the trepanned cylinder analysed in the preceding chapters, as shown above in Fig. 4.1b and later in 6.7a. Once again, sections were metallographically prepared before etching in 10% aqueous nitric acid. The effect of forging on the appearance of the A-segregation measured in Ingot 2 was visualised using the Flow Mesh tool in DEFORM, Fig. 6.4b, in conjunction with an image distortion programme written in MATLAB [326], Fig. 6.4c.

6.2.3 Results

6.2.3.1 Ingot 1

The orientation of the section of Ingot 1 examined is shown in Fig. 6.5a. Fig. 6.5b shows the corresponding Rayleigh number map calculated for this section. Regions in which A-segregates are not predicted to form are coloured light grey, black regions denote regions where they are expected to appear, and the zone of uncertainty between (where $Ra = 17 \pm 8$) is multicoloured. By comparing this map to the experimental XRF results presented in Fig. 6.5c, it is evident that the predicted and measured regions of A-segregation agree reasonably well. However, the A-segregation observed appears to begin at a lower value than the lowest limit of the 17 ± 8 range suggested by Torabi Rad et al.. Closer inspection revealed this to be when $Ra > 6$, Fig. 6.6.

It can be seen that the criterion predicts A-segregation where it is not present: in the central region of the ingot, where there is no A-segregation through the ingot height, and within the head, where A-segregation is predicted to occur closer to the mould than is observed. The highest value of Ra predicted for Ingot 1 was ≈ 180 , and was found in the head of the ingot as indicated in Fig. 6.5d.

6.2.3.2 Ingot 2

The Rayleigh number map down the full length of Ingot 2 is shown in Fig. 6.7a. The start and finished forging geometries are indicated in Fig. 6.7b, along with the location of the sections analysed (c.f. the sectioning of the trepanned cylinder in Fig. 4.1b). Fig. 6.7c shows the surface of one of the sections in the macroetched state, where the onset of A-segregation is indicated. The results of tracking this onset back to the original ingot casting are shown in Fig. 6.7d. Is it evident that the tracked onset overlaps with the critical Rayleigh numbers predicted in ProCast, and lies towards the upper end of the 17 ± 8 regime.

When setting the onset for Ingot 2, A-segregates were identified by assessing whether they passed through thickness of the slice taken for analysis (as in previous chapters). This, however, meant that some regions of positive segregation that resembled A-segregates, which were observed further from the centre of the shell forging (i.e., towards the outside), were ignored. So, in order to account for the possibility that these positive-segregated regions were A-segregates near their nucleation or finishing point (and hence did not pass through the section thickness), the onset used for tracking was moved to include them. This revised estimate for the start of A-segregation also provided a more conservative case for the validation of the Rayleigh number. The results of tracking this revised onset did indeed move to lower Rayleigh numbers (the onset lying closer to 10), but still lay within the 17 ± 8 range, >6 . Note the significant uncertainty in the result, which reflects the complexity of the forging route modelled and the associated inhomogeneous deformation that resulted (i.e., results varied along lines of constant radius). The maximum calculated Ra values for this ingot were higher than for Ingot 1, being ≈ 900 , Fig. 6.7e. The effect of the total deformation associated

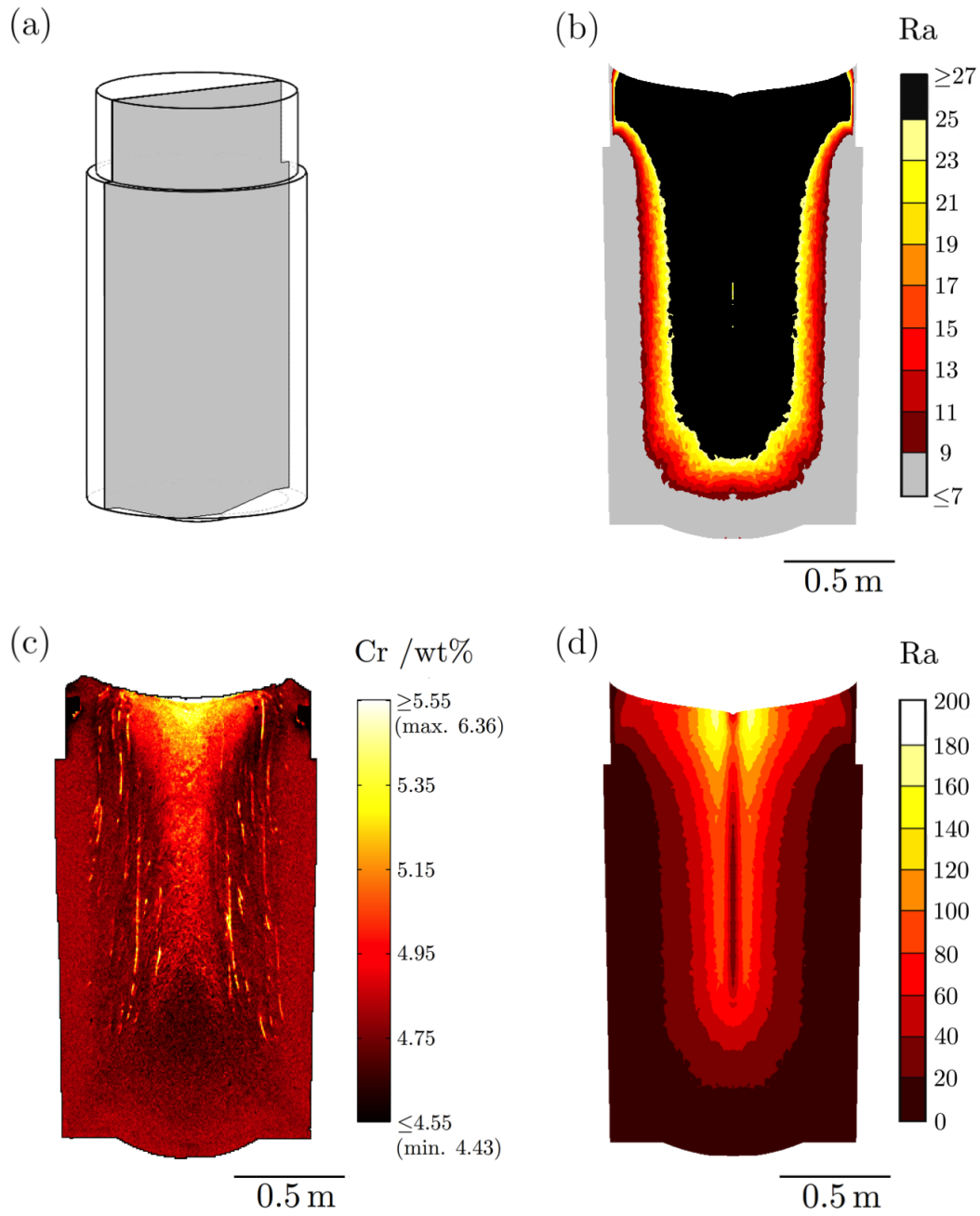


Figure 6.5: (a) The location of longitudinal section of Ingot 1 examined (highlighted in grey), (b) the predicted Rayleigh-number map, and (c) a macro-scale XRF map in which A-segregates appear as bright channels running near vertically. Note the presence of two lifting points, which appear as black squares (due to their low Cr composition) in head of the ingot in (c). (d) A re-scaled version of (b), in which the maximum values for Ra are indicated.

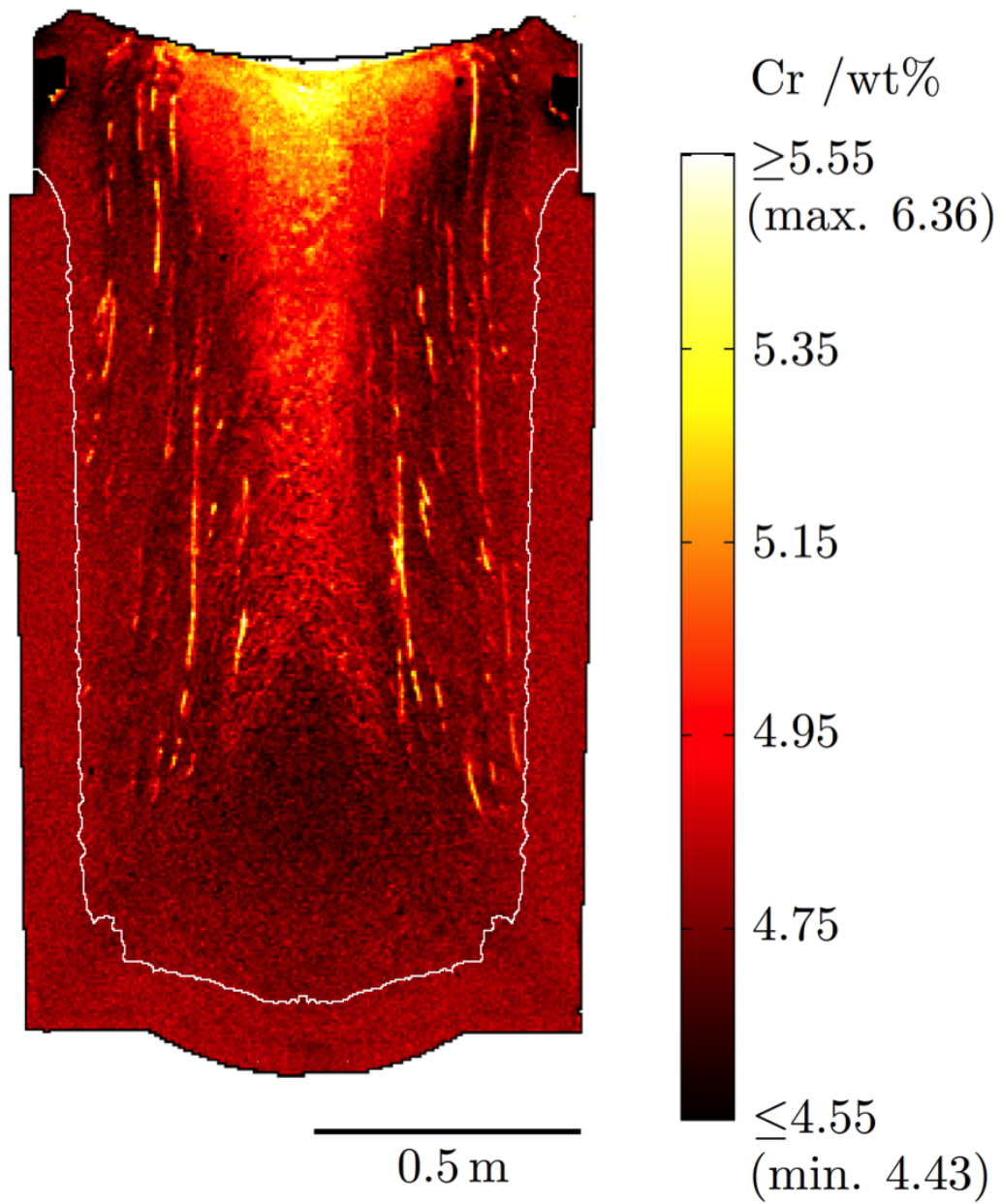


Figure 6.6: Macro-scale XRF map of Ingot 1 with line of $Ra = 6$ marked. Note that the asymmetry at the top of the ingot is due to the asymmetry of the head tiling (insulation).

with all the forging operations made on the A-segregation in Ingot 2 is visualised in Fig. 6.8.

6.2.4 Discussion

The two case studies examined here have demonstrated the effectiveness of the Rayleigh criterion developed by Torabi Rad et al. at predicting the onset of A-segregation in steel ingots. The use of this criterion is not only computationally inexpensive in comparison to more complex macromodel approaches (the CPU computing times for the ProCast simulations of Ingots 1 and 2 were 2,600 and 20,000 seconds, respectively, using two Intel Xenon E5530 2.4 GHz processors), but also represents a significant improvement over previous simple criterion (such as the Suzuki criterion [211]). This was demonstrated here by the fact that the two ingots examined, which differed significantly in terms of size and composition, could have utilised a similar critical value for the criterion.

Although the number of ingots investigated in this study has been minimal, results for Ingot 1 suggest that if a conservative lower limit to the Rayleigh criterion is desired, then a value of 6 appears to be a sensible choice. Indeed, the lowest value reported by the original study of Torabi Rad et al., in which 27 ingots of various sizes and compositions were retrospectively examined, was 6.7, and hence their results support this proposal. Although the value of 17 ± 8 is useful in that it shows explicitly the uncertainty associated with the Rayleigh-number calculation (principally derived from issues associated with the calculation of dendrite arm spacings [217]), the setting of a lower bound is an important step for ingot manufacturers who would ideally wish to use a single value for conservative estimations (i.e., the worst-case scenario, with maximum A-segregation).

6.2.4.1 Limitations and Sensitivities

A key limitation of the Rayleigh number approach, as highlighted by Torabi Rad et al. in their original study, is that the criterion cannot be used to predict where A-segregates do form, only where they do not form. This is not only because A-segregate nucleation is probabilistic in nature, which means the Rayleigh number

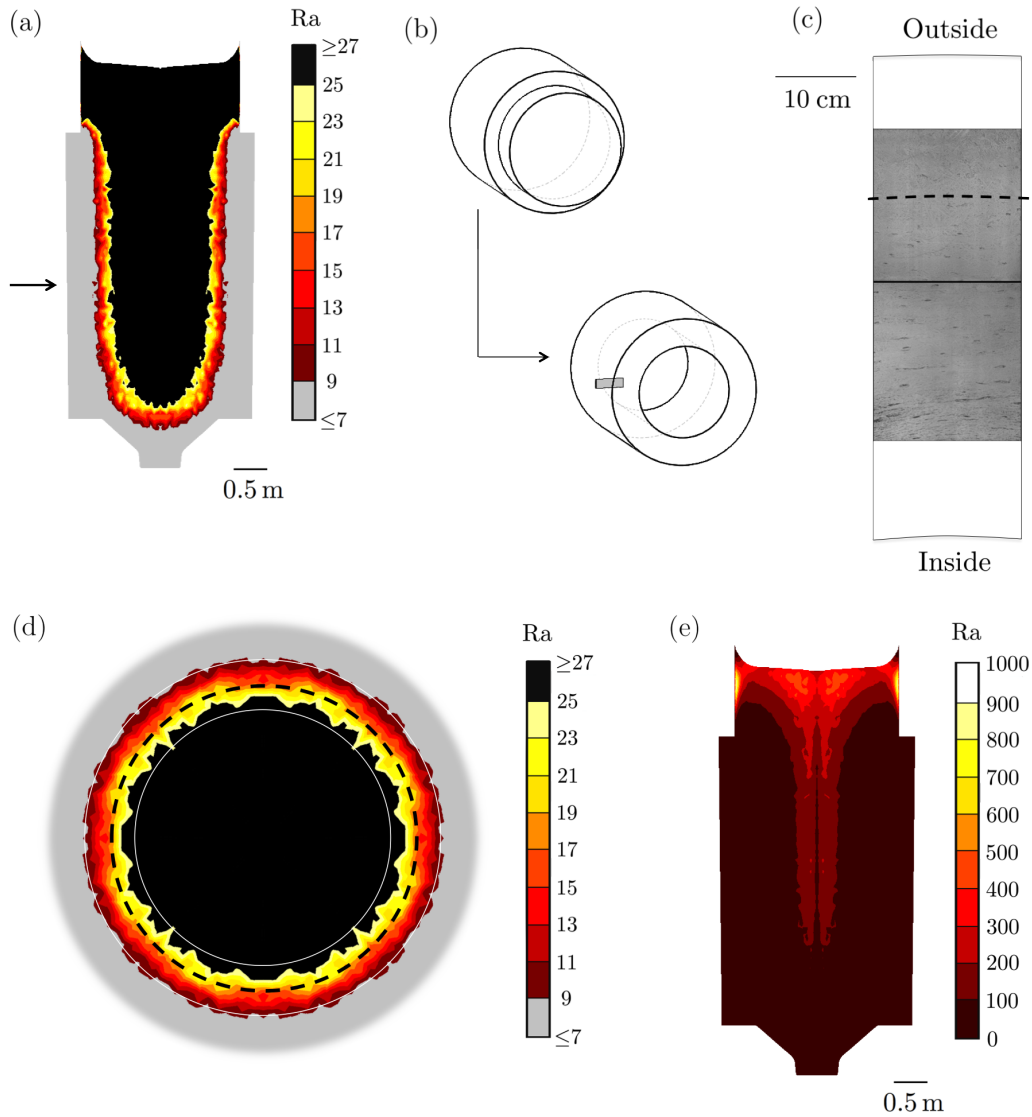


Figure 6.7: (a) Rayleigh-number map for Ingot 2. (b) Schematic of the high-integrity shell forging route applied (start and end geometries), with the location of the trepanned section analysed highlighted (grey). (c) The macroetched section—white areas denote regions removed by machining. The onset of segregation indicated with a black dashed line. (d) A Rayleigh map of a transverse section of the ingot located at the arrow point in (a). The onset line, tracked back to the original casting, is shown as a black dashed line, with the upper and lower limits of the error indicated using thinner continuous lines. (e) Re-scaled version of (a), showing the maximum Ra values calculated.

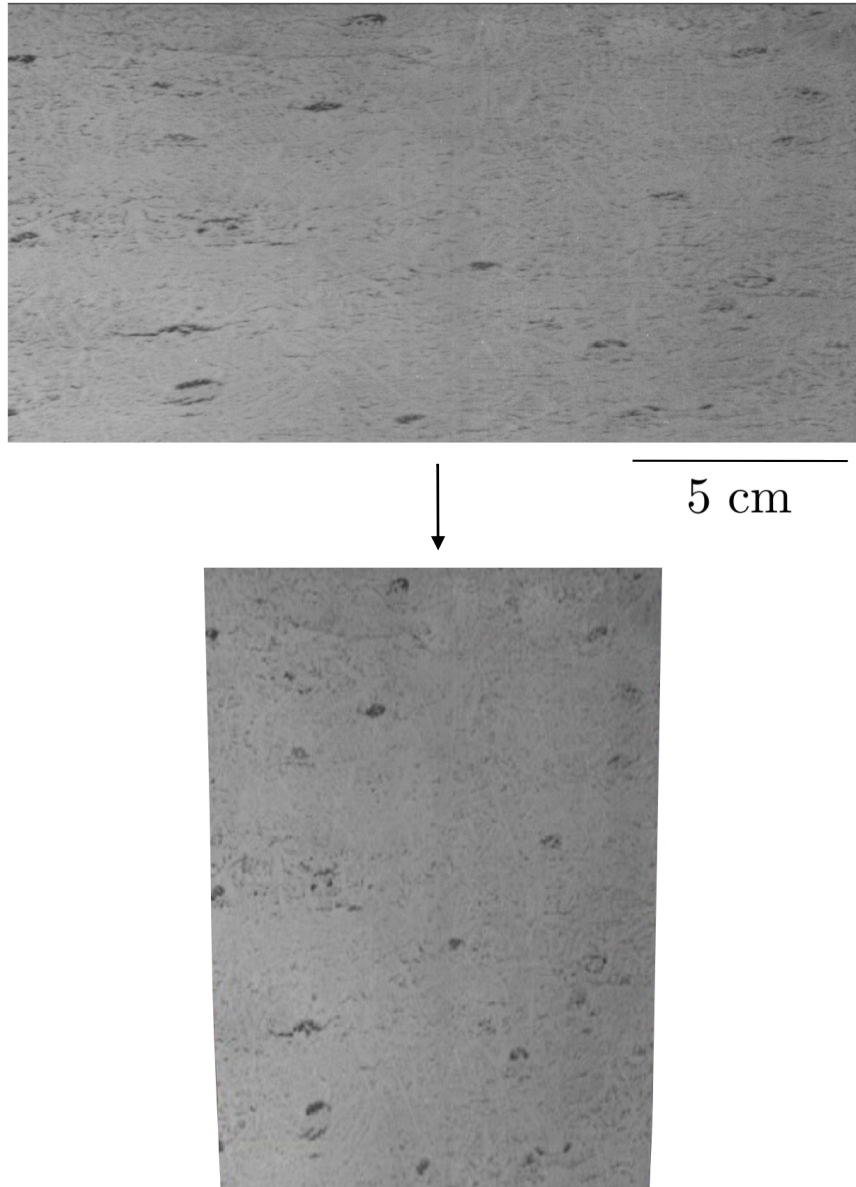


Figure 6.8: The total deformation associated with forging Ingot 2, illustrated using a section of the material with prevalent A-segregation.

Table 6.2: Composition of Grade 4N ingot, which was used to test sensitivity to S and P concentrations.

Chemistry /wt%					
C	Si	Mn	P	S	Cr
0.21	0.041	0.044	0.004*	0.004*	1.90
Ni	Mo	V	Cu	Al	
3.64	0.54	0.04	0.019	0.004	

*No P and S were added to generate Fig. 6.9b

can only indicate where it is possible for the segregates to form, but also because it fails to account for other solidification phenomena that prevent A-segregate formation in certain regions. As seen in Fig. 6.5, this is particularly the case in the central region of the casting. Here, the solidification is more likely to be equiaxed than columnar (A-segregates do not form in moving structures, and equiaxed networks tend to be non-static), and other types of segregation, such as negative base segregation and V-segregation, are more prominent. The results of the criterion should also be treated with care when applied to the head region of the casting, as in this area the effect of insulating materials (and the properties assigned to them), and any components cast into the top of the ingot for lifting (see Ingot 1, Fig. 6.5), introduces more uncertainty into calculations. Fortunately, this material is usually scrapped.

The author has observed that values for $\Delta\rho$, computed in JMatPro for use in calculating Ra through Equation 1, can vary significantly based on the chemical composition of the steel inputted. In particular, small changes in trace elements such as S and P can have a marked effect. P and S both decrease the density of the liquid steel, increasing $\Delta\rho$, and their potency is such that for some cases an addition of >10 times as much Si (by weight) to the bulk alloy is needed to produce the same decrease in density. This is acutely demonstrated in Fig. 6.9, for the case of a steel with the Grade 4N composition given in Table 6.2. It is shown that the addition of very small amount of S and P to the alloy not only changes the distribution of Ra, but also its sign - in the case with no P or S

(Fig. 6.9b), the Rayleigh criterion suggests interdendritic fluid flow would be in a downwards direction, and hence inverted A-segregates could form (although this is a matter for debate - see Section 6.3. It is clear, then, that an effort must be made to ensure the chemical composition used is as accurate as possible. For a conservative result, the elements that have the greatest influence on $\Delta\rho$, namely C, Si, S and P, should be set at their upper limits to maximise the driving force for interdendritic flow.

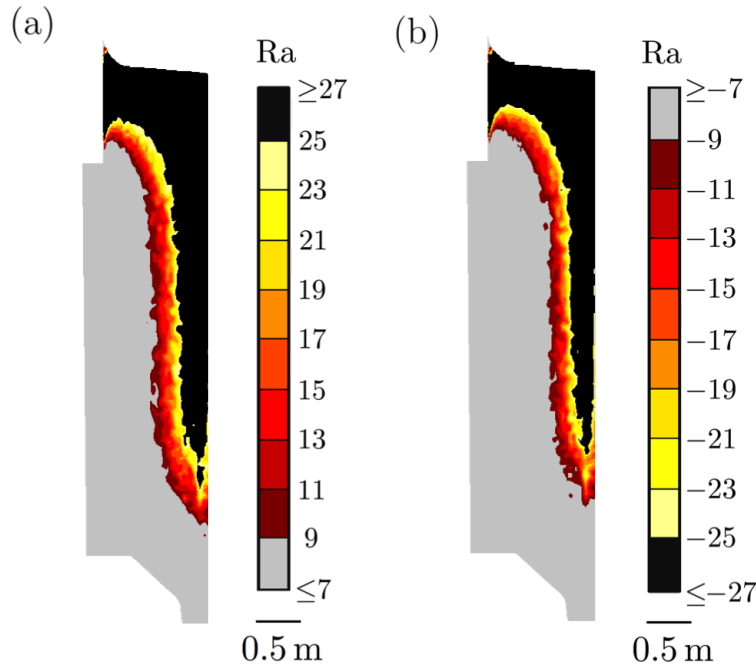


Figure 6.9: Half-ingot Rayleigh-number maps for the Grade 4N composition given in Table 6.2, (a) with P and S, and (b) without P and S. The ingot modelled was the same size and shape as Ingot 2.

As well as changes in $\Delta\rho$, it is obvious that changes in the calculated temperature field for an ingot can also significantly impact the value of the Rayleigh number through its dependence on thermal parameters (R , G and \dot{T}). For a given ingot, variations in these parameters (and Ra values) can be observed, for instance, by the inclusion or neglect of shrinkage gap formation when models are created, Fig. 6.10. In this case, the inclusion of a shrinkage gap significantly increases Ra

values, therefore representing a more conservative approach, which is unfortunate as it requires increased computation times. By extension, it can be argued that complex fluid-flow phenomena should also be included, as they too will affect the thermal field (even if the effects have been found to be small). This is true, of course, but would defeat the purpose of using the Rayleigh criterion. If there are concerns with the fidelity of a calculated thermal field, then the use of an artificially-low heat transfer rate from the ingot (within sensible limits, guided by straightforward experimental measurement) would provide a cautious approach.

In general, the results generated for smaller ingots will be more sensitive to the issues highlighted above than for larger ingots, as the differences between the minimum and maximum Rayleigh numbers calculated in larger ingots will tend to be higher, see comparison of Fig. 6.5d and Fig. 6.10c. This is because a greater range of solidification rates is expected when a larger piece of steel is cast - the mould of a larger ingot will typically represent a smaller heat sink relative to the case of a smaller ingot, and will hence heat up and limit heat extraction at an earlier stage of solidification, slowing down the process to a greater extent. It is worth noting that the maximum value of the Rayleigh number is not usually found at the centre of the casting, as the rate of solidification increases at the end of casting process because the surface area of heat loss increasing in comparison to the volume of liquid remaining.

Despite the issues highlighted above, if applied in a consistent manner the Rayleigh criterion presented by Torabi Rad et al. continues to represent the most effective simple criterion for A-segregation to date. It is certainly unrivalled in terms of its capability to rapidly compare the A-segregation susceptibilities of different alloys.

6.2.4.2 A Comparison of Grade 3 and Grade 4N

As was highlighted in Section 3.1, there is a strong possibility that many future high-integrity forgings will be produced from SA508 Grade 4N steel, as opposed to Grade 3. This is primarily due to the increased strength and toughness asso-

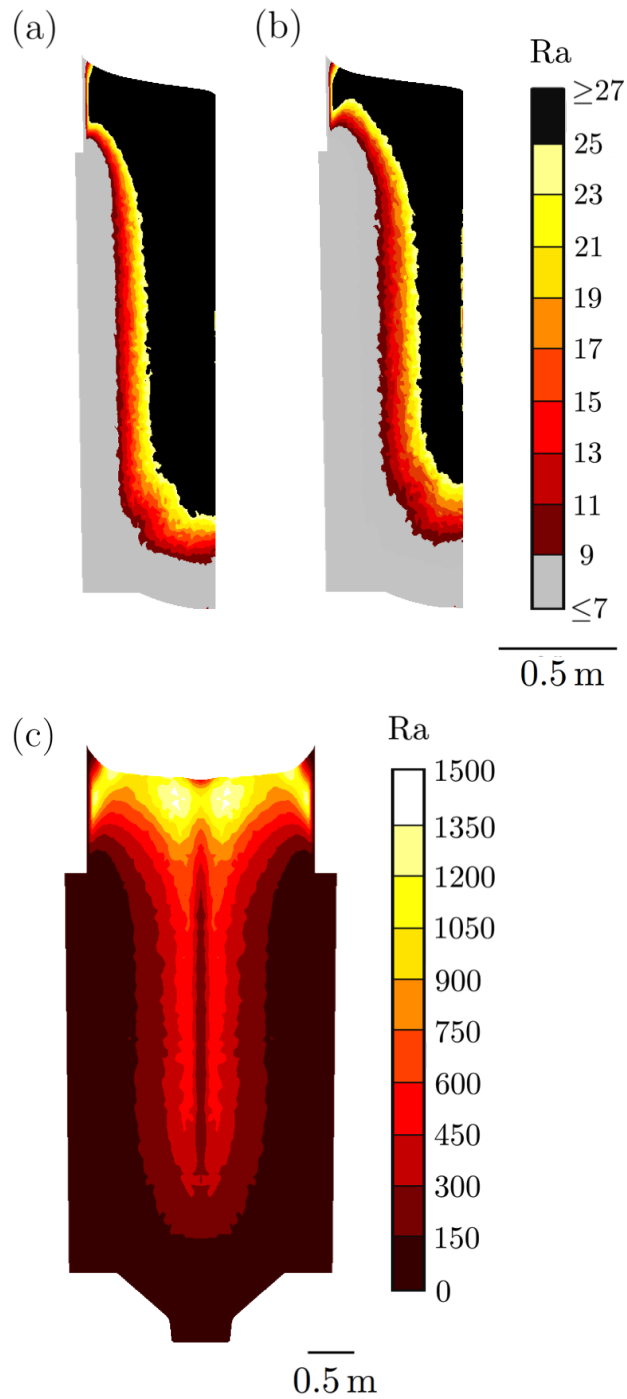


Figure 6.10: The half-ingot Rayleigh maps for Ingot 1, (a) accounting for, and (b) not accounting for, shrinkage gap formation. (c) shows the maximum Ra values obtained when the same alloy composition as Ingot 1 was used in an ingot the same size and shape as Ingot 2 (i.e., much larger).

ciated with the higher-Ni Grade 4N, but there are also likely to be advantages in terms of macrosegregation susceptibility. Fig. 6.11 compares the predicted Rayleigh maps for Grades 3 and 4N (using 6 as the critical value); the particular chemistries used being those in Tables 4.1 (top) and 6.2, respectively. It is clear that A-segregation is predicted to be far more widespread in Grade 3 than in Grade 4N. This difference is due to the lower density change associated with the Grade 4N composition, which can be attributed to a lower level of Si (note that the decrease in liquid density is slight enough that if Si, S and P contents are lowered, the interdendritic liquid can actually become heavier than the bulk, Fig. 6.9b).

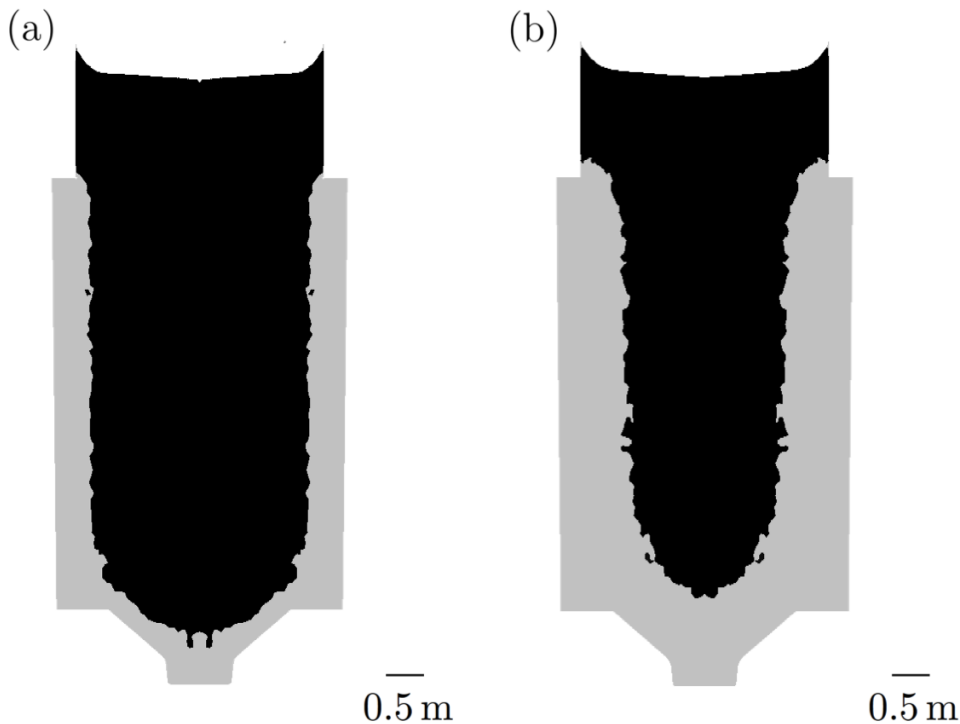


Figure 6.11: A comparison of the critical Rayleigh number maps for (a) Grade 3 and (b) Grade 4N 200-ton ingots. 6 is used as the critical value of the Rayleigh number.

The onset of A-segregation in both alloys, as predicted through the Rayleigh criterion, was tracked forward through the forging operations associated with

high-integrity shells using DEFORM (in the opposite direction to the Ingot 2 case study above). The specific aim of this tracking was to predict where A-segregation is likely to start in any trepannings taken from future forgings. It is anticipated that these trepannings will be taken in a similar location to the trepannings examined in this thesis (see Fig. 4.1 above), and hence the starting height of the tracked points was the ‘finishing height’ for Ingot 2 as indicated in Fig. 6.7a. The results of this tracking are shown in Fig. 6.12, utilising the same trepanned section as in Fig. 6.7c. Two values of the Rayleigh number were tracked for Grade 4N: $Ra = 6$ and $Ra = 17$ (back-tracking the onset of A-segregation in Grade 3 shown in Fig. 6.7c suggested the critical value was somewhere around $Ra = 17$ for the alloy, Fig. 6.7d). The position for $Ra = 17$ in Grade 4N was found to be located at a much lower radius than for Grade 3. Indeed, $Ra = 6$ for Grade 4N was found to lie slightly inside the $Ra = 17$ value for Grade 3. It is expected that the true onset for Grade 4N to lie somewhere between $Ra = 6$ and $Ra = 17$ (given that tracking a revised onset for Grade 3 gave $Ra \approx 10$, Section 6.2.3.2).

6.2.5 Summary and Conclusions

1. The Rayleigh criterion recently presented by Torabi Rad et al. [217] is an effective tool for the prediction of A-segregation in large steel ingots, as demonstrated here using two case studies.
2. If Rayleigh-number values are calculated in the same way as described in this study, then it is suggested that a value of 6 can be used as a critical value for the criterion. The author believes this represents a sensible conservative lower bound in light of results to date.
3. It must be recognised that, as highlighted previously by Torabi Rad et al., the criterion is only suitable for predicting material that is free from A-segregation, and should not be used to predict precise location of the segregates throughout the ingot. It may, however, also be useful for judging general segregation susceptibility (the higher the value of Ra , the more likely A-segregation is).
4. Calculated Ra values have been found to be highly sensitive to the concen-

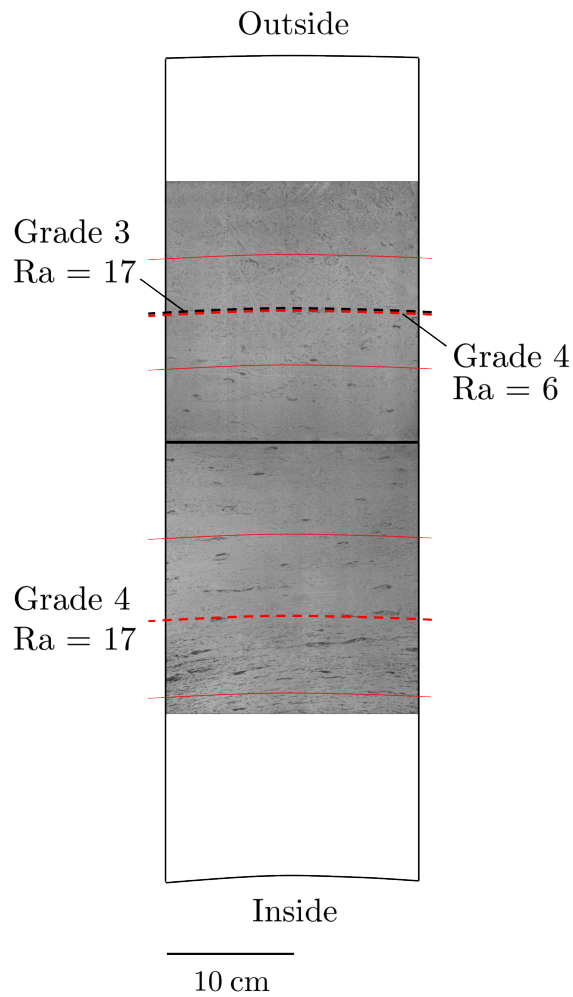


Figure 6.12: The results of tracking Ra results for Grade 4N from ingot to high-integrity forging, superimposed on the macroetched Grade 3 slice shown in Fig. 6.7c. The dashed red lines show the tracked Grade 4N positions, with the solid red lines indicating the uncertainty. The dashed black line is identical to that shown in Fig. 6.7c for Grade 3 - it was an experimentally-determined onset that was tracked back to a position in the original ingot consistent with Ra = 17, Fig. 6.7d.

trations of trace elements P and S in the alloys examined. Ra values are also affected by the changes in thermal parameters induced by altering the phenomena modelled, such as the inclusion or neglect of shrinkage gap formation during casting. The results for smaller ingots are more sensitive to these influences than larger ingots.

5. In recognition of the sensitivities highlighted, the users of the Rayleigh criterion may wish to consider changes to their models which would produce conservative estimations, such as the use of high concentrations for P and S. These can be guided by straightforward experimental measurements.

6.3 The Validity of Torabi Rad et al.'s Criterion

The Rayleigh criterion derived above for channel formation appears to work well when applied to steel ingots. It certainly seems to encompass some key parameters that must influence A-segregate formation, including the density inversion in the mushy zone, the permeability, and the casting speed. However, the use of a *critical* Rayleigh number is strictly not an appropriate criterion to apply to A-segregation in ingots, where the solidification is near-horizontal from the sides of the casting. Unlike the directional solidification shown in Fig. 6.3, which produces a density field that can be stable, a horizontally-solidifying system is never stable relative to a convecting state, Fig. 6.13. Hence, a Rayleigh criterion cannot strictly be applied to characterise when fluid flow can begin - the fluid is always in motion.

In order to develop an alternative criterion for A-segregates, it is worth revising their formation mechanism. They form due to the flow of interdendritic liquid to warmer parts of the mushy zone, where the enriched fluid causes remelting of the solid and formation of persistent channels. This occurs when the interdendritic fluid velocity exceeds the isotherm velocity, see equation 2.4 in Section 2.3.1, such that fluid moves across isotherms from warmer to colder parts of the casting. For perfectly-sideways solidification (in which we ignore the top/bottom constraints of the ingot mould) this condition should never be met, as the interdendritic fluid

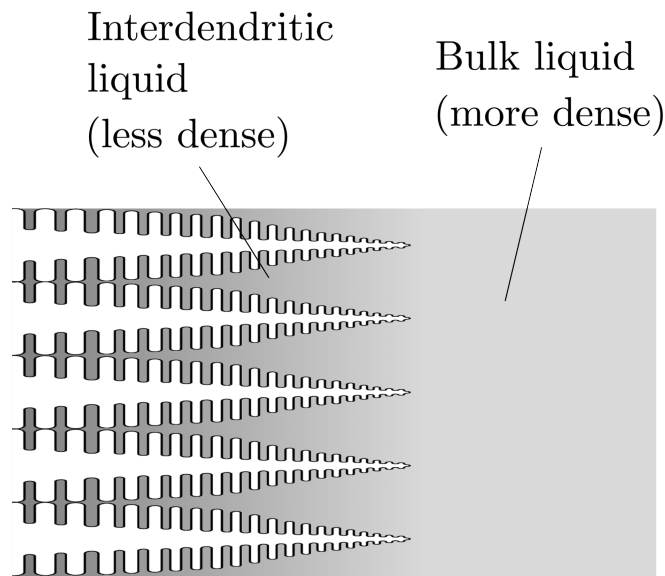


Figure 6.13: Sideways solidification, as seen in ingots. Convective fluid flow would be upwards in the mushy zone, and downwards in the bulk liquid. Isotherms are aligned vertically.

velocity will be perpendicular to the isotherm velocity.¹ For ingots, however, which are hot at the top and cooled from the base, the isotherms are not perfectly vertical and the condition can be fulfilled.

6.3.1 Development of New Criterion

Given the formation mechanism of A-segregates, a suitable starting point for the development of a criterion is to consider the temperature change of moving interdendritic fluid packets. This is accomplished using the material derivative, for the temperature change with time, that is seen by an observer moving with a

¹Note that this also ignores the effect of flows to feed solidification shrinkage, although such flows would make channel formation even more unlikely as they cause fluid to move from warmer to colder regions. Flemings showed that the magnitude of such flows (if they exactly provide for solidification shrinkage) is given by $R(\beta/(1-\beta))$, where β is the solidification shrinkage $(\rho_s - \rho_l)/\rho_s$ [40]. $\beta/(1-\beta)$ is approximately 0.1 for steels.

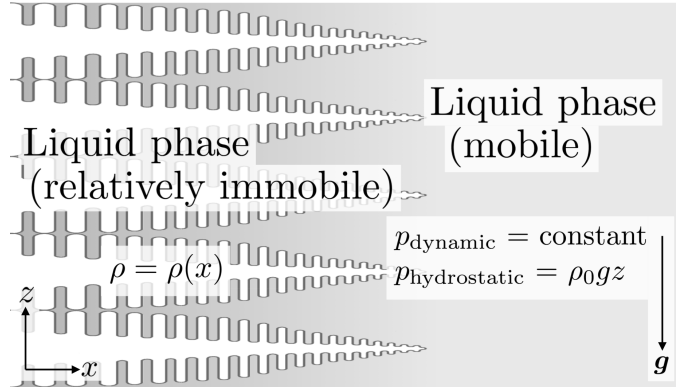


Figure 6.14: Schematic identifying the pressure and density fields accompanying sideways solidification.

fluid packet. This must be positive if channel formation is to take place:

$$\frac{DT}{Dt} \equiv \frac{\partial T}{\partial t} + \mathbf{v} \cdot \nabla T > 0 \quad (6.21)$$

where \mathbf{v} is the velocity of the fluid packet. The $\partial T/\partial t$ term is the local cooling rate of the casting, and can be written in terms of the local isotherm velocity, \mathbf{R} , and local temperature gradient, ∇T , such that:

$$\frac{\partial T}{\partial t} = -\mathbf{R} \cdot \nabla T \quad (6.22)$$

Combining Equations 6.21 and 6.22, we have:

$$-\mathbf{R} \cdot \nabla T + \mathbf{v} \cdot \nabla T > 0 \quad (6.23)$$

$$\mathbf{v} \cdot \nabla T > \mathbf{R} \cdot \nabla T \quad (6.24)$$

This can now be developed further by using Darcy's law (see equation 2.2) to give an estimation of potential values for \mathbf{v} :

$$\mathbf{v} = -\frac{K}{\mu} (\nabla p + \rho \mathbf{g}) \quad (6.25)$$

By considering the pressure and density field accompanying solidification, Fig. 6.14, this expression can be simplified (note that although a sideways example is used here, it is similarly valid for solidification in any direction). We find the pressure gradient term, ∇p , reduces to $\rho_0 \mathbf{g}$ due to the consistent hydrostatic pressure, $\rho_0 g z$, across the mushy and bulk-liquid zones. The $\rho \mathbf{g}$ term is rewritten $\rho(x) \mathbf{g}$ to draw attention to the variation of ρ along the x direction in the mushy zone:

$$\mathbf{v} = \frac{K}{\mu} (\rho(x) - \rho_0) \mathbf{g} \quad (6.26)$$

All the fluid movement is now along the z direction, so we can replace \mathbf{v} with W , the interdendritic fluid speed in the vertical direction. It is also useful to use a local average permeability, \bar{K} , as opposed to the absolute value, since flow is through a section of mush:

$$W = \frac{\Delta \rho g \bar{K}}{\mu} \quad (6.27)$$

This can now be substituted into Equation 6.24:

$$\frac{\Delta \rho g \bar{K}}{\mu} \frac{\partial T}{\partial z} > \mathbf{R} \cdot \nabla T \quad (6.28)$$

And recognising that \mathbf{R} and ∇T are in the same direction, we have:

$$\frac{\Delta \rho g \bar{K}}{\mu} \frac{\partial T}{\partial z} > |\mathbf{R}| |\nabla T| \quad (6.29)$$

In the metallurgical literature, $|\nabla T|$ is commonly denoted with the symbol G :

$$\frac{\Delta \rho g \bar{K} G_z}{\mu} > R G \quad (6.30)$$

$$\frac{\Delta \rho g \bar{K} G_z}{\mu R G} > 1 \quad (6.31)$$

where G_z is the temperature gradient in the z direction. Note that if the Rayleigh number in Equation 6.19 was scaled by the factor G_z/G , it would be identical in form to Equation 6.31. Indeed, the criteria are equivalent in the case of directional solidification along z .

6.3.2 Application of the New Criterion

Just as the Rayleigh number can be evaluated using the simple methodology proposed by Torabi Rad et al., so can Equation 6.31 be applied to casting scenarios with relative ease. Here, using many of the same auxillary models and assumptions adopted by Torabi Rad et al. for the Rayleigh number [217], an example of how the proposed criterion can be applied is given.

The variables contained within Equation 6.31 are set as follows. g is set at $-9.81 \text{ m}^2 \text{ s}^{-1}$. There are a number of different models that could be used to calculate \bar{K} , but here one based on a Blake-Kozeny treatment is applied [217]. A local average solid fraction, \bar{f}_s , is used:

$$\bar{K} = 6 \times 10^{-4} \lambda_1^2 \frac{(1 - \bar{f}_s)^3}{f_s^2} \quad (6.32)$$

where it is assumed that $\lambda_1 \approx 2\lambda_2$, and λ_2 is calculated using Won and Thomas' relation shown in Equation 6.33 below (although, again, a number of relationships could be used here) [196].

$$\lambda_2 = 143.9 \times 10^{-6} \dot{T}^{-0.362} C_C^{0.550 - 1.996 C_C} \quad (6.33)$$

where the local cooling rate is now denoted \dot{T} . Substituting Equation 6.33 into 6.32, and using the result in Equation 6.31 we have:

$$-4.88 \times 10^{-10} \dot{T}^{-0.72} C_C^{1.10 - 3.99 C_C} \frac{(1 - \bar{f}_s)^3}{\bar{f}_s^2} \frac{\Delta \rho G_z}{\mu R G} > 1 \quad (6.34)$$

The density field $\rho(x)$ needs to be found in order to determine $\Delta \rho$, but this also requires a temperature (i.e., a position in the mushy zone, with a particular solid fraction) to be set as a suitable point for evaluation. This temperature will determine the temperature range over which the criterion is assessed (e.g., $\Delta \rho$ is found), and this in turn will determine the temperature at which μ is calculated. It will also determine the temperature at which the isotherm speed, R , should be computed, as well as the temperature gradients G and G_z , and the cooling rate \dot{T} . One might initially suggest that the temperature range should be centred

around the temperature at which $\bar{K}\Delta\rho$ is maximised, but this is found at very low fractions solid, Fig. 6.15, due to the dominance of \bar{K} . It is not desirable to make calculations around such low solid fractions for two reasons: first, because it does not agree with experimental findings (which suggest channel formation nearer $f_s = 0.3$ [13]), and second, because it has been observed that values calculated for $\Delta\rho$ (by using the software package JMatPro [143]) can fluctuate in sign at low solid fractions before a clear trend is established.

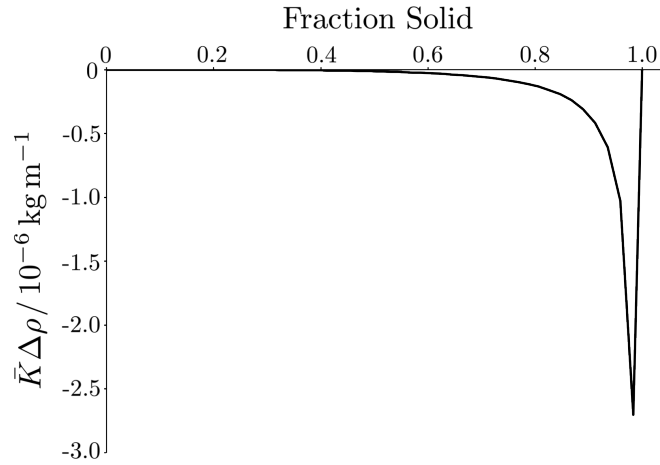


Figure 6.15: Plot showing the variation of $\bar{K}\Delta\rho$ with fraction solid. Values for \bar{K} were found using a cooling rate of $0.01 \text{ }^\circ\text{C s}^{-1}$ and the alloy composition was a steel with 0.8 wt% C, 0.8 wt% Si and 5 wt% Cr. Values for $\Delta\rho$ and f_s were found for the alloy using JMatPro [143].

Torabi Rad et al. calculated \bar{K} and $\Delta\rho$ over the temperature range from liquidus to fraction solid = 0.3, and it is proposed that the same temperature range is used here. Hence, JMatPro (or similar) can be used to determine this range for any given alloy, and $\Delta\rho$ found accordingly. \bar{f}_s should then be set to 0.15, and that the temperature corresponding to this fraction solid is used to find a value for μ (also via JMatPro). The same temperature should then be used to compute R , G , G_z and \dot{T} for a given casting scenario, which is straightforward to achieve in a software package like ProCast.

Overall, using $\bar{f}_s = 0.15$, we have:

$$-1.33 \times 10^{-8} \dot{T}^{-0.72} C_C^{1.10-3.99C_C} \frac{\Delta\rho G_z}{\mu R G} > 1 \quad (6.35)$$

6.3.3 Criterion Development

Future work on the development of this newly-proposed criterion should include the confirmation of its critical value. During this work, it may also be necessary to change the procedure through which the criterion is computed - Torabi Rad et al. made their particular choices, for instance in regard to dendrite-arm spacing model, such that their calculated Rayleigh numbers for different scenarios collapsed more completely onto a single critical value.

So far, the permeability of the mushy zone has been considered to be isotropic. Hence, the permeability has been denoted as a scalar, K when by definition it is a tensor, \mathbf{K} . The use of an isotropic permeability is likely to be appropriate for equiaxed solidification, but it is not so appropriate for columnar growth, where the permeability parallel and perpendicular to primary dendrite arms is known to be easier than in other directions. It is true that for perfectly-horizontal solidification, Fig. 6.13, the use of \mathbf{K} in place of K should make no difference, since all flow is in one direction - perpendicular to primary arms. In reality, however, isotherms are never aligned vertically away from the walls of a casting, and the primary dendrite arms are instead inclined to the horizontal, Fig. 6.16. In such cases, the direction of fluid flow will be changed by the mush if \mathbf{K} is used.

Using \mathbf{K} for columnar solidification appears to be important if certain features of segregation defects in large metallic castings are to be predicted. The non-vertical form of A-segregates (that is, the A shape of the channels that is often seen) is one example, which is likely to be derived from the non-horizontal dendrite orientation causing the fluid velocity to take on a sideways component. Similarly, the prediction of inverted A-segregates (in alloys in which the enriched fluid is more dense than the bulk liquid) only seems possible if the fluid velocity is allowed to take on a horizontal component. Note that altering the fluid flow direction in

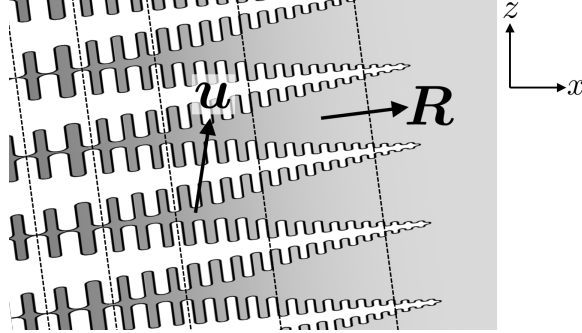


Figure 6.16: If isotherms are non-vertical (dashed lines), then columnar dendrites are likely to be inclined to the horizontal.

order to predict these phenomena is also likely to increase the speed of the fluid relative to the speed of the isotherms, accelerating solid melting and channel formation.

A revised form of the criterion, which utilises \mathbf{K} in place of K , can be found by combining Equations 6.24 and 6.26:

$$\mathbf{K} \frac{\Delta \rho \mathbf{g}}{\mu} \cdot \nabla T > \mathbf{R} \cdot \nabla T \quad (6.36)$$

Or, because \mathbf{R} is in the same direction as ∇T :

$$\mathbf{K} \frac{\Delta \rho \mathbf{g}}{\mu} \cdot \hat{\mathbf{R}} > R \quad (6.37)$$

where $\hat{\mathbf{R}}$ is a unit vector in the same direction as \mathbf{R} . This is now a direct expression of the idea that channel segregation only occurs when the velocity of the interdendritic fluid exceeds the isotherm velocity, when resolved in the direction of \mathbf{R} . The implementation of the criterion in this form would certainly require extra computational effort, but may provide more representative results, and it appears to be necessary if inverted A-segregates are to be predicted. This modification is unlikely to be appropriate for equiaxed solidification.

Just as the use of a critical Rayleigh number is not appropriate for sideways solid-

ification, it must also be borne in mind that this new criterion may not sufficient on its own to predict A-segregation. This is illustrated by considering how the criterion behaves at the bottom of the casting, where the solidification is vertically upwards. Here, we not only need to consider whether fluid velocities exceed isotherm velocities, but also whether fluid motion is possible (i.e., whether the critical Rayleigh number for flow is exceeded). Indeed, the criterion is identical to the Rayleigh number at this point - does that mean its critical value changes with position in the casting?

6.3.3.1 A Sticking Point: Compensatory Flows

The criterion developed here does not account for the effect of compensatory flows in the casting, i.e., the flows that replace fluid moving upwards. These are highlighted using red lines in Fig. 6.17. Unfortunately, the particular nature of these flows it likely to be such that liquid motion in the mushy zone in parts of the casting will not be vertical as assumed by the criterion developed above. Mushy-zone flows at the base of the casting, and at the corners where there is a change from upwards to sideways solidification, are likely to be notably affected. This renders the criterion developed above somewhat flawed, and further work will need to be completed to assess these flows and determine whether they can be accounted for in a simple criterion.

Consideration of the probable pattern of compensatory flows can lead to some interesting speculations. If fluid flow is upwards in the mushy zone to the sides of the casting, then we might expect the fluid flow in the bulk liquid to be mainly downwards, Fig. 6.17, which is exactly opposite to what might be expected from purely thermally-driven flows. There may also need to be sideways flows into the mushy zone as fluid leaves it in channels, or as its volume of the solid-liquid zone changes through the height of the ingot. Indeed, consideration of Fig. 6.17 leads to the proposal that the absence of A-segregates at the centre and base of ingots may not be because the thermal conditions are less favourable in these locations (it should in fact be easier to cross isotherms with vertical flow at the ingot centre), but because they are being suppressed by flows from above.

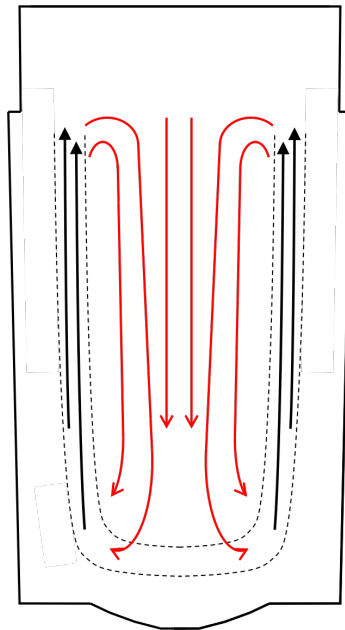


Figure 6.17: Schematic of possible fluid flow pattern in the ingot. Upwards flows through channels in the mushy zone is indicated using black lines with solid arrows, whilst compensatory flows are represented by red lines with unfilled arrows. Flow in the mushy zone (bounded by dashed lines) is upwards, and generally downwards in the bulk zone.

6.4 Synoptic Discussion: Reducing the Occurrence of A-segregation

There is little doubt that A-segregation can be reduced in any alloy by reducing the density change associated with the enrichment of the liquid in alloying elements ($\Delta\rho$), subject to the alloy specifications. Of the common alloying elements, C, Si, P and S are all known to cause liquid density to decrease, whilst heavy elements like Mo and V make the interdendritic liquid more dense. Therefore, for an alloy like Grade 3 in which the interdendritic liquid is lighter than the bulk liquid, $\Delta\rho$ can be reduced by using the minimum C and Si concentrations in the alloy specification, eliminating as much impurity S and P as possible, and by using the maximum amount of Mo allowed [10; 11; 217; 327]. Indeed, it has been suggested that these changes not only reduce the buoyancy differences driving fluid flow, but may also decrease the permeability of the mushy zone by changing the dendrite spacing and morphology [11; 211; 327].

Owing to critical nature of Grade 3's applications, the effect of the suggested compositional change on microstructural and mechanical properties should certainly be investigated before any changes are made. However, there are a number of reasons for why this change is likely to prove beneficial. S forms MnS inclusions and P leads to material embrittlement, so their elimination will surely improve properties. Si is added to the alloy for deoxidation purposes, but there are alternative methods for deoxidation and improved modern steelmaking processes mean this addition is not an essential as it has been in the past (c.f. Grade 4N composition, Table 3.1). Furthermore, decreasing Si content has been associated with better impact properties [327] and its hardening effect is easily accounted for by increasing Mo. Adding more Mo has been shown to encourage the growth of more Mo_2C in competition with Fe_3C , reducing the volume fraction of coarse cementite particles, improving mechanical properties and reducing the ductile-to-brittle transition temperature without adverse irradiation effects [268; 269; 270; 272; 328; 329]. The hardening effect of Mo would then allow for a lower C content, which should presumably reduce the precipitation of coarse carbides (that initiate brittle failure). Increased microsegregation of Mo could be a

potential problem, but if dendrite arm spacings are decreased by the composition changes then this may be less of an issue.

Of course, alloy composition is only one of a number of variables that manufacturers can alter in order to minimise segregation. Casting practices (such as superheats used, the choice of mould and insulation materials, pouring rates, etc), as well as ingot geometries and weights, can also influence the thermal and fluid parameters that determine the severity of segregation. The use of criteria, like those involving Rayleigh numbers, should make the comparison of segregation susceptibility for various conditions a rapid process.

6.4.1 Segregation vs Porosity and Inclusion Retention

An issue that ingot manufacturers should always bear in mind when making changes to minimise chemical segregation is that such changes will often have undesirable consequences, usually associated with increased porosity and inclusion retention. Increasing the rate of solidification, increasing liquid viscosity and decreasing the mushy zone permeability would all reduce macrosegregation, but would also lead to increased porosity (more difficult feeding) and more inclusion retention (less time/harder for inclusions to float out of the melt). Decreasing the freezing range of the alloy (and reducing the size of the mushy zone) is perhaps the only mutually beneficial change.

6.5 Managing Segregation Defects and Porosity

Given the unavoidable conflict between porosity and segregation, manufacturers need to develop the capability to strike a balance between the two. For instance, it may be that low porosity can be sacrificed in favour of low segregation, given that closing or removing porosity (through forging) is likely to be easier than removing segregation. It is also more straightforward to detect pore-based defects through non-destructive testing during quality control.

Another aspect of ingot processing that can be addressed with improved de-

fect prediction is that of discard practice, i.e., the removal of scrap material from forgings, usually by machining. By using tracking methods to precisely locate defective material, or by changing forging routes such that defective material is moved into particular locations, material removal can be done more efficiency and scrap reduced. Guided discard practice can have a positive feedback effect in that it may allow for the casting of smaller ingots (perhaps with smaller heads) that take less time to solidify and hence exhibit less segregation in the first place.

6.5.1 Assessment of Tracking Procedure

Superior discard practice requires not only the ability to predict the location of defects in as-cast ingots, but also to accurately track defective material through forging processes. Hence, the establishment of a robust methodology for tracking material during forging operations is a highly-desirable objective. Unfortunately, the tracking procedure utilised here, which employed point tracking in DEFORM, was sometimes found to deliver results with excessive uncertainties that would not have allowed for tracking in any useful sense.

There will always be some spread and uncertainty in point tracking results from forging simulations, particularly for the multiple-operation procedures outlined in Section 3.2.3. In these complex processes, the true starting orientation of the workpiece is rarely known, the forging bite depth and workpiece rotations are often inconsistent, and the effects of scale and temperature gradients are difficult to capture. They are inherently asymmetrical in that they start at one given location and rotate in one particular direction. Nevertheless, uncertainties can be often reduced to a level at which the results are useful (such that manufacturers can use results with some confidence), and were for the shell forging operations used above. Take, for example, the case of tracking points for the cogging operation schematised in, Fig. 6.18a, in which points are typically tracked from equal radius, Fig. 6.18b. Experience using the software has indicated that if a fine mesh size is used relative to the forging bite depths, forging bites are small relative to the dimensions of the workpiece, and the points tracked are not located at regions of high strain (and not near the surface of the workpiece), then the spread

in tracked radii will tend to be low. However, if coarse mesh sizes and large bite depths are used, and the tracked points are in regions of high strain, then a large spread in results often results, Fig. 6.18c. In such cases, tracked points that start near the surface will often move to the surface and stay there for the duration of the simulation. There were also instances of apparent random relocation of points, which may have resulted from automated remeshing.

It is unclear how the particularities of the DEFORM point tracking procedure have affected results like this, and what the relative effect of the user-inputted forging sequence is. However, if mesh sizes do need to be significantly decreased to obtain good results, then this will likely lead to impracticable computing times. It may often be difficult to generate useful results in manageable time frames.

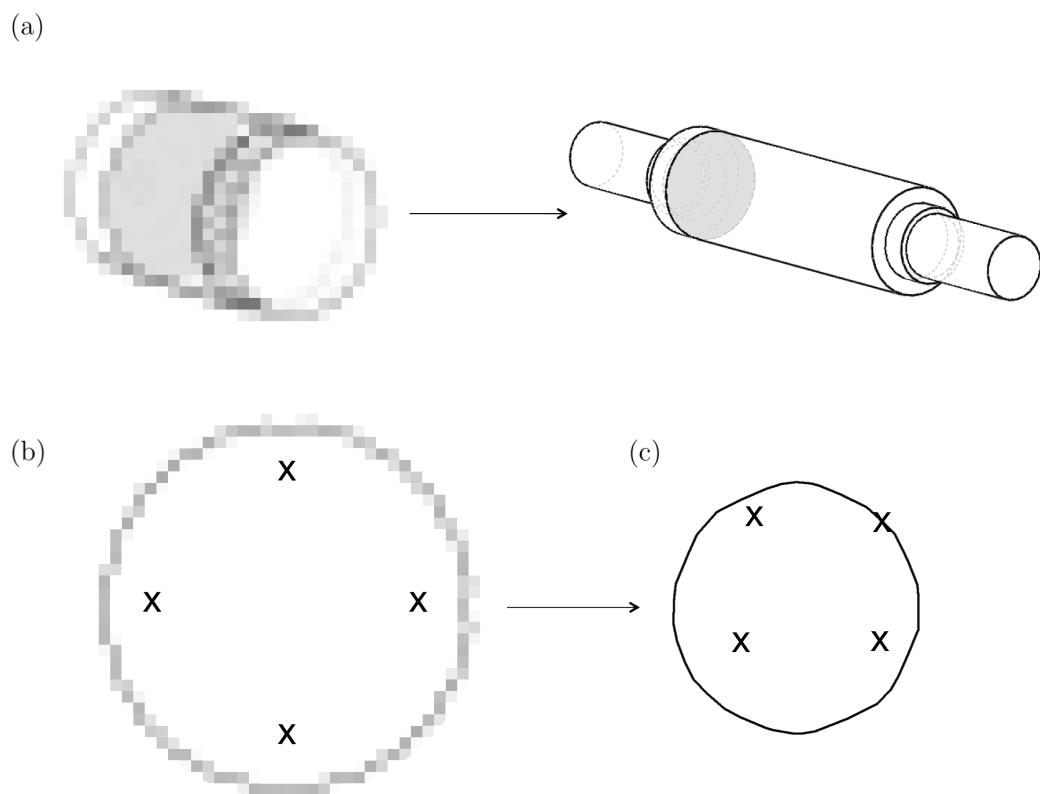


Figure 6.18: (a) Schematic of a cogging procedure, in which the same slice is highlighted in grey at the start and end of forging. (b) The position of the points tracked in the as-cast ingot. (c) The position of the points tracked through the forging process. IMAGE HAS BEEN PIXELATED - COMMERCIALY SENSITIVE.

Chapter 7

Measuring Macrosegregation

7.1 Introduction

The detection of segregation over large distances is a useful capability, permitting the control of quality in manufactured parts and providing much-needed information and guidance to those predicting macrosegregation phenomena. Unfortunately, measuring macrosegregation can be an arduous task, particularly if historic methods are used, and in the past incomplete datasets have often been taken and results spuriously interpolated. This chapter investigates the implementation of a technique that is capable of fully mapping long-range compositional variations in metal components, without the need for extensive sample preparation.

As highlighted in Chapter 2, techniques such as energy-dispersive or wavelength-dispersive X-ray analysis in the electron microscope, optical-emission spectroscopy, combustion analysis and wet chemical methods are common chemical analysis tools, but are often destructive, time-consuming and are only able to analyse small volumes, thus rendering them impractical for large components. To map segregation in the past, these analysis methods have usually been used on small samples extracted from the ingot at regularly-spaced intervals (i.e., via trepanning), with the data extrapolated to produce composition maps [30; 107; 258; 259], Fig. 2.12. Such a method may not detect small regions of heavily-segregated ma-

terial, and is both expensive and requires the removal of significant quantities of material. X-ray fluorescence (XRF) spectroscopy, on the other hand, can be used to build up a detailed picture of composition over large distances, without the component being enclosed in a vacuum or destroyed beyond basic surface preparation.

XRF spectroscopy has its origins in the pioneering investigations into the use of X-rays carried out a century ago, but it is only over more recent decades that significant advances in instrumentation and analysis have been made which have led to its wider application [330; 331]. Now XRF is used as an analysis technique in applications as diverse as medical and biological imaging [332], art and archaeological examination [333], scrap metal sorting, and the analysis of geological cores and soil samples [334]. Specialist instruments and data analysis methods have allowed for the detection of minute concentrations of all but a few of the lightest elements (down to the microscopic scale), whilst the mass-produced hand-held analysers commonplace in industry are used for less specialised purposes. It is true to say that automated XRF mapping is not a new technique (it is used, for example, in geological core logging and artwork examination [333; 334]), and it has been applied to the mapping of solute distribution in metals at a large-scale fixed facility on two occasions in the literature [335; 336]. However, the particular system used here differs in several key ways to the appliances used previously: it employs standard off-the-shelf components, can be expanded to larger sizes (limited by robotics only), it can make measurements on surfaces which are not ideally flat (i.e., the detector can move vertically), and the equipment can be moved relatively straightforwardly.

In this work, emphasis is placed upon investigating the pragmatic application of the system employed, rather than the on the precise calibration of the equipment for accurate quantitative analysis. Such calibrations require significant experimental undertakings and expertise (for example, see Lachance and Classie [337] and Rousseau [338]), and instead it is assumed these calibrations have been sufficiently accomplished by the supplier of the XRF equipment (it would generally be very difficult for a casting engineer to fully optimise their XRF technique

for every alloy they encounter). The effect of dwell times and surface finish on segregation detection, and the reproducibility of the data, are examined. The primary aim was to qualitatively identify the minimum dwell times and surface preparations required to reliably detect segregates.

7.2 Experimental

An Olympus Innov-X Delta Dynamic hand-held XRF analyser was employed, with robotics designed and constructed by Geotek Ltd [339]. The analyser and robotics were controlled using the following software packages: Geotek's Multi-Sensor Core Logging XYZ [340], Microsoft ActiveSync [341] and Innov-X Delta Advanced PC [342]. The analyser incorporated a Rh source and a 10 mm silicon drift detector. Fig. 7.1 shows the experimental set-up. The analyser was standardised using a reference metallic sample supplied by Olympus. The same production Grade 3 steel that was examined in earlier chapters was also used in this investigation: the trepanned cylinder composition is given in Table 4.1, whilst EPMA region analyses are given in Table 4.3. Fig. 7.3 shows a slab of this material after grinding and etching in 5% nitric acid. During investigations, the surface of this slab was prepared to four different finishes, shown in Table 7.1, with the roughness measured using a Veeco Dektak 6M Stylus Profiler. Energy-dispersive X-ray analysis was carried out using a field emission gun scanning electron microscope, CamScan MX2600.

The hand-held XRF was used in a mode that utilises two X-ray beams, the first of energy 40 kV and current 52 μ A to detect transition metals, and the second with energy 13 kV and current 20 μ A for lighter elements such as Mg, Al, Si, P and S. Olympus' own peak-fitting and quantisation algorithms were employed via the Innov-X software. The raw spectra were also retained.



Figure 7.1: The automated XRF apparatus. A standard hand-held XRF is mounted on a robotic gantry system with laser-guided movement.

7.3 Results

7.3.1 Spatial Resolution

The spatial resolution of the XRF instrument was investigated using an Fe-Ni dissimilar metal bond produced using a diffusion-bonding process at 1050 °C for 30 minutes [343]. Energy dispersive X-ray analysis revealed that the interdiffusion layer produced was approximately 20 μm in width. Fig. 7.2 shows the blurring of the composition profile due to spatial resolution of the XRF instrument, and was obtained by gradually stepping across the interface using a 1 mm step size. It is evident that the vast majority of characteristic X-rays are collected from a region 5-7 mm in width in both x and y .

7.3.2 Mapping

A preliminary map of the slab's surface chemistry was obtained using both analytical X-ray beams. The live time for the 40 kV beam was set to 30 s (42 s

Table 7.1: Surface roughness data. For each surface finish, four 2.5 mm scans were made in two perpendicular directions, and the mean result found. Error given is one standard deviation of the mean result. The stylus tip radius used was 12.5 μm . R_a is the mean deviation centreline, whilst R_t is the maximum peak-valley distance.

Label	R_a / μm	R_t / μm	Method of Surface Preparation
A	0.038 ± 0.008	0.429 ± 0.099	SiC grinding, diamond polishing
B	1.546 ± 0.782	7.286 ± 3.256	Milling with WC tip (fine)
C	2.118 ± 0.818	13.982 ± 6.333	Surface grinding with Al_2O_3 disc
D	6.723 ± 3.265	29.849 ± 13.498	Milling with WC tip (coarse)

real time), whilst the live time for the 13 kV beam was 2.5 s (60 s real time). The surface of the slab was prepared to roughness C in Table 7.1, and the sample measured in the unetched state. A step size of 5 mm was used throughout the work. Maps for Cr, Mn, Ni, Mo and Si are shown in Fig. 7.3. It is immediately clear that segregation features are detected in the maps for Mn, Mo and Ni, although are less well defined for Ni. In the case of Cr and Si, there is not such a clear identification of segregated material, and the maps appear noisier. Comparing absolute concentrations to those in Tables 4.1 and 4.3, the bulk values measured for Cr, Mn, Ni and Mo are relatively close to the EPMA and OES values, perhaps being a little lower, whilst the Si concentrations measured are significantly lower. For A-segregated regions, the maximum concentrations measured by XRF are

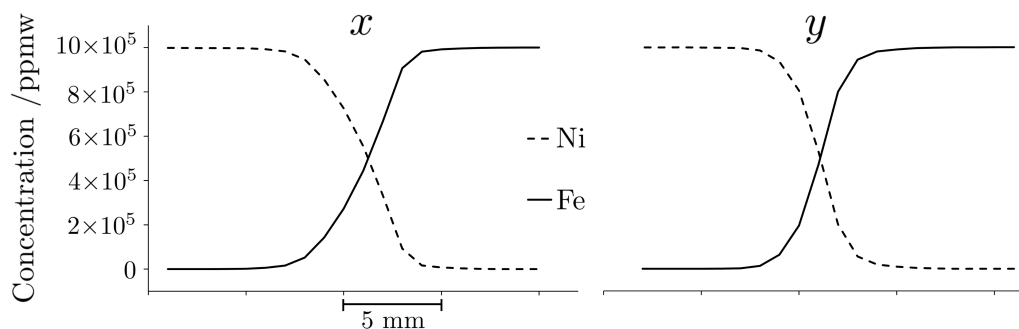


Figure 7.2: Measurement of the spatial resolution of the XRF instrument using a Fe-Ni dissimilar metal bond and a 1 mm step size.

consistently much lower than those measure by both EPMA and OES.

7.3.3 Dwell-Time Variation

The effect of dwell time variation was investigated to determine whether using a small dwell time would consistently lead to the detection of segregated material. The small region of the slab highlighted in Fig. 7.3 was measured with a retained surface finish given by Roughness C in Table 7.1. Only the 40 kV analytical beam was utilised, in light of the apparent difficulty in measuring Si, meaning that only the concentrations of Cr, Mn, Ni and Mo were measured. An indication of the reproducibility of segregate detection was found by triplicating measurements on this region, i.e., making three measurement runs over the same region, as shown in Fig. 7.4. Detected variations of Mo are by far the most reproducible, with the location of enriched material readily apparent at dwell times as low as 1 s. Mn results are informative and reasonably consistent with 10 s dwell, whilst Ni appears to require 30 s and Cr closer to 60 s.

7.3.4 Surface Roughness

To examine the effect of surface roughness on the reproducibility of measurements, the surface finishes listed in Table 7.1 were used and the region highlighted in Fig. 7.3 analysed once again. Only the 40 kV beam was used with a 30 s dwell time, and runs were triplicated. Fig. 7.1 shows the results. It is evident that, within the range of roughness assessed, the surface finish had little significant effect on the reproducibility of results. Adequate detection is achieved even with the roughest surface finish. Note that because material was removed between measurements, it cannot be guaranteed the segregated material analysed was always in precisely the same position or the same shape (see results for Roughness C vs Roughness D), but no significant changes in composition were detected when layers were removed - this is a natural result of channel-type segregation - and hence the reproducibility can still be compared.

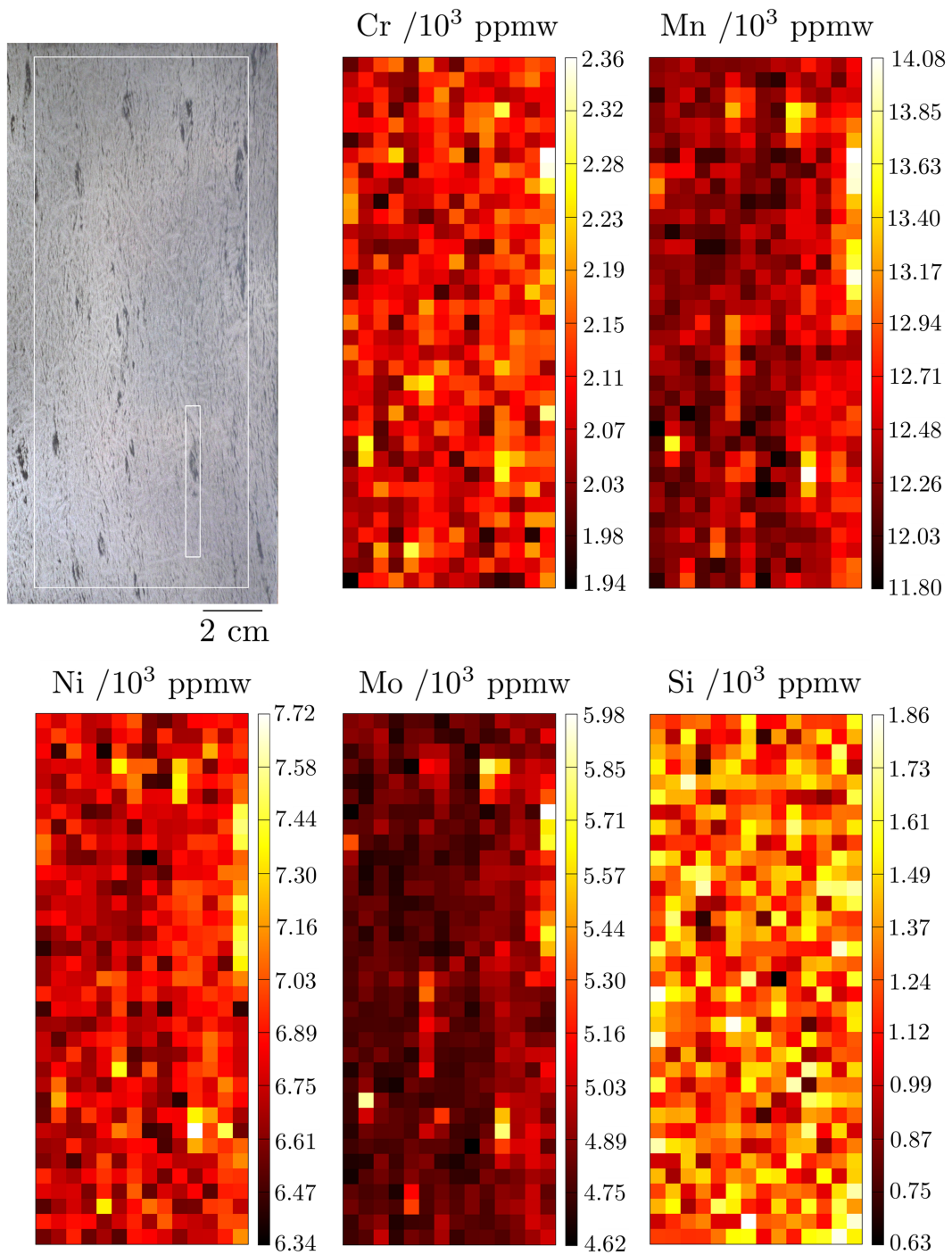


Figure 7.3: A photograph of the etched slab analysed. The coloured images are the corresponding composition maps from the large rectangle in the photograph. The smaller rectangle was used for the maps presented in Figs. 7.4 and 7.5.

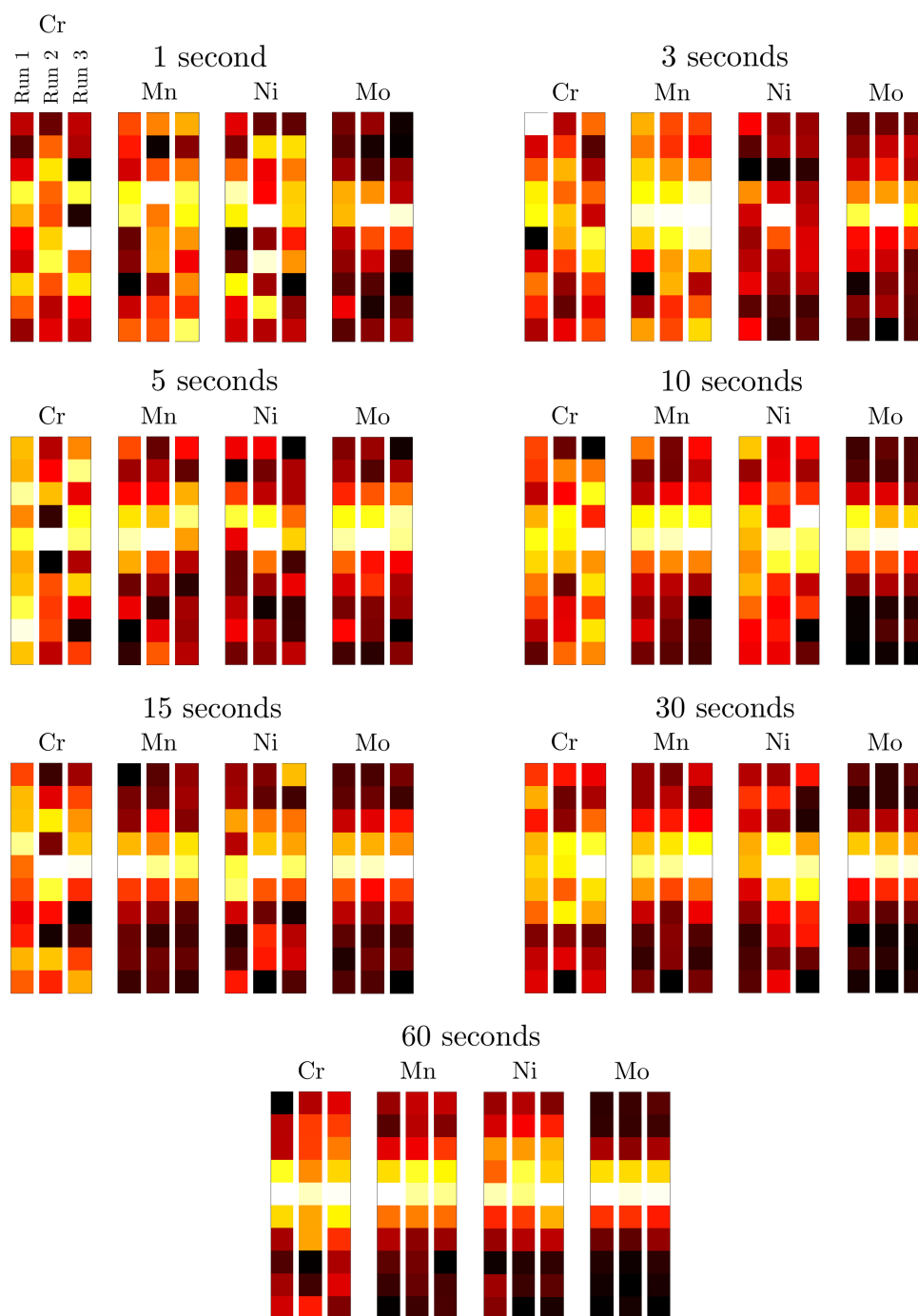


Figure 7.4: Results of dwell-time investigations. Measurements of Cr, Mn, Ni and Mo were triplicated for each dwell time on the small region highlighted in Fig. 7.3. Note that a different concentration scale is used for each dwell time due to the changes in range - in general the lower dwell times produced a higher range of detected concentrations due to increased noise.

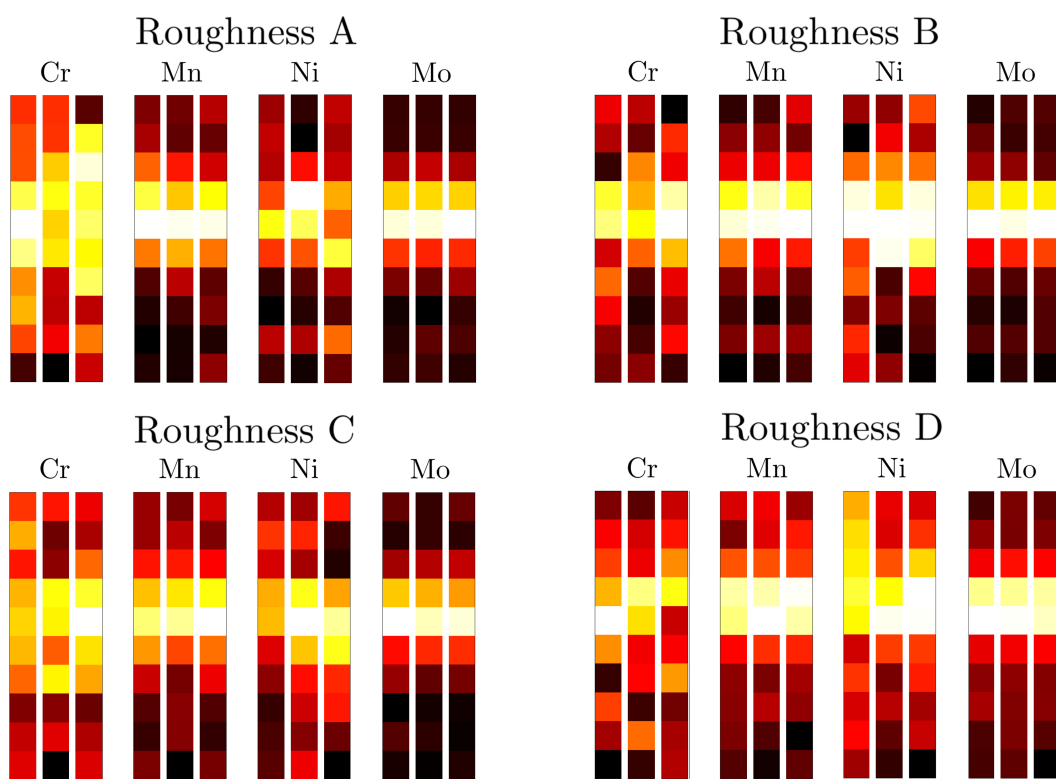


Figure 7.5: Results of surface-roughness investigations.

7.4 Discussion

Concentrations in XRF analysis are calculated using the net peak signal, i.e., the difference in the measured peak signal and the measured background signal. The standard counting error associated with the net signal is therefore influenced not only by the error in the peak signal, σ_p , but also by the error in the background signal, σ_b . The total error in the net signal, σ_{net} (i.e., the noise), can be found by the following expression, which is a result of assuming the distributions of peak and background values are Gaussian and independent:

$$\sigma_{\text{net}}^2 = \sigma_p^2 + \sigma_b^2 \quad (7.1)$$

It is known that X-ray emission is a probabilistic process which can be described by Poisson statistics. A standard result of this is that, at sufficiently high count rates, the Poisson distribution of the total number of counts approaches a Gaussian distribution. The theoretical standard deviation in this distribution, σ_* , is a function of the total number of counts, C , as given by $\sigma_* = \sqrt{C}$. Therefore, the combined standard deviation in the net signal can be expressed:

$$\sigma_{\text{net}} = \sqrt{C_p + C_b} \quad (7.2)$$

where C_p and C_b are the total peak and background counts. It is this noise in the signal that prevents the detection of small changes in it, and hence influences the detection of changes in concentration of an element. The change in signal due to a real change in concentration must be discernable over the noise in order to be reproducibly detected. This simple framework can be used to help explain, qualitatively here, the effect of dwell times and surface roughness on segregation detection. It is true to say that a statistical analysis could have been used to calculate the required dwell time to detect a certain variation (i.e., the number of counts needed to ensure the noise is small enough to reliably detect a particular change in signal), rather than embarking on the replication of measurements. However, the calculation through which the Innov-X software finds concentrations will be far more complex, taking into account factors including atomic number effects, cross-fluorescence, absorption and background profile. The errors associ-

ated with these will all contribute to the final uncertainty, potentially changing it significantly, and hence no such statistical calculations were made. Instead, an empirical study of reproducibility was undertaken with the aim of identifying whether sensible dwell times could be used.

It was found that for the steel studied, variations in composition of Mo could be most readily and reproducibly revealed over the range of dwell times and surface finishes studied. This capability then decreased from Mn, to Ni, to Cr, and finally Si. Table 7.2 gives an indication of the relative magnitudes of the maximum and background number of counts for the elements analysed, with Fig. 7.2 showing these graphically (the true signal is, of course, all the counts which are taken to produce the peak, not just the maximum value). It is clear that by considering counting statistics alone, the error for Si should be greatest due to the high level of the background (a result of Compton X-rays at low energies) with a modest peak signal. Mo and Mn have high peak-to-background ratios, and high peak signals, delivering improved signal-to-noise ratio. The peak signals for Cr and Ni are lower, delivering relatively more noise. The Ni signal is low due to absorption of characteristic X-rays by the iron matrix.[344]

The better detection of segregated material found at longer dwell times was simply a result of the improved signal-to-noise ratio delivered by a higher number of counts. The effect is most pronounced for elements with a low baseline number of counts, i.e., Cr and Ni. The apparent insensitivity of results to surface roughness variations can also be explained in a similar manner: changing the roughness did not significantly affect the number of registered counts or the background signal, for any element analysed (the total number of counts dropped by only $\approx 12\%$ between the smoothest and roughest surfaces). The use of specific abrasives during sample surface preparation can lead to significant contamination issues in metal XRF, particularly in the case of Si,[344] but are unlikely to have been significant here (SiC grinding paper was used for Roughness A, but was followed by diamond paste stages, and the grinding and milling procedures used no Si-based abrasives).

It is likely that the consistent measurement of lower concentrations of alloying

elements here by XRF in comparison to EPMA and OES (Tables 4.1 and 4.3) was in part due to a issue with calibration of the gun used. Despite using Alloy Plus mode, which designed for analysis of metallic samples, the instrument had not been subject to a calibration specifically for low-alloy steels (unlike the gun used for measurements in Chapter 8). Hence, it is possible that the readings it was delivering were systematically too low. For the specific analysis of A-segregate material, the area of measurement of the XRF is likely to have further diluted concentrations in comparison to EPMA and OES - enriched areas did not completely fill the sampling window and may have been only partially assessed in any given data point because of the step-wise motion of the machine.

Table 7.2: X-ray count spectrum data for the elements analysed. The peak maximum is given as a relative guide for the strength of the signal, whilst the peak minimum is given as an approximate guide to the influence of the background and/or other characteristic peaks which may have made quantitative calculations more challenging.

Peak and beam	Peak maximum /counts per s	Peak minimum /counts per s
Cr K_{α} , Beam 1	14	2
Mn K_{α} , Beam 1	47	2
Ni K_{α} , Beam 1	10	0
Mo K_{α} , Beam 1	58	1
Si K_{α} , Beam 2	44	20

7.5 Practical Implications

It is clear, and not surprising, that more consistent and accurate results can be obtained by increasing the number of characteristic X-rays counted by the detector. However, the aim of this investigation was to determine whether reproducible detection of segregates could be achieved using *practical* dwell times and surface finishes. Although the material examined in this study has been a highly-specific example, it has been demonstrated that the segregation present can be readily detected using dwell times of only a few seconds, particularly if species like Mo

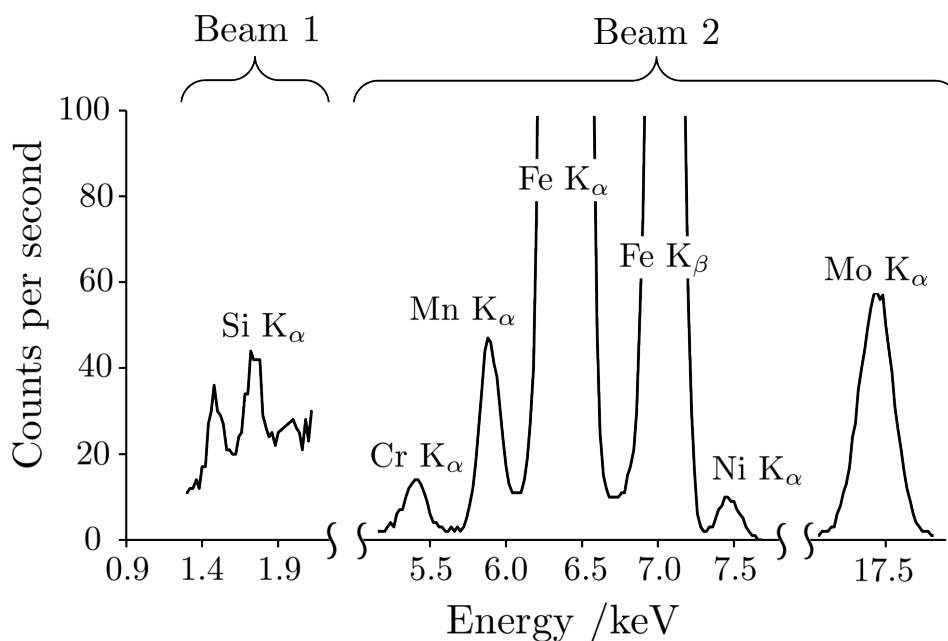


Figure 7.6: Characteristic peaks for the elements analysed. Note that although the absolute number of counts for the Si K α peak is relatively high, it is not compared to the peak height for Fe K α using Beam 2: the maximum values for the Fe K α peak for Beam 1 and Beam 2 were 3794 and 94292 counts per second respectively. The peak signal for each element will have been a function of both element concentration and the strength of X-ray interaction (i.e., characteristic X-ray yield).

are targeted. This is certainly of great importance for potential incorporation into quality-control procedures. Longer dwells can lead to dramatic improvements in results - with 30 s dwell, variations of the order of a few hundred ppmw are reproducibly measured for Mo - and it is therefore capable of detecting long-range gradual variations if necessary. The same cannot be said for Si, however, and it is clear that to significantly improve results would require prohibitively long dwell times if the same experimental apparatus were used. In practice, the required dwell time will be dependent on the magnitude of concentration variations and particular element of interest.

The insensitivity of results to surface finish is a promising result, as the careful preparation of large surfaces areas would be a costly task. It is likely surface finish will only become important for the accurate quantitative detection of minute concentrations and light elements (the depth from which characteristic X-rays escape is much lower for lighter elements, and hence surface contamination and scattering become more important [344].) In terms of potential spatial resolution for the technique, the 5 mm sampling interval used here will have meant some material will have been sampled more than once, smearing results. It would theoretically be possible to improve the resolution of the technique to the magnitude of the step size if a 'reference' section of material had a known concentration profile and the spatial X-ray sampling profile of the detector was known, but this is not of concern here. Nevertheless, an XRF instrument capable of switching the size of its sampling window, from broad to very small, is available and may be of use to quickly detect segregated areas and then precisely analyse them [345]. Another distinct possibility is the incorporation of other analysis techniques, such as optical imaging and hardness measurements, into the same automated robotics, thereby yielding further useful information concurrently. Recently, a portable OES gun capable of measuring C concentrations has become available on the market, and could prove to be even more powerful than the XRF used here.

7.6 Summary and Conclusions

1. It was found that an automated XRF technique which employed readily-available equipment was capable of accurately and reproducibly detecting the macrosegregation present in a low-alloy steel sample.
2. Adequate detection was achieved at dwell times of only a few seconds for some elements, and results appeared insensitive to the surface finishes investigated.
3. There is no reason why the technique cannot also be used to assess long-range gradual variations, and there is potential for other measurement techniques to be combined with XRF using the same automated mapping apparatus.
4. Such a system could readily form part of a manufacturing quality-control procedure.

Chapter 8

A Case Study of Macrosegregation in a Steel Ingot

8.1 Introduction

Chapter 2 of this thesis highlighted the shortcomings associated with modern-day macromodels; a primary deficiency being the excessive computing times required for simulations. Indeed, computing power is arguably the most prominent restraint on model development and use at present, and is not an issue that can be easily dealt with. However, in addition there is also a definite lack of suitable case studies against which model results can be compared. This chapter seeks to address this concern.

Here, a comprehensive experimental evaluation of macrosegregation in a steel ingot is presented. A 12 tonne steel ingot with high C, Si and Cr additions is used as the case study. In order to create a study that can act as a suitable validation tool for macromodellers, as much information as possible has been collected about the casting assembly and procedure, as well as the resulting ingot characteristics. For instance, temperature distributions during casting were measured using thermocouples and a thermal imaging camera, ingot and mould dimensions were measured using lasers, and chemistry distributions were mapped using macro-scale XRF. The application of macro-scale XRF here repre-

Table 8.1: Composition (wt%) of the steel ingot investigated.

C	Si	Mn	P	S	Cr	Mo
0.79	0.80	0.26	0.007	0.005	4.88	0.33
Ni	V	Al	Cu	Sn	H	
0.22	0.005	0.008	0.08	0.009	2 ppm	

sents a significant improvement over previous methods used for chemical analyses of steel ingots, which have usually involved periodic trepanning of material and, on occasion, questionable interpolation of such data to produce contour maps [30; 107; 259]. Here a cross section of the ingot is mapped in its entirety - never before has a steel ingot been mapped for chemistry in such detail. Indeed, to the author's knowledge no metallic specimen has ever been mapped so completely on such a scale [335].

8.2 Experimental

8.2.1 Ingot Selection

The composition of the ingot cast, which was measured at the point of pouring, is given in Table 8.1. This particular steel composition was chosen because its high C and Si levels were predicted to deliver particularly prominent macrosegregation (C and Si strongly enrich the interdendritic liquid and cause its density to decrease significantly, hence they promote advection of alloying elements). This allowed for the ingot size to be kept small, eliminating practical issues associated with the analysis of a larger ingot - larger ingots would usually be preferred for such studies, as their longer solidification times naturally generate more macrosegregation.

8.2.2 Casting Apparatus and Procedure

The shape and approximate size of the ingot cast are given in Fig. 8.1. The full casting set up is shown in Figs. 8.2 and 8.3; each component labelled is described in Table 8.2. Appropriate physical properties of the materials used are

Table 8.2: Casting assembly: descriptions and materials.

Label	Description	Material	Reference
(i)	Ingot	Steel	Table 8.1
(ii)	Mould	Gray cast Iron	Appendix A.1
(iii)	Insulating tiles	Ceramic	Appendix A.2
(iv)	Hollow ware	Ceramic	Appendix A.2
(v)	Packing sand	Silica (mostly)	Appendix A.3
(vi)	Cover plate	Gray cast Iron	Appendix A.1
(vii)	Base plate	Gray cast Iron	Appendix A.1
(viii)	Trumpet for pouring	Gray cast Iron	Appendix A.1
(ix)	Lifting hooks	Mild steel	-
(x)	Flux	Oxide mixture	-

given in Appendix A. A FARO Focus3D S laser scanner was used to verify the dimensions of these components before casting and produce three-dimensional CAD (computer-aided design) models of the components for reference; examples of this are shown later.

Molten steel for the ingot was produced by heating scrap material in an electric arc furnace. The steel produced was then transferred into a ladle and vacuum-arc degassed. The ladle contained ≈ 100 tons of steel at a temperature above 1500°C at the end of degassing. The ingot investigated was the last of five ingots to be cast, and it was poured approximately 50 min after the end of degassing. It is therefore probable that the melt was below 1500°C at the time of casting. The ingot was bottom-poured, Fig. 8.4a, and the mould was filled approximately to the top of the insulating tiles. A flux comprising various oxides was added to the surface of the melt to capture any floating inclusions. Anti-piping compound (APC) was added to the top of the ingot after pouring, Fig. 8.4b, to ensure adequate hot topping. Lifting hooks were cast into the top of the head to allow for the ingot to be extracted at the end of solidification (this extraction process is referred to as ‘stripping’). The temperature of the outside of the mould was monitored continuously throughout the casting procedure using thermocouples

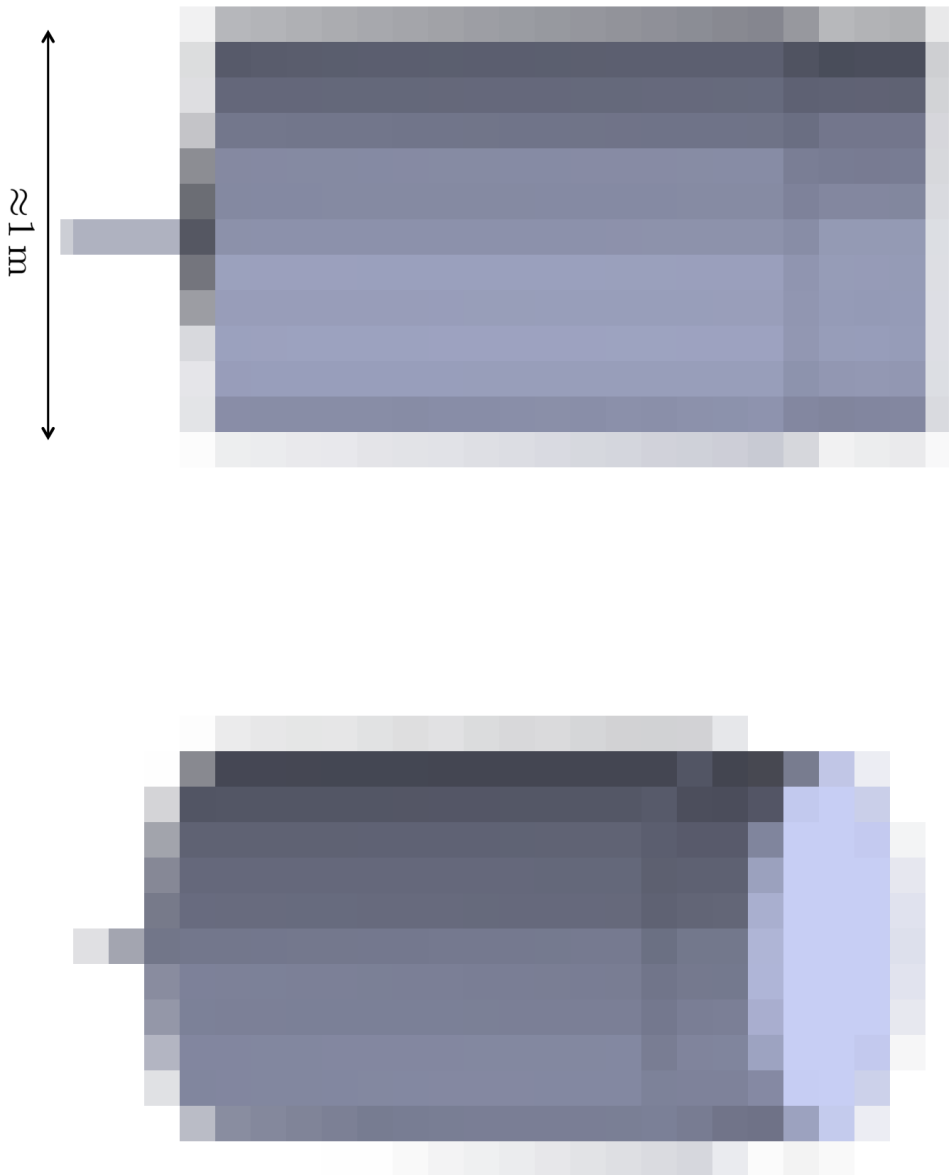


Figure 8.1: Computer-aided design (CAD) model of the ingot cast. Approximate dimensions are given. IMAGE HAS BEEN PIXELATED - COMMERCIALY SENSITIVE.

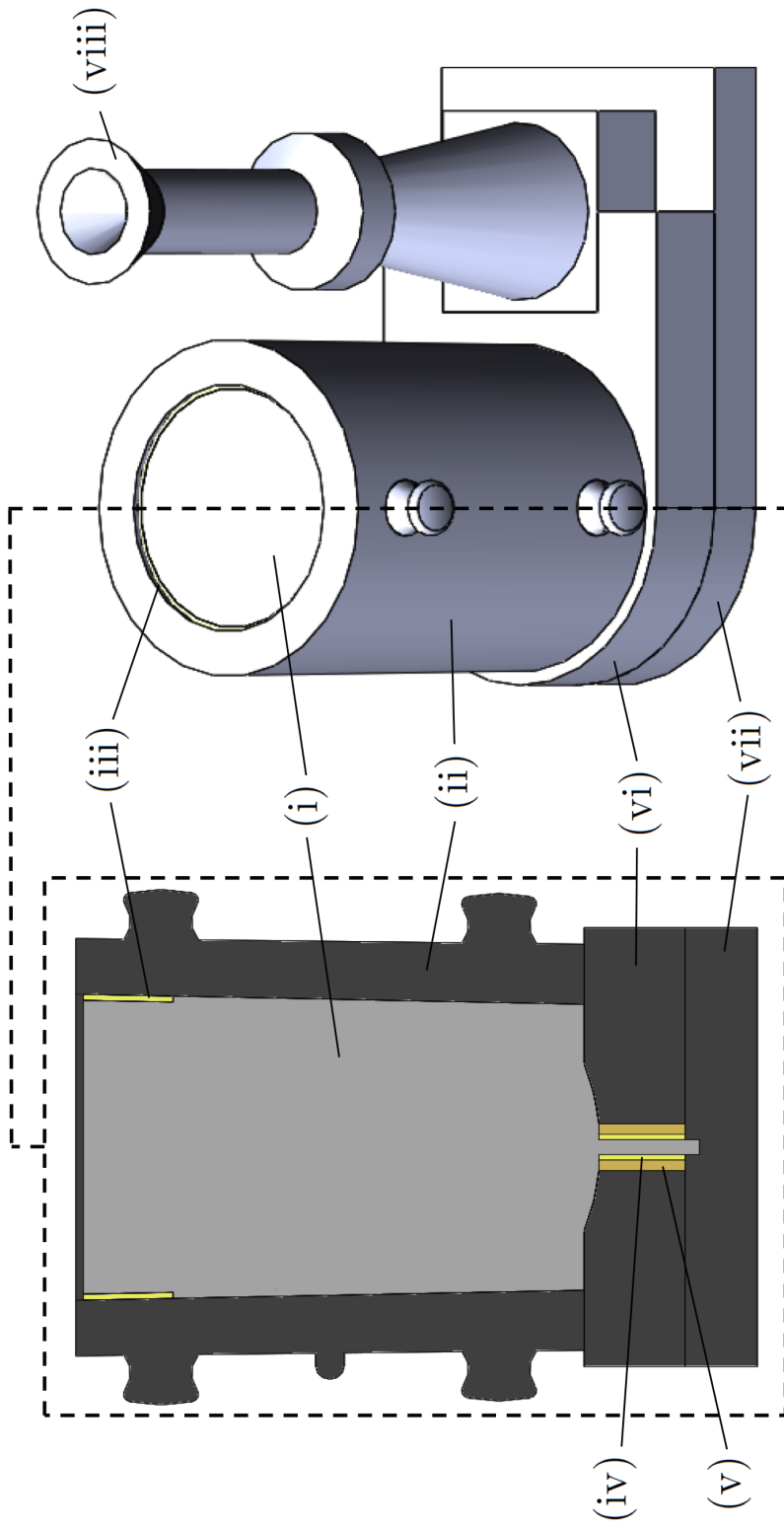


Figure 8.2: CAD drawings of the casting setup. Each component is described in Table 8.2.

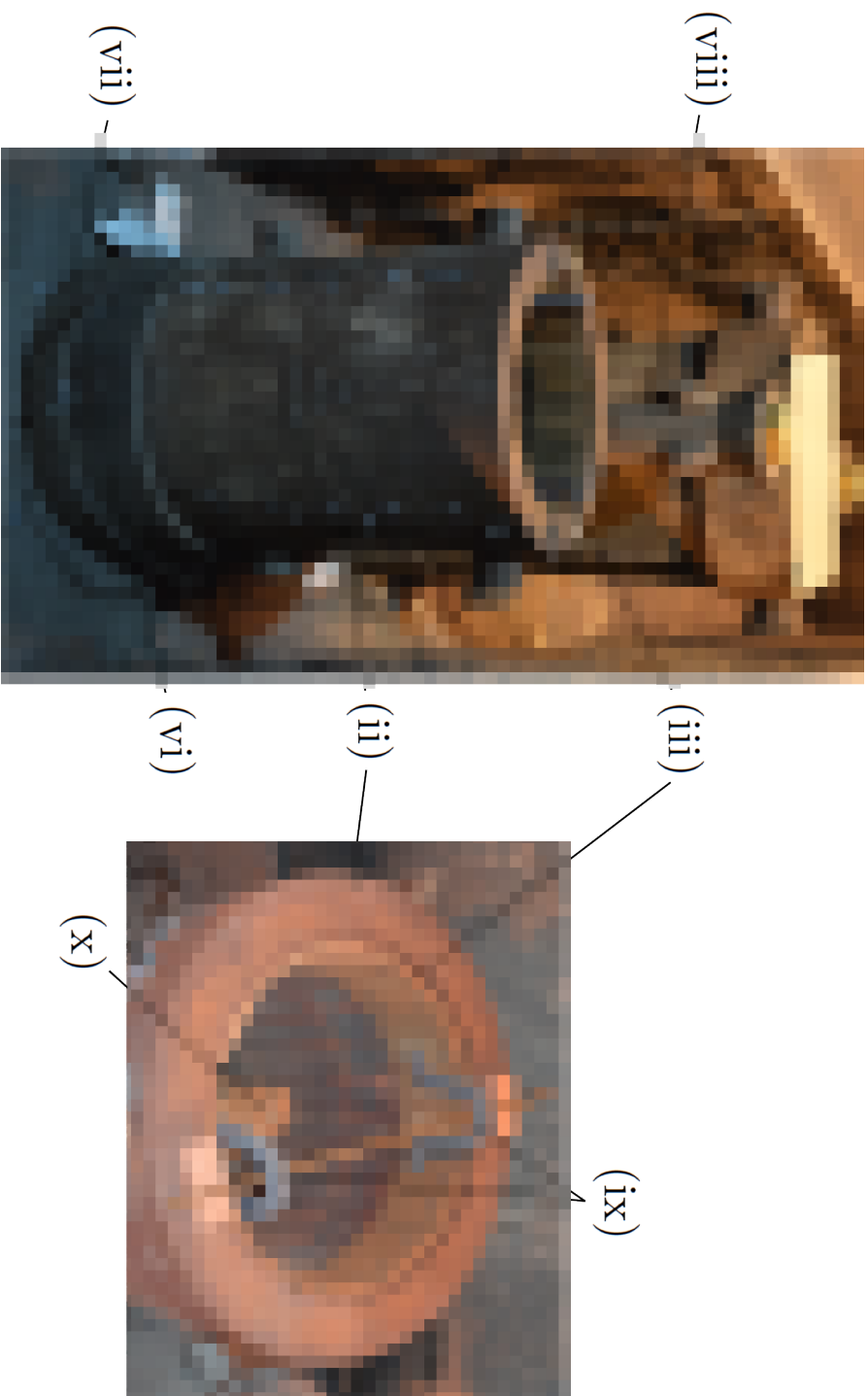


Figure 8.3: Photographs of the casting assembly, with the labelled components described in Table 8.2. IMAGES HAVE BEEN PIXELATED - COMMERCIALY SENSITIVE.

and a thermal imaging camera. The thermal imaging camera used was a FLIR ThermaCAM SC640 instrument, which was calibrated up to 2000 °C. It was used with a target emissivity value of 0.8 and in high-temperature mode, which meant it was only capable of accurately measuring temperatures above 200 °C. K-type (chromel-alumel) thermocouples were located as shown in Fig. 8.5: TC1-4 were placed in the top of the mould between the mould and insulating tiles (labelled with superscript ‘*’). TC1 and TC3 were held in place by friction (labelled with superscript ‘f’), whilst TC2 and TC4 were cemented. TC5-14 were placed in 10 mm holes drilled into the mould at regularly-spaced intervals, and held in place with cement. TC15 and TC16 were cemented in place in gaps between the cover plate and the base plate. TC17 was placed underneath one of the lifting hooks and also cemented in place. Temperature measurements from each thermocouple were made every second from steel pouring until the ingot was removed from the mould. Thermal images of the ingot were also taken immediately after removal from the mould.

8.2.3 Post-Casting Analysis

The ingot was removed from the mould after ≈ 7 hours (25,000 s), Fig. 8.6. Temperature measurements were made at this stage using the thermal-imaging camera, and dimensional measurements were also made using the laser scanner. The ingot was then transferred to a furnace for the heat treatment given in Table 8.3. This heat treatment was designed to minimise changes to the as-cast structure of the ingot whilst providing adequate stress relief. Following heat treatment, the ingot was sectioned to examine the faces labelled A-D in Fig. 8.7.

Faces A, B, C and D were metallographically prepared to a near-mirror finish. Face A was then subject to chemical mapping using an automated macro-scale XRF technique, the implementation of which was described in Chapter 7. As in Chapter 7, an Olympus Innov-X Delta Dynamic hand held XRF analyser was employed, with robotics designed and constructed by Geotek Ltd [339]. The beam energy used was 40 kV, with a beam of current 52 μ A. The step size used was 5 mm in both orthogonal directions of movement, and the dwell time was 10 s. Faces A,

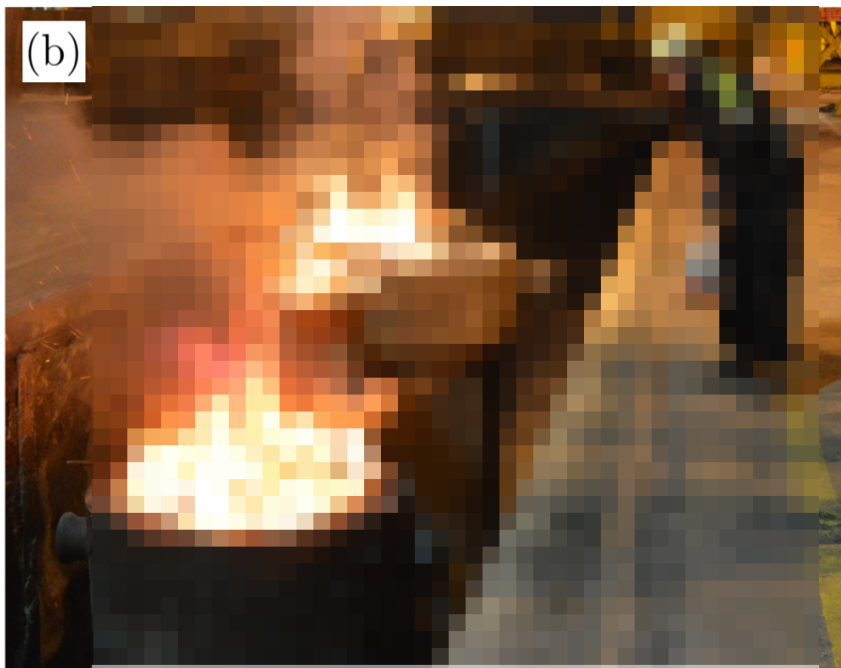
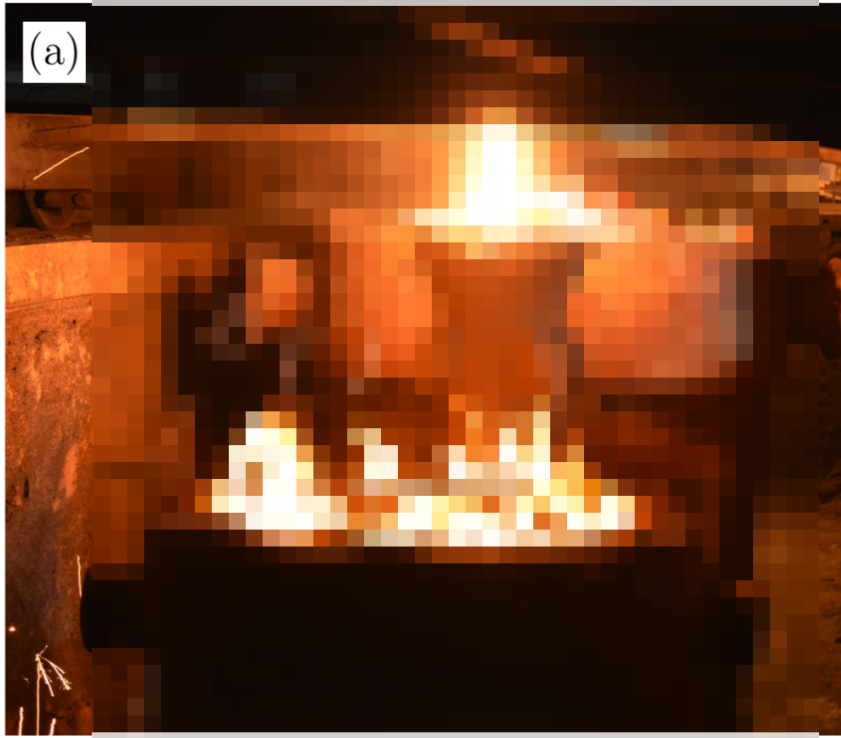


Figure 8.4: Photographs of (a) ingot pouring (steel flows down the trumpet through the base plate and up into the mould) and (b) exothermic powder addition. IMAGES HAVE BEEN PIXELATED - COMMERCIALY SENSITIVE.

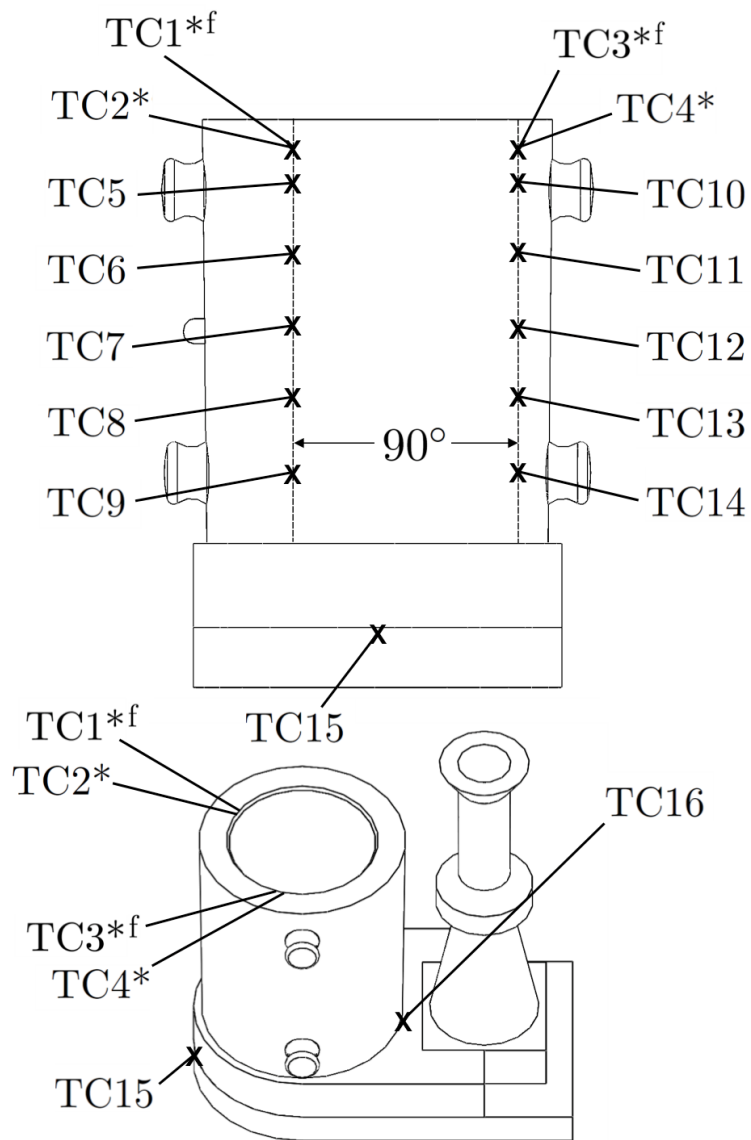


Figure 8.5: Placement of thermocouples on casting assembly.

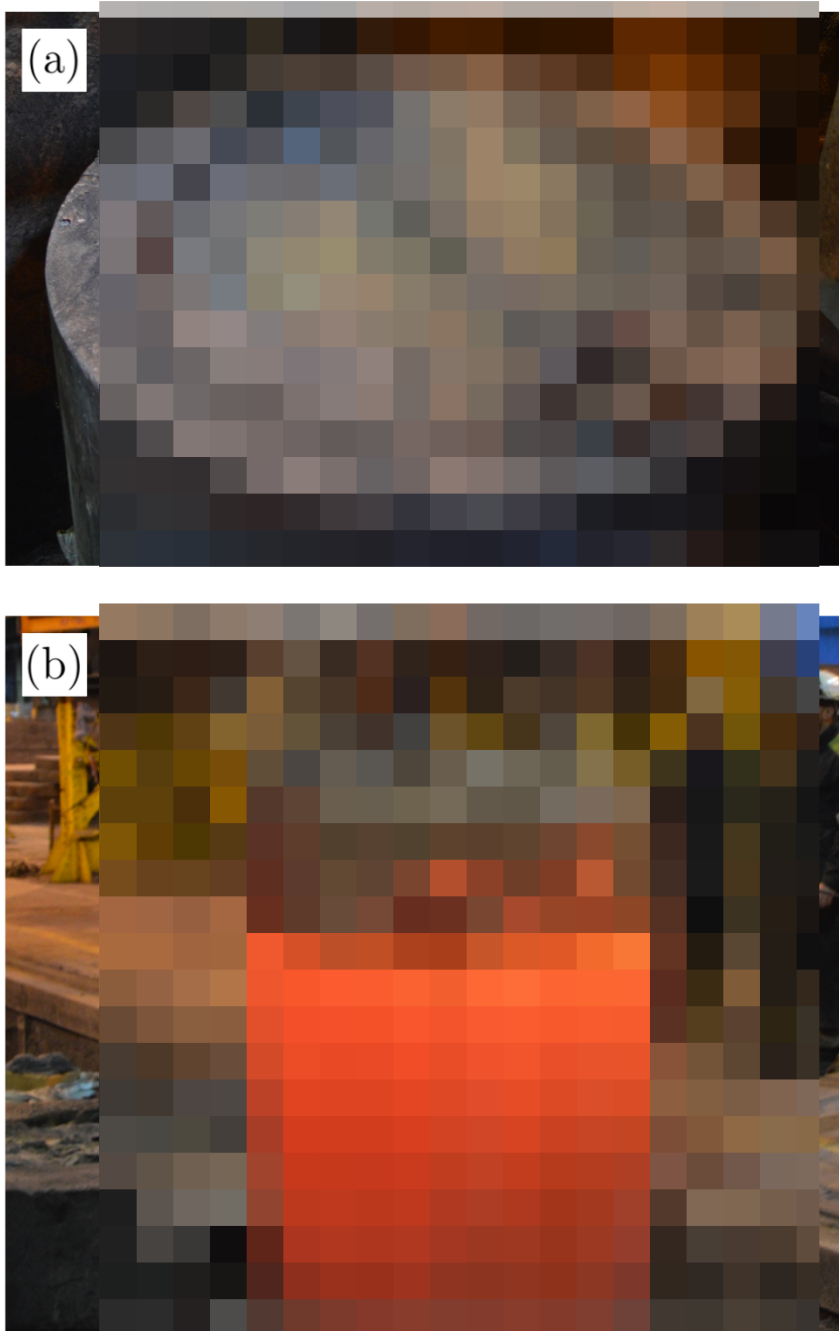


Figure 8.6: Photographs of (a) the ingot before stripping, in which the exothermic powder has cooled and a shrinkage gap formed, and (b) ingot stripping. IMAGES HAVE BEEN PIXELATED - COMMERCIALY SENSITIVE.

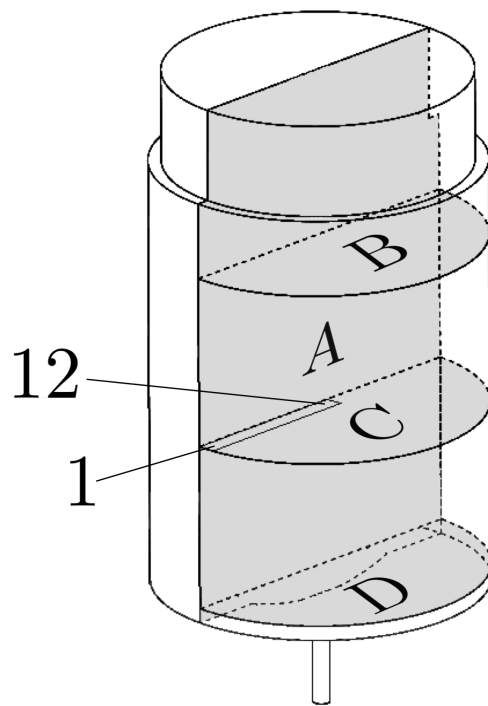


Figure 8.7: Schematic of ingot sectioning to reveal four faces, A-D. Also labelled is the radial strip in Face C, which was used for microstructural examination. Flutes on the outside have been removed.

Table 8.3: The stress-relief heat treatment used for the ingot.

Stage details	Duration /min
1. Equalisation at 400 °C	900
2. Heat 400 °C to 650 °C @ 20 °C h ⁻¹	750
3. Hold at 650 °C	900
4. Cool 650 °C to 600 °C @ 6 °C h ⁻¹	500
5. Cool 600 °C to 500 °C @ 8 °C h ⁻¹	750
6. Cool 500 °C to 400 °C @ 10 °C h ⁻¹	600
7. Cool 400 °C to 240 °C @ 12 °C h ⁻¹	800
8. Cooled in furnace (off) to room temperature	-

B, C and D were then all macroetched in 10% aqueous nitric acid. A radial slice of Face C was subsequently sectioned, metallographically prepared and etched in 2% nital to reveal variations in microstructure. Optical micrographs were taken using a stereo microscope, whilst secondary-electron imaging and EDX analyses were carried out with a CamScan MX2600 FEG-SEM.

8.3 Results

8.3.1 Thermal Data

Temperature profiles for all the thermocouples used are shown in Figs. 8.8 and Figs. 8.9. There is good agreement between the two sets of thermocouples placed down the outside of the mould (TC5-9 and TC10-14). Of the thermocouples placed between the mould and tiles, TC1 displays a very different profile to TC2-4. At the point indicated with an arrow in Fig. 8.8, TC1 broke free from its position and fell to the floor, which appears to have disturbed TC2. The sudden change in temperature measured after 25,000 s for TC17 was due to its removal during ingot stripping. Thermal images of the mould after 2500, 10,000 and 25,000 s are shown in Fig. 8.10. A comparison of these results to the thermocouple results suggests (assuming the thermocouple results are accurate) that the

Table 8.4: Estimations of the expansion (or shrinkage) of the mould and ingot, and shrinkage gap magnitude. The positions refer to those indicated in Fig. 8.13b.

Position	Shrinkage gap /mm
1	13.38 ± 0.15
2	14.27 ± 0.93
3	14.80 ± 0.75

emissivity used for calibration of the thermal imaging camera (0.8) was too low - the temperatures measured by the thermal imaging camera were consistently higher than the thermocouple readings (the discrepancy rose with temperature, and was $\approx 25^\circ\text{C}$ at 540°C), and should only be used qualitatively.

A thermal image of the ingot taken immediately following its removal from the mould is shown in Figure 8.11. An approximate temperature variation from $\approx 850^\circ\text{C}$ at base of the head (just below the tiles, at the top of the chill) to $\approx 500^\circ\text{C}$ at the very bottom of the ingot is observed. It should be noted, however, that again an emissivity of 0.8 was used for the acquisition of this data, which could have introduced a systematic error as described above.

8.3.2 Dimensional Data

The dimensions of the ingot were measured using laser scanning after cooling to room temperature ($\approx 15^\circ\text{C}$) following heat treatment, Fig. 8.12, as were the dimensions of the mould. This allowed for an estimation of the shrinkage gap to be made, see Fig. 8.13 and Table 8.4. Note that a more appropriate measurement of the shrinkage gap would have been that measured immediately after stripping, but it is hoped that this can provide a suitable starting point for estimations.

8.3.3 Porosity

Figs. 8.14 and 8.15 show the porosity observed in Faces A, B, C and D of the ingot. It is evident that very little porosity is observed in the head and the base, but that it is prevalent in the mid section, where it forms chevrons which branch

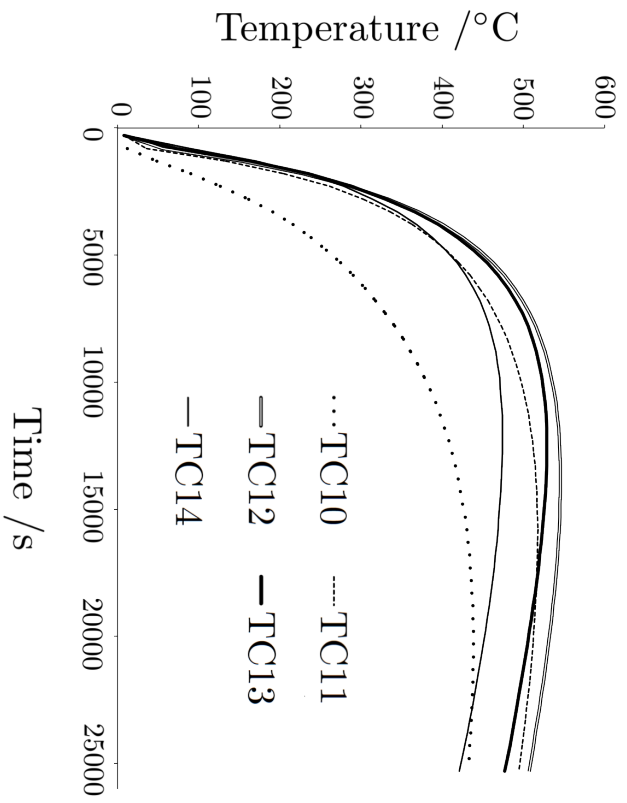
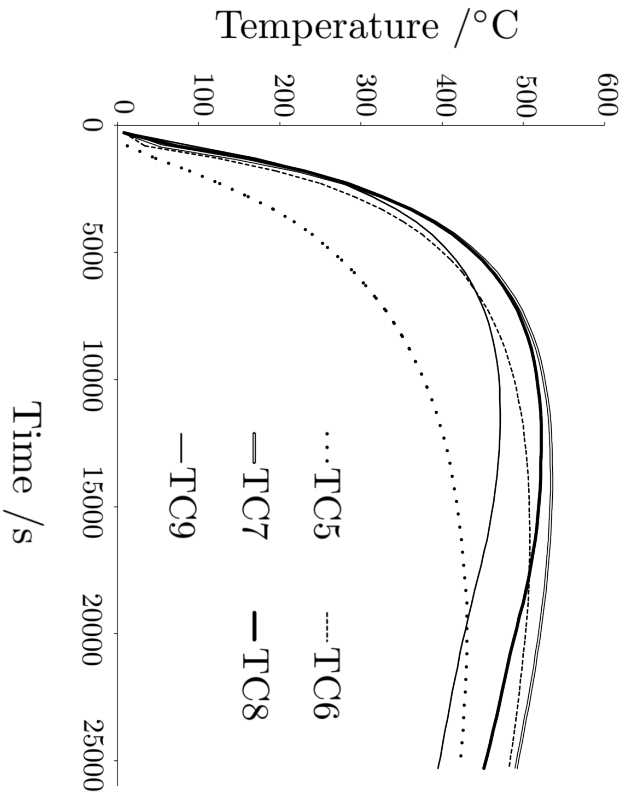


Figure 8.8: A comparison of thermocouple temperature readings for TC5-9 and TC10-14.

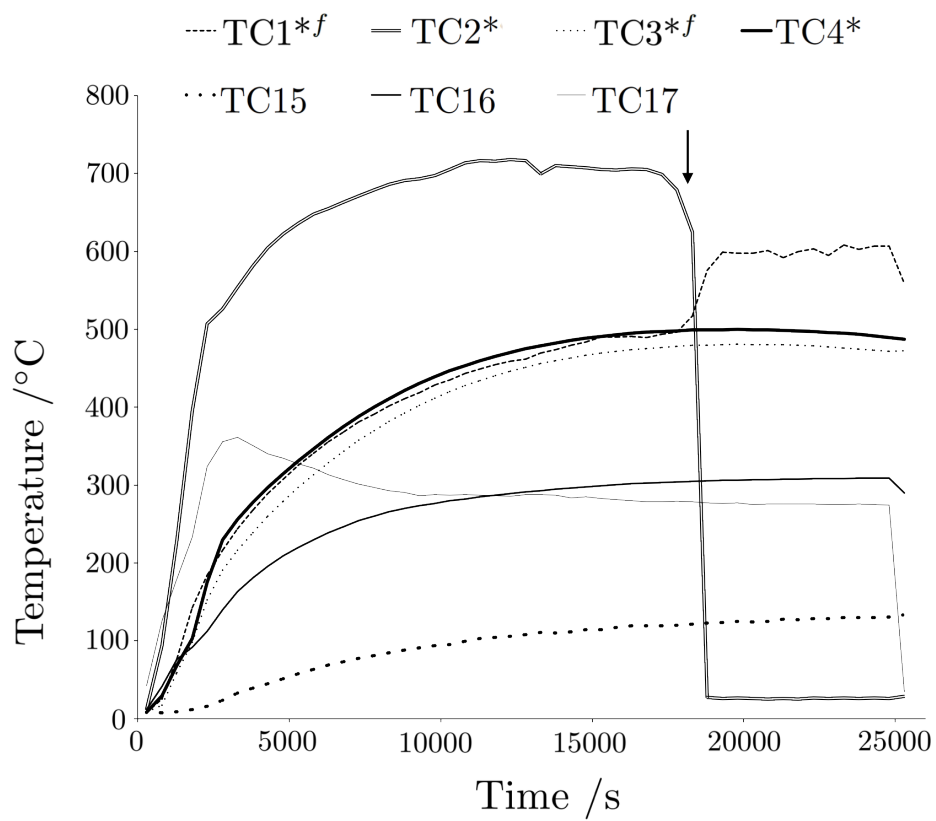


Figure 8.9: Thermocouple temperature readings TC1-4 and TC15-17.

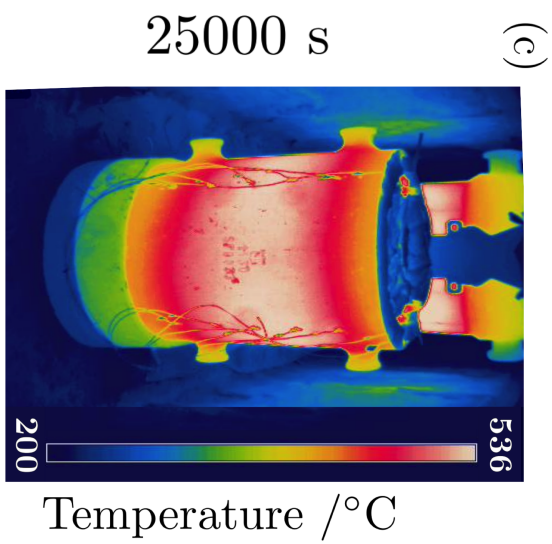
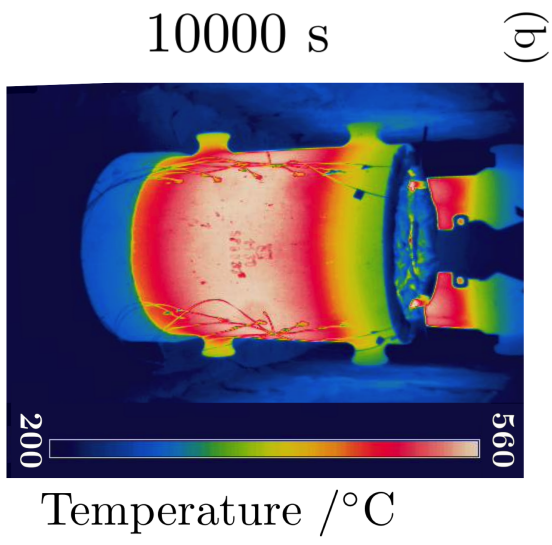
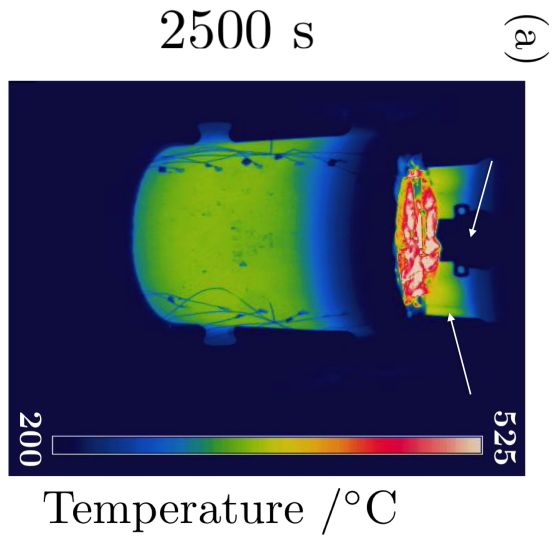


Figure 8.10: Thermal images of ingot casting at 2,500, 10,000 and 25,000 seconds.

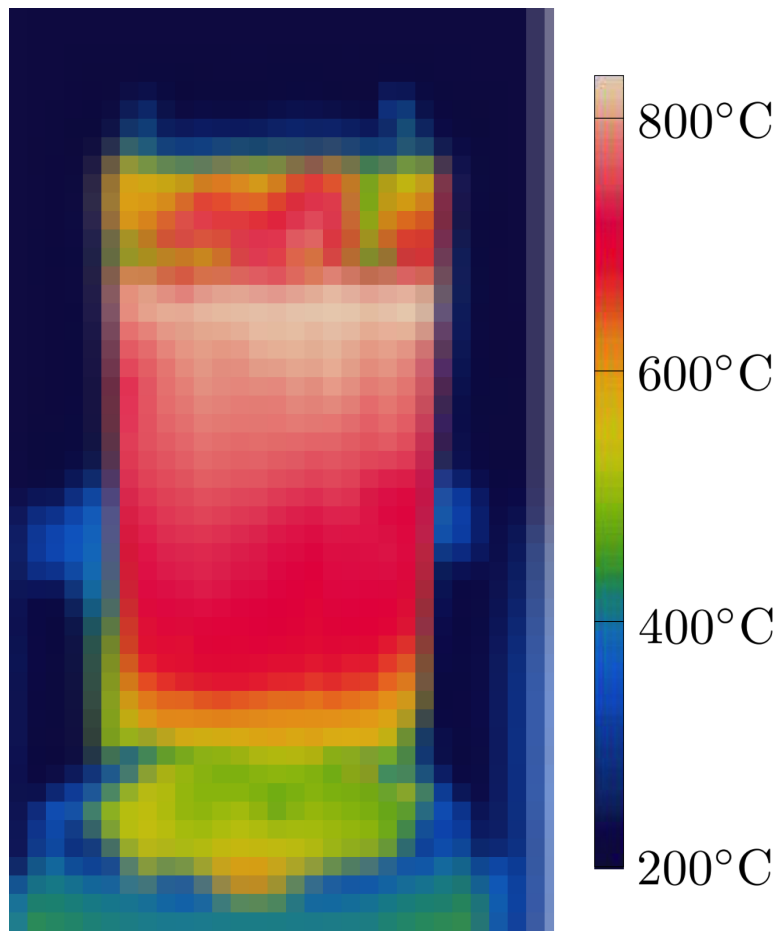


Figure 8.11: The temperature distribution on the outside of the ingot, immediately following its removal from the mould. IMAGE HAS BEEN PIXELATED - COMMERCIALY SENSITIVE.

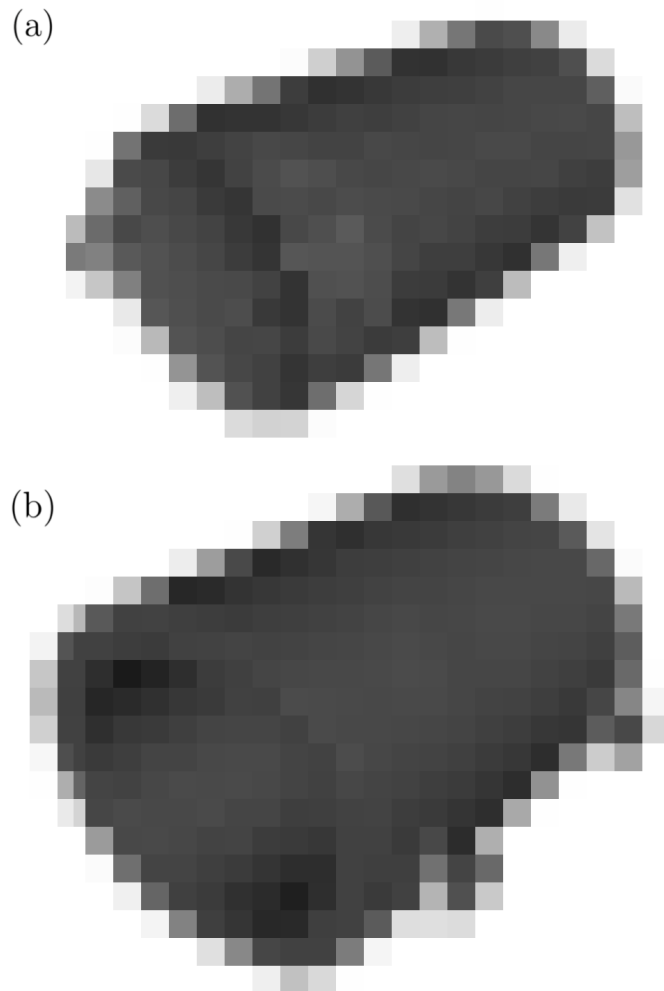


Figure 8.12: Laser scanning data of (a) the ingot and (b) the mould (both at $\approx 15^\circ\text{C}$). IMAGES HAVE BEEN PIXELATED - COMMERCIALY SENSITIVE.

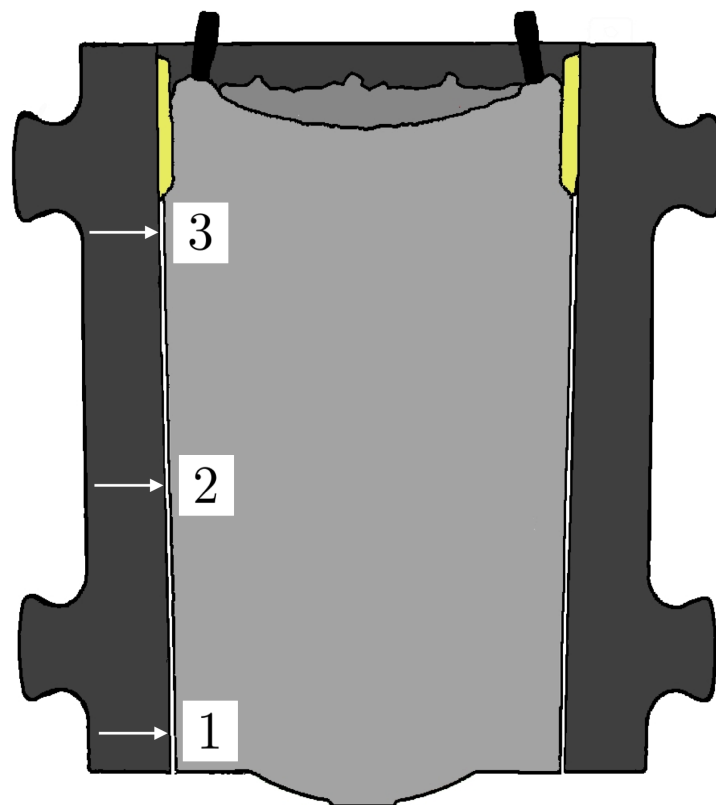


Figure 8.13: Illustration of the as-cast ingot sitting inside the mould, created using laser-measured dimensional data (hence, the shape of the components, as well as the size of the shrinkage gap, are real). The shrinkage gap was measured at points 1-3 indicated, see Table 8.4.

out from the middle to the base of the ingot. Smaller strings of porosity were also observed to lie along channels with near-vertical alignment, further from the centre of the ingot, which did extend further towards the top of the ingot, see highlighted areas in Face B.

8.3.4 Macrosegregation Measurements

The results of the macro-scale XRF measurements are presented in Figs. 8.16 and 8.17 for Cr and Mo, respectively. Each map comprises over 71,000 datapoints. The presence of A-segregates strings, as well as top-bottom and centreline segregation patterns, is clearly demonstrated. A cone of negative segregation at the base of the ingot is also observed, and the material surrounding A-segregates is likewise depleted in solute relative to the edges of the ingot. Maps for Mn and Ni are not presented here due to the excessive noise found in their results - this is almost certainly due to their relatively low concentrations and the intensity of the background around their K_{α} peaks (the background was essentially zero at the Mo K_{α} energy), as discussed in Chapter 7.

Fig. 8.18 shows an overlay of measured porosity on measured macrosegregation in a mid section of the ingot. This demonstrates that the strings of porosity observed at higher radii are associated with A-segregate channels.

8.3.5 Macrostructure

The results of macroetching Faces A-D are shown in Figs. 8.19 to 8.25. First, it must be stressed that the macroetching procedure introduced artefacts into the appearance of the etched slices that should not be confused with structural features. De-smutting of the etching surfaces has led to streaking: in a vertical direction in Fig. 8.19, and vertically and circumferentially in Figs. 8.23 to 8.25. Streaking on a similar scale was also introduced by uneven lacquering of the surfaces following etching (the slices had to be quickly protected from the environment, and were to be stored outside after etching). No particular features of the ingot were observed on the length scale of the streaking due to de-smutting or lacquering; the etching revealed no marked large-scale trends radially or along

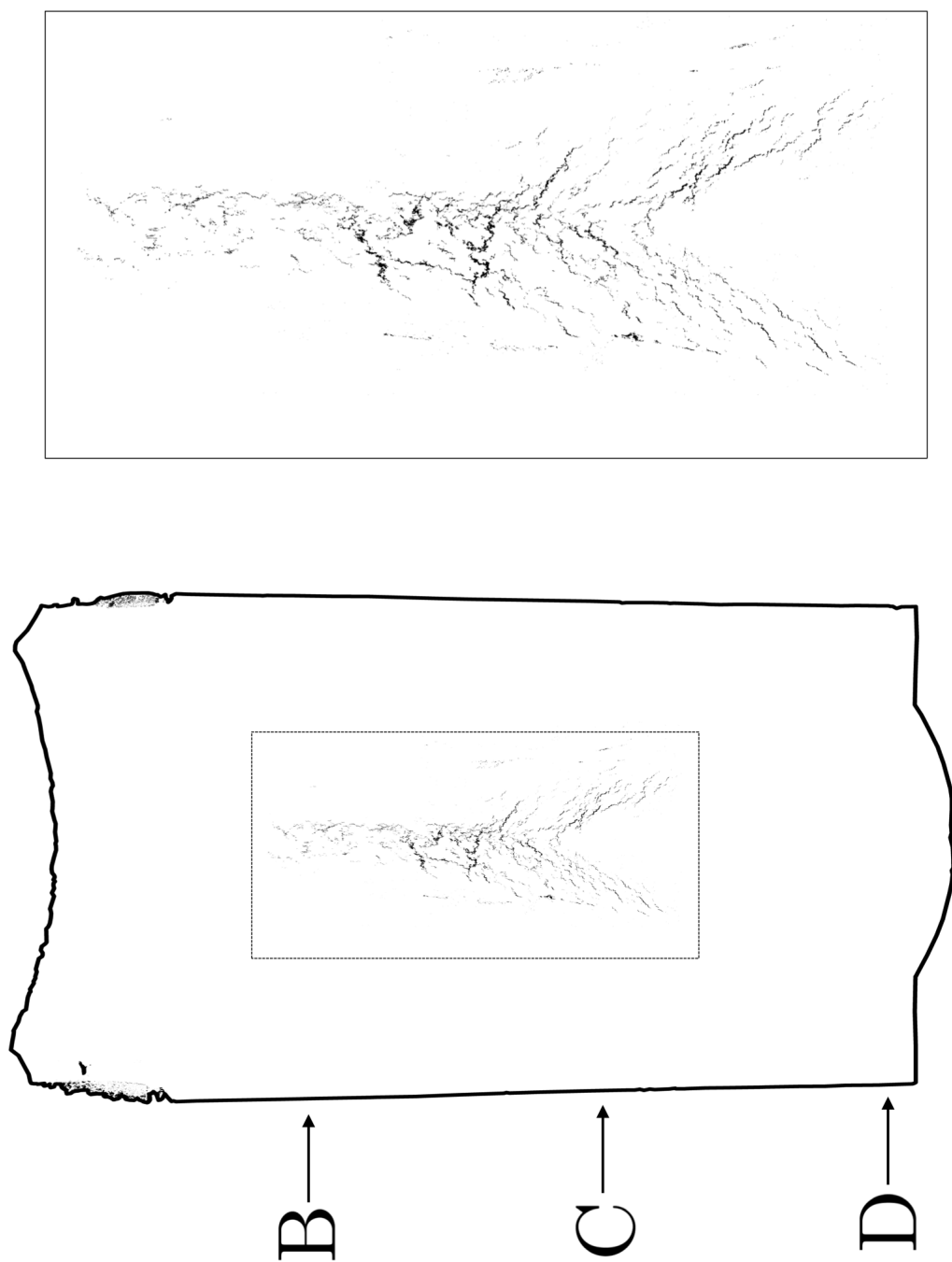


Figure 8.14: The porosity present in Face A. The placement of faces B, C and D is indicated; the porosity present in these faces is shown in Fig. 8.15. IMAGES HAVE BEEN PIXELATED - COMMERCIALY SENSITIVE.

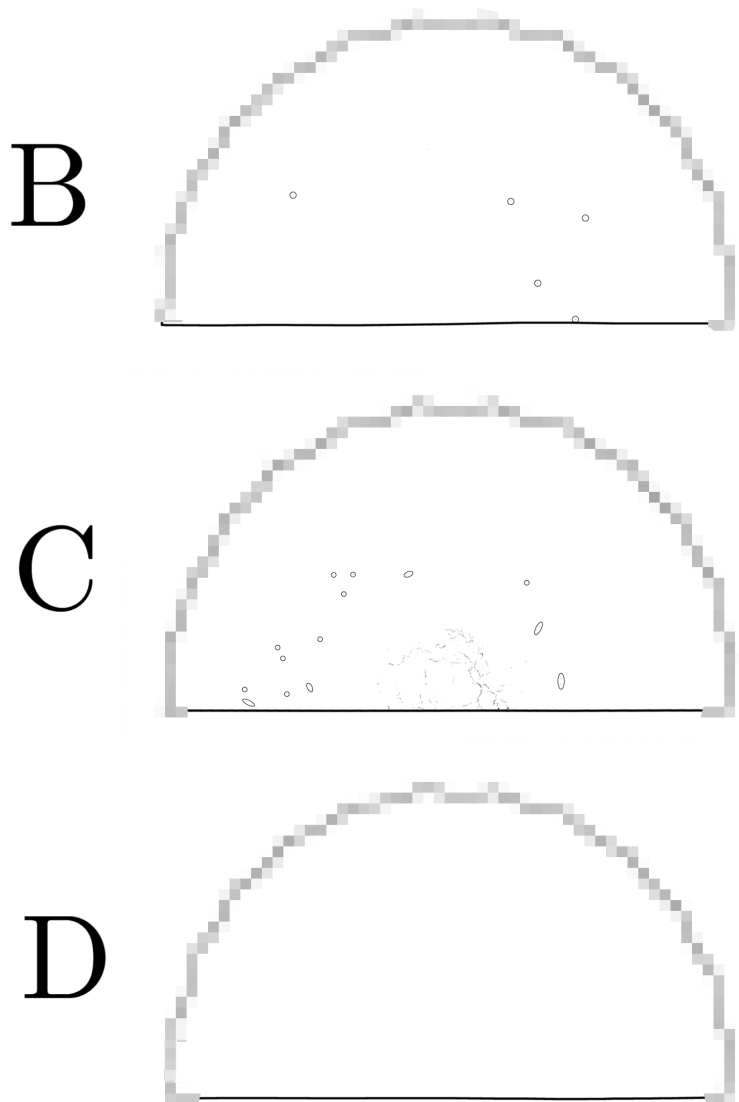


Figure 8.15: The porosity present in Faces B-D. Small areas of porosity, not easily visible at the image size printed, are outlined.

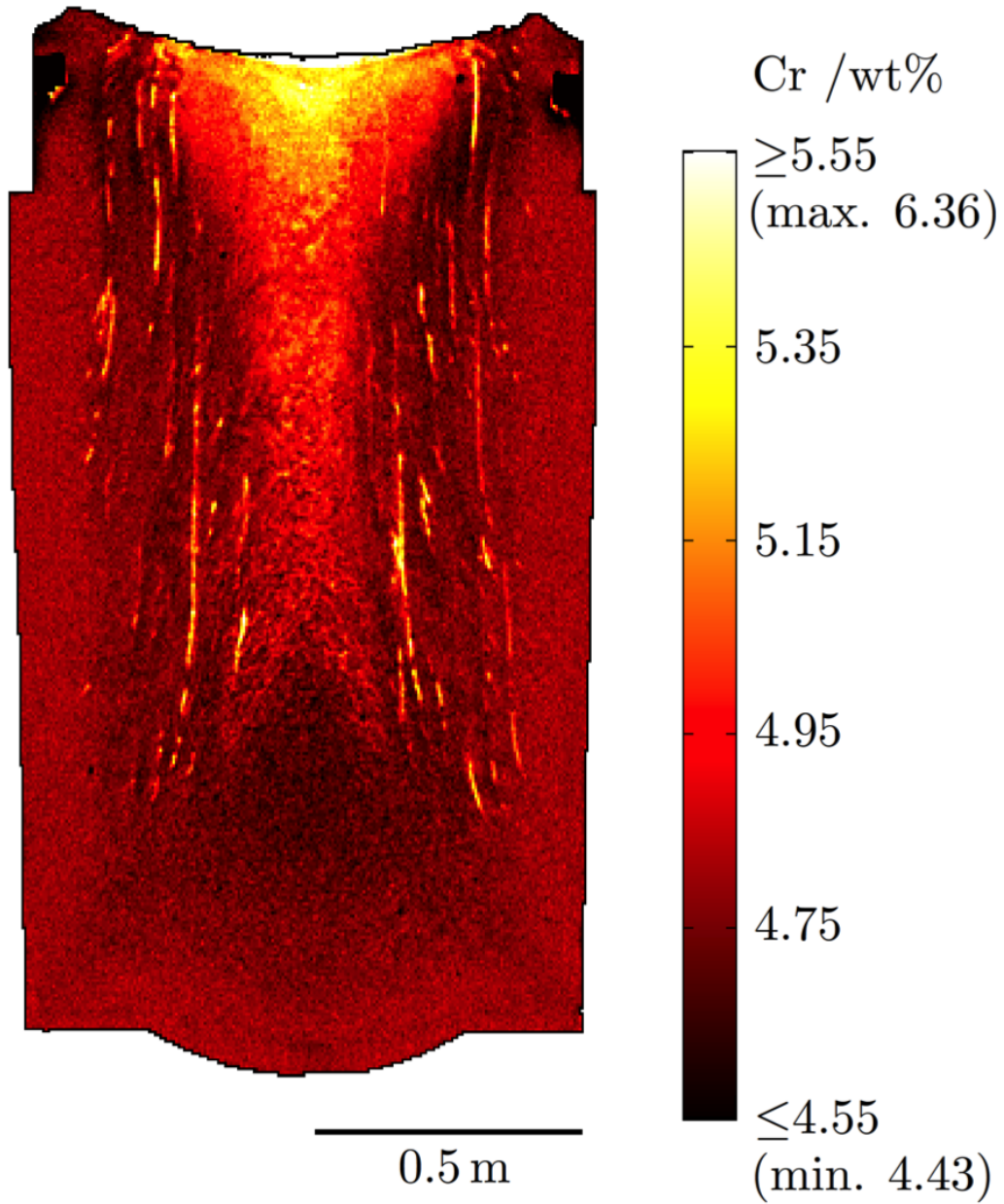


Figure 8.16: XRF map for Cr.

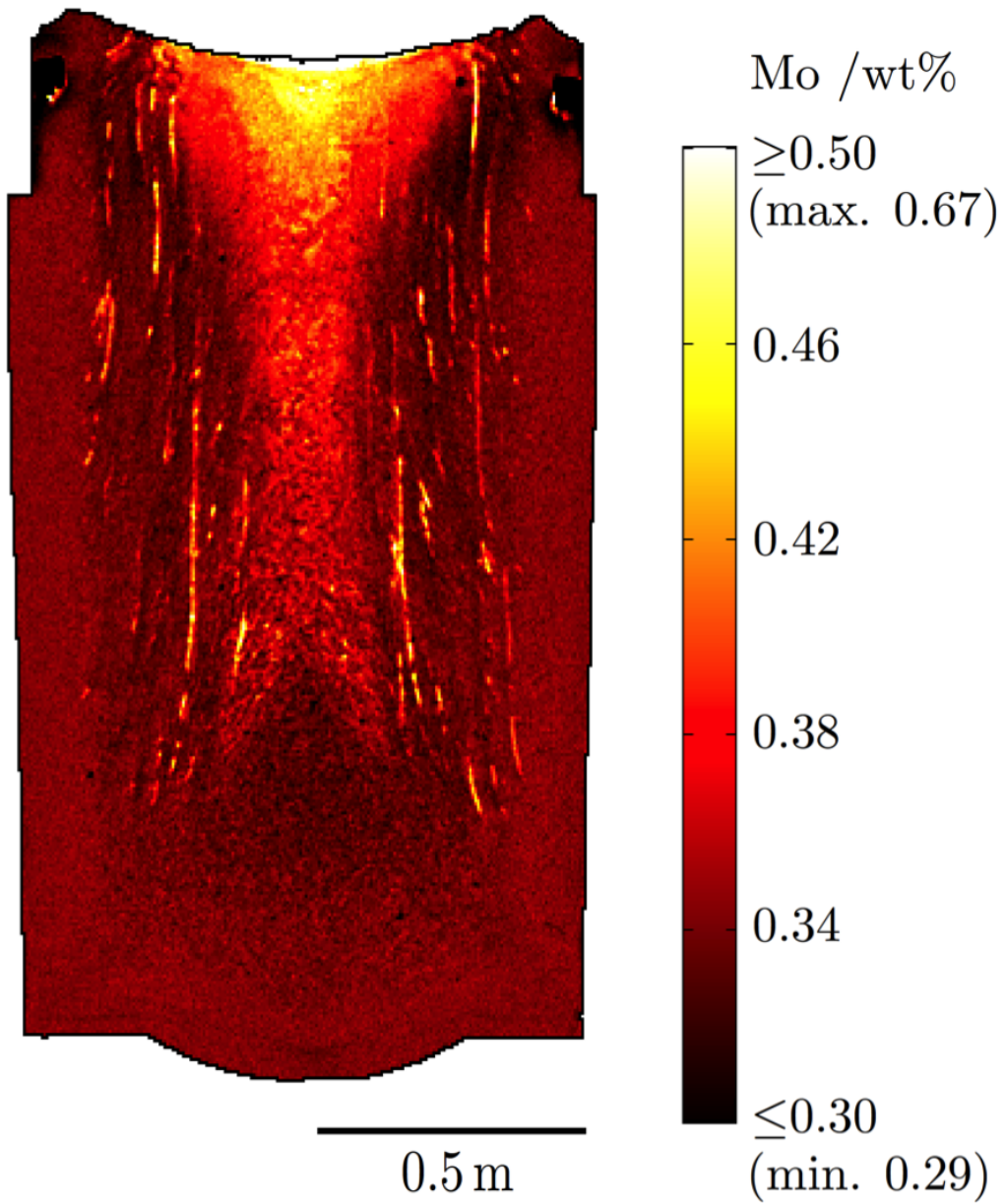


Figure 8.17: XRF map for Mo.

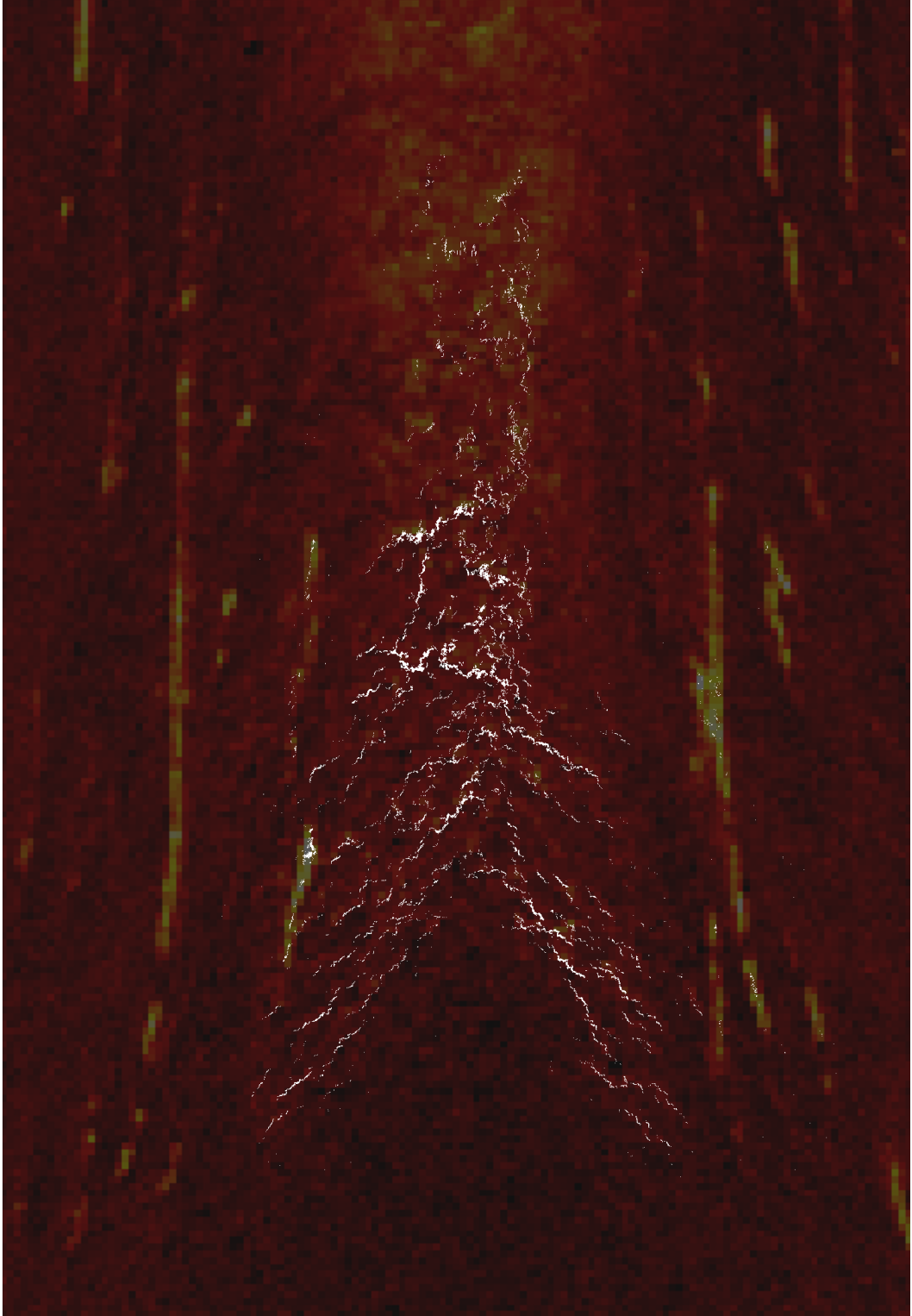


Figure 8.18: An overlay of maps for porosity and segregation.

the axis of the ingot.

In a number of areas at the edge of the ingot, macroetching revealed structures that appeared to be columnar-like in morphology, Figs. 8.21 and 8.22. These structures protruded into the ingot for ≈ 100 mm, after which a second growth morphology was observed. This new morphology, which was predominant throughout the bulk of the ingot, consisted of well-defined grains with boundaries that etched to give a lighter colour than their interiors, see Fig. 8.20 for example. The shape of these grains appeared to be relatively equiaxed, although there was some indication of elongation along the radial direction, see the fine structure of Figs. 8.23 and Fig. 8.24. At the base of the ingot above the columnar zone (box iv in Fig. 8.19), the grain structure appeared finer and was not readily discernable at the macroscopic scale.

8.3.6 Microstructure

Microstructural analysis was performed on the radial strip highlighted in Fig. 8.24, which was sectioned into 12 pieces. The variation in dendritic structure along this strip is shown in Fig. 8.26, looking along the axial direction. It is clear that the dendrite arm spacing is finer near the wall and increases as the cooling rate decreases towards the centre of the ingot, although the change is most pronounced close to the mould (and spacings appear to plateau in the mid thickness). By over-etching these samples, the grains generated by these dendrites could be observed as in Fig. 8.20. The result of outlining these grains by hand is presented in Fig. 8.27. Despite the subjectivity of this assessment, when taken together with the other macrostructure and microstructure results they present clear evidence that the grains in much of the ingot were not consistently orientated or elongated. Viewing tangentially, the only samples in which differences were found (when compared to viewing axially) were samples 1-3, in which a columnar structure could be readily discerned, Figs. 8.28a-c. These columnar dendrites ceased in sample 3 (after ≈ 100 mm), and the near-equiaxed morphology predominated from then onwards. The strings of porosity present in the ingot appeared to follow the boundaries between equiaxed grains.

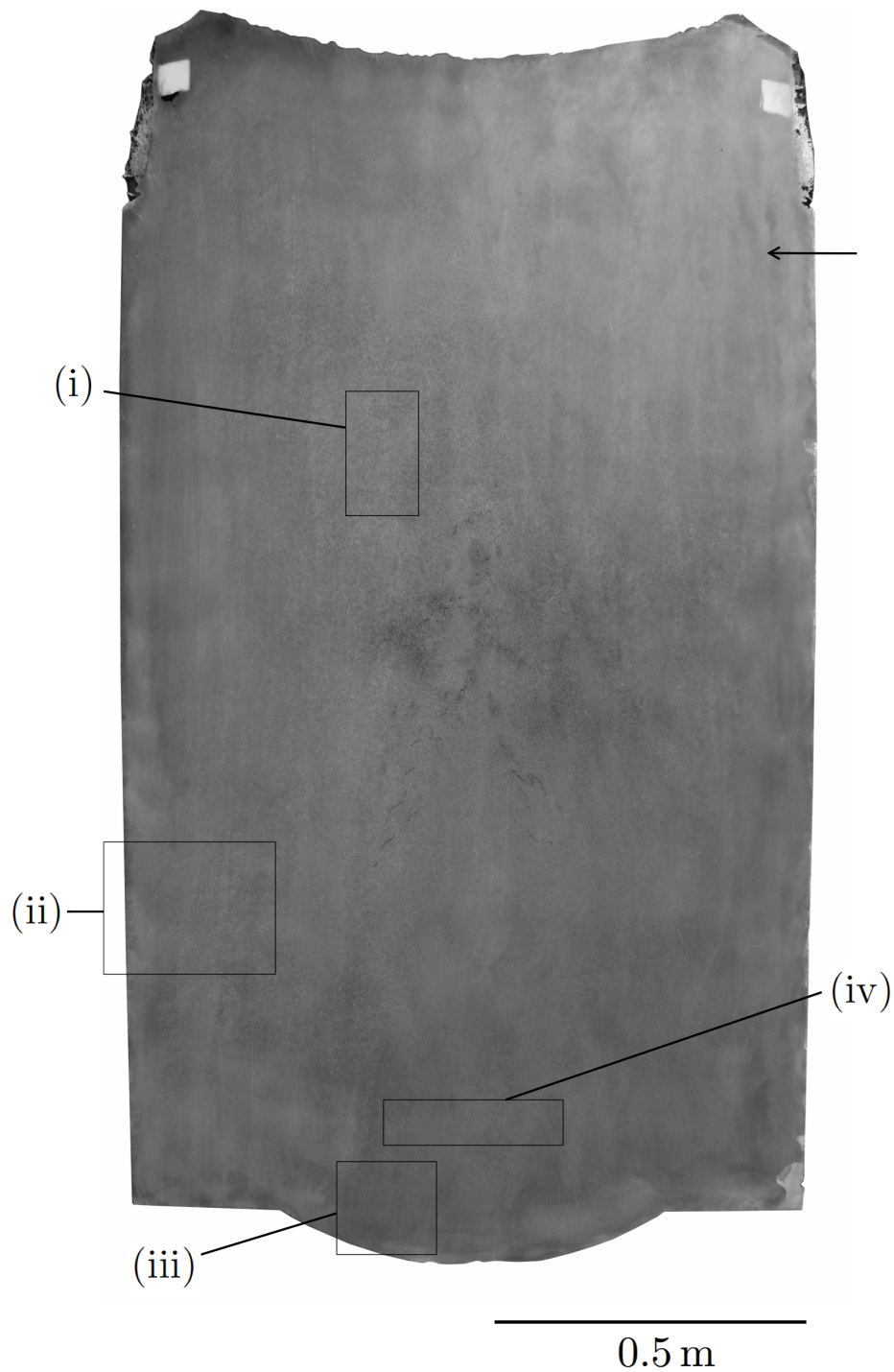


Figure 8.19: Face A in the macroetched state. Note that the vertical streaks, as arrowed, are associated with de-smutting and lacquering, not any structural features (like A-segregates, etc). The areas highlighted with boxes i-iii are shown in Figs. 8.20-8.22, respectively.

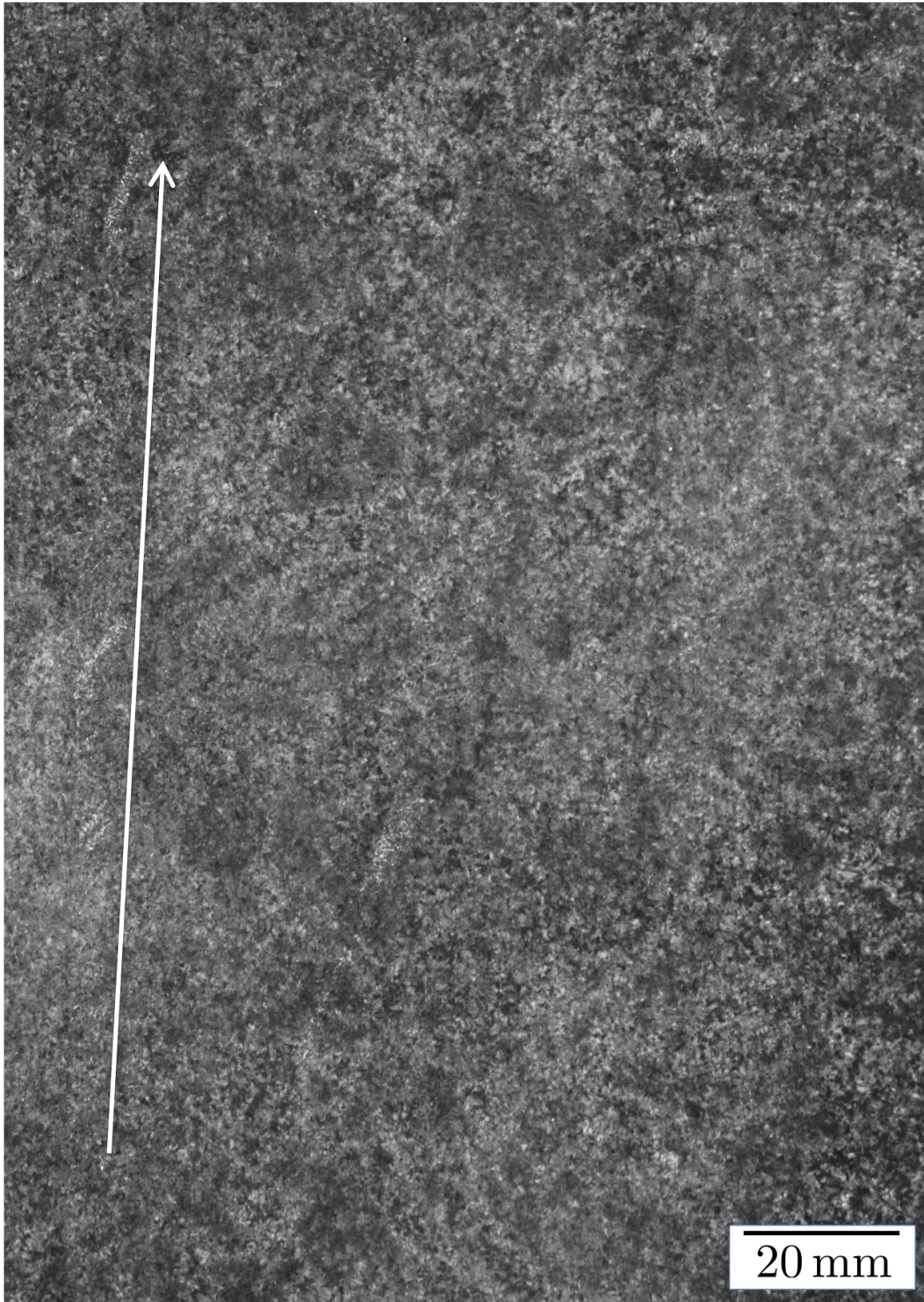


Figure 8.20: Area of Face A labelled (i). An A-segregate channel can be seen running vertically, to the left of the white arrow.



Figure 8.21: Area of Face A labelled (ii). Columnar dendritic formations can be seen protruding in from the left-hand edge at an upwards angle to the horizontal. They appear to stop after growing ≈ 12 cm into the ingot.



Figure 8.22: Area of Face A labelled (iii), found at the base of the ingot. Columnar dendritic formations appear to have grown from the bottom edge for ≈ 12 cm.

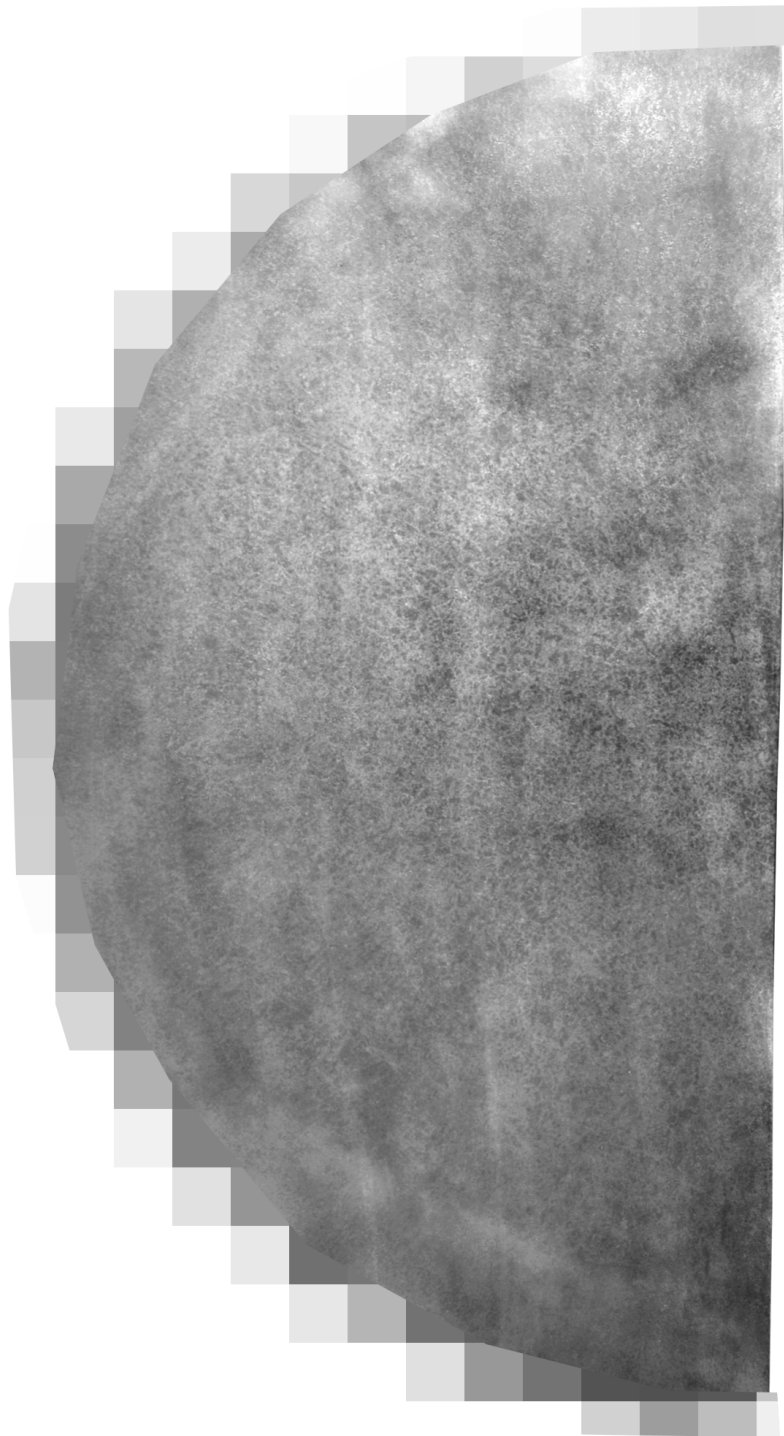


Figure 8.23: Face B in the macroetched state. Note that vertical and circumferential streaks are associated with de-smutting and lacquering, not any structural features. IMAGE HAS BEEN PIXELATED - COMMERCIALY SENSITIVE.

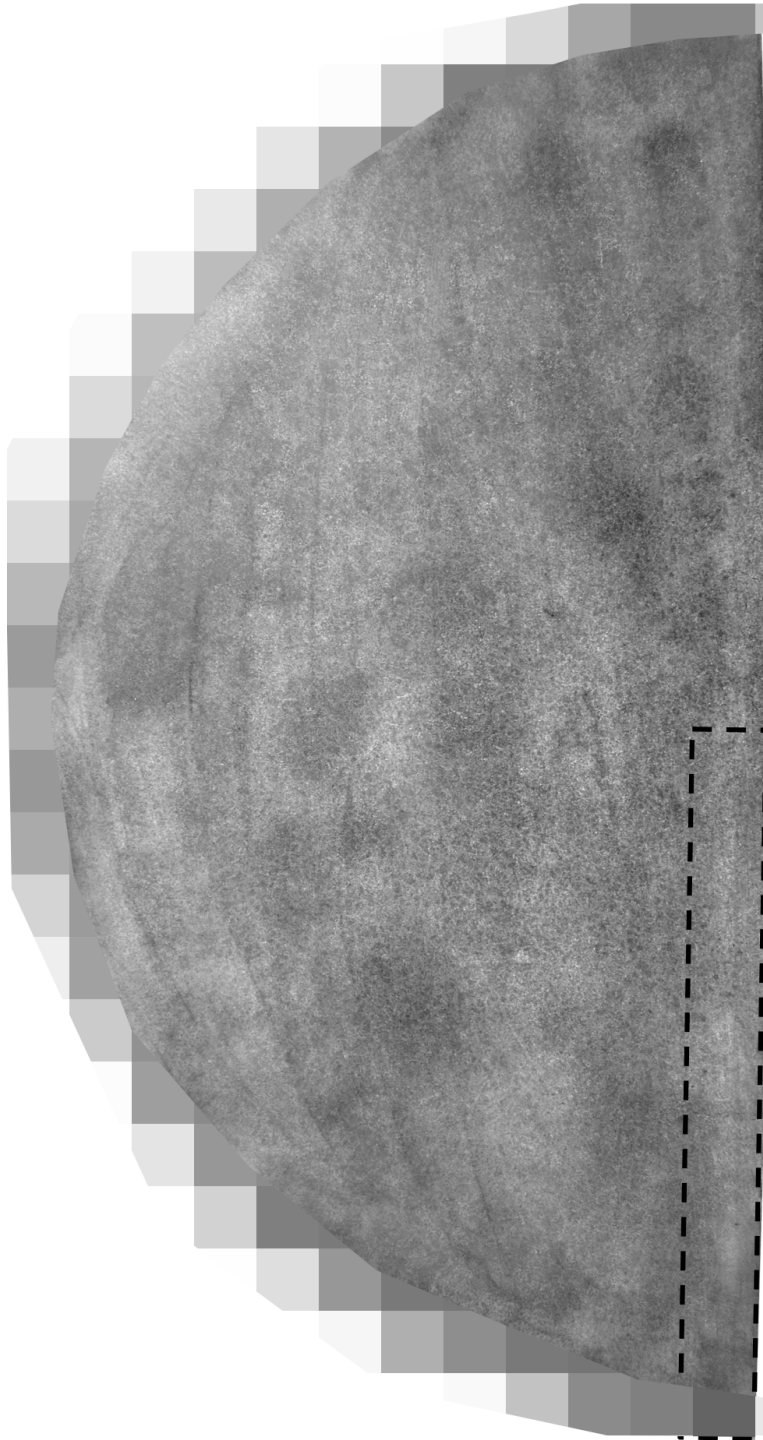


Figure 8.24: Face C in the macroetched state. Note that vertical and circumferential streaks are associated with de-smutting and lacquering, not any structural features. The radial strip taken for microstructural examination is highlighted. IMAGE HAS BEEN PIXELATED - COMMERCIAL SENSITIVE.

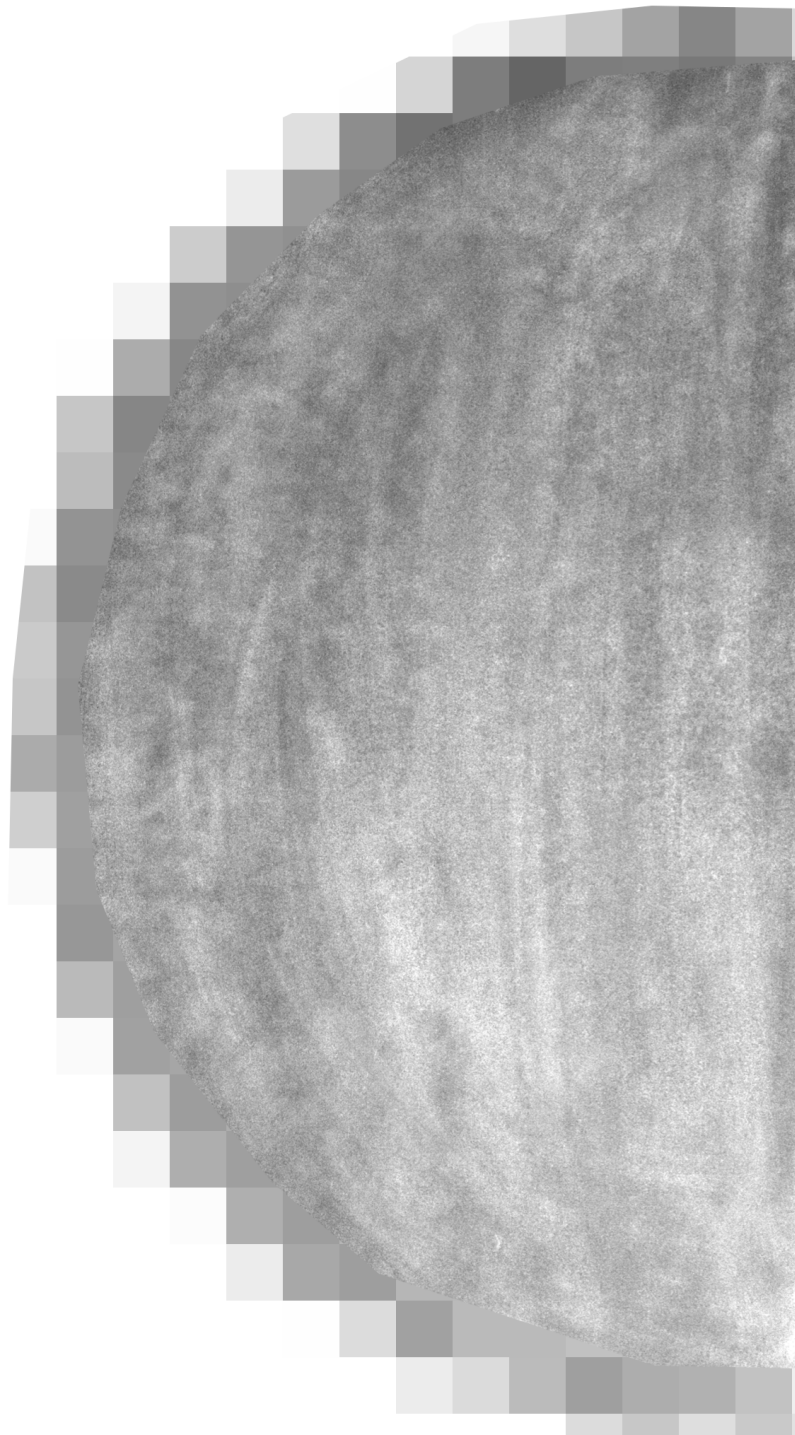


Figure 8.25: Face D in the macroetched state. Note that vertical and circumferential streaks are associated with de-smutting and lacquering, not any structural features. Macroetching this slice did not reveal many features of interest. IMAGE HAS BEEN PIXELATED - COMMERCIALY SENSITIVE.

Analysis of the structure of the ingot at its base (above the columnar zone, box (iv) in Fig. 8.19, examined by sectioning Face D), again revealed a near-equiaxed structure, with grain size and distribution similar to samples 10-12 in Fig. 8.27, see Fig. 8.28d. The boundaries of these grains were not as easily discernable as for the material in Face C.

8.3.7 A-segregates

A-segregate channels were visible in all the faces after etching as channels of material rich in a silver-coloured phase not attacked by the etchant, Fig. 8.29, but the contrast was such that they were not clearly discernable in macroshots of the slices. Channels were found in Face A at the locations measured using XRF, and were all ≈ 5 mm in diameter. The ‘silvery’ phase appeared to have formed in interdendritic regions, Fig. 8.30 and Fig. 8.31a. Flecks of this ‘silvery’ phase were found throughout the ingot in lower concentrations, but were sparse at the base of the ingot and increased in number towards the enriched top and centre (see the radial variation in Fig. 8.26). The amount of silvery phase in the channels was not always consistent along channel lengths and strings appeared to be interrupted, Figs. 8.20 and 8.29.

Closer examination of the silvery phase under the SEM revealed it to comprise many fine Cr-rich carbides, Figs. 8.31b-c. JMatPro and MTDATA calculations suggest that this carbide is likely to be $(\text{Fe,Cr})_7\text{C}_3$, although this has not been confirmed experimentally.

8.4 Discussion

It is evident that the ingot cast, sectioned and analysed here displays all of the classical macrosegregation defects that might be expected in a large steel ingot, apart from V-segregation. Nevertheless, their presence (or absence) is not explained easily given the context of the results presented, and some careful deliberation is needed.

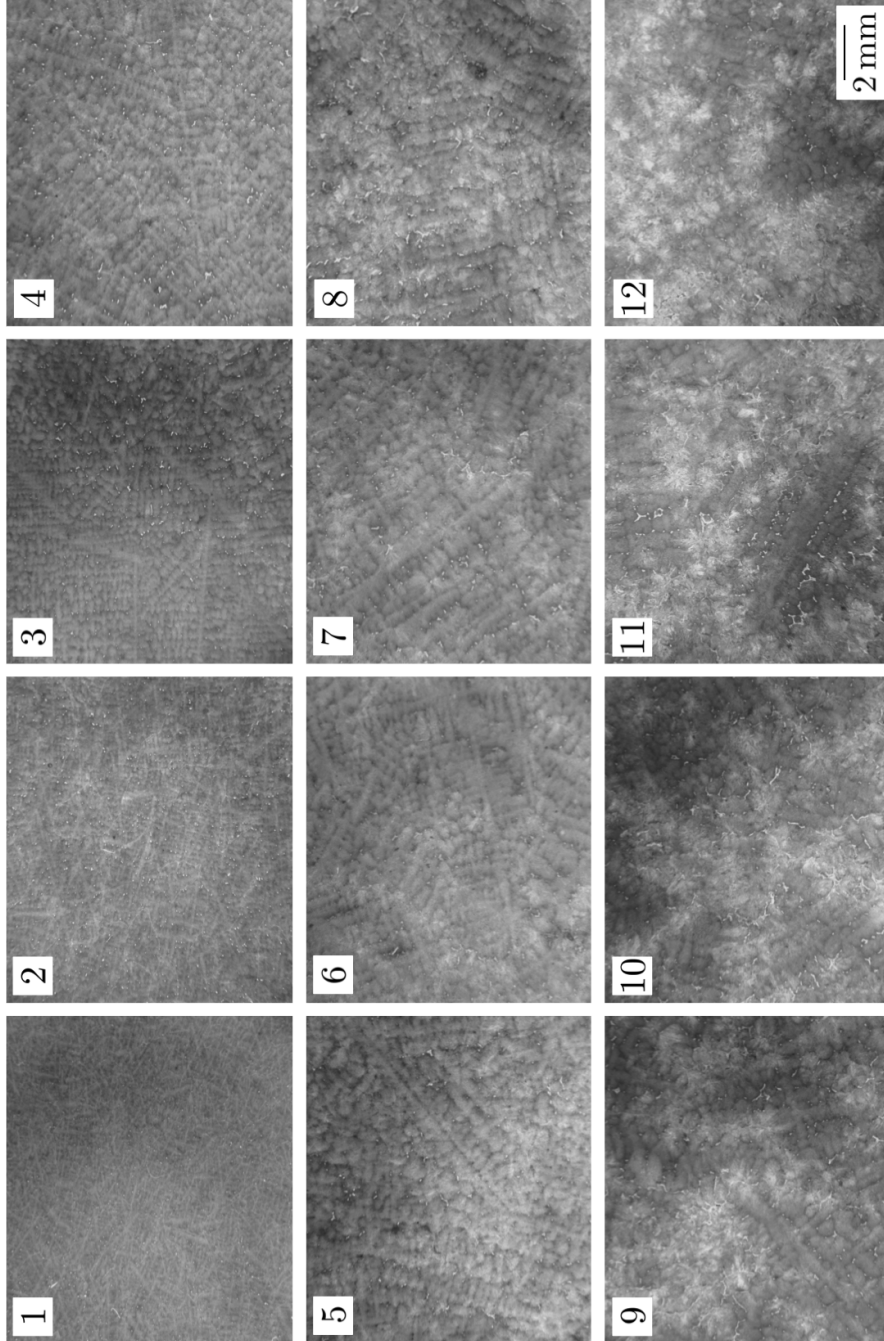


Figure 8.26: The variation in dendritic structure of the ingot along a radial section of Face C, viewing along the axial direction. Sample 1 was positioned at the outer edge of the ingot and sample 12 directly adjacent to the centre.

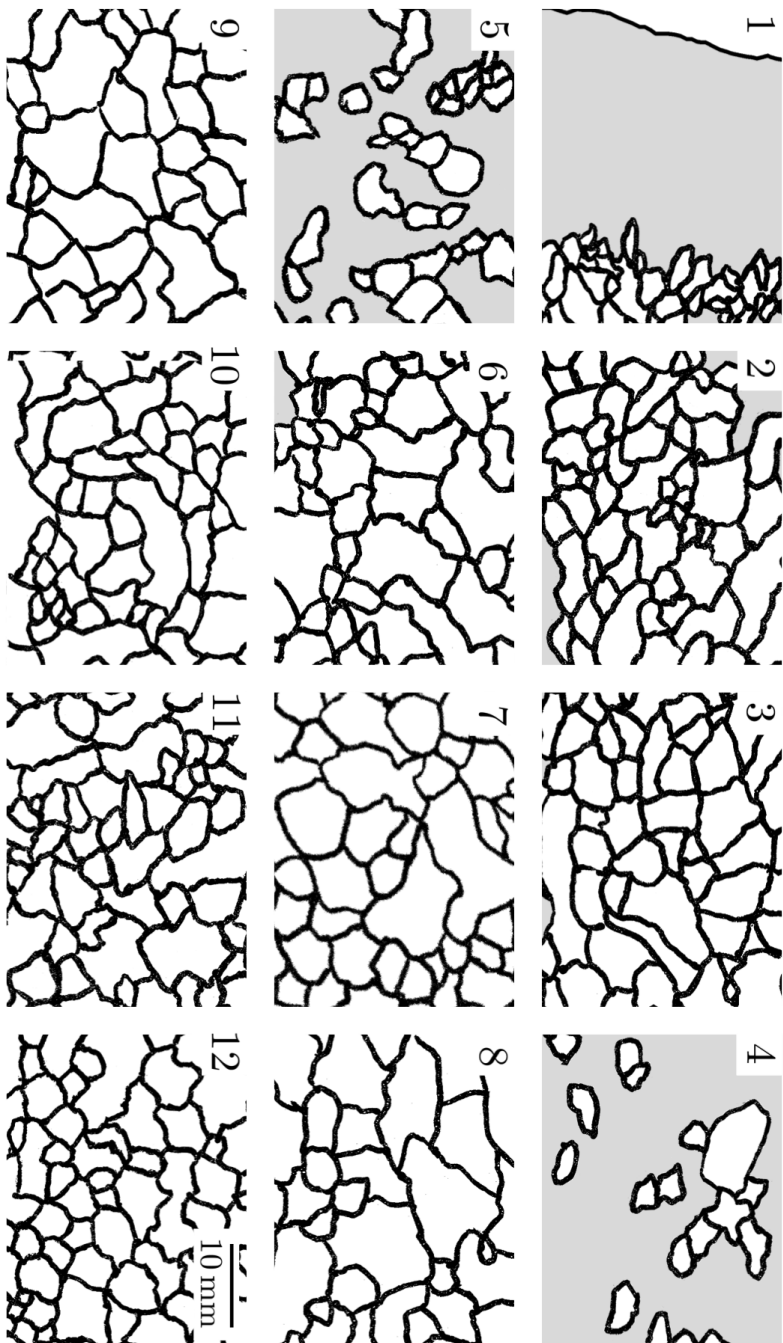


Figure 8.27: The grain structure of the ingot along a radial section of Face C, viewing along the axial direction. Grains were identified by overetching and outlining by hand. Areas where this could not be achieved are shaded grey.

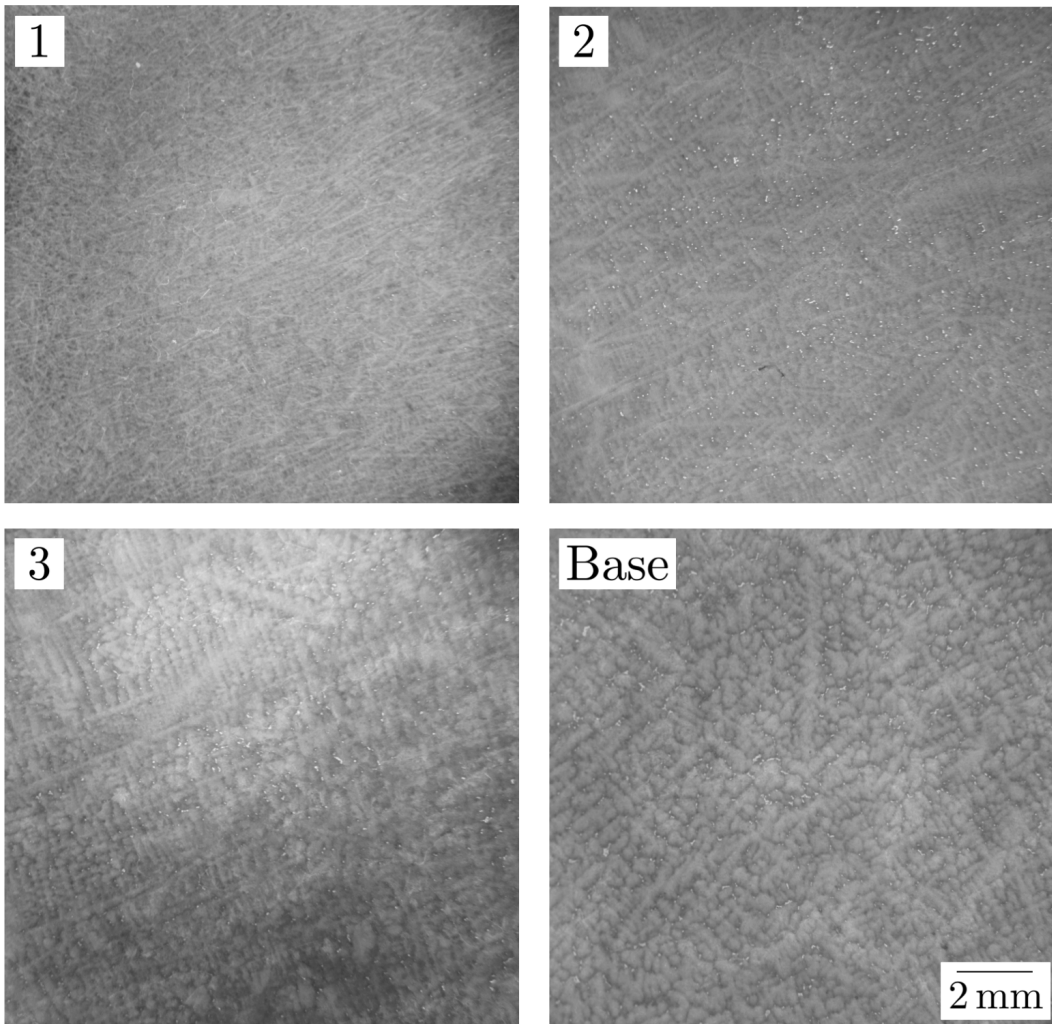


Figure 8.28: (a)-(c) The columnar dendrites in samples 1-3, respectively, when viewing tangentially. They are angled away from the horizontal, towards the top of the ingot. Note that in (c) the beginning of a transition to a near-equiaxed morphology is observed. (d) The dendritic structure in the negatively-segregated cone at the base of the ingot, at height of Face D.



Figure 8.29: A-segregate strings, present towards the bottom of the ingot. The channels were ≈ 5 mm in diameter.

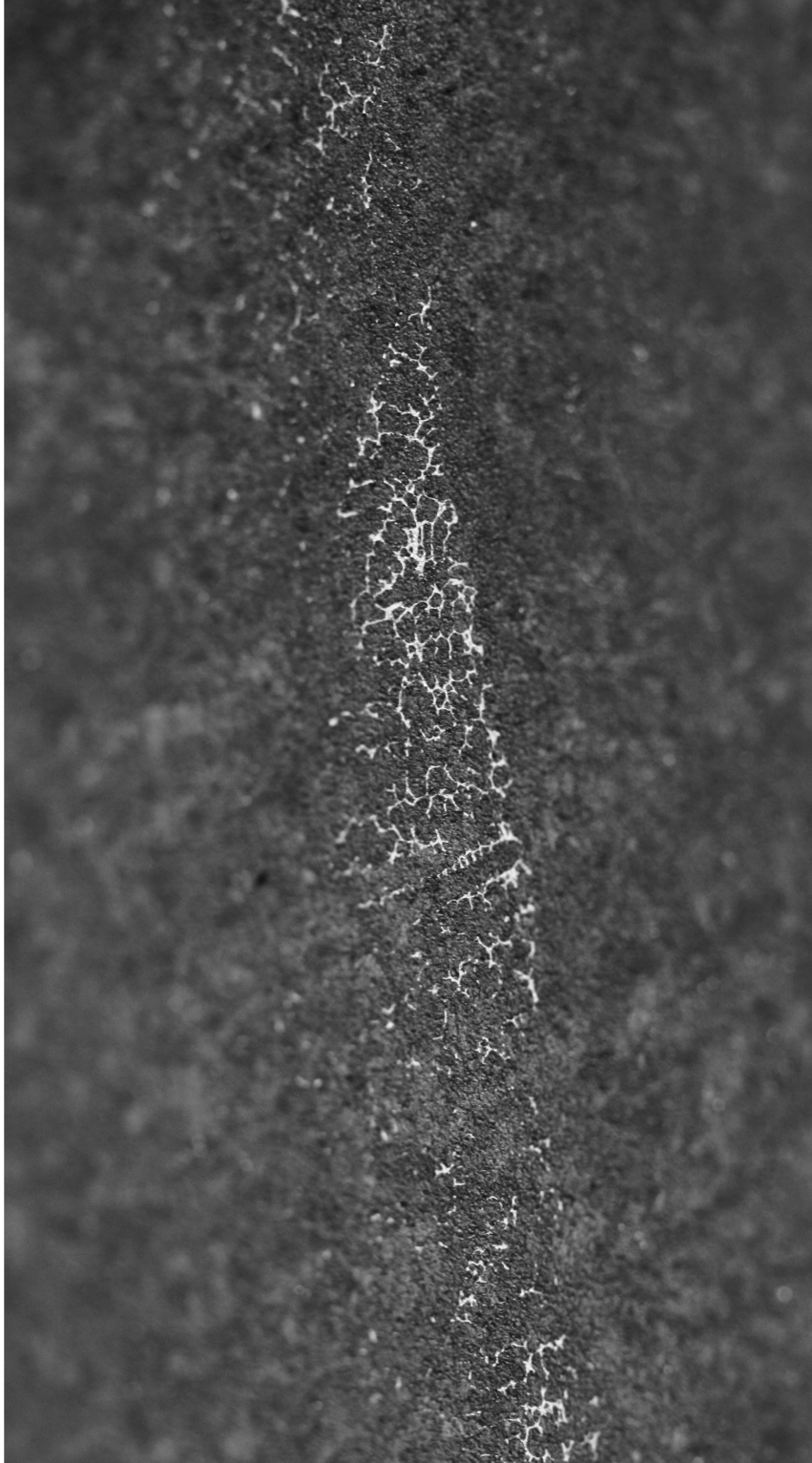


Figure 8.30: A close-up photograph of an A-segregate channel (≈ 5 mm diameter), taken at a non-perpendicular angle to the surface. A silvery phase has precipitated in the interdendritic regions of fine dendrites.

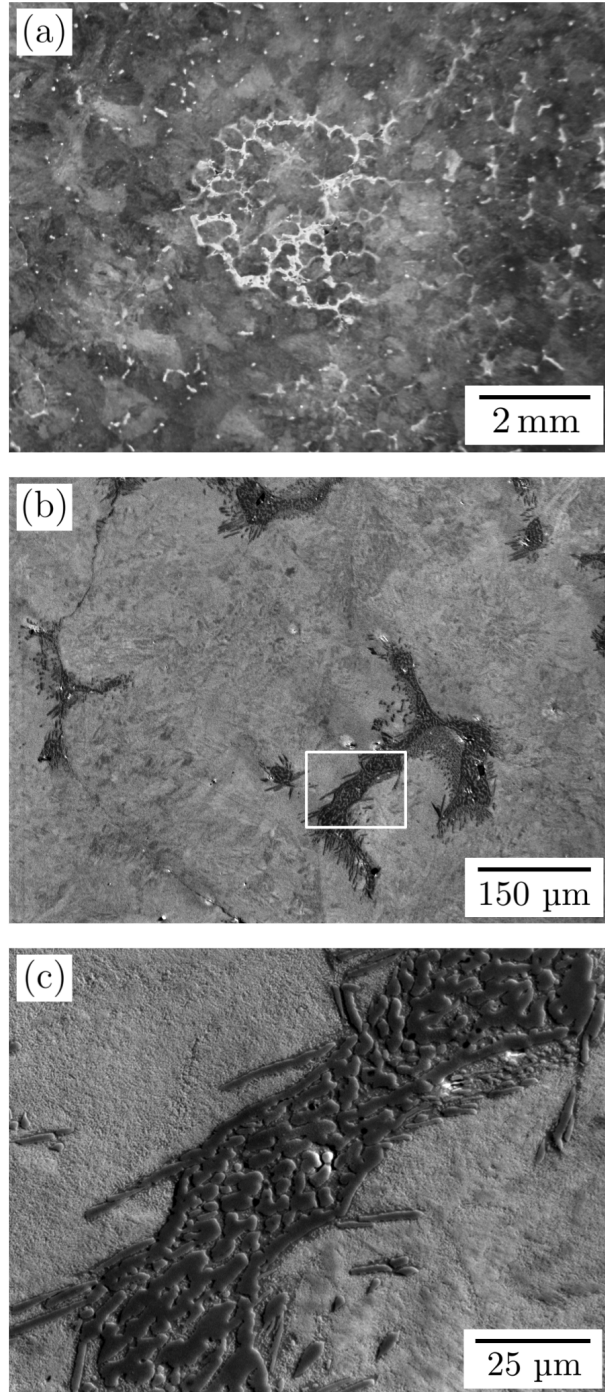


Figure 8.31: (a) The fine structure of an A-segregate channel, viewed axially in sample 5. (b)-(c) Secondary-electron images of the interdendritic 'silvery' phase that is most prominent in A-segregates - the area in (c) is boxed in (b).

The results of XRF suggest there has been substantial advection of both enriched interdendritic liquid and depleted solid. Cr and Mo have evidently enriched the interdendritic liquid and depleted the solid, and it seems reasonable to expect that this will also have been the case for the other alloying elements C, Si, Ni and Mn (although this will be confirmed using OES in further work). The enrichment of the interdendritic liquid has apparently caused its density to decrease, leading to pronounced A-segregation and enrichment at the top of the ingot. It is likely that the negatively-segregated cone measured at the base of the ingot was formed by the sedimentation of depleted solid.

In terms of grain structure, solidification appears to have started through columnar growth of fine dendrites from the outer skin of the ingot (angled due to non-vertical isotherms), and then transitioned quite rapidly into a near-equiaxed mode of freezing with coarser dendrites as the cooling rate dropped (near-equiaxed because sometimes the grains tended to be elongated slightly along the growth direction). The presence of a CET is interesting not only because one would usually expect such a transition to be associated with an increase in the speed of solidification,¹ but also because it is difficult to see how A-segregates could have formed in an equiaxed network, particularly ones so straight and long. Of course, there is no reason why A-segregates cannot form in equiaxed structures, but the network needs to be stationary and stable. It is unclear how this could have been the case in the ingot studied. It may have been possible if the equiaxed network had formed across the entirety of the ingot quickly and then solidified over a long period, but this is incompatible with the presence of a negatively-segregated cone and centreline enrichment.² Clearly there was a significant pool of liquid

¹Values for \dot{T} , G and R will all have been decreasing away from the mould when the transition occurred - the effect of decreasing G was perhaps the key factor, in that a flattening of the temperature gradient ahead of the columnar front may have allowed more space for nuclei in the melt to grow and trigger a CET. Ingots with equally-large equiaxed or “branched” regions have been regularly reported, so this is clearly not an usual occurrence in massive steel ingots [1; 346; 347].

²It is interesting to note that the cone appears to have become more negatively segregated the more it has grown. This indicates that the solid that was adding to it at the end of its growth

remaining when the A-segregates began to form, otherwise no enrichment of the centre would have been possible. The only remaining possibility is, then, that somehow equiaxed grains quickly found themselves in a stable network shortly after nucleating and persisted in the same location until fully solid. The mechanism for this, however, is not clear by any means. It is evident that this topic needs further investigation and discussion.

A-segregates appear to have formed very soon after the end of the columnar zone. Their onset corresponds to a loss of chemical homogeneity in the solid, which is significantly depleted in solute by their formation. Before the start of A-segregation, there will have been significantly less top-bottom segregation in the ingot, and no macrosegregation would have been visible at all if only the material before this point was assessed (i.e., the outer columnar skin). It is evident that A-segregates have not formed at the centre of the ingot, despite there being no change in grain structure. They have also not formed in the negatively-segregated cone, despite it being equiaxed like the rest of the ingot. The reasons for this are not immediately obvious, particularly given that the thermal conditions in these regions appear to be more favourable for channel formation (in order to cross isotherms and warm up, interdendritic liquid moving vertically has to do so faster for near-vertical isotherms than for near-horizontal isotherms, for the same isotherm speed). Possible explanations include the notion that the equiaxed networks in these regions were more likely to be in motion, thereby inhibiting channel formation by blocking them/shearing them off. This is certainly viable for the negative cone, which was likely growing via the sedimentation of equiaxed grains from above. Shrinkage stresses could likewise have caused grain movement in the centre of the ingot (they certainly caused voiding). Other factors that may have influenced the negative cone include a change in the local composition of the alloy, and therefore $\Delta\rho$ (enriched liquid would have been washed out of sedimenting grains and replaced with relatively solute-poor bulk liquid), and a decrease in the

was more depleted in solute, which is consistent with the solid originating from regions with A-segregates (that are more depleted than regions without A-segregates). The sharp boundary between the top of the cone and the centreline enrichment is not easily explained, but may be attributed to the growth of the equiaxed front from the sides over the sedimented cone.

local permeability due to the compaction of the equiaxed grains and/or a change in their morphology (they may have become more globular whilst moving in the liquid). The validity and relative importance of these factors is unclear, however.

The apparent interruption of the channels observed in Figs. 8.20 and 8.29 is probably due to the weaving of the enriched liquid between the solid network, when it follows a less tortuous path that is not always perfectly straight. The XRF measurements indicate that the material within A-segregate channels was not enriched to a consistent level across the whole ingot. This result may have been due to sectioning effects and the particular placement of each XRF measurement, but the change in the concentration of the remaining liquid at each stage should also have affected the concentration of the enriched interdendritic fluid.

The porosity found in the ingot is also a compelling topic for discussion. First, it is evident that the hot top anti-piping compound has worked very well, eliminating a pipe and insulating the head of the ingot such that the last liquid to solidify was at the very top (based on the level of enrichment found here). No porosity is observed in the head of the ingot apart from in A-segregate channels, indicating excellent feeding as the isotherms moved towards the top of the ingot. The bulk of the porosity present is in the ingot mid section, and appears to start directly above the sedimented cone. This suggests that completed feeding was difficult at this stage, and certainly the length of the fissures suggests that they formed late on across a sizeable equiaxed network, which would have been difficult to feed. It is worth noting that if these pores had been fed by enriched liquid, they would have resembled something akin to inverted V-segregates. Their chevron shape appears to have been derived from the shape of the sedimented cone, but could also have been influenced by shrinkage stresses.

8.4.1 XRF as an Assessment Technique

The results of this chapter have further demonstrated that XRF is a very effective tool for the measurement of macrosegregation and the detection of macrosegre-

gation defects. Indeed, after seeing the results of macroetching like those in Figs. 8.19 and 8.23-8.25, one might even argue that it is superior to macroetching in terms of its ability to detect segregation. The results of macroetching are dependent on the microstructure, and microstructures may sometimes appear insensitive to chemistry given a particular heat treatment. If an alloy is very hardenable, for example, then it may form martensite or bainite throughout a large thickness regardless of size or variations chemistry, and it would appear homogeneous when macroetched. Furthermore, macroetching cannot reliably inform the user of whether the material is enriched or depleted in solute, as they are not necessarily consistent in terms of appearance (i.e., enriched material might usually be expected to etch darker, but this was not found here).

8.5 Summary and Conclusions

1. The results presented here form a complete and detailed case study of the solidification of a steel ingot, which was cast under conditions that were well documented and are representative of a typical commercial production route. It is hoped that this study provides macromodellers with a valuable validation tool.
2. Macro-scale XRF revealed that there had been marked macroscopic chemical segregation during the solidification of the ingot. A-segregate channels were prevalent and a negatively-segregated cone was also present. There was significant top-bottom segregation. It was evident that microsegregation had enriched the interdendritic liquid such that its density has decreased, causing it to rise in the casting.
3. Careful examination of the bulk grain structure of ingot revealed that it had solidified in a near-equiaxed manner, with dendritic grains that were usually randomly oriented and not significantly elongated. The presence of A-segregates within a network of grains of this morphology is not readily explained, and requires further discussion.
4. A-segregation appeared to cease (and feeding become difficult) when solidi-

fication fronts met over the sedimented cone. This result is consistent with the new criterion proposed for A-segregation in Section 6.3, as it is likely that isotherms accelerated in the vertical direction when the fronts met.

5. In many respects, XRF represents a superior method for measuring macrosegregation (and determining the location of macrosegregation defects) than macroetching.
6. Future work should include comparison of the results with simulations of ingot casting. These should not only be complex macromodels, but also more simple models that predict characteristics like shrinkage gaps and porosity.
7. The author hopes to compare the results of XRF to OES measurements made from trepannings from the ingot. This will allow for variations in C, Si, Mn and Ni to be matched with the changes Cr and Mo concentrations measured.

Chapter 9

Concluding Remarks

The following conclusions have been drawn from the work described in this thesis:

1. Much of the severe segregation that can be found in large ingots can be removed during the forging operations associated with producing a high-integrity pressure vessel shell. However, A-segregates can still be retained through the wall thicknesses of such shell forgings.
2. A-segregation in SA508 Grade 3 steel can have a significant impact on microstructural evolution in the alloy during continuous cooling from austenitisation. Enriched A-segregate material was found to develop finer and harder microstructural features than the bulk material, including martensite-austenite islands, and remained harder than the bulk even after tempering. Contrary to previous reports examining continuously-cooled SA508 Grade 3, which have always described the bulk microstructure to comprise upper bainite, partial transformation experiments and TEM have suggested that the bulk microstructure is composed of Widmanstätten ferrite laths with pockets of lower bainite containing coarse carbides (at a cooling rate representative of the mid-thickness of a large shell forging).
3. Harder, finer microstructures are typically preferred in tempered SA508 Grade 3 due to their increased toughness, but Charpy impact testing has revealed that the properties of A-segregates are inferior to the bulk material. This is because A-segregated material has been found to fail by intergranular brittle fracture - in this work, this was observed in tests performed at room

temperature. It is almost certain that the enrichment of embrittling P in A-segregates is the primary cause of this, but the embrittling effect has also been augmented by the increased hardnesses of these regions as well as by the presence of large prior-austenite grains. The presence of A-segregates within a material is hence likely to contribute to the scatter found in impact test results.

4. Macrosegregation modelling is a field of great complexity. The most advanced macrosegregation models today cannot be relied upon to give quantitative predictions, and their ability even to predict basic macrosegregation patterns and trends is questionable. Fortunately, it seems that the use of simple criteria can be an effective alternative; the Rayleigh-number criterion recently presented by Torabi Rad et al. being a prime example. This criterion can be applied rapidly using a straightforward procedure, and appears to be particularly useful for the comparison of different casting conditions and alloy grades. Torabi Rad et al.'s criterion appears to work well for the casting scenarios it has been applied to so far, but care must be taken with respect to its sensitivities to certain input parameters, as well as the interpretation of its results.
5. It has been recognised in this thesis that Torabi Rad et al.'s Rayleigh criterion, like all the simple criteria for A-segregation presented historically, does not have a sound physical basis. This does not mean it does not deliver useful results, but it is desirable for a criterion to be backed up by theory. A new criterion for A-segregation was outlined in Chapter 6, which is physically meaningful.
6. Regions predicted to be susceptible to A-segregation in ingots can be tracked through forging operations to final products, but the methodology employed in this work is not very resilient and there can be high levels of uncertainty in results. This is of concern, as if improvements are going to be made to casting practice, ingot selection and discard practice, then a robust method of material tracking is needed.
7. It is likely that A-segregation in SA508 Grade 4N will be less prevalent

than in SA508 Grade 3. This is primarily due to the decreased level of Si present in Grade 4N. In order to suppress A-segregation in SA508 Grade 3, it is suggested that levels of C, Si, P and S in the alloy are reduced, whilst the amount of Mo added is maximised (within the alloy's specification). The effect of these changes should be investigated to ensure they have no negative repercussions, but the literature implies there will be a number of benefits.

8. Most of the changes that can be made to reduce the macrosegregation in steel ingots will tend to increase levels of porosity and inclusion retention. Manufacturers should bear this in mind when implementing changes to casting practices.
9. It is difficult to predict the severity of the enrichment in alloying elements associated with A-segregates. This is not only because their concentration is likely to vary throughout the volume of ingot, but also because their composition does not appear to be well predicted by existing microsegregation models.
10. Macroscopic X-ray fluorescence provides an effective method of mapping macrosegregation in large steel components. The particular form of the technique applied in this work is very robust, and in theory can be combined with other techniques to map properties other than chemistry.

Chapter 10

Scope for Future Work

The following points outline potential topics of interest for future research:

- It was proposed in Chapter 5 that the A-segregation observed in Grade 3 in this thesis would not significantly affect fracture properties, so long as sufficient bulk material was present along the crack path. However, it was highlighted that the segregates might still act as sites for crack nucleation, and that if welds were made in segregated material it was not clear whether this might lead to cracking. Therefore, given that segregated material almost certainly exists on the inside surface of the pressure-vessel forgings (where welds can be made) it would be useful to assess the weldability of A-segregate material, and whether welding is likely to lead to crack formation. Further to this, the effect of A-segregation on the susceptibility of Grade 3 to environmentally-assisted cracking during service should also be examined.
- Historically, it has been shown that A-segregation can have a negative impact on upper shelf properties in Grade 3, as well as on the DBTT. It may prove useful to ascertain whether this is still the case for modern-day Grade 3 material, which tends to be cleaner than the steel used for older forgings.
- The results of Chapter 6 predicted that the A-segregation present in Grade 4N would be less severe than in Grade 3. It would be useful to experimentally verify this. If material could be trepanned from a high-integrity forging of a similar size and shape as the component sampled here, then a

direct comparison could be made (see Fig. 6.12).

- Further work is required to develop the new criterion for A-segregation proposed in Chapter 6. It requires validation as well as development in order to be effectively implemented. Not only will its critical value for steels need to be determined, but hurdles associated with its practical implementation will need to be overcome.
- Changes that manufacturers can make to production processes to reduce segregation will usually lead to increased porosity and inclusion retention. However, this does not mean that such changes should not be attempted, as there will exist an optimum scenario for a given component. For instance, it may be the case that increased levels of porosity can be tolerated because pores are easier to remove than segregation defects. The capability to appropriately balance these phenomena would be highly beneficial for ingot producers. Changes to casting practice, ingot selection and discard practice could then be made routinely to reduce scrap and improve component quality.
- Assessing the potential impacts of segregation and porosity on component integrity not only requires their prediction in the as-cast state, but also tracking through forging and machining processes. Unfortunately, as Chapter 6 highlighted, the tracking procedure used here in DEFORM was not always particularly useful in this regard. An investigation determining the best practice for tracking material through forging processes is needed.
- Chapters 7 and 8 demonstrated the power of the macro-scale XRF technique. It may prove valuable for manufacturers to explore potential applications for technique as a quality control measure, and to gauge whether other assessment methods can be combined with it in a scanning capacity (e.g., hardness).
- Work to further develop the case study presented in Chapter 8 is being planned. Not only will this include validation of the XRF measurements using OES, but might also include differential-scanning calorimetry as-

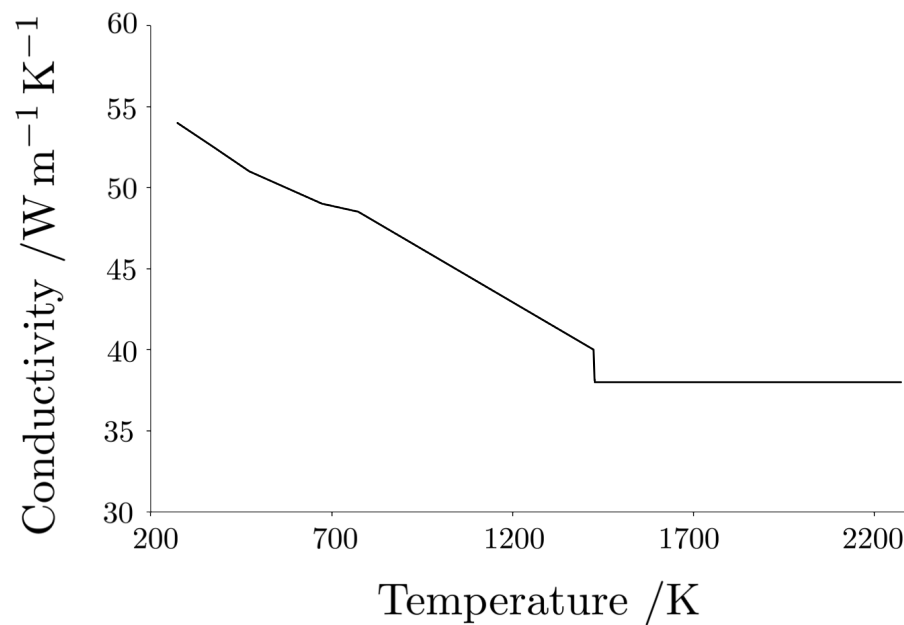
sessments, estimations of the permeability of mushy zone, hardness profiling, and further microstructural characterisation (confirmation of phases present). A closer examination of the A-segregation present in the ingot may also be undertaken, with the aim of determining whether the extent of solute enrichment in the channels is consistent.

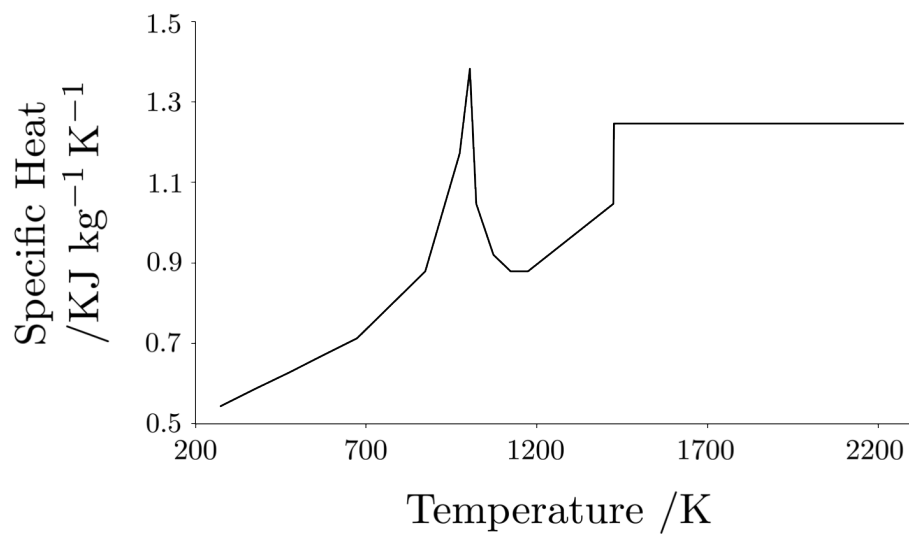
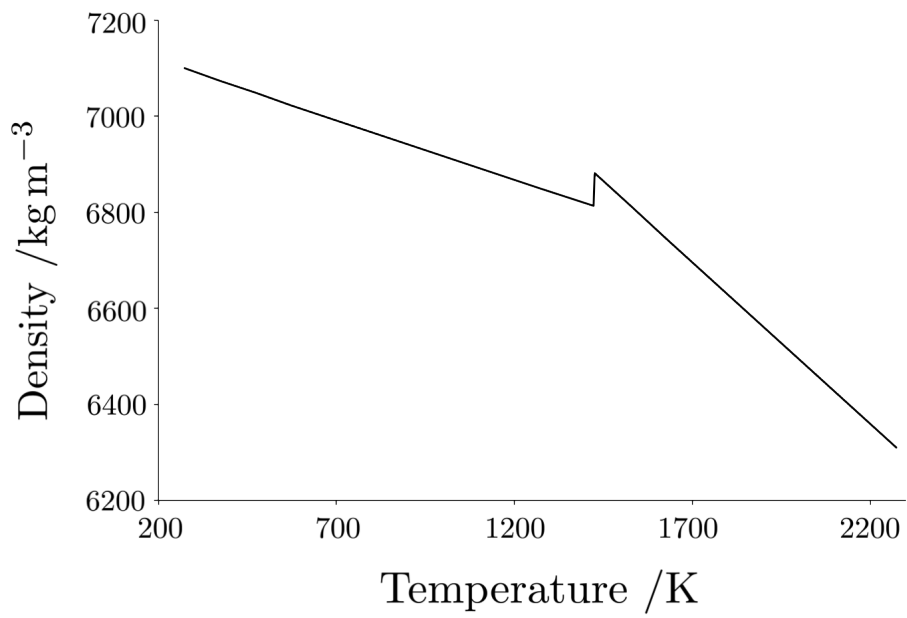
Appendix A

Materials Properties

Source: Sheffield Forgemasters International internal data.

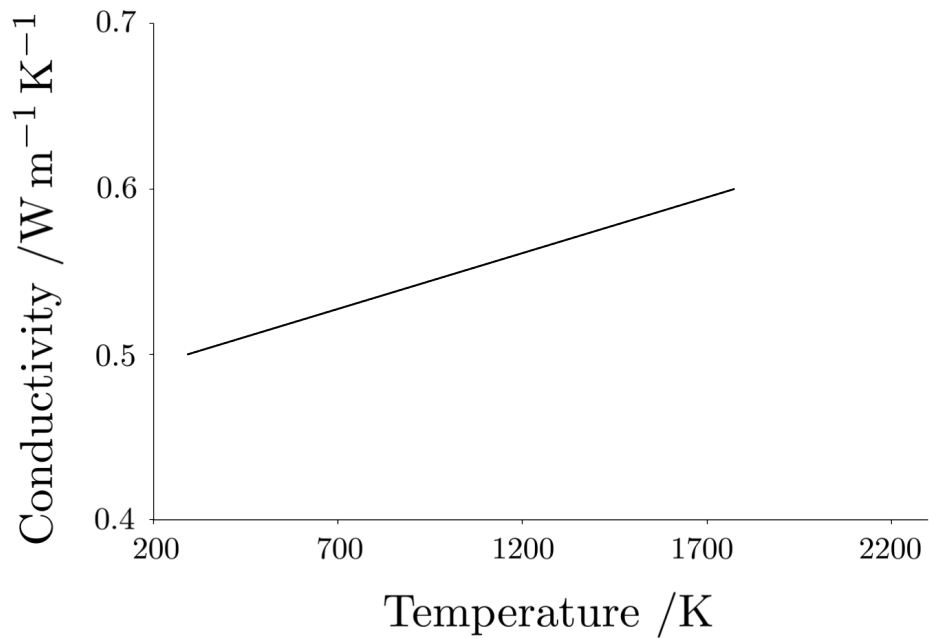
A.1 Gray Cast Iron Properties





A.2 Ceramic Properties

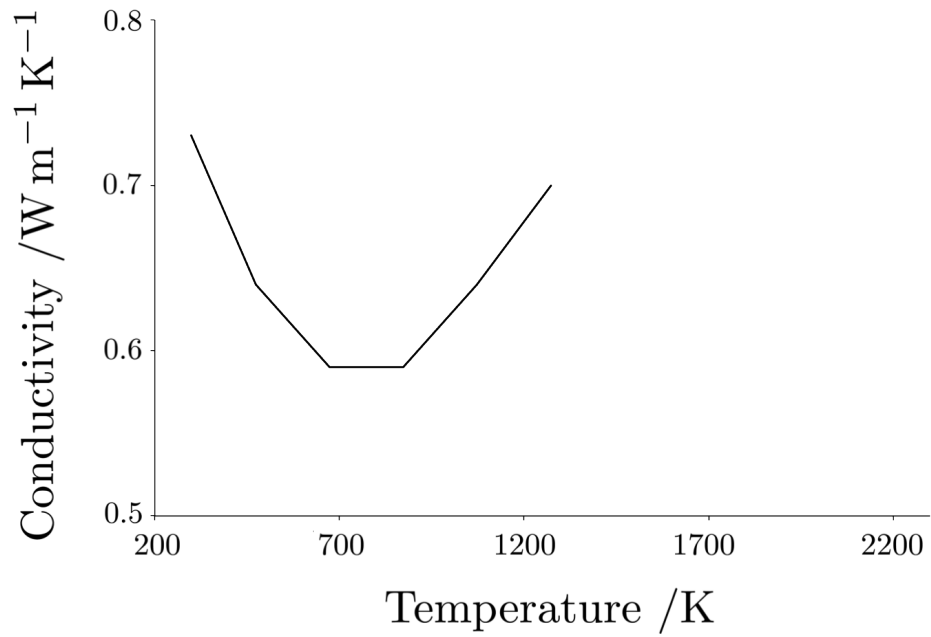
Typical composition (wt%)	
SiO ₂	55.0
Al ₂ O ₃	39.0
K ₂ O + Na ₂ O	1.3
Al _{total}	-
CaO	0.2
MgO	0.4
TiO ₂	1.4
Fe ₂ O ₃	2.6



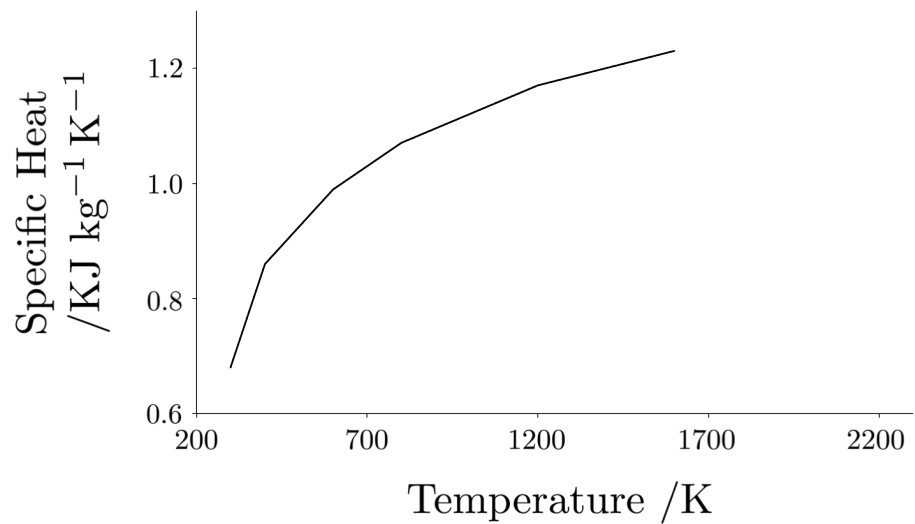
Density = 1350 kg m^{-3}

Specific Heat = $1.0 \text{ kJ kg}^{-1} \text{K}^{-1}$

A.3 Sand Properties



Density = 1520 kg m⁻³



References

- [1] Heterogeneity Sub-Committee of the British Iron and Steel Institute. Report on the Heterogeneity of Steel Ingots. *Journal of the Iron and Steel Institute*, 113:39–151, 1926. [33](#), [34](#), [111](#), [241](#)
- [2] A. Hultgren. Crystallization and Segregation Phenomena in 1.10 Per Cent Carbon Steel Ingots of Smaller Sizes. *Journal of the Iron and Steel Institute*, 120(2):69–125, 1929. [33](#)
- [3] E. Marburg. Accelerated Solidification in Ingots: Its Influence on Ingot Soundness. *Journal of Metals*, pages 157–172, 1953. [34](#), [38](#)
- [4] Physical Chemistry of Steelmaking Committee (ed. Gerhard Derge). *Basic Open Hearth Steelmaking*. AIME, third edition, 1964. [34](#), [118](#)
- [5] Heterogeneity Sub-Committee of the British Iron and Steel Institute. Report on the Heterogeneity of Steel Ingots. *Journal of the Iron and Steel Institute, Seventh Report*, page 12, 1937. [34](#), [38](#)
- [6] L. Northcott and V. Dickin. Influence of Centrifugal Casting on Metals. *Journal of the Institute of Metals*, 70:301–323, 1944. [34](#)
- [7] W. Kurz and D.J. Fisher. *Fundamentals of Solidification*. Trans Tech Publications LTD, Switzerland, third edition, 1986. [34](#), [60](#)
- [8] M. C. Flemings. Solidification Processing. *Metallurgical Transactions*, 5:2121–2134, 1974. [34](#), [40](#), [41](#)

- [9] M. Kawai. On the A Segregated Zone of Large Carbon Steel Ingot (II). *Tetsu To Hagane*, 42:14–18, 1956. [37](#)
- [10] C.E. Smeltzer. Solving the Steel “Freckle” Problem. *Iron Age*, 184(188-189), 1959. [37](#), [179](#)
- [11] K. Suzuki and K. Taniguchi. The Mechanism of Reducing “A” Segregates in Steels Ingots. *Transactions ISIJ*, 21:235–242, 1981. [37](#), [179](#)
- [12] Y. Tsuchida, M. Nakada, Y. Kunisada, and T. Teshima. Influence of Ingot Shape and Chemical Composition on the Inverse-V Segregation in Killed Steel Ingots. *Tetsu To Hagane*, 73:1125–1132, 1987. [37](#)
- [13] K. Suzuki and T. Miyamoto. Direction Observation of ”A” Segregation by Dump Test. *Tetsu To Hagane*, 63:45–52, 1977. [37](#), [74](#), [174](#)
- [14] R.J. McDonald and J.D. Hunt. Fluid Motion Through the Partially Solid Regions of a Casting and Its Importance in Understanding A Type Segregation. *Transactions of TMS AIME*, 245:1993–1997, 1969. [37](#)
- [15] R.J. McDonald and J.D. Hunt. Convective Fluid Motion Within the Interdendritic Liquid of a Casting. *Metallurgical Transactions*, 1:1787–1788, 1970. [37](#)
- [16] S.M. Copley, A.F. Giamei, S.M. Johnson, and M.F. Hornbecker. The Origin of Freckles in Unidirectionally Solidified Castings. *Metallurgical Transactions*, 1:2193–2204, 1970. [37](#), [63](#), [151](#)
- [17] A. Ohno. The Formation Mechanism of Inverse Segregation of Steel Ingots. *Tetsu To Hagane*, 54:401–10, 1968. [37](#)
- [18] S. Asai, T. Sahara, and I. Muchi. Theoretical Analysis and Model Study of the Formation of A-Type Segregation in Ingot. *Tetsu To Hagane*, 63:1512–1519, 1977. [37](#)
- [19] A.F. Giamei and B.H. Kear. On the Nature of Freckles in Nickel Base Superalloys. *Metallurgical Transactions*, pages 2185–2192, 1970. [37](#), [72](#)

- [20] N. Streat and F. Weinberg. Pipe Formation in Pb-Sn Alloys. *Metallurgical Transactions*, 3:3181–3184, 1972. [37](#)
- [21] N. Streat and F. Weinberg. Macrosegregation During Solidification Resulting From Density Differences in the Liquid. *Metallurgical Transactions*, 5:2539–2548, 1974. [37](#), [56](#)
- [22] N. Streat and F. Weinberg. Interdendritic Fluid Flow in a Lead-Tin Alloy. *Metallurgical Transactions B*, 7B:417–423, 1976. [37](#), [56](#)
- [23] H. Fredriksson and S.O. Nilsson. On the Formation of Macroseggregations in Ingots. *Metallurgical Transactions B*, 9B:111–120, 1978. [37](#), [72](#)
- [24] K.M. Fisher and J.D. Hunt. Observations on the Nature and Extent of Gravitational Interdendritic Fluid Flow. *Proc. Int. Conference on Solidification, Sheffield*, pages 325–330, 1977. [37](#)
- [25] A. Sample and A. Hellawell. The Effect of Mold Precession on Channel and Macro-Segregation in Ammonium Chloride-Water Analog Castings. *Metallurgical Transactions B*, 13B:495–501, 1982. [37](#), [69](#)
- [26] A. Sample and A. Hellawell. The Mechanisms of Formation and Prevention of Channel Segregation during Alloy Solidification. *Metallurgical Transactions B*, 15A:2163–2173, 1984. [37](#)
- [27] J.R. Sarazin and A. Hellawell. Channel Formation in Pb-Sn, Pb-Sb, and Pb-Sn-Sb Alloy Ingots and Comparison with the System $\text{NH}_4\text{Cl-H}_2\text{O}$. *Metallurgical Transactions A*, 19A:1861–1871, 1988. [37](#)
- [28] G. Lesoult. Macrosegregation in Steel Strands and Ingots: Characterisation, Formation and Consequences. *Materials Science and Engineering A*, 413-414:19–29, 2005. [38](#), [49](#), [74](#)
- [29] B. Crawshaw and A.D. Choudhury. Solidification Behaviour in Alloy Steel Ingots and Influence of Heterogeneity on Wrought Product. In *Proc. Conference 'The Solidification of Metals'*, pages 377–392, London, 1967. The Iron and Steel Institute. [38](#)

- [30] H. Combeau, M. Založnik, S. Hans, and P.E. Richey. Prediction of Macrosegregation in Steel Ingots: Influence of the Motion and the Morphology of Equiaxed Grains. *Metallurgical and Materials Transactions B*, 40B:289–304, 2009. [38](#), [48](#), [49](#), [51](#), [52](#), [53](#), [72](#), [73](#), [185](#), [202](#)
- [31] I. Vannier, H. Combeau, and G. Lesoult. Numerical Model for Prediction of the Final Segregation Pattern of Bearing Steel Ingots. *Materials Science and Engineering A*, 173:317–321, 1993. [38](#), [48](#)
- [32] K.A. Jackson and J.D. Hunt. Lamellar and Rod Eutectic Growth. *Transactions of TMS AIME*, 236:1129, 1966. [38](#)
- [33] S. Onodera and Y. Arakida. A Unified and Systematic Interpretation for the Mechanism of Formation of the Three Major Segregations. *Tetsu To Hagane*, 45:16–21, 1959. [39](#)
- [34] M.C. Flemings. *Solidification Processing*. McGraw-Hill, January 1974. [39](#), [40](#), [59](#)
- [35] B. Gray. *Journal of the Iron and Steel Institute*, 182:366–374, 1956. [39](#)
- [36] M. C. Flemings, R. Mehrabian, and G. E. Nereo. Macrosegregation, Part II. *Transactions of TMS AIME*, 242:41–49, 1968. [40](#), [41](#)
- [37] M. C. Flemings. Principles of Control of Soundness and Homogeneity of Large Ingots. *Scandinavian Journal of Metallurgy*, 5:1–15, 1976. [40](#), [41](#), [42](#)
- [38] J.S. Kirkaldy and W.V. Youdelis. Contribution to the Theory of Inverse Segregation. *Transactions of TMS AIME*, 212:233–240, 1958. [41](#)
- [39] W.V. Youdelis. Theory of Inverse Segregation. In *Proc. Conference ‘The Solidification of Metals’*, pages 112–118, London, 1967. The Iron and Steel Institute. [41](#)
- [40] M. C. Flemings and G. E. Nereo. Macrosegregation, Part I. *Transactions of TMS AIME*, 239:1449–1461, 1967. [41](#), [42](#), [170](#)

- [41] E. Scheil. Bemerkungen zur Schichtkristallbildung. *Zietschrift fur Metallkunde*, 34:70, 1942. [42](#), [54](#)
- [42] G.H. Gulliver. The Quantitative Effect of Rapid Cooling Upon The Constitution of Binary Alloys. *The Journal of the Institute of Metals*, 9:70, 1913. [42](#), [54](#)
- [43] W.G. Pfann. Principles of Zone Melting. *Transactions of TMS AIME*, 194:747, 1952. [42](#), [54](#)
- [44] M. C. Flemings and G. E. Nereo. Macrosegregation, Part III. *Transactions of TMS AIME*, 242:50–55, 1968. [42](#)
- [45] R. Mehrabian and M.C. Flemings. Macrosegregation in Ternary Alloys. *Metallurgical Transactions*, 1:455–464, 1970. [42](#)
- [46] M. C. Flemings. Our Understanding of Macrosegregation: Past and Present. *ISIJ International*, 40(9):833–841, 2000. [43](#)
- [47] R. Mehrabian, M. Keane, and M.C. Flemings. Interdendritic Fluid Flow and Macrosegregation; Influence of Gravity. *Metallurgical Transactions*, 1:3238–3241, 1970. [42](#)
- [48] T.S. Piwonka and M. C. Flemings. Pore Formation in Solidification. *Transactions of the Metallurgical Society of AIME*, 236:1157–1165, 1966. [43](#), [56](#)
- [49] S. Ganesan and D.R. Poirier. Conservation of Mass and Momentum for the Flow of Interdendritic Liquid During Solidification. *Metallurgical and Materials Transactions B*, 21B:173–181, 1990. [43](#), [46](#)
- [50] T. Fujii, D.R. Poirier, and M.C. Flemings. Macrosegregation in a Multi-component Low Alloy Steel. *Metallurgical Transactions B*, 10B:331–339, 1979. [44](#)
- [51] S.D. Ridder, S. Kou, and R. Mehrabian. Effect of Fluid Flow on Macrosegregation in Axi-Symmetric Ingots. *Metallurgical Transactions B*, 12B:435–447, 1981. [45](#)

- [52] S.D. Ridder, F.C. Reyes, S. Chakravorty, R. Mehrabian, J.D. Nauman, J.H. Chen, and H.J. Klein. Steady State Segregation and Heat Flow in ESR. *Metallurgical Transactions B*, 9B:415–425, 1978. [45](#)
- [53] J. Szekely and A.S. Jassal. An Experimental and Analytical Study of the Solidification of a Binary Dendritic System. *Metallurgical Transactions B*, 9B:389–398, 1978. [45](#)
- [54] W.D. Bennon and F.P. Incropera. A Continuum Model for Momentum, Heat and Species Transport in Binary Solid-Liquid Phase Change System - I. Model formulation . *Internation Journal of Heat and Mass Transfer*, 30(10):2161–2170, 1987. [45](#)
- [55] W.D. Bennon and F.P. Incropera. A Continuum Model for Momentum, Heat and Species Transport in Binary Solid-Liquid Phase Change System - II. Application to solidification in a rectangular cavity. *Internation Journal of Heat and Mass Transfer*, 30(10):2171–2187, 1987. [46](#)
- [56] C. Beckermann and R. Viskanta. Double-Diffusive Convection During Dendritic Solidification of a Binary Mixture. *PhysioChemical Hydrodynamics*, 10(2):195–213, 1988. [46](#)
- [57] C. Beckermann and R. Viskanta. Mathematical Modeling of Transport Phenomena During Alloy Solidification. *Applied Mechanics Reviews*, 46:1–25, 1993. [46](#), [47](#)
- [58] V.R. Voller and A.D. Brent. The Modelling of Heat, Mass and Solute Transport in Solidification Systems. *Internation Journal of Heat and Mass Transfer*, 32(9):1719–1731, 1989. [46](#)
- [59] S.D. Felicelli, J.C. Heinrich, and D.R. Poirier. Simulation of Freckles during Vertical Solidification of Binary Alloys. *Metallurgical Transactions B*, 22B:847–859, 1991. [46](#), [52](#)
- [60] S.D. Felicelli, J.C. Heinrich, and D.R. Poirier. Numerical Model for Dendritic Solidification of Binary Alloys. *Numerical Heat Transfer, Part B*, 23:461–481, 1993. [46](#), [52](#)

- [61] D.R. Poirier and J.C. Heinrich. Continuum Model for Predicting Macrosegregation in Dendritic Alloys. *Materials Characterisation*, 32:287–298, 1994. [46](#), [56](#)
- [62] P. Nandapurkar, D.R. Poirier, J.C. Heinrich, and S. Felicelli. Thermosolutal Convection during Dendritic Solidification of Alloys: Part I. Linear Stability Analysis. *Metallurgical Transactions B*, 20B:711–721, 1989. [46](#)
- [63] J.C. Heinrich, S. Felicelli, P. Nandapurkar, and D.R. Poirier. Thermosolutal Convection during Dendritic Solidification of Alloys: Part II. Nonlinear Convection. *Metallurgical and Materials Transactions B*, 20B:883–891, 1989. [46](#)
- [64] P. Nandapurkar, D.R. Poirier, and J.C. Heinrich. Momentum Equation for Dendritic Solidification. *Numerical Heat Transfer, Part A*, 19:297–311, 1991. [46](#)
- [65] D. Xu and Q. Li. Numerical Simulation of Heat, Mass and Momentum Transfers in Metallic Ingots and Prediction of Macrosegregation. *Acta Metallurgica Sinica (English Letters)*, 4(1):37–41, 1991. [46](#)
- [66] D. Xu and Q. Li. Numerical Method for Solution of Strongly Coupled Binary Alloy Solidification Problems. *Numerical Heat Transfer, Part A*, 20:181–201, 1991. [46](#)
- [67] D. Xu and Q. Li. Gravity- and Solidification-Shrinkage-Induced Liquid Flow in a Horizontally Solidified Alloy Ingot. *Numerical Heat Transfer, Part A*, 20:203–221, 1991. [46](#)
- [68] K.C. Chiang and H.L. Tsai. Shrinkage-Induced Fluid Flow and Domain Change in Two-Dimensional Alloy Solidification. *International Journal of Heat and Mass Transfer*, 35(7):1763–1770, 1992. [46](#)
- [69] K.C. Chiang and H.L. Tsai. Interaction Between Shrinkage-Induced Fluid Flow and Natural Convection During Alloy Solidification. *International Journal of Heat and Mass Transfer*, 35(7):1771–1778, 1992. [46](#)

- [70] G.F. Naterer. Simultaneous Pressure-Velocity Coupling in the Two-Phase Zone for Solidification Shrinkage in an Open Cavity. *Modelling and Simulation in Materials Science and Engineering, IOP*, 5(595-613), 1997. [46](#)
- [71] M.C. Schneider and C. Beckermann. A numerical study of the combined effects of microsegregation, mushy zone permeability and flow, caused by volume contraction and thermosolutal convection, on macrosegregation and eutectic formation in binary alloy solidification. *International Journal of Heat and Mass Transfer*, 38(18):3455–3473, 1995. [46](#), [58](#)
- [72] E. McBride, J.C. Heinrich, and D.R. Poirier. Numerical Simulation of Incompressible Flow Driven by Density Variations During Phase Change. *International Journal for Numerical Methods in Fluids*, 31:787–800, 1999. [46](#), [58](#)
- [73] J.C. Heinrich and E. McBride. Calculation of Pressure in a Mushy Zone. *International Journal for Numerical Methods in Engineering*, 47:735–747, 2000. [46](#), [58](#)
- [74] J.C. Heinrich and D.R. Poirier. The Effect of Volume Change During Directional Solidification of Binary Alloys. *Modelling and Simulation in Materials Science and Engineering, IOP*, 12:881–899, 2004. [46](#), [58](#)
- [75] M. El-Bealy. Modeling of Interdendritic Strain and Macrosegregation for Dendritic Solidification Processes: Part I. Theory and Experiments. *Metallurgical and Materials Transactions B*, 31B:331–343, 2000. [46](#)
- [76] M. El-Bealy. Modeling of Interdendritic Strain and Macrosegregation for Dendritic Solidification Processes: Part II. Computation of Interdendritic Strain and Segregation Fields in Steel Ingots. *Metallurgical and Materials Transactions B*, 31B:345–355, 2000. [46](#)
- [77] M. El-Bealy and H. Fredriksson. Modeling of the Peritectic Reaction and Macro-segregation in Casting of Low Carbon Steel. *Metallurgical and Materials Transactions B*, 27B:999–1014, 1996. [46](#), [114](#)

- [78] M. Rappaz and V.R. Voller. Modeling of Micro-Macrosegregation in Solidification Processes. *Metallurgical Transactions A*, 21A:749–753, 1990. [46](#)
- [79] D.R. Poirier, P. Nandapurkar, and S. Ganesan. The Energy and Solute Conservation Equations for Dendritic Solidification. *Metallurgical Transactions B*, 22B:889–900, 1991. [46](#)
- [80] D.R. Poirier and P. Nandapurkar. Enthalpies of a Binary Alloy during Solidification. *Metallurgical Transactions A*, 19A:3057–3061, 1988. [46](#)
- [81] M.C. Schneider and C. Beckermann. Effects of Simplified Enthalpy Relations on the Prediction of Heat Transfer during Solidification of a Lead-Tin Alloy. *Applied Mathematical Modelling*, 15:596–605, 1991. [46](#), [52](#)
- [82] C.M. Oldenburg and F. J. Spera. Hybrid Model for Solidification and Convection. *Numerical Heat Transfer, Part B*, 92B:217–229, 1992. [47](#)
- [83] P.J. Prescott, F.P. Incropera, and D.R. Gaskell. The Effects of Undercooling, Recalescence and Solid Transport on the Solidification of Binary Metal Alloys The Effects of Undercooling, Recalescence and Solid Transport on the Solidification of Binary Metal Alloys. In *28th National Heat Transfer Conference*. ASME, New York, 1992. [47](#)
- [84] S.C. Flood, L. Katgerman, and V.R. Voller. The Calculation of Macrosegregation and Heat and Fluid Flows in the DC Casting of Aluminium Alloys. In M. Rappaz, M.R. Ozgu, and K.W. Mahin, editors, *Modeling of Casting, Welding and Advanced Solidification Processes V*, pages 683–690. Warrendale, PA, 1991. [47](#)
- [85] V.R. Voller. Effect of Solidification Morphology on the Macroscopic Behavior of Solidification Systems. In *NATO Advanced Research Workshop on Interactive Dynamics in Convection and Solidification, Chamonix, France*, 1992. [47](#)

- [86] J. Ni and C. Beckermann. A Volume-Average Two-Phase Model for Transport Phenomena during Solidification. *Metallurgical Transactions B*, 22B:349–361, 1991. [47](#)
- [87] C. Prakash. Two-Phase Model for Binary Solid-Liquid Phase Change, Part I: Governing Equations. *Numerical Heat Transfer, Part B*, 18:131–145, 1990. [47](#)
- [88] C. Prakash. Two-Phase Model for Binary Solid-Liquid Phase Change, Part II: Some Illustrative Examples. *Numerical Heat Transfer, Part B*, 18:147–167, 1990. [47](#)
- [89] C.Y. Wang and C. Beckermann. Equiaxed Dendritic Solidification with Convection: Part I. Multiscal/Multiphase Modeling. *Metallurgical and Materials Transactions A*, 27A:2754–2764, 1996. [47](#), [49](#)
- [90] C.Y. Wang and C. Beckermann. Equiaxed Dendritic Solidification with Convection: Part II. Numerical Simulations for an Al-4 Wt Pct Cu Alloy. *Metallurgical and Materials Transactions A*, 27A:2765–2783, 1996. [47](#), [49](#)
- [91] C. Beckermann and C.Y. Wang. Equiaxed Dendritic Solidification with Convection: Part III. Comparisons with $\text{NH}_4\text{Cl-H}_2\text{O}$. *Metallurgical and Materials Transactions A*, 27A:2784–2795, 1996. [47](#)
- [92] M.C. Schneider and C. Beckermann. Formation of Macrosegregation by Multicomponent Thermosolutal Convection During the Solidification of Steel. *Metallurgical and Materials Transactions A*, 26A:2373–2388, 1995. [48](#), [51](#), [52](#), [58](#), [62](#)
- [93] M.C. Schneider, J.P. Gu, C. Beckermann, W.J. Boettinger, and U.R. Kattner. Modelling of Micro- and Macrosegregation and Freckle Formation in Single-Crystal Nickel-Base Superalloy Directional Solidification. *Metallurgical and Materials Transactions A*, 28A:1517–1531, 1997. [48](#), [58](#)
- [94] W.J. Boettinger, U.R. Kattner, S.R. Coriell, Y.A. Chang, and B.A. Mueller. Development of Multicomponent Solidification Micromodels Using a Thermodynamic Phase Diagram Data Base. In M. Cross and J. Campbell, ed-

- itors, *Modeling of Casting, Welding and Advanced Solidification Processes VII*, pages 649–656. Warrendale, PA, 1995. [48](#)
- [95] S.D. Felicelli, D.R. Poirier, A.F. Giamei, and J.C. Heinrich. Simulating Convection and Macroseggregation in Superalloys. *Journal of Metals*, pages 21–25, March 1997. [48](#), [52](#)
- [96] S.D. Felicelli, D.R. Poirier, and J.C. Heinrich. Modeling Freckle Formation in Three Dimensions during Solidification of Multicomponent Alloys. *Metallurgical and Materials Transactions B*, 29B:847–855, 1998. [48](#), [58](#)
- [97] S.D. Felicelli, J.C. Heinrich, and D.R. Poirier. Finite Element Analysis of Directional Solidification of Multicomponent Alloys. *International Journal for Numerical Methods in Fluids*, 27:207–227, 1998. [48](#), [58](#)
- [98] S.D. Felicelli, J.C. Heinrich, and D.R. Poirier. Three-Dimensional Simulations of Freckles in Binary Alloys. *Journal of Crystal Growth*, 191:879–888, 1998. [48](#)
- [99] M.J.M. Krane and F.P. Incropera. Solidification of Ternary Metal Alloys - I. Model Development. *International Journal of Heat and Mass Transfer*, 40(16):3827–3855, 1997. [48](#), [58](#)
- [100] M.J.M. Krane and F.P. Incropera. Solidification of Ternary Metal Alloys - II. Predictions of Convective Phenomena and Solidification Behaviour in Pb-Sb-Sn Alloys. *International Journal of Heat and Mass Transfer*, 40(16):3837–3847, 1997. [48](#)
- [101] C. Beckermann. Modeling of Macroseggregation: Past, Present and Future. *Flemings Symposium, Boston, MA, June 2000*, 2000. [49](#), [51](#), [58](#), [60](#)
- [102] M. Wu, A. Ludwig, A. Buhrig-Polaczek, M. Fehlbier, and P.R. Sahm. Influence of Convection and Grain Movement on Globular Equiaxed Solidification. *International Journal of Heat and Mass Transfer*, 46:2819–2832, 2003. [49](#)

- [103] A.I. Ciobanas and Y. Fautrelle. Ensemble Averaged Multiphase Eulerian Model for Columnar/Equiaxed Solidification of a Binary Alloy: I. The Mathematical Model. *Journal of Physics D: Applied Physics*, 40:3733–3762, 2007. [49](#)
- [104] A.I. Ciobanas and Y. Fautrelle. Ensemble Averaged Multiphase Eulerian Model for Columnar/Equiaxed Solidification of a Binary Alloy: II. Simulation of the Columnar-to-Equiaxed Transition (CET). *Journal of Physics D: Applied Physics*, 40:4310–4336, 2007. [49](#)
- [105] M. Wu and A. Ludwig. A Three-Phase Model for Mixed Columnar-Equiaxed Solidification. *Metallurgical and Materials Transactions A*, 37A:1613–1631, 2006. [49](#), [50](#), [52](#)
- [106] A. Ludwig and M. Wu. Modeling the Columnar-to-Equiaxed Transition with a Three-Phase Eulerian Approach. *Materials Science and Engineering A*, 413-414:109–114, 2005. [49](#), [51](#)
- [107] R. Tanzer, W. Schutzenhofer, G. Reiter, H.P. Fauland, L. Konozy, A. Ishmurzin, M. Wu, and A. Ludwig. Validation of a Multiphase Model for the Macrosegregation and Primary Structure of High-Grade Steel Ingots. *Metallurgical and Materials Transactions B*, 40B:305–311, 2009. [49](#), [72](#), [185](#), [202](#)
- [108] M.A. Martorano, C. Beckermann, and C.A. Gandin. A Solutal Interaction Mechanism for the Columnar-to-Equiaxed Transition in Alloy Solidification. *Metallurgical and Materials Transactions A*, 34A:1657–1674, 2003. [49](#)
- [109] M. Rappaz and P. Thevoz. Solute Diffusion Model for Equiaxed Dendritic Growth. *Acta Metallurgica*, 35:1487–1497, 1987. [49](#)
- [110] M. Rappaz and P. Thevoz. Solute Diffusion Model for Equiaxed Dendritic Growth: Analytical Solution. *Acta Metallurgica*, 12:2929–2933, 35. [49](#)
- [111] C.Y. Wang and C. Beckermann. A Unified Solute Diffusion Model for Columnar and Equiaxed Dendritic Alloy Solidification. *Materials Science and Engineering A*, 171:199–211, 1993. [49](#), [54](#)

- [112] M. Wu and A. Ludwig. Modeling Equiaxed Solidification with Melt Convection and Grain Sedimentation - I: Model Description. *Acta Materialia*, 57:5621–5631, 2009. [49](#)
- [113] M. Wu and A. Ludwig. Modeling Equiaxed Solidification with Melt Convection and Grain Sedimentation - I: Model Verification. *Acta Materialia*, 57:5632–5644, 2009. [49](#)
- [114] M. Wu, A. Fjeld, and A. Ludwig. Modelling Mixed Columnar-Equiaxed Solidification with Melt Convection and Grain Sedimentation - Part I: Model Description. *Computational Materials Science*, 50:32–42, 2010. [50](#)
- [115] M. Wu, A. Fjeld, and A. Ludwig. Modelling Mixed Columnar-Equiaxed Solidification with Melt Convection and Grain Sedimentation - Part II: Illustrative Modelling Results and Parameter Studies. *Computational Materials Science*, 50:43–58, 2010. [50](#), [52](#)
- [116] J. Li, M. Wu, A. Ludwig, and A. Kharicha. Modelling Macrosegregation in a 2.45 ton Steel Ingot. *MCWASP XIII: IOP Conference Series: Materials Science and Engineering*, 33:012091, 2012. [50](#), [51](#), [52](#)
- [117] J. Li, M. Wu, A. Ludwig, and A. Kharicha. Simulation of Macrosegregation in a 2.45-ton Steel Ingot Using a Three-Phase Mixed Columnar-Equiaxed Model. *International Journal of Heat and Mass Transfer*, in press, 2014. [50](#), [73](#)
- [118] P.K. Sung, D.R. Poirier, and S.D. Felicelli. Sensitivity of Mesh Spacing on Simulating Macrosegregation During Directional Solidification of a Superalloy. *International Journal for Numerical Methods in Fluids*, 35:357–370, 2001. [50](#), [52](#)
- [119] S. Gouttebroze, W. Liu, M. Bellet, and H. Combeau. 2D/3D Simulation of Macrosegregation: A Comparison Between Codes on a Small Cavity and on a Large Ingot. *Proc. MCWASP XI, TMS*, pages 227–234, 2006. [50](#), [52](#)

- [120] S. Gouttebroze, M. Bellet, and H. Combeau. 3D Macrosegregation Simulation with Anisotropic Remeshing. *C. R. Mecanique*, 335:269–279, 2007. [50](#), [52](#)
- [121] V.R. Voller, A. Mouchmov, and M. Cross. An Explicit Scheme for Coupling Temperature and Concentration Fields in Solidification Models. *Applied Mathematical Modelling*, 28:79–94, 2004. [50](#)
- [122] R. Pardeshi, V.R. Voller, A.K. Singh, and P. Dutta. An Explicit-Implicit Time Stepping Scheme for Solidification Models. *International Journal of Heat and Mass Transfer*, 51:3399–3409, 2008. [50](#)
- [123] I.L. Ferreira, V.R. Voller, B. Nestler, and A. Garcia. Two-Dimensional Numerical Model for the Analysis of Macrosegregation During Solidification. *Computational Materials Science*, 46:358–366, 2009. [50](#)
- [124] D.R. Liu, B.G. Sang, X.H. Kang, and D.Z. Li. Numerical simulation of macrosegregation in large multiconcentration poured steel ingot. *International Journal of Cast Metals Research*, 23(6):354–363, 2010. [50](#), [67](#)
- [125] N. Ahmad, H. Combeau, J.L. Desbiolles, T. Jalanti, G. Lesoult, J. Rappaz, M. Rappaz, and C. Stomp. Numerical Simulation of Macrosegregation: a Comparison between Finite Volume Method and Finite Element Method Predictions and a Confrontation with Experiments. *Metallurgical and Materials Transactions A*, 29A:617–630, 1998. [50](#)
- [126] W. Liu. *Finite Element Modelling of Macrosegregation and Thermomechanical Phenomena in Solidification Processes*. PhD thesis, Ecole des Mines de Paris, 2005. [50](#)
- [127] M. Bellet, O. Boughanmi, and G. Fidel. A Partitioned Resolution for Concurrent Fluid Flow and Stress Analysis During Solidification: Application to Ingot Casting. *MCWASP XIII: IOP Conference Series: Materials Science and Engineering*, 33:012052, 2012. [50](#)
- [128] A.K. Singh, R. Pardeshi, and B. Basu. Modelling of Convection During Solidification of Metal and Alloys. *Sadhana*, 26:139–162, 2001. [50](#), [51](#), [58](#)

- [129] A.K. Singh, B. Basu, and A. Ghosh. Role of Appropriate Permeability Model on Numerical Prediction of Macrosegregation. *Metallurgical and Materials Transactions B*, 37B:799–809, 2006. 50, 51, 58
- [130] P.K. Sung, D.R. Poirier, and S.D. Felicelli. Continuum Model for Predicting Microporosity in Steel and Castings. *Modelling and Simulation in Materials Science and Engineering, IOP*, 10:551–568, 2002. 50, 51
- [131] C.W. Ma, H.F. Shen, T.Y. Huang, and B.C. Liu. Numerical Simulation of Macro-Segregation in Steel Ingot During Solidification. *Acta Metallurgica Sinica (English Letters)*, 17(3):288–294, 2004. 50, 51
- [132] D. Liu, X. Kang, B. Sang, and D. Li. Numerical Study of Macrosegregation Formation of Ingot Cast in Normal Sand Mold and Water-Cooled Sand Mold. *Acta Metallurgica Sinica (English Letters)*, 24(1):54–64, 2011. 50, 51
- [133] W. Li, H. Shen, X. Zhang, and B. Liu. Modeling of Species Transport and Macrosegregation in Heavy Steel Ingots. *Metallurgical and Materials Transactions B*, pages 1–8, May 2013. 50, 67
- [134] A. Ludwig. Private Communication. 50
- [135] C. Beckermann. Private Communication. 50
- [136] J.P. Gu and C. Beckermann. Simulation of Convection and Macrosegregation in a Large Steel Ingot. *Metallurgical and Materials Transactions A*, 30A:1357–1366, 1999. 51, 62, 153
- [137] V.R. Voller and F. Porte-Agel. Moore’s Law and Numerical Modeling. *Journal of Computational Physics*, 179:698–703, 2002. 51
- [138] J. Guo and C. Beckermann. Three-Dimensional Simulations of Freckle Formation During Binary Alloy Solidification: Effect of Mesh Spacing. *Numerical Heat Transfer, Part A*, 44:559–576, 2003. 52
- [139] THERCAST software, Transvalor S.A., <http://www.transvalor.com/thercastpresentation.php>. 52, 62

- [140] M. Bellet, V.D. Fachinotti, S. Gouttebroze, W. Liu, and H. Combeau. A 3D-FEM Model Solving Thermomechanics and Macrosegregation in Binary Alloys Solidification. In M. Rappaz, C. Beckermann, and R. Trivedi, editors, *Proc. Symposium on Solidification Processes and Microstructures, in Honor of Wilfried Kurz, TMS Annual Meeting, Charlotte (NC, USA)*, pages 41–46. TMS, 2004. [52](#)
- [141] MAGMA software, <http://www.magmaflow.com/>. [52](#), [62](#)
- [142] ProCAST software, version 2014.0, ESI, <http://www.esi-group.com/products/casting/procast>. [52](#), [62](#), [152](#)
- [143] JMatPro software, <http://www.sentecsoftware.co.uk/jmatpro.aspx>. [52](#), [75](#), [153](#), [174](#)
- [144] M. Rappaz. Modelling of Microstructure Formation in Solidification Processes. *International Materials Reviews*, 34(3):93–123, 1989. [52](#)
- [145] H.D. Brody and M.C. Flemings. Solute Redistribution in Dendritic Solidification. *Transactions of the Metallurgical Society of AIME*, 236:615–624, 1966. [54](#)
- [146] T.W. Clyne and W. Kurz. Solute Redistribution During Solidification with Rapid Solid State Diffusion. *Metallurgical Transactions A*, 12A:965–971, 1981. [54](#), [55](#)
- [147] T. Ohnaka. Redistribution of Solute Accompanied with Diffusion Inside Solid Phase During Solidification. *Tetsu To Hagane*, 70:S913, 1984. [54](#)
- [148] S. Kobayashi. Solute Redistribution During Solidification with Diffusion in Solid Phase: A Theoretical Analysis. *Journal of Crystal Growth*, 88:87–96, 1988. [54](#)
- [149] S. Ganesan and D.R. Poirier. Solute Redistribution in Dendritic Solidification with Diffusion in the Solid. *Journal of Crystal Growth*, 97:851–859, 1989. [54](#)

- [150] V.R. Voller and C. Beckermann. A Unified Model of Microsegregation and Coarsening. *Metallurgical and Materials Transactions A*, 30A:2183–2189, 1999. [54](#), [60](#)
- [151] K.S. Yeum, V. Laxman, and D.R. Poirier. Efficient Estimation of Diffusion during Dendritic Solidification. *Metallurgical Transactions A*, 20A:2847–2856, 1989. [54](#)
- [152] Y. Ueshima, S. Mizoguchi, T. Matsumiya, and H. Kajioka. Analysis of Solute Distribution in Dendrites of Carbon Steel with δ/γ Transformation during Solidification. *Metallurgical Transactions B*, 17B:845–859, 1986. [54](#)
- [153] A.A. Howe. Development of a Computer Model of Dendritic Microsegregation for use with Multicomponent Steels. *Applied Scientific Research*, 44:51–59, 1987. [54](#)
- [154] A.A. Howe. In M. Rappaz, M.R. Ozgu, and K.W. Mahin, editors, *Modeling of Casting, Welding and Advanced Solidification Processes V*, pages 461–466. Warrendale, PA, 1991. [54](#)
- [155] S.W. Chen, Y.Y. Chuang, Y.A. Chang, and M.G. Chu. Calculation of Phase Diagrams and Solidification Paths of Al-Rich Al-Li-Cu Alloys. *Metallurgical Transactions A*, 22A:2837–2848, 1991. [54](#)
- [156] J. Miettinen. Mathematical Simulation of Interdendritic Solidification of Low-Alloyed and Stainless Steels. *Metallurgical Transactions A*, 23A:1155–1170, 1992. [54](#)
- [157] M. Hillert, L. Hoglund, and M. Schalin. Role of Back-Diffusion Studied by Computer Simulation. *Metallurgical and Materials Transactions A*, 30A:1635–1641, 1999. [54](#)
- [158] Q. Chen and B. Sundman. Computation of Partial Equilibrium Solidification with Complete Interstitial and Negligible Substitutional Solute Back Diffusion. *Materials Transactions*, 43(3):551–559, 2002. [54](#)

- [159] A.J.W. Ogilvy and D.H. Kirkwood. A Model for the Numerical Computation of Microsegregation in Alloys. *Applied Scientific Research*, 44:43–49, 1987. [54](#)
- [160] C.Y. Wang and C. Beckermann. A Multiphase Solute Diffusion Model for Dendritic Alloy Solidification. *Metallurgical Transactions A*, 24A:2787–2802, 1993. [54](#)
- [161] X. Dore, H. Combeau, and M. Rappaz. Modelling of Microsegregation in Ternary Alloys: Application to the Solidification of Al-Mg-Si. *Acta Materialia*, 48:3951–3962, 2000. [54](#)
- [162] L. Thinet and H. Combeau. Prediction of Macrosegregation during the Solidification Involving a Peritectic Transformation for Multicomponent Steels. *Journal of Materials Science*, 39:7213–7219, 2004. [54](#)
- [163] L. Thinet and H. Combeau. A New Model of Microsegregation for Macrosegregation Computation in Multicomponent Steels. Part I: Theoretical Formulation and Algorithm. *Computational Materials Science*, 45:294–304, 2009. [54](#)
- [164] L. Thinet and H. Combeau. A New Model of Microsegregation for Macrosegregation Computation in Multicomponent Steels. Part II: Application to Fe-Ni-C Alloys. *Computational Materials Science*, 45:285–293, 2009. [54](#)
- [165] H. Zhang, C.A. Gandin, K. Nakajima, and J. He. A Multiphase Segregation Model for Multicomponent Alloys with a Peritectic Transformation. *MCWASP XIII: IOP Conference Series: Materials Science and Engineering*, 33:012063, 2012. [54](#)
- [166] A.A. Howe. Simple Approaches for Solidification and Diffusive Homogenisation. *Ironmaking and Steelmaking*, 38(7):534–539, 2011. [54](#), [75](#)
- [167] T. Kraft and Y.A. Chang. Predicting Microstructure and Microsegregation in Multicomponent Alloys. *Journal of Metals*, pages 20–28, December 1997. [54](#)

- [168] J. Fridberg, L.E. Torndahl, and M. Hillert. Diffusion in Iron. *Jernkont. Ann.*, 153:263–276, 1969. [55](#)
- [169] D. Apelian, M. C. Flemings, and R. Mehrabian. Specific permeability of partially solidified dendritic networks of al-si alloys. *Metallurgical Transactions*, 5:2533–2537, 1974. [56](#)
- [170] D.R. Poirier. Permeability for Flow of Interdendritic Liquid in Columnar-Dendritic Alloys. *Metallurgical Transactions B*, 18B:245–255, 1987. [56](#)
- [171] R. West. On the Permeability of the Two-Phase Zone during Solidification of Alloys. *Metallurgical Transactions A*, 16A:693, 1985. [56](#), [58](#)
- [172] K. Murakami, A. Shiraishi, and T. Okamoto. Interdendritic Fluid Flow Normal to Primary Dendrite-Arms in Cubic Alloys. *Acta Metallurgica*, 31(9):1417–1424, 1983. [56](#)
- [173] K. Murakami, A. Shiraishi, and T. Okamoto. Fluid Flow in Interdendritic Space in Cubic Alloys. *Acta Metallurgica*, 32(9):1423–1428, 1984. [56](#)
- [174] R. Nasser-Rafi, R. Deshmukh, and D.R. Poirier. Flow of Interdendritic Liquid and Permeability in Pb-20 Wt Pct Sn Alloys. *Metallurgical Transactions A*, 16A:2263–2271, 1985. [56](#)
- [175] D.R. Poirier and S. Ganesan. Permeabilities for Flow of Interdendritic Liquid in Equiaxial Structures. *Materials Science and Engineering A*, 157:113–123, 1992. [56](#)
- [176] D.R. Poirier and P. Ocansey. Permeability for Flow of Liquid Through Equiaxial Mushy Zones. *Materials Science and Engineering A*, 171:231–240, 1993. [56](#)
- [177] J.F. McCarthy. Lattice Gas Cellular Automata Method for Flow in the Interdendritic Region. *Acta Metallurgica*, 42(5):1573–1581, 1994. [56](#)
- [178] M.S. Bhat, D.R. Poirier, and J.C. Heinrich. Permeability for Cross Flow through Columnar-Dendritic Alloys. *Metallurgical and Materials Transactions B*, 26B:1049–1056, 1995. [56](#), [57](#)

- [179] M.S. Bhat, D.R. Poirier, and J.C. Heinrich. A Permeability Length Scale for Cross Flow Through Model Structures. *Metallurgical and Materials Transactions B*, 26B:1091–1092, 1995. [56](#)
- [180] D. Nagelhout, M.S. Bhat, J.C. Heinrich, and D.R. Poirier. Permeability for Flow Normal to a Sparse Array of Fibres. *Materials Science and Engineering A*, 191:203–208, 1995. [56](#)
- [181] M.S. Bhat, D.R. Poirier, J.C. Heinrich, and D. Nagelhout. Permeability Normal to Columnar Dendrites at High Fraction Liquid. *Scripta Metallurgica et Materialia*, 31(3):339–344, 1994. [56](#)
- [182] S. Ganesan, C.L. Chan, and D.R. Poirier. Permeability for Flow Parallel to Primary Dendrite Arms. *Materials Science and Engineering A*, 151:97–105, 1992. [56](#)
- [183] J.C. Heinrich, D.R. Poirier, and D.F. Nagelhout. Mesh generation and flow calculations in highly contorted geometries. *Computational Methods in Applied Mechanical Engineering*, 133:79–92, 1996. [56](#)
- [184] B. Goyeau, T. Benihaddadene, D. Gobin, and M. Quintard. Numerical Calculation of the Permeability in a Dendritic Mushy Zone. *Metallurgical and Materials Transactions B*, 30B:613–622, 1999. [56](#)
- [185] R.G. Santos and M.L.N.M. Melo. Permeability of Interdendritic Channels. *Materials Science and Engineering A*, 391:151–158, 2005. [56](#)
- [186] H. Yoo and R. Viskanta. Effect of Anisotropic Permeability on the Transport Process During Solidification of a Binary Mixture. *International Journal of Heat and Mass Transfer*, 35(10):2335–2346, 1992. [58](#)
- [187] C.Y. Wang, S. Ahuja, C. Beckermann, and H.C. de Groh III. Multiparticle Interfacial Drag in Equiaxed Solidification. *Metallurgical and Materials Transactions B*, 26B:111–119, 1995. [58](#)
- [188] A. Suzuki, T. Suzuki, Y. Nagaoka, and Y. Iwata. On Secondary Dendrite Arm Spacing in Commercial Carbon Steels with Different Carbon Content. *Nippon Kingaku Gakkai Shuho*, 32:1301–1305, 1968. [59](#), [61](#), [114](#)

- [189] H. Jacobi and K. Schwerdtfeger. Dendrite Morphology of Steady State Unidirectionally Solidified Steel. *Metallurgical Transactions A*, 7A:811–820, 1976. [59](#), [60](#), [61](#), [114](#)
- [190] G.R. Kotler, K.W. Casey, and G.S. Cole. Experimental Observations of Dendritic Growth. *Metallurgical Transactions*, 3:723–726, 1972. [59](#), [60](#)
- [191] K.P. Young and D.H. Kirkwood. The Dendrite Arm Spacings of Aluminium-Copper Alloys Solidified Under Steady-State Conditions. *Metallurgical Transactions A*, 6A:197–205, 1975. [59](#), [60](#)
- [192] R. Alberny, J. Serra, and M. Turpin. Use of cavariograms for dendrite arm spacing measurements. *Transactions of the Metallurgical Society of AIME*, 245:55–59, 1969. [59](#)
- [193] G.F. Bolling and D. Fainstein-Pedraza. Arrayed Dendritic Growth. *Acta Metallurgica*, 22:1033–1040, 1974. [59](#)
- [194] T.F. Bower, H.D. Brody, and M.C. Flemings. Measurements of Solute Redistribution in Dendritic Solidification. *Transactions of the Metallurgical Society of AIME*, 236:624–634, 1966. [59](#)
- [195] M. El-Bealy and B.G. Thomas. Prediction of Dendrite Arm Spacing for Low Alloy Steel Casting Processes. *Metallurgical and Materials Transactions B*, 27B:689–693, 1996. [59](#), [60](#), [61](#)
- [196] Y.M. Won and B.G. Thomas. Simple Model of Microsegregation during Solidification of Steels. *Metallurgical and Materials Transactions B*, 32A:1755–1767, 2001. [59](#), [60](#), [61](#), [114](#), [173](#)
- [197] T. Okamoto, S. Matsuo, and K. Kishitake. Dendrite Arm Spacings in Iron-Carbon-Chromium Alloys. *Transactions ISIJ*, 18:289–294, 1978. [59](#), [60](#)
- [198] C. Cicutti and R. Boeri. On the Relationship Between Primary and Secondary Dendrite Arm Spacing in Continuous Casting Products. *Scripta Materialia*, 45:1455–1460, 2001. [59](#), [61](#)

- [199] T.Z. Kattamis, J.C. Coughlin, and M. C. Flemings. Influence of Coarsening on Dendrite Arm Spacing of Aluminium-Copper Alloys. *Transactions of the Metallurgical Society of AIME*, 239:1504–1511, 1967. [60](#), [114](#)
- [200] T.Z. Kattamis, V.T. Holmberg, and M.C. Flemings. Influence of Coarsening on Dendrite Arm Spacing and Grain Size of a Magnesium-Zinc Alloy. *Journal of the Institute of Metals*, 95:343–347, 1967. [60](#)
- [201] R.M. Sharp and A. Hellawell. Solute Distributions at Non-Planar, Solid-Liquid Growth Fronts. *Journal of Crystal Growth*, 11:77–91, 1971. [60](#)
- [202] M. Rappaz and W.J. Boettinger. On Dendritic Solidification of Multicomponent Alloys with Unequal Liquid Diffusion Coefficients. *Acta Materialia*, 47(11):3205–3219, 1999. [60](#)
- [203] D.H. Kirkwood. A Simple Model for Dendrite Arm Coarsening During Solidification. *Materials Science and Engineering*, 73:L1–L4, 1985. [60](#)
- [204] J.A.E. Bell and W.C. Winegard. *Journal of the Institute of Metals*, 92:357–359, 1964. [60](#)
- [205] J.A. Horwath and L.F. Mondolfo. Dendritic Growth. *Acta Metallurgica*, 10:1037–1042, 1962. [60](#)
- [206] Jernkontoret. *A Guide to the Solidification of Steels*. Jernkontoret, Stockholm, 1977. [61](#)
- [207] J. Miettinen, S. Louhenkilpi, H. Kytönen, and J. Laine. IDS: Thermodynamic–Kinetic–Empirical Tool for Modelling of Solidification, Microstructure and Material Properties. [61](#)
- [208] E. Niyama, T. Uchida, and M. Morikawa. A Method of Shrinkage Prediction and its Application to Steel Casting Practice. *International Cast Metals Journal*, 54:507–516, 1982. [62](#)
- [209] K. Carlson and C. Beckermann. Use of the Niyama Criterion to Predict Shrinkage-Related Leaks in High-Nickel Steel and Nickel-Based Alloy Cast-

- ings. In *Proceedings of the 62nd SFSA Technical and Operating Conference*, number 5.6, Chicago, IL, 2008. Steel Founders' Society of America. [63](#)
- [210] T.M. Pollock and W.H. Murphy. The Breakdown of Single-Crystal Solidification in High Refractory Nickel-Base Alloys. *Metallurgical and Materials Transactions A*, 27A:1081–1094, 1996. [63](#), [151](#)
- [211] K. Suzuki and T. Miyamoto. Influence of Alloying Elements on the Formation of “A” Segregates in Steel Ingot. *Transactions ISIJ*, 20:377–383, 1980. [63](#), [72](#), [74](#), [151](#), [159](#), [179](#)
- [212] H. Yamada, T. Sakurai, and T. Takenouchi. Critical Conditions for the Formation of “A” Segregation in Forging Ingots. *ISIJ*, 75:97–104, 1989. [64](#), [151](#)
- [213] C. Beckermann, J.P. Gu, and W.J. Boettinger. Development of a Freckle Predictor via Rayleigh Number Method for Single-Crystal Nickel-Base Superalloy Castings. *Metallurgical and Materials Transactions A*, 31A:2545–2557, 2000. [64](#)
- [214] J.C. Ramirez and C. Beckermann. Evaluation of a Rayleigh-Number-Based Freckle Criterion for Pb-Sn Alloys and Ni-Base Superalloys. *Metallurgical and Materials Transactions A*, 34A:1525–1536, 2003. [64](#)
- [215] M.G. Worster. Instabilities of the Liquid and Mushy Regions during Solidification of Alloys. *Journal of Fluid Mechanics*, 237:649–669, 1992. [64](#)
- [216] M.G. Worster. Convection in Mushy Layers. *Annual Reviews of Fluid Mechanics*, 29:91–122, 1997. [64](#), [148](#)
- [217] M. Torabi, P. Kotas, and C. Beckermann. Rayleigh Number Criterion for Formation of A-Segregates in Steel Castings and Ingots. *Metallurgical and Materials Transactions A*, 44A:4266–4281, 2013. [64](#), [143](#), [150](#), [152](#), [153](#), [159](#), [167](#), [173](#), [179](#)
- [218] B. Sang, X. Kang, and D. Li. A Novel Technique for Reducing Macrosegregation in Heavy Steel Ingots. *Journal of Materials Processing Technology*, 210:703–711, 2010. [65](#)

- [219] G. Hoyle. *Electroslag Processes: Principles and Practice*. Applied Science Publishers, 1983. [66](#)
- [220] A. Mitchell, R.O. Jackson, and A.S. Ballantyne. Macrosegregation, Liquid Movement and Heat Flow in the ESR Process. In *Proceedings of the Fourth International Symposium on Electroslag and Other Special Melting Technologies, Tokyo, Japan, June 1973*. [66](#)
- [221] F.W. Thomas, F. Knell, and E. Weingartner. Magnetic Field Effects in Vacuum Arc and Electroslag Remelting. In *Proceedings of the Fifth International Symposium on Electroslag and Other Special Melting Technologies, Carnegie-Mellon Institute of Research, October 1974*. [66](#)
- [222] K.O. Yu, J.A. Domingue, G.E. Maurer, and H.D. Flanders. Macrosegregation in ESR and VAR Processes. *Journal of Metals*, 38:46–50, 1986. [66](#)
- [223] J.A. Van Den Avyle, J.A. Brooks, and A.C. Powell. Reducing Defects in Remelting Processes for High-Performance Alloys. *Journal of Metals*, 50:22–26, 1998. [66](#)
- [224] S. Kou. *Macrosegregation in Electroslag Remelted Ingots*. PhD thesis, Massachusetts Institute of Technology, 1978. [66](#)
- [225] A. Mitchell. Solidification in Remelting Processes. *Materials Science and Engineering A*, 413-414:10–18, 2005. [66](#), [71](#)
- [226] L.R. Cooper. Central Zone Remelting of Ingots Using an Electroslag Process. In *Proceedings of the Fifth International Symposium on Electroslag and Other Special Melting Technologies, Carnegie-Mellon Institute of Research, October 1974*. [66](#)
- [227] M. Tateno. Development of Large Size High Quality Steels and Their Future Prospects as “Near Net Shape” Material. *Transactions ISIJ*, 25:97 – 108 (Special Lecture), 1985. [67](#)
- [228] M.J. Stewart, L.C. MacAulay, and F. Weinberg. Macrosegregation in Castings Rotated and Oscillated During Solidification. *Metallurgical Transactions*, 2:169–173, 1971. [69](#)

- [229] G.F. Bolling. Rotary Method of Casting. US Patent 3614976, October 1971. [69](#)
- [230] S. Kou, D.R. Poirier, and M.C. Flemings. Macrosegregation in Rotated and Remelted Ingots. *Metallurgical Transactions B*, 9B:711–719, 1978. [69](#)
- [231] D.G. Neilson and F.P. Incropera. Effect of Rotation on Fluid Motion and Channel Formation During Unidirectional Solidification of a Binary Alloy. *International Journal of Heat and Mass Transfer*, 36:489–505, 1993. [69](#)
- [232] D.G. Neilson and F.P. Incropera. Experimental Study of Unidirectional Solidification of Aqueous Ammonium Chloride in a Cylindrical Mold With and Without Rotation. *Experimental Heat Transfer*, 6:131–155, 1993. [69](#)
- [233] J.A. Brinell. Method of Treating Steel and Iron Ingots. US Patent 410119, November 1910. [69](#), [70](#)
- [234] T. Tanoue. Method of Centrifugal Casting of Clean Ingots. US Patent 3364978, January 1968. [69](#), [70](#)
- [235] A. Hellawell. Method for Reducing Macrosegregation in Alloys. US Patent 4462454, July 1984. [69](#), [70](#)
- [236] J. Campbell. Effects of Vibration During Solidification. *International Materials Reviews*, (2):71–108, 1981. [69](#)
- [237] A. Hultgren. Method of Casting Steel and Other Metals. US Patent 1775859, September 1930. [69](#)
- [238] D.A. Currey and C.A. Pickles. Electromagnetic Stirring of Aluminium-Silicon Alloys. *Journal of Materials Science*, 23:3756–3763, 1988. [69](#)
- [239] W.D. Griffiths and D.G. McCartney. The Effect of Electromagnetic Stirring on Macrostructure and Macrosegregation in the Aluminium Alloy 7150. *Materials Science and Engineering*, A222:140–148, 1997. [69](#)
- [240] J.P. Birat and J. Chone. Electromagnetic Stirring on Billet, Bloom and Slab Continuous Casters: State of the Art in 1982. In *Continuous Casting:*

4th International Iron and Steel Congress, London, pages 12/1 – 12/11, May 1982. [69](#)

- [241] J.J. Moore, editor. *Continuous Casting: Vol. III, The Application of Electromagnetic Stirring (EMS) in the Continuous Casting of Steel*. Iron and Steel Society of AIME, Warrendale, PA, 1984. [69](#)
- [242] E.A. Nelson. Centrifugal Casting Method. US Patent 2193537, March 1940. [70](#)
- [243] J.J. Moore. *Continuous Casting: Vol. III, The Application of Electromagnetic Stirring (EMS) in the Continuous Casting of Steel*, chapter Review of Axial Segregation in Continuously Cast Steel, pages 11–20. Iron and Steel Society of AIME, Warrendale, PA, 1984. [69](#)
- [244] J. Campbell and J.W. Bannister. Grain Refinement of Electroslag Remelted Iron Alloys. *Metals Technology*, 2:409–415, 1975. [71](#)
- [245] M. Chatterjee, M.S.N. Balasubramanian, K.M. Gupt, and P.K. Rao. Development of Ultrahigh Strength Steel Through Electroslag Remelting with Inoculation. *Ironmaking and Steelmaking*, 21(5):399–407, 1994. [71](#)
- [246] M. Wang, G. Cheng, S. Qiu, P. Zhao, and Y. Gan. Roles of Titanium-Rich Precipitates as Inoculants During Solidification in Low Carbon Steel. *International Journal of Minerals, Metallurgy and Materials*, 17(3):276–281, 2010. [71](#)
- [247] T.R. Bandyopadhyay, P.K. Rao, and N. Prabhu. Effect of Inoculation During Electroslag Refining on Grain Size of 15CDV6 and Modified 15CDV6 Steels. *Ironmaking and Steelmaking*, 33(4):331–336, 2006. [71](#)
- [248] W.J. Poole, A. Mitchell, and F. Weinberg. Inoculating Stainless Steel with Titanium Nitride. *High Temperature Materials and Processes*, 16(3):173–182, 2011. [71](#)
- [249] A. Pacz. Alluminum Alloy. US Patent 1596020, August 1926. [71](#)

- [250] D.G. McCartney. Grain Refining of Aluminium and its Alloys Using Inoculants. *International Materials Reviews*, 34:247–260, 1989. [71](#)
- [251] B.G. Sang, X.H. Kang, D.R. Liu, and D.Z. Li. Study on Macrosegregation in Heavy Steel Ingots. *International Journal of Cast Metals Research*, 23(4):205–210, 2010. [72](#)
- [252] G.F. Vander Voort. *Metallography: Principles and Practice*. ASM International, 1984. [72](#)
- [253] G.F. Vander Voort, editor. *ASM Handbook: Volume 9 - Metallography and Microstructures*. ASM International, 2004. [72](#)
- [254] I. Taguchi K. Miramura and H. Soga. New Evaluation Techniques of Segregation in Continuously Cast Steel. *Transactions ISIJ*, 24:883–890, 1984. [72](#), [73](#)
- [255] A. Kohn. Autoradiographic Study of the Process of Solidification in Killed Steel Ingots. In *Proc. Conference ‘The Solidification of Metals’*, pages 357–362, London, 1967. The Iron and Steel Institute. [72](#)
- [256] K.W. Andrews and C.R. Gomer. Use of Radioactive Isotopes in Solidification Studies of Steel. In *Proc. Conference ‘The Solidification of Metals’*, pages 363–369, London, 1967. The Iron and Steel Institute. [72](#)
- [257] F. Weinberg, J. Lait, and R. Pugh. Solidification of High-Carbon Steel Ingots. pages 334–339, 1977. [72](#)
- [258] A.K. Singh, B. Basu, and A. Ghosh. Experimental Investigation of Macrosegregation During Vertical Solidification of Lead-Tin Alloys. *Transactions of the Indian Institute of Metallurgy*, 65:85–96, 2012. [72](#), [185](#)
- [259] C. Maidorn and B. Blind. Solidification and Segregation in Heavy Forging Ingots. *Nuclear Engineering and Design*, 84:285–296, 1985. [73](#), [124](#), [185](#), [202](#)

- [260] M. Tkadleckova, P. Machovcak, M. Kovac, K. Gryc, K. Michalek, B. Smetana, and L. Socha. The Effect of Boundary Conditions of Casting on the Size of Macrosegregation in Heavy Steel Ingots. In *Proceedings of the 22nd International Conference on Metallurgy and Materials, Metal 2013, Brno, Czech Republic*, 2013. [73](#)
- [261] D. Cogswell. The Development of Processing to Mechanical Property Relationships via Quantitative Microstructure Assessment in Low Alloy Steel Heavy Section Forging Materials. *Proc. ASME 2011 Pressure Vessels & Piping Div. Conf.*, pages 1–5, 2011. [78](#)
- [262] D. Cogswell, D. Swan, R. Mitchell, and S. Garwood. Materials and Structural Integrity Challenges for the Next Nuclear Generation. *63rd Ann. Ass. & Int. Conf. Int. Instit. Welding*, 2010. [78](#)
- [263] ASTM Standard Specification for Quenched and Tempered Vacuum-treated Carbon and Alloy Steel Forgings for Pressure Vessel Components A508A/A508M, 2004. [78](#)
- [264] S.G. Druce. Investigation of the Homogeneity of Chemical Composition and Mechanical Properties in a Large A508 Class 3 Steel Pressure Vessel Forging. volume AERE - R9581. September 1979. [79](#), [111](#), [124](#)
- [265] P. Soulat, B. Houssin, P. Bocquet, and M. Bethmont. Analysis of Radiation Embrittlement Results from a French Forging Examined in the Second Phase of an IAEA-Coordinated Research Program. In L.E. Steele, editor, *Radiation Embrittlement of Nuclear Reactor Pressure Vessel Steels: An International Review*, ASTM STP 1170, pages 249–265. 1993. [79](#), [111](#), [124](#), [125](#), [135](#)
- [266] M. Bethmont, J-M. Frund, B. Houssin, and P. Soulat. The Toughness of Irradiated Pressure Water Reactor (PWR) Vessel Shell Rings and the Effect of Segregation Zones. In D.S. Gelles, R.K. Nanstad, A.S. Kumar, and E.A. Little, editors, *Effects of Radiation on Materials: 17th International Symposium*, ASTM STP 1270, pages 320–330. 1996. [79](#), [124](#), [125](#), [135](#)

- [267] H-S. Yang and H.K.D.H. Bhadeshia. Uncertainties in Dilatometric Determination of Martensite Start Temperature. *Materials Science and Technology*, 23(5):556–560, 2007. [93](#)
- [268] Y.R. Im, Y.J. Oh, B.J. Lee, J.H. Hong, and H.C. Lee. Effects of Carbide Precipitation on the Strength and Charpy Impact Properties of Low Carbon Mn-Ni-Mo Bainitic Steels. *Journal of Nuclear Materials*, 297:138–148, 2001. [98](#), [179](#)
- [269] S. Kim, Y.R. Im, S. Lee, H.C. Lee, Y.J. Oh, and J.H. Hong. Effects of Alloying Elements on Mechanical and Fracture Properties of Base Metals and Simulated Heat-Affected Zones of SA 508 Steels. *Metallurgical and Materials Transactions A*, 32A:903–911, 2001. [98](#), [179](#)
- [270] S. Lee, S. Kim, B. Hwang, B.S. Lee, and C.G. Lee. Effect of Carbide Distribution on the Fracture Toughness in the Transition Temperature Region of an SA 508 Steel. *Acta Materialia*, 50:4755–4762, 2002. [98](#), [179](#)
- [271] Y.R. Im, B.J. Lee, Y.J. Oh, J.H. Hong, and H.C. Lee. Effect of Microstructure on the Cleavage Fracture Strength of Low Carbon Mn-Ni-Mo Bainitic Steels. *Journal of Nuclear Materials*, 324:33–40, 2004. [98](#)
- [272] S. Kim, S. Lee, Y.R. Im, H.C. Lee, S.J. Kim, and J.H. Hong. Effects of Alloying Elements on Fracture Toughness in the Transition Temperature Region of Base Metals and Simulated Heat-Affected Zones of Mn-Mo-Ni Low-Alloy Steels. *Metallurgical and Materials Transactions A*, 35A:2027–2037, 2004. [98](#), [123](#), [179](#)
- [273] B.S. Lee, M.C. Kim, J.H. Yoon, and J.H. Hong. Characterisation of High Strength and High Toughness Ni-Mo-Cr Low Alloy Steels for Nuclear Application. *International Journal of Pressure Vessels and Piping*, 87:74–80, 2010. [98](#)
- [274] Y. Bagaryatski. *Dokl. Akad. Nauk. SSSR*, 73:1161, 1950. [100](#)

- [275] D.N. Shackleton and P.M. Kelly. The Crystallography of Cementite Precipitation in the Bainite Transformation. *Acta Metallurgica*, 15:979–992, 1967. [100](#)
- [276] H.K.D.H. Bhadeshia. *Bainite in Steels*. The Institute of Materials, 1992. [100](#)
- [277] H.K.D.H. Bhadeshia and R.W.K. Honeycombe. *Steels: Microstructure and Properties*. Butterworth-Heinemann, 3rd edition, 2006. [100](#)
- [278] G. Ostberg. A Review of Present Knowledge Concerning the Influence of Segregates on the Integrity of Nuclear Pressure Vessels. *International Journal of Pressure Vessels and Piping*, 74:153–158, 1997. [111](#)
- [279] A-A Tavassoli, P. Soulat, and A. Pineau. Temper Embrittlement Susceptibility and Toughness of A508 Class 3 Steel. In A.S. Melilli and E.G. Nisbett, editors, *Residual and Unspecified Elements in Steel*, ASTM STP 1042, pages 100–113. ASTM, Philadelphia, 1989. [111](#), [135](#)
- [280] P.G. Bastien. The Mechanism of Formation of Banded Microstructures. *Journal of the Iron and Steel Institute*, 187:281–291, 1957. [114](#)
- [281] J.S. Kirkaldy, J. von Destinon-Forstmann, and R.J. Brigham. Simulation of Banding in Steels. *Canadian Metallurgical Quarterly*, pages 59–81, 1962. [114](#), [118](#)
- [282] L.E. Samuels. *The Optical Microscopy of Carbon Steels*. ASM, 1980. [114](#)
- [283] S.W. Thompson and P.R. Howell. Factors Influencing Ferrite/Pearlite Banding and Origin of Large Pearlite Nodules in a Hypoeutectoid Plate Steel. *Materials Science and Technology*, 8:777–784, 1992. [114](#)
- [284] R. Grossterlinden, R. Kawalla, U. Lotter, and H. Pircher. Formation of Pearlitic Banded Structures in Ferritic-Pearlitic Steels. *Steel Research*, 63:331–336, 1992. [114](#)

- [285] J.D. Verhoeven. A Review of Microsegregation Induced Banding Phenomena in Steels. *Journal of Materials Engineering and Performance*, 9:286–296, 2000. [114](#)
- [286] H. Pous-Romero and H.K.D.H. Bhadeshia. Continuous Cooling Transformations in Nuclear Pressure Vessel Steels. *Metallurgical and Materials Transactions A*, 45A:4897–4906, 2014. [116](#)
- [287] T.B. Massalski, H. Okamoto, P.R. Subramanian, and L. Kacprzak, editors. *Binary Alloy Phase Diagrams*. ASM International, 1990. [118](#)
- [288] J.T. Kim, H.K. Kwon, H.S. Chang, and Y.W. Park. Improvement of Impact Toughness of the SA 508 Class 3 Steel for Nuclear Pressure Vessel Through Steel-Making and Heat-Treatment Practices. *Nuclear Engineering and Design*, 174:51–58, 1997. [123](#), [133](#)
- [289] P. Bowen, S.G. Druce, and J.F. Knott. Effects of Microstructure on Cleavage Fracture in Pressure Vessel Steel. *Acta Metallurgica*, 34:1121–1131, 1986. [123](#)
- [290] K.D. Haverkamp, K. Forch, K.H. Piehl, and W. White. Effect of Heat Treatment and Precipitation State on Toughness of Heavy Section Mn-Mo-Ni-Steel for Nuclear Power Plants Components. *Nuclear Engineering and Design*, 81:207–217, 1984. [123](#)
- [291] C. Naudin, J.M. Frund, and A. Pineau. Intergranular Fracture Stress and Phosphorus Grain Boundary Segregation of a Mn-Ni-Mo Steel. *Scripta Materialia*, 40:1013–1019, 1999. [124](#), [135](#)
- [292] O.M.L. Yahya, F. Borit, R. Piques, and A. Pineau. Statistical Modelling of Intergranular Brittle Fracture in a Low Alloy Steel. *Fatigue and Fracture of Engineering Materials and Structures*, 21:1485–1502, 1998. [124](#), [135](#)
- [293] A. Andrieu, A. Pineau, P. Joly, and F. Roch. On Modeling of Thermal Embrittlement in PWR Steels using the Local Approach to Fracture. In *13th Conference on Fracture, June 16-21, 2013, Beijing, China*, 2013. [124](#), [135](#)

- [294] *ASTM E23 - 12c: Standard Test Methods for Notched Bar Impact Testing of Metallic Materials*. ASTM International, West Conshohocken, PA, US. [124](#), [126](#)
- [295] E.J. Pickering and H.K.D.H. Bhadeshia. Macrosegregation and Microstructural Evolution in a Pressure-Vessel Steel. *Metallurgical and Materials Transactions A*, in press, 2014. [130](#)
- [296] B.S. Lee, J.H. Hong, W.J. Yang, M.Y. Huh, and S.H. Chi. Master Curve Characterisation of the Fracture Toughness in Unirradiated and Irradiated RPV Steels Using Full and 1/3-Size Pre-Cracked Charpy Specimens. *International Journal of Pressure Vessels and Piping*, 77:599–604, 2000. [133](#)
- [297] F.M. Beremin. A Local Criterion for Cleavage Fracture of a Nuclear Pressure Vessel Steel. *Metallurgical Transactions A*, 14A:2277–2287, 1984. [133](#), [135](#)
- [298] K.H. Lee, M.C. Kim, B.S. Lee, and D.M. Wee. Master Curve Characterisation of the Fracture Toughness Behavior in SA508 Gr.4N Low Alloy Steels. *Journal of Nuclear Materials*, 403:68–74, 2010. [133](#)
- [299] C.J. McMahon Jr and M. Cohen. Initiation of Cleavage in Polycrystalline Iron. *Acta Metallurgica*, 13:591–604, 1965. [135](#)
- [300] D.A. Curry and J.F. Knott. The Relationship Between Fracture Toughness and Microstructure in the Cleavage Fracture of Mild Steel. *Metal Science*, 10:1–6, 1976. [135](#)
- [301] D.A. Curry and J.F. Knott. Effects of Microstructure on Cleavage Fracture Stress in Steel. *Metal Science*, pages 511–514, November 1978. [135](#)
- [302] J.C. Lautridou and A. Pineau. Crack Initiation and Stable Crack Growth Resistance in A508 Steels in Relation to Inclusion Distribution. *Engineering Fracture Mechanics*, 15(1-2):55–71, 1981. [135](#)
- [303] M. Guttman. The Role of Residuals and Alloying Elements in Temper Embrittlement. *Philosophical Transactions of the Royal Society of London*, 295:169–196, 1980. [135](#), [136](#)

- [304] D. McLean and L. Northcott. Micro-Examination and Electrode-Potential Measurements of Temper-Brittle Steels. *Journal of the Iron and Steel Institute*, 158:169–177, 1948. [135](#)
- [305] D. McLean. *Grain Boundaries in Metals*, chapter 5, pages 116–149. Oxford: Clarendon Press, 1957. [135](#)
- [306] M. Guttman. Equilibrium Segregation in a Ternary Solution: A Model for Temper Embrittlement. *Surface Science*, 53:213–227, 1975. [135](#)
- [307] E.D. Hondros. The Influence of Phosphorus in Dilute Solid Solution on the Absolute Surface and Grain Boundary Energies of Iron. *Proceedings of the Royal Society of London Annual*, 286:479–498, 1965. [135](#)
- [308] R.P. Messmer and C.L. Briant. The Role of Chemical Bonding in Grain Boundary Embrittlement. *Acta Metallurgica*, 30:457–462, 1982. [135](#)
- [309] C.L. Briant and R.P. Messmer. An Electronic Model for the Effect of Alloying Elements on the Phosphorus Induced Grain Boundary Embrittlement of Steel. *Acta Metallurgica*, 30:1811–1818, 1982. [135](#)
- [310] M. P. Seah and E.D. Hondros. Grain Boundary Segregation. *Proceedings of the Royal Society of London Annual*, 335:191–212, 1973. [135](#)
- [311] E. Kantidis, B. Marini, and A. Pineau. A Criterion for Intergranular Brittle Fracture of a Low Alloy Steel. *Fatigue and Fracture of Engineering Materials and Structures*, 17:619–633, 1994. [135](#)
- [312] E.D. Hondros and M. McLean, editors. *The Donald McLean Symposium: Structural Materials - Engineering Application Through Scientific Insight.*, chapter Grain Boundary Segregation and Embrittlement in Multicomponent Systems: Recent Literature Revisited, pages 59–81. Maney Publishing, 1995. [136](#)
- [313] R.R. de Allivez and P.R. Rios. The Influence of Carbon on the Phosphorus Segregation in Iron Alloys. *Scripta Metallurgica*, 17:677–680, 1983. [136](#)

- [314] S. Suzuki, M. Obata, K. Abiko, and H. Kimura. Effect of Carbon on the Grain Boundary Segregation of Phosphorus in Alpha-Iron. *Scripta Metallurgica*, 17:1325–1328, 1983. [136](#)
- [315] J. Wu, S.-H. Song, L.-Q. Weng, T.-H. Xi, and Z.-X. Yuan. An Auger Electron Spectroscopy Study of Phosphorus and Molybdenum Grain Boundary Segregation in a 2.25Cr1Mo Steel. *Materials Characterization*, 59:261–265, 2008. [136](#)
- [316] H. Ohtani and C.J. McMahon Jr. Modes of Fracture in Temper Embrittled Steels. *Acta Metallurgica*, 23:377–386, 1975. [136](#)
- [317] T. Ogura, C.J. McMahon Jr, H.C. Feng, and V. Vitek. Structure-Dependent Intergranular Segregation of Phosphorus in Austenite in a Ni-Cr Steel. *Acta Metallurgica*, 26:1317–1330, 1978. [136](#)
- [318] J.M. Capus. Austenite Grain Size and Temper Brittleness. *Journal of the Iron and Steel Institute*, pages 922–927, November 1962. [136](#)
- [319] R.A. Mulford, C.J. McMahon Jr, D.P. Pope, and H.C. Feng. Temper Embrittlement of Ni-Cr Steels by Phosphorus. *Metallurgical and Materials Transactions A*, 7A:1183–1195, 1976. [136](#)
- [320] S.G. Druce, G. Gage, and G. Jordon. Effect of Ageing on Properties of Pressure Vessel Steels. *Acta Metallurgica*, 34:641–652, 1986. [136](#)
- [321] H. Pous-Romero, I. Lonardelli, D. Cogswell, and H.K.D.H. Bhadeshia. Austenite Grain Growth in a Nuclear Pressure Vessel Steel. *Materials Science and Engineering A*, 567:72–79, 2013. [136](#)
- [322] P. Doig, P.E.J. Flewitt, and R.K. Wild. A Comparison of X-ray (STEM) and Auger Electron Spectroscopy for the Microanalysis of Grain Boundary Segregation. *Philosophical Magazine A*, 37(6):759–768, 1978. [137](#)
- [323] S.F. Pugh. *Defects and Fracture*, chapter Macroscopic Segregation in Ingots and its Implications in Modelling of Structures Made From Heavy Sections, pages 241–251. Springer Netherlands, 1982. [139](#)

- [324] P. Bocquet, R. Blondeau, I. Portrault, J.P. Badeau, and R. Dumont. Improvement in the Reliability of Shells for Light Water Reactors by Manufacture from Hollow Ingots. *Nuclear Engineering and Design*, 130:467–475, 1991. [139](#)
- [325] DEFORM, version 10.2, Scientific Forming Technologies Corporation, <http://www.deform.com/products/>. [153](#)
- [326] MATLAB software, version 2012b, <http://www.mathworks.co.uk>. [155](#)
- [327] S. Kawaguchi, H. Tsukada, K. Suzuki, I. Sato, M. Kusuhashi, and S. Onodera. Application of 20 MnMoNi 5 5 Steel with Lowered Si Content to Heavy Thick STeam Generator Tube Sheet Forgings. *Nuclear Engineering and Design*, 87:249–257, 1985. [179](#)
- [328] B. Tanguy, J. Besson, and A. Pineau. Comment on “Effect of Carbide Distribution on the Fracture Toughness in the Transition Temperature Region of an SA 508 Steel”. *Scripta Materialia*, 49:191–197, 2003. [179](#)
- [329] J.R. Hawthorne. Composition Influences and Interactions in Radiation Sensitivity of Reactor Vessel Steels. *Nuclear Engineering and Design*, 89:223–232, 1985. [179](#)
- [330] H.G.J. Moseley. The High-Frequency Spectra of the Elements. *Philosophical Magazine*, 1913. [186](#)
- [331] R. Jenkins. *X-Ray Fluorescence Spectroscopy*. John Wiley & Sons, Inc., 2nd edition, 1999. [186](#)
- [332] T. Paunesku, S. Vogt, J. Maser, B. Lai, and G. Woloschak. X-Ray Fluorescence Microprobe Imaging in Biology and Medicine. *J. Cellular Biochemistry*, 99:1489–1502, 2006. [186](#)
- [333] M. Mantler and M. Schreiner. X-Ray Fluorescence Spectrometry in Art and Archaeology. *X-Ray Spectrometry*, 29:3–17, 2000. [186](#)

- [334] R.G. Rothwell, editor. *New Techniques in Sediment Core Analysis*. Geological Society Special Publication No. 267. The Geological Society, London, 2006. [186](#)
- [335] J.S. Krafcik and J.A. Brooks. Compositional Mapping of Large Samples Using X-Ray Fluorescence. In G.F. Vander Voort, editor, *Developments in Materials Characterization Technologies*, pages 111–118. ASM International, 1996. [186](#), [202](#)
- [336] H.M. Volz, G.J. Havrilla, R. M. Aikin Jr., and V.M. Montoya. Macroscopic X-ray Fluorescence Capability for Large-Scale Elemental Mapping. In *Advances in X-Ray Analysis, Proceedings from the 2010 Denver X-Ray Conference, Aug. 1-6, 2010, Denver, CO, USA.*, 2010. [186](#)
- [337] G.R. Lachance and F. Claisse. *Quantitative X-Ray Fluorescence Analysis*. John Wiley & Sons, Ltd, 1995. [186](#)
- [338] R.M. Rousseau. Detection Limit and Estimate of Uncertainty of Analytical XRF Results. *The Rigaku Journal*, 18(2):33–47, 2001. [186](#)
- [339] Geotek Ltd, Daventry, UK, <http://www.geotek.co.uk/>. [187](#), [207](#)
- [340] Geotek MSCL XYZ software, version 3.4. Geotek Ltd, Daventry, UK. [187](#)
- [341] Microsoft®ActiveSync®Version 4.5.0 (Build 5096), Microsoft Corporation. [187](#)
- [342] Innov-X Delta Advanced PC Software, Olympus Corporation. [187](#)
- [343] Patented Diffusion-Bonding Process, A.A. Shirzadi: USA Patent 6,669,534 B2; UK Patent 2380491. [188](#)
- [344] V.E. Burke, R. Jenkins, and D.K. Smith. *A Practical Guide for the Preparation of Specimens for X-Ray Fluorescence and Z-Ray Diffraction Analysis*. John Wiley & Sons, Inc., 1998. [195](#), [198](#)
- [345] P. Schultheiss, Geotek Ltd, private communication. [198](#)

- [346] A. Hultgren. A and V Segregation in Killed Steel Ingots. *Scandinavian Journal of Metallurgy*, 2:217–227, 1973. [241](#)
- [347] M. Durand-Charre. *Microstructure of Steels and Cast Irons*. Springer, 2004. [241](#)
- [348] P.W. Waterworth and P.C. Morgan. Segregation in Wide-End-Up Ingots (Part II). Technical Report EUR 7723/II, Commission of the European Communities, Technical Steel Research: British Steel Corporation, Brussels, Luxembourg, 1982.